MID-AMERICA
TRANSPORTATION CENTER

Report # MATC-UNL: 004-13

Final Report
WBS: 25-1121-0005-004-13

Investigation and Development of a MASH Test Level 6 Barrier - Phase III

Jennifer Rasmussen, PhD, PE
Research Assistant Professor
Department of Civil and Environmental Engineering
University of Nebraska-Lincoln

Ronald K. Faller, PhD, PE
Research Professor
Department of Civil and Environmental Engineering

Joshua S. Steelman, PhD, PE
Assistant Professor
Department of Civil and Environmental Engineering

Cody S. Stolle, PhD
Research Assistant Professor
Department of Mechanical and Materials Engineering

Elisa Vasquez, BSME
Graduate Research Assistant
Department of Mechanical and Materials Engineering

University of Nebraska Lincoln

2021

A Cooperative Research Project sponsored by
U.S. Department of Transportation- Office of the Assistant Secretary for Research and Technology

University of Nebraska Lincoln
The University of Iowa
The University of Kansas
Missouri S&T
Lincoln University Missouri
Nebraska Indian Community College
University of Nebraska Omaha
University of Nebraska Medical Center
KU Medical Center The University of Kansas

Investigation and Development of a MASH Test Level 6 Barrier - Phase III

Final Report

Jennifer Rasmussen, Ph.D., P.E. (PI)
Research Assistant Professor
Midwest Roadside Safety Facility
Department of Civil and Environmental Engineering
University of Nebraska-Lincoln

Ronald K. Faller, Ph.D., P.E. (Co-PI)
Research Professor
Midwest Roadside Safety Facility
Department of Civil and Environmental Engineering
University of Nebraska-Lincoln

Joshua S. Steelman, PhD., P.E. (Co-PI)
Assistant Professor
Department of Civil and Environmental Engineering
University of Nebraska-Lincoln

Cody S. Stolle, Ph.D.
Research Assistant Professor
Midwest Roadside Safety Facility
Department of Mechanical and Materials Engineering
University of Nebraska-Lincoln

Elisa Vasquez, B.S.M.E.
Graduate Research Assistant
Department of Mechanical and Materials Engineering
University of Nebraska-Lincoln

A Report on Research Sponsored by

Mid-America Transportation Center

University of Nebraska–Lincoln

October 2021

INVESTIGATION AND DEVELOPMENT OF A MASH TEST LEVEL 6 BARRIER, PHASE III

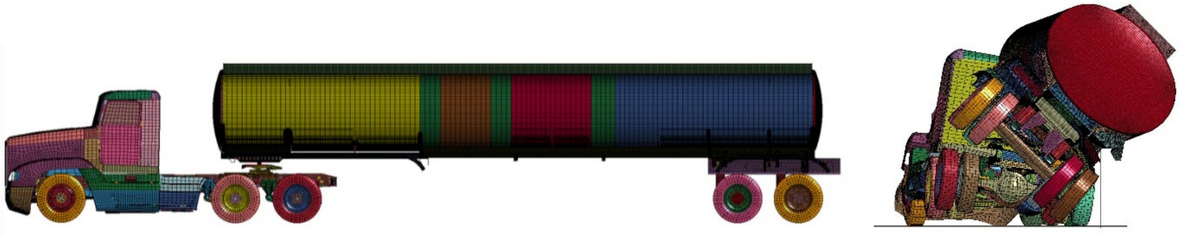

Submitted by

Elisa Vasquez, B.S.M.E.
Graduate Research Assistant

Jennifer D. Rasmussen, Ph.D., P.E.
Research Assistant Professor

Cody S. Stolle, PhD.
Research Assistant Professor

Ronald K. Faller, Ph.D., P.E.
Research Professor and MwRSF Director

Joshua S. Steelman, Ph.D., P.E.
Assistant Professor

MIDWEST ROADSIDE SAFETY FACILITY
Nebraska Transportation Center
University of Nebraska-Lincoln

Main Office
Prem S. Paul Research Center at Whittier School
Room 130, 2200 Vine Street
Lincoln, Nebraska 68583-0853
(402) 472-0965

Outdoor Test Site
4630 N.W. 36th Street
Lincoln, Nebraska 68524

Submitted to

MID-AMERICA TRANSPORTATION CENTER
2200 Vine Street
Lincoln, Nebraska 68583

MwRSF Research Report No. TRP-03-457-21

October, 2021

TECHNICAL REPORT DOCUMENTATION PAGE

1. Report No. 25-1121-0005-004-13	**2. Government Accession No.**	**3. Recipient's Catalog No.**

4. Title and Subtitle Investigation and Development of a MASH Test Level 6, Cost-Effective, Barrier System for Containing Heavy Tractor Tank-Trailer Vehicles and Mitigating Catastrophic Crash Event – Phase III	**5. Report Date** October, 2021
	6. Performing Organization Code
7. Author(s) Rasmussen, J. D., PhD ORCID: 0000-0003-0909-0850 Stolle, C., PhD ORCID: 0000-0001-6674-7383 Faller, R. K., PhD ORCID: 0000-0001-7660-1572 Steelman, J., PhD ORCID: 0000-0002-8664-7520 Vasquez, E.	**8. Performing Organization Report No.** 25-1121-0005-004-13
9. Performing Organization Name and Address Midwest Roadside Safety Facility (MwRSF) Nebraska Transportation Center University of Nebraska-Lincoln	**10. Work Unit No.**
Main Office: Prem S. Paul Research Center at Whittier School Room 130, 2200 Vine Street Lincoln, Nebraska 68583-0853 Outdoor Test Site: 4630 N.W. 36th Street Lincoln, Nebraska 68524	**11. Contract** 69A3551747107
12. Sponsoring Agency Name and Address Midwest Pooled Fund Program Nebraska Department of Transportation 1500 Nebraska Highway 2 Lincoln, Nebraska 68502	**13. Type of Report and Period Covered** Final Report: Jan – Dec 2020
	14. Sponsoring Agency Code TRB RiP 91994-63

15. Supplementary Notes

Prepared in cooperation with U.S. Department of Transportation, Federal Highway Administration

16. Abstract

The objective of this research project was to replicate the dynamic behavior of a truck-tank trailer combination vehicle using representative dimensions, properties, and inertias of the trailer/fluid ballast combination. A literature review was completed describing techniques for modeling fluids and fluid-container interactions using finite element analysis. Various fluid modeling techniques were identified, and parameters associated with those models were archived. Next, researchers utilized the tank geometry of the elliptical straight-frame 5949 trailer produced by LBT Inc. to generate a finite element mesh using finite element analysis preprocessors HyperMesh and LS PrePost. Material properties were taken from reference guides, research papers, and specifications from LBT, a tank trailer manufacturer. Component constraints were added to the model to mimic fasteners such as bolts and nuts. Contacts were also added to allow the tank to impact external features, as well as to allow tank components to interact with each other during dynamic events. Different techniques were employed to generate fluid meshes to reside within the interior tank structure. Next, preliminary properties for the fluids were generated using reference materials from published papers. Finally, fluid components were implemented into the tank-trailer model. The recommended barrier height to contain a tractor-tank vehicle was determined to be 60 in. for a rigid, vertical-faced barrier by a barrier height analysis done through LS-DYNA computer simulation. Recommendations for how to improve the tank-trailer model were also presented.

17. Key Words Highway Safety, Roadside Appurtenances, TL-6, Tractor-Trailer, Computer Simulation, MASH 2016	**18. Distribution Statement** No restrictions. This document is available through the National Technical Information Service.

19. Security Classification (of this report) Unclassified	**20. Security Classification (of this page)** Unclassified	**21. No. of Pages** 183	**22. Price**

Form DOT F 1700.7 (8-72) Reproduction of completed page authorized

Disclaimer Statement

This report was completed with funding from the Mid-America Transportation Center (MATC), a US Department of Transportation (USDOT) Region VII University Transportation Center (UTC). The contents of this report reflect the views and opinions of the authors who are responsible for the facts and the accuracy of the data presented herein. The contents do not necessarily reflect the official views or policies of LBT, Inc, MATC, USDOT, nor the Federal Highway Administration (FHWA). This report does not constitute a standard, specification, regulation, product endorsement, or an endorsement of manufacturers.

Acknowledgements

The authors wish to acknowledge several sources that made a contribution to this project: (1) the Mid-America Transportation Center (MATC), the USDOT Region VII University Transportation Center (UTC), for funding this research effort; (2) LBT, Inc., for providing information on tank trailers; and (3) the Holland Computing Center at the University of Nebraska, which receives support from the Nebraska Research Initiative. Acknowledgement is also given to the following individuals who made a contribution to the completion of this research project.

Midwest Roadside Safety Facility
J.D. Reid, Ph.D., Professor
J.C. Holloway, M.S.C.E., E.I.T., Assistant Director –Physical Testing Division
K.A. Lechtenberg, M.S.M.E., E.I.T., Research Engineer
R.W. Bielenberg, M.S.M.E., E.I.T., Research Engineer
S.K. Rosenbaugh, M.S.C.E., E.I.T., Research Engineer
M. Asadollahi Pajouh, Ph.D., Post-Doctoral Research Associate
A.T. Russell, B.S.B.A., Testing and Maintenance Technician II
E.W. Krier, B.S., Construction and Testing Technician II
S.M. Tighe, Construction and Testing Technician I
D.S. Charroin, Construction and Testing Technician I
R.M. Novak, Construction and Testing Technician I
J.E. Kohtz, B.S.M.E., CAD Technician
E.L. Urbank, B.A., Research Communication Specialist
Undergraduate and Graduate Research Assistants

SI* (MODERN METRIC) CONVERSION FACTORS

APPROXIMATE CONVERSIONS TO SI UNITS

Symbol	When You Know	Multiply By	To Find	Symbol
		LENGTH		
in.	inches	25.4	millimeters	mm
ft	feet	0.305	meters	m
yd	yards	0.914	meters	m
mi	miles	1.61	kilometers	km
		AREA		
in^2	square inches	645.2	square millimeters	mm^2
ft^2	square feet	0.093	square meters	m^2
yd^2	square yard	0.836	square meters	m^2
ac	acres	0.405	hectares	ha
mi^2	square miles	2.59	square kilometers	km^2
		VOLUME		
fl oz	fluid ounces	29.57	milliliters	mL
gal	gallons	3.785	liters	L
ft^3	cubic feet	0.028	cubic meters	m^3
yd^3	cubic yards	0.765	cubic meters	m^3
		NOTE: volumes greater than 1,000 L shall be shown in m^3		
		MASS		
oz	ounces	28.35	grams	g
lb	pounds	0.454	kilograms	kg
T	short ton (2,000 lb)	0.907	megagrams (or “metric ton”)	Mg (or "t")
		TEMPERATURE (exact degrees)		
°F	Fahrenheit	5(F-32)/9 or (F-32)/1.8	Celsius	°C
		ILLUMINATION		
fc	foot-candles	10.76	lux	lx
fl	foot-Lamberts	3.426	candela per square meter	cd/m^2
		FORCE & PRESSURE or STRESS		
lbf	poundforce	4.45	newtons	N
lbf/in^2	poundforce per square inch	6.89	kilopascals	kPa

APPROXIMATE CONVERSIONS FROM SI UNITS

Symbol	When You Know	Multiply By	To Find	Symbol
		LENGTH		
mm	millimeters	0.039	inches	in.
m	meters	3.28	feet	ft
m	meters	1.09	yards	yd
km	kilometers	0.621	miles	mi
		AREA		
mm^2	square millimeters	0.0016	square inches	in^2
m^2	square meters	10.764	square feet	ft^2
m^2	square meters	1.195	square yard	yd^2
ha	hectares	2.47	acres	ac
km^2	square kilometers	0.386	square miles	mi^2
		VOLUME		
mL	milliliter	0.034	fluid ounces	fl oz
L	liters	0.264	gallons	gal
m^3	cubic meters	35.314	cubic feet	ft^3
m^3	cubic meters	1.307	cubic yards	yd^3
		MASS		
g	grams	0.035	ounces	oz
kg	kilograms	2.202	pounds	lb
Mg (or "t")	megagrams (or “metric ton”)	1.103	short ton (2,000 lb)	T
		TEMPERATURE (exact degrees)		
°C	Celsius	1.8C+32	Fahrenheit	°F
		ILLUMINATION		
lx	lux	0.0929	foot-candles	fc
cd/m^2	candela per square meter	0.2919	foot-Lamberts	fl
		FORCE & PRESSURE or STRESS		
N	newtons	0.225	poundforce	lbf
kPa	kilopascals	0.145	poundforce per square inch	lbf/in^2

*SI is the symbol for the International System of Units. Appropriate rounding should be made to comply with Section 4 of ASTM E380.

Table of Contents

List of Figures

List of Tables

Chapter 1 Introduction

1.1 Background

Roadside and median barriers, including bridge rails, have been commonly used to prevent run-off-road (ROR) events and to prevent errant motorists from striking hazardous fixed objects or geometric features. For ROR situations, it is deemed appropriate to utilize barrier systems that are capable of safely containing and redirecting passenger vehicles. These barriers are most commonly evaluated according to the Test Level 3 (TL-3) safety performance guidelines published in either National Cooperative Highway Research Program (NCHRP) Report No. 350, Recommended Procedures for the Safety Performance Evaluation of Highway Features [1] or the American Association of State highway and Transportation Officials (AASHTO) Manual for Assessing Safety Hardware [3]. A TL-3 test condition utilizes two types of vehicles, a 2,420-lb passenger car and a 5,000-lb pick-up truck, to impact the barrier at a speed of 62 mph at a 25-degree angle.

There are situations in which it may be necessary to use higher-performance vehicle containment barriers (i.e., TL-4 through TL-6). These include when the percentage of trucks or heavy vehicle traffic is high and when the probability of vehicle penetration beyond the longitudinal barrier could produce substantial injury or infrastructure damage. TL-4, TL-5, and TL-6 test vehicles are a 22,000-lb single unit truck; an 80,000-lb tractor-van trailer truck; and an 80,000-lb tractor-tank trailer truck, respectively. TL-4, TL-5, and TL-6 impact conditions are 56 mph at 15 degrees, 50 mph at 15 degrees, and 50 mph at 15 degrees, respectively.

To date, only one TL-6 vehicle containment system was successfully tested and evaluated according to NCHRP Report 230 [4] safety performance criteria using a tractor tank-trailer vehicle. This combination barrier system consisted of a lower reinforced concrete solid parapet with an upper beam and post railing system and measured 90 in. tall. Unfortunately, the cost, height, and appearance of this TL-6 containment barrier have discouraged widespread implementation. Due to its current configuration and cost, few TL-6 barriers have been utilized in the real world thus far. Real-world uses for the TL-6 barrier could include prevention and mitigation of: (1) cross median, opposing-traffic, vehicle crashes involving hazardous heavy tanker trucks along urban freeways and interstates and (2) tanker vehicle penetration or override of existing TL-4 or TL-5 barriers located on bridges, elevated road structures, or high volume roadways, which could result in potentially-catastrophic events near schools, malls, sports venues, concert arenas, military bases, international airports, critical government buildings, or other high-risk facilities. As such, there exists a need to develop a new, cost-effective, structurally adequate, reduced-height, vehicle containment system that is safe for motorists, is capable of containing errant vehicle impacts with heavy tanker-truck vehicles, and prevents and/or mitigates the consequences of catastrophic crashes into high-risk facilities or highly-populated areas.

1.2 Research Objective

The research described in this thesis is one component of a larger research effort. The principal objective of this project was to develop a new, cost-effective, MASH TL-6 barrier to safely redirect vehicles ranging from 2,420-lb small passenger cars to 80,000-lb tractor-tank trailers. For this thesis report, the objective was to replicate the dynamic behavior of a truck-tank trailer vehicle using representative dimensions, properties, and inertias of the trailer/fluid ballast combination.

1.3 Research Scope

The objective was achieved through the completion of several tasks. First, a literature review was completed describing techniques for modeling fluids and fluid-container interactions using finite element analysis. Various fluid modeling techniques were identified, and parameters associated with those models were archived. Next, researchers developed a finite element analysis (FEA) model of an elliptical straight-frame 5949 trailer produced by LBT Inc. and connected it to a previously-developed model of a day cab tractor to produce a full tractor-tank trailer combination vehicle model. Component geometries, material properties, connections, and contacts were modeled to represent the dynamic behavior of the tank trailer. Finally, preliminary properties for the fluids were generated using reference materials from published papers. Lagrangian and ALE formulations were modeled and evaluated. The Lagrangian fluid model was successfully implemented into the TL-6 vehicle model. A model validation was done with an existing crash test. After the vehicle validation, a barrier height analysis was done to evaluate and recommend a minimum barrier height for a TL-6 barrier.

Because the research regarding the modeling of the tractor-tank trailer vehicle was performed spanning multiple research years, modeling results were broken into Phases. Phase I of the research effort was completed by Whitfield [1] and Phase II, described herein, was performed by Vasquez.

Chapter 2 Literature Review

2.1 Scope of Review

Tank-truck trailer ROR crashes can result in a catastrophic outcome. Trailers may carry hazardous contents such as chemicals, gasoline, and fuel oils, and damaging or rolling the trailers could result in a dangerous and environmentally destructive chemical release that requires costly cleanup and causes significant traffic congestion. For the purposes of computer simulation of these tractor-tank trailer combination vehicles, it is important to reasonably replicate the internal liquid sloshing behavior of the fluid, which may dynamically load against the side of a tank and create vehicle/trailer rollover instability. Slosh refers to the periodic movement of a liquid inside a container, in this case the oscillatory motion of the liquid inside the tank structures. For this reason, the literature review was primarily focused on the Fluid Structure Interaction (FSI) inside the tank for stable tank-trailer interactions during dynamic impact events.

The cited research reports relevant to fluid slosh were reviewed to formulate the current knowledge and status for the fluid modeling analysis. The reviewed reports are briefly summarized below, particularly focused on (1) methods for modeling fluid moving inside a tank container and (2) vehicle simulation.

2.2 Highway Barrier Safety Performance Criteria

A full-scale crash test is a method to measure the impact performance of a roadside safety feature based on criteria for (1) structural adequacy, (2) occupant risk, and (3) post-impact vehicular response. Since 2009, MASH [3] has been the standard testing manual for roadside safety feature evaluation. Prior to MASH, NCHRP Report No. 230 [4] and 350 [1] provided guidance for evaluating safety hardware. MASH defines the impact conditions and evaluation criteria for each type of roadside safety hardware. For roadside parapets and barriers, MASH provides six different test levels, TL-1 through TL-6. Each test level represents different vehicle classes and impact conditions under which the barrier must safely contain and redirect errant vehicles. A TL-6 barrier must be able to safely contain and redirect TL-6 vehicles, which include a tractor-van trailer weighing 80,000 lb. and tractor-tank trailer weighing 80,000 lb.

Table 2.1 MASH Vehicle Criteria

Test Level	**Barrier Section**	**Test No.**	**Vehicle**	**Impact Speed mph**	**Impact Angle deg**	**Acceptable IS Range kip-ft**	**Evaluation Criteria**[1]
6	Length-of-need	6-10	1100C	62	25	≥51	A,D,F,H,I
		6-11	2270P	62	25	≥106	A,D,F,H,I
		6-12	36000T	50	15	≥404	A,D,G

Table 2.2 MASH Evaluation Criteria

<table>
<tr><th>Evaluation Factors</th><th colspan="4">Evaluation Criteria</th></tr>
<tr><td>**Structural Adequacy**</td><td>A.</td><td colspan="3">Test article should contain and redirect the vehicle or bring the vehicle to a controlled stop; the vehicle should not penetrate, underride, or override the installation although controlled lateral deflection of the test article is acceptable.</td></tr>
<tr><td rowspan="12">**Occupant Risk**</td><td>D.</td><td colspan="3">Detached elements, fragments, or other debris from the test article should not penetrate or show potential for penetrating the occupant compartment, or present undue hazard to other traffic, pedestrians, or personnel in a work zone.
Deformations of, or intrusions into, the occupant compartment should not exceed limits set forth in Section 5.2.2 and Appendix E of MASH.</td></tr>
<tr><td>F.</td><td colspan="3">The vehicle should remain upright during and after collision. The maximum roll and pitch angles are not to exceed 75 degrees.</td></tr>
<tr><td>G.</td><td colspan="3">It is preferable, although not essential, that the vehicle remain upright during and after collision</td></tr>
<tr><td rowspan="5">H.</td><td colspan="3">Occupant impact velocities (OIV) (see Appendix A, Section A5.2.2 of MASH for calculation procedure) should satisfy the following limits:</td></tr>
<tr><td colspan="3">Occupant Impact Velocity Limits, ft/s (m/s)</td></tr>
<tr><td>Component</td><td>Preferred</td><td>Maximum</td></tr>
<tr><td>Longitudinal and Lateral</td><td>30 ft/s</td><td>40 ft/s</td></tr>
<tr><td>Longitudinal</td><td>10 ft/s</td><td>16 ft/s</td></tr>
<tr><td rowspan="4">I.</td><td colspan="3">The occupant ridedown acceleration (see Appendix A, Section A5.2.2 of MASH for calculation procedure) should satisfy the following limits:</td></tr>
<tr><td colspan="3">Occupant Ridedown Acceleration (ORA) Limits (G)</td></tr>
<tr><td>Component</td><td>Preferred</td><td>Maximum</td></tr>
<tr><td>Longitudinal and Lateral</td><td>15.0 G</td><td>20.49 G</td></tr>
</table>

2.3 Phase I: Whitfield TL-6 Truck-Tank Trailer Combination Vehicle Modeling [1]

Investigation of the tractor-tank trailer combination vehicle was completed in two phases. During the first phase, Whitfield investigated and developed new, cost-effective, MASH TL-6 concepts [1]. The author’s research main objective was to design a barrier capable of containing and redirecting vehicles ranging from 2,420-lb small passenger cars to 79,300-lb tractor-tank trailers. This was achieved by researching about previous TL-6 and TL-5 barrier designs and estimating the cost of current TL-5 and TL-6 barriers. Barrier designs were brainstormed, developed, and evaluated based on their ability to meet the design criteria. A minimum barrier height study was conducted to determine a minimum barrier height for the concept designs. The barrier concepts were evaluated using FEA.

2.3.1 Vehicle Model

Whitfield created a simplified TL-6 tractor-tank trailer vehicle model in LS-DYNA to evaluate the barrier concepts. This tractor-tank trailer model was created by modifying an existing TL-5 tractor-van trailer model. The van trailer was removed, leaving the original tractor and rear tandem axle. The tank-trailer geometry was determined based on a vehicle dimension survey. The tank model was designed as an elliptical cylinder 92 in. wide, 63 in. tall, and 488 in. long. The tank was attached to two C-channels rails with 4-in. wide flanges and 8-in. tall x ½-in. thick. Two 4 in. x 4 in. square tube spacer rails were also added between the C-channel rails and the rear tandem axle to suspend the tank at the correct height.

The fluid inside the tank-trailer was modeled with pure Lagrangian solid elements (ELFORM=1) with the properties of water at 20°C (72°F), with a density of 1.0E-6 kg/mm^3, Poisson's ratio of 0.2, and a bulk modulus of 2.15 GPa. The empty vehicle model had a weight of 25,050 lb. With the addition of 54,793 lb of water ballast into vehicle model, the resulting total weight was 79,843 lb.

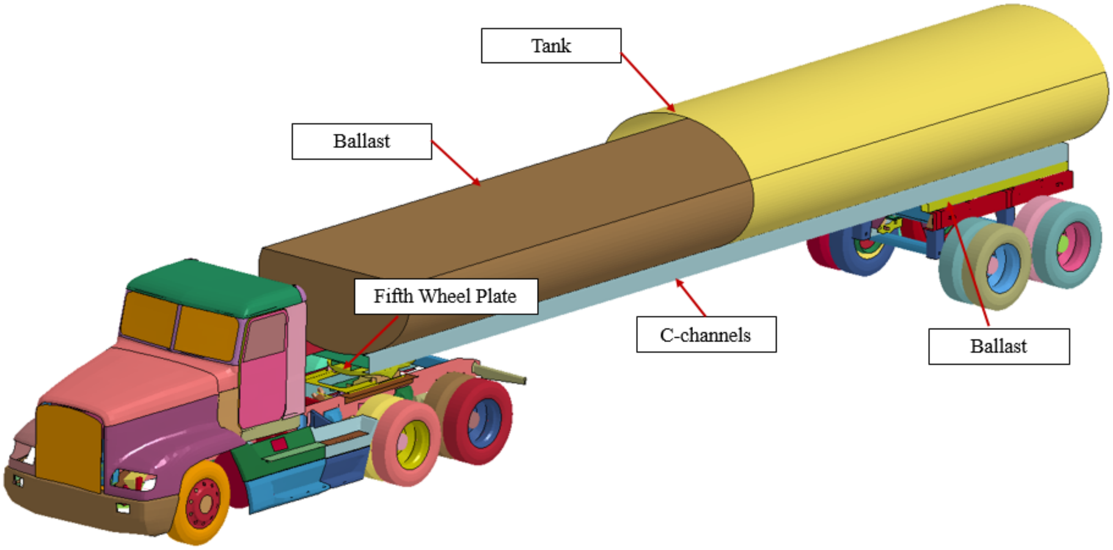

Figure 2.1 Phase I Vehicle Model [1]

2.3.2 Vehicle Mode Validation

To validate the TL-6 vehicle model, Whitfield created a simulation of an existing full-crash test, Instrumented Wall (1988), to compare with the simulation results. Seven smaller rigid walls and one long “downstream” rigid wall were created using *RIGIDWALL_PLANAR_FINITE to simulate 16 load cells. The truck model impacted the barrier model at 15 degrees and 55 mph at a point approximately 90 in. from the upstream edge of the barrier, which is similar to the impact condition in the full-scale crash test.

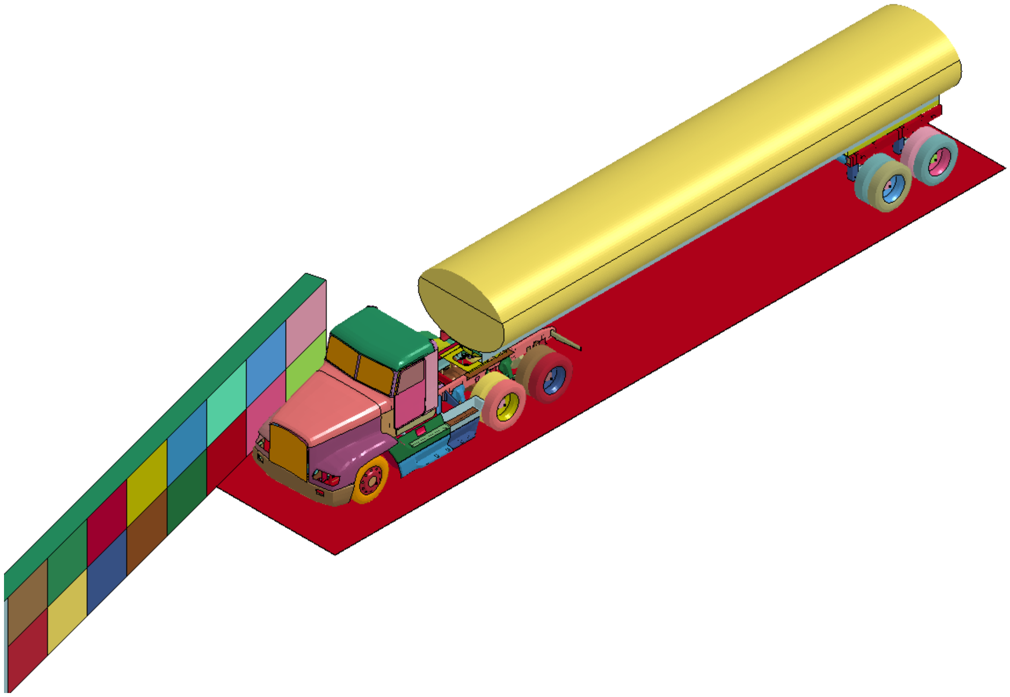

Figure 2.2 Instrumented Wall Simulation [1]

To validate the created vehicle model, Whitfield compared the angular displacements from the full-crash test, which were recorded at the center of gravity (c.g.) of the tractor, with the angular displacements from the simulation. The author extracted x, y, and z rotational velocities from the simulation, and the Euler roll, pitch, and yaw were calculated. Angular displacements were compared, as shown figure 2.3. Using the angular displacement, the author concluded that since the initial roll was similar between the simulation and the test, the tractor impact into the barrier was representative of the full-scale crash test with the exception of the tank impact, which was less accurate.

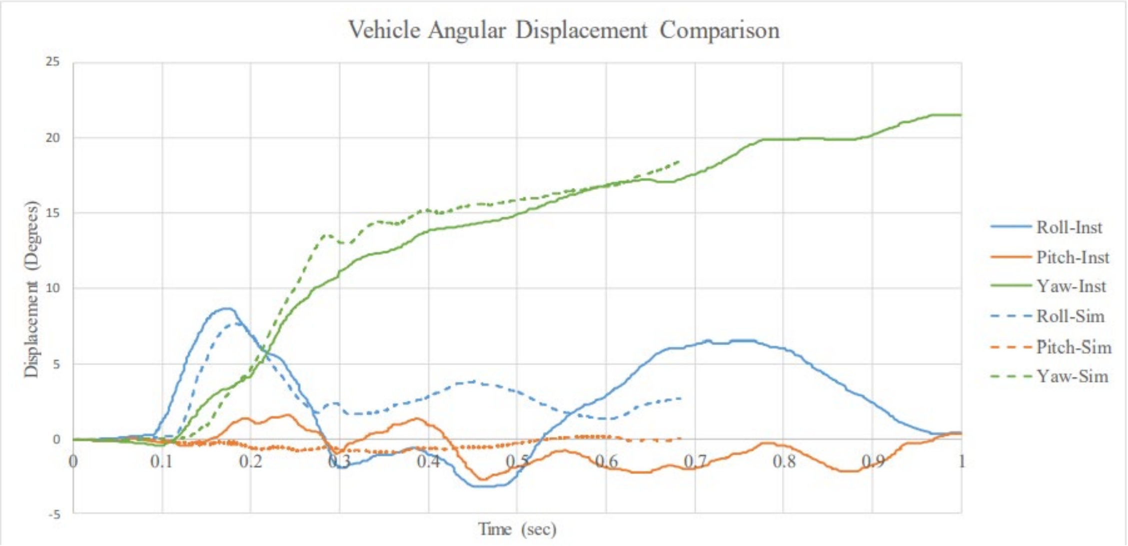

Figure 2.3 Angular Displacement Comparison [1]

The accelerations at the tractor model's c.g. were extracted and compared to the acceleration data from the Instrumented Wall crash test, which was located at the tractor's c.g. A 50-ms rolling average was applied to the resultant data, which was similar to the methods used when processing data from the Instrumented wall test.

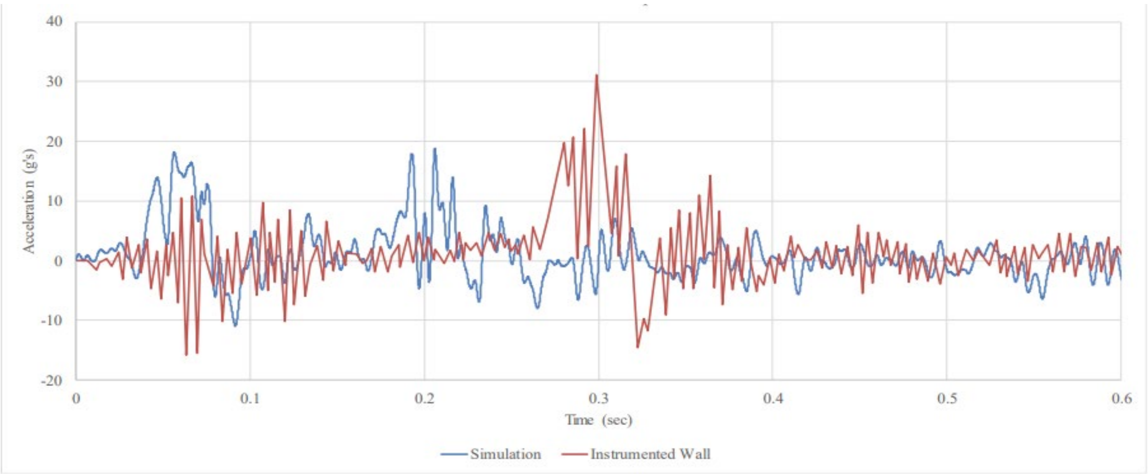

Figure 2.4 Lateral Acceleration Comparison [1]

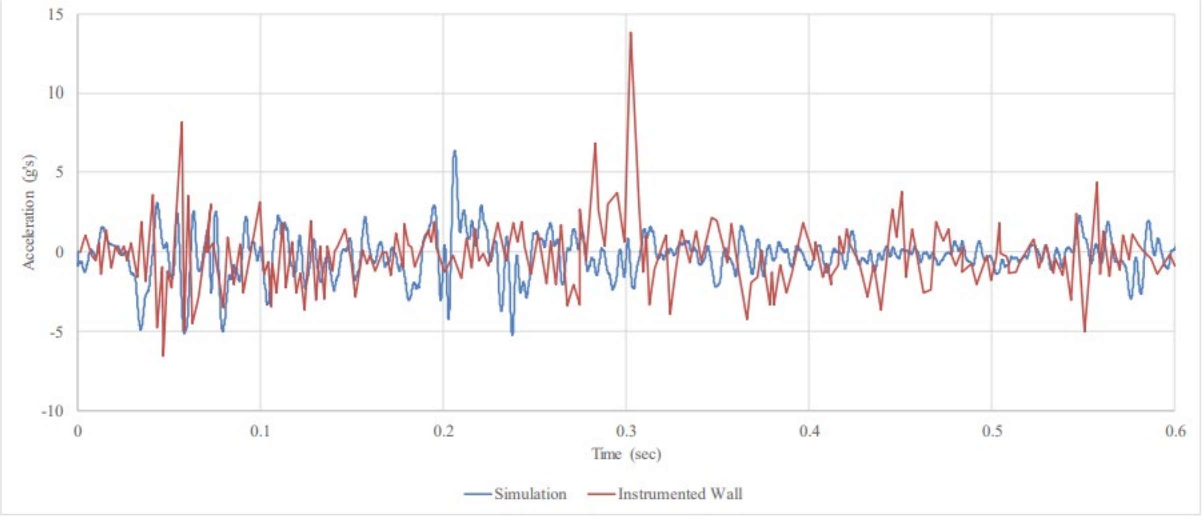

Figure 2.5 Longitudinal Acceleration Comparison [1]

As seen in the lateral acceleration comparison, the initial impact of the tractor (the first set of peaks) was larger in the simulation than the Instrumented Wall test, but not significantly larger. The second peak, which occurred about 100 ms sooner in the simulation than the full scale test and was a result of the front of the tank impacting the barrier, was larger in the full scale test than the simulation. The largest 50-msec average in the Instrumented Wall test was reported as 12.3 g as compared to 8.7 g in the simulation. Overall, the general trend of the two tests was similar, but the magnitude and timing were shifted.

The longitudinal acceleration shows trends similar to those found in the lateral acceleration: increased accelerations during the tractor and front trailer impact occurred in the full scale test versus the simulation and the largest 50-msec average in the full scale test was 2.1 g versus 1.0 g in the simulation data. The general trend was similar, with the full scale test having higher values throughout.

Whitfield extracted the forces exerted on the barrier from the rigid walls and applied a 50-ms rolling average to match the filtering performed on the Instrumented Wall test data. The forces from all rigid walls were summed to obtain the resulting total load. The loads from the simulation and the Instrumented Wall test are shown in figure 2.6 and figure 2.7 When comparing the forces, three distinct peaks can be seen corresponding to three impact events: the front of the tractor, the front of the trailer and tractor-tandem axle, and the rear-tandem axle tail slap. The time at which these impacts occurred are shifted, however, the time between peaks was similar between the Instrumented Wall test and the simulation.

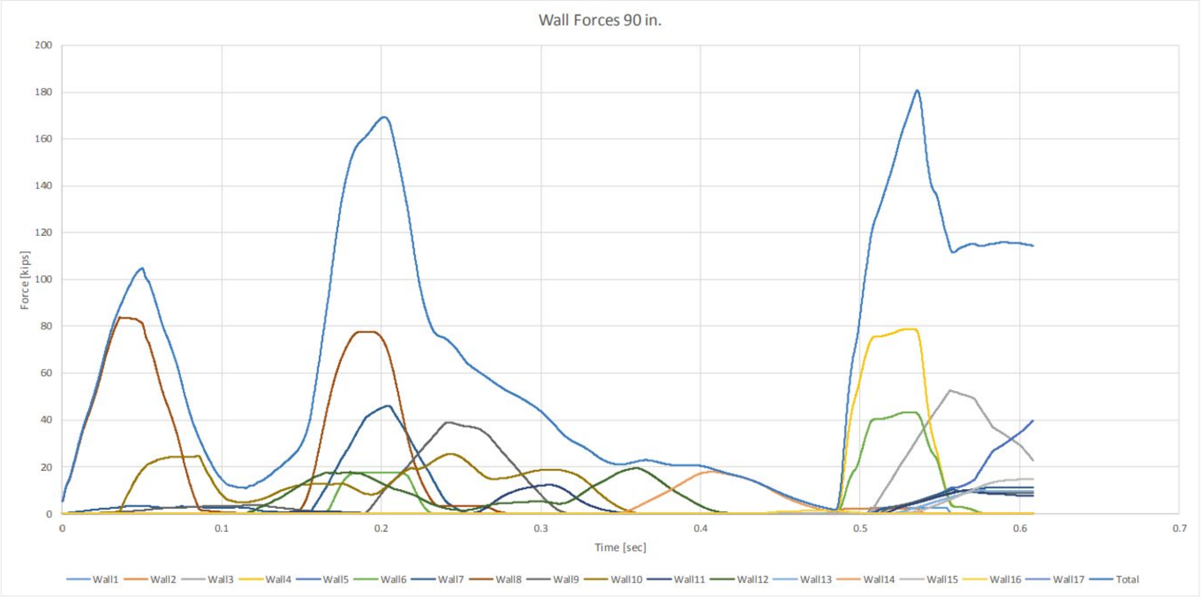

Figure 2.6 90 in. Model Wall Forces [1]

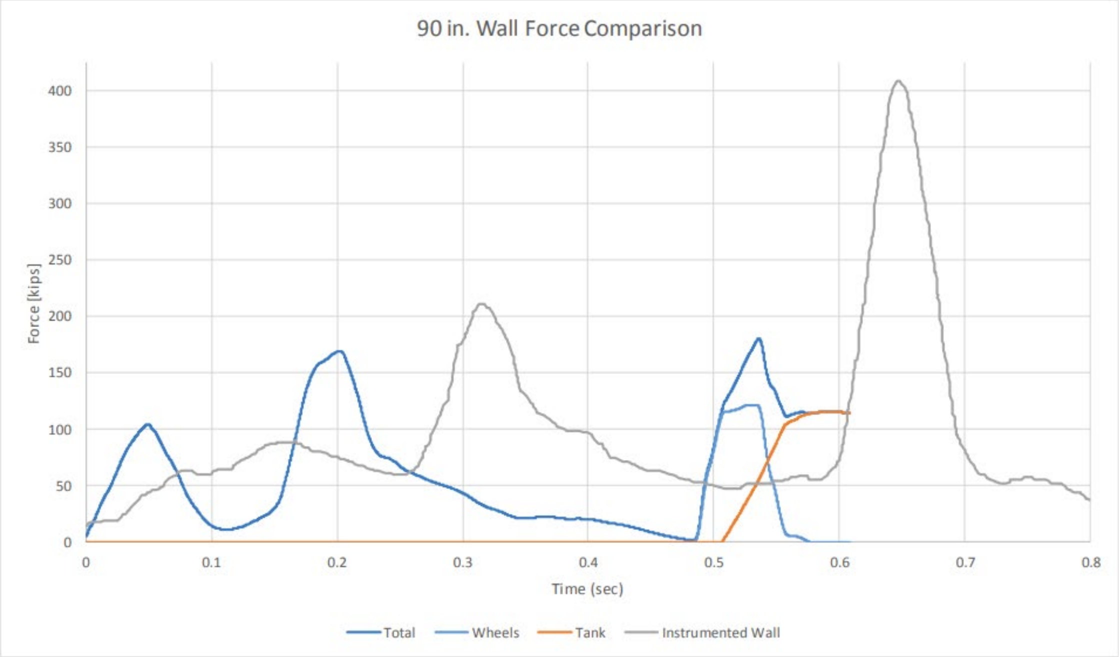

Figure 2.7 Wall Force Comparison [1]

Whitfield concluded that the preliminary TL-6 vehicle model did not accurately represent the impact loads and accelerations from the Instrumented Wall test. The author mentioned the differences in the results may be due to the differences in the 1968 test vehicle and the preliminary vehicle model, which had a geometry based on newer tractor and trailer vehicles. The author listed several components that could be improved in the TL-6 vehicle model to enable more realistic behavior: (1) the fifth wheel plate; (2) the connection between the fifth wheel plate and the tank; (3) the support rails and lateral bracing; (4) the baffles and bulkheads inside the tank; (5) the rails in top of the tank; (6) many of the additional tubes and additional components located underneath the tank; and (7) the ballast inside the tank.

2.4 Computational Methods for Fluid Simulation

A review of common methods for evaluating material flow, including fluids, is presented below. This literature review focuses on the comparison of computational methods and was used to identify preferred methods for simulating fluid inside a tank-trailer.

2.4.1 Lagrangian Formulation

The computational mesh of the Lagrangian formulation is used to describe the behavior of deformable structures, but for some fluid problems a Lagrangian mesh may provide a reasonable fluid behavior. In Lagrangian formulation, nodes are connected to each other with a material medium and the mesh is attached to the material; therefore the mesh follows the fluid material. If the fluid material experiences a large distortion, it may lead to an increase in time processing or analysis termination [8]. For this formulation, the interaction between the fluid and structure was modeled using a contact in which the fluid was defined as a slave. Because the fluid material is continuous and utilizes discrete and deterministic surfaces defined by the user, only a single fluid mass can be modeled (no fluid mixing).

Figure 2.8 illustrates the motion in the mesh and nodes of Lagrangian formulation where ΔX is the change in distance of the meshing and ΔP is the change of position of the nodes as they follow the material deformation.

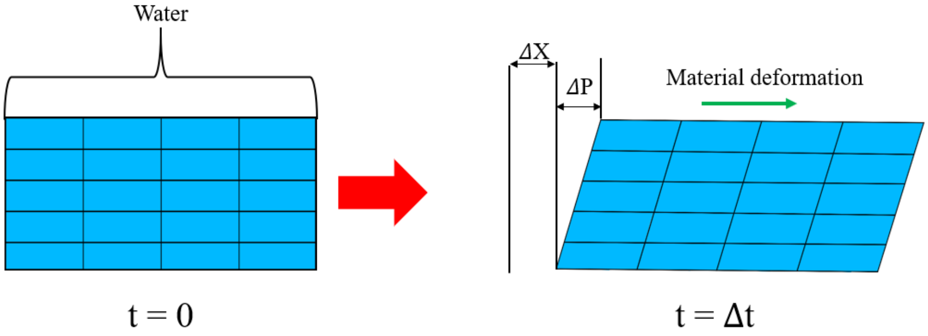

Figure 2.8 Lagrangian Mesh Motion

2.4.2 Eulerian Formulation

The Eulerian formulation for fluid flow analysis advances solutions in time on a mesh fixed on space. The Eulerian method avoids the Lagrangian problem of mesh distortion by fixing nodes in space and calculating future discrete time steps at each iteration for computational efficiency [8]. As a result, the Eulerian method allows mass flow between elements. The Eulerian method consists of a Lagrangian computation at every time step, followed by a re-map phase which restores the distorted mesh to its original state. A disadvantage of the Eulerian approach is that a fine mesh is required to capture the material response which makes the method computationally expensive. Figure 2.9 shows how the Eulerian formulation works. The reference mesh is the air, which remains fixed in space while the water material flows through the reference mesh. ΔP represents the change in position of the water component moving inside the air.

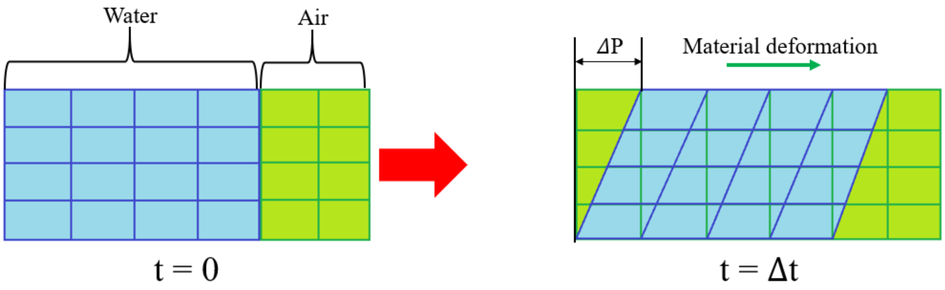

Figure 2.9 Eulerian Mesh Motion

2.4.3 Arbitrary Lagrangian-Eulerian (ALE) Formulation

The computational ALE is a finite element formulation created by combining features of Lagrangian and Eulerian computational methods [9]. The Lagrangian domain evaluates the movement and/or deformation of the structural components of the model. The Eulerian domain deals with the movement of the air or general fluid. With this method, the motion of the mesh is independent from the motion of the analyzed material. Figure 2.10 demonstrates how the ALE formulation works. The water material flows through the air mesh while the mesh can move according to applied boundary conditions. In this case, *Δ*X represents the translation of the mesh and *Δ*P represents the change in position of the material flowing through the reference mesh. The advantage of the ALE computational method is that it allows smoothing of a distorted mesh without performing a complete re-mesh. However, ALE methods require careful consideration of contacts, material definition, and flow.

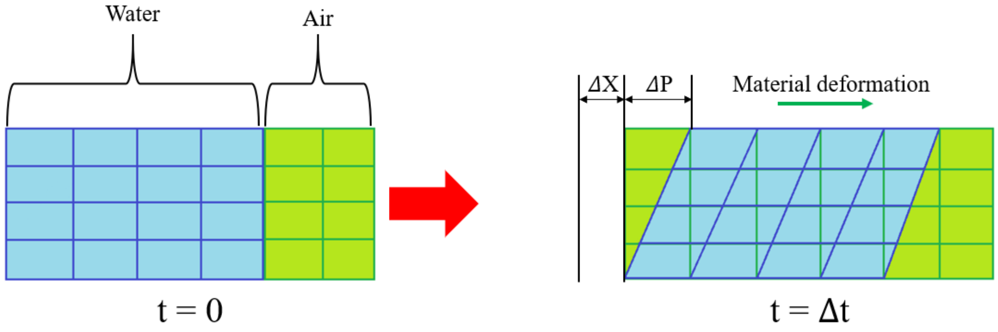

Figure 2.10 ALE Mesh Motion

2.4.4 Smooth Particle Hydrodynamics Formulation

Smooth Particle Hydrodynamics (SPH) is a meshless Lagrangian method that does not suffer from mesh distortion in large deformation problems [9]. Models comprising SPH definitions evaluate the movement of packets of material, evaluated as smooth spherical particles, which can interact with each other with surface-to-surface contacts, Van der Waals forces, mixing friction, and tensile or compressive forces. Each SPH element remains rigid and spherical throughout the simulation. Because this requires the computation of inter-particle dynamics and the kinematics of many particles and a fine mesh is often required to accurately model fluid behaviors, SPH methods tend to be computationally expensive.

An example of motion in the SPH method is shown in figure 2.11. This formulation allows the user to apply any boundary condition, such as translation (*Δ*X) and change in position (*Δ*P) of the particles.

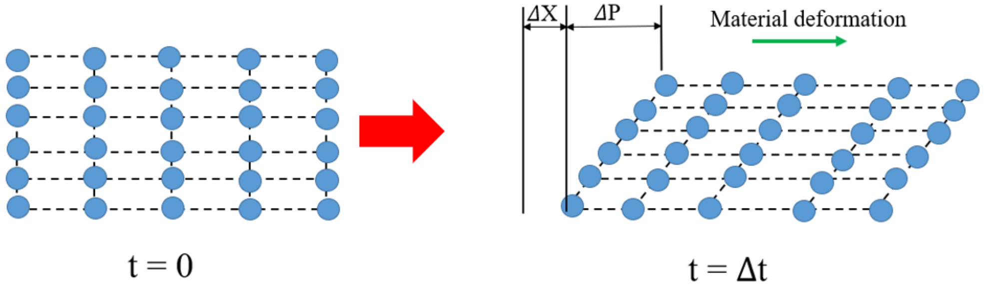

Figure 2.11 Illustration of SPH Deformations

2.5 Computational Fluid Dynamic Method in LS-DYNA

The problem of fluid sloshing motion inside a spherical or cylindrical tank, which is usually described using three-dimensional flow [7], has been studied since the 1960s. The liquid sloshing influences the safety performance of tank-trailer vehicles because of the hydrodynamic forces and moments created from the liquid oscillation inside the tank, thus reducing the stability of the filled or partially filled tank. Tank-trailers have anti-slosh devices, known as baffles, shown in figure 2.12. These devices can reduce the motion of the liquid and provides stability to the tank vehicle. FEA has been performed to optimize the safety performance of tank-trailer vehicles, focusing on the sloshing behavior inside the tank to develop new techniques in fuel tanks to reduce this phenomenon.

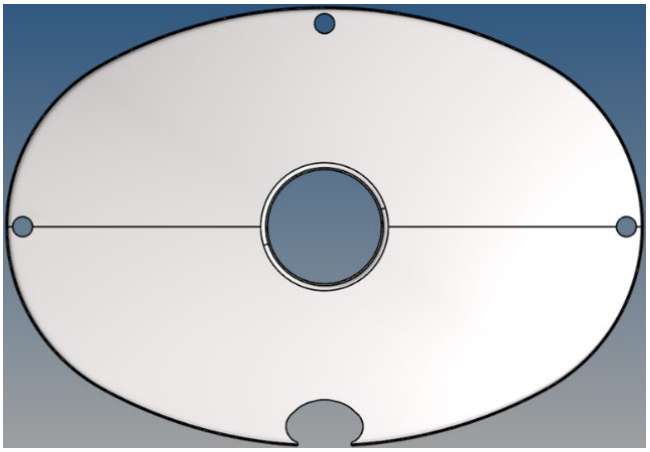

Figure 2.12 Baffle Component

For more than 50 years the problem of sloshing was investigated as a new field called Fluid Structure Interaction (FSI), focusing on improving accuracy and developing new modeling techniques. These techniques have been utilized to investigate the behavior of fluids due to the variation of fluid flow and pressure during an impact, and the complexity of water when flasked inside a tank.

Gautman and Mucino were the first to study the rollover stability of a partially filled tanker truck using FEA [10]. This was achieved by modeling a simple mechanical pendulum inside the tank to simulate the fluid sloshing effect.

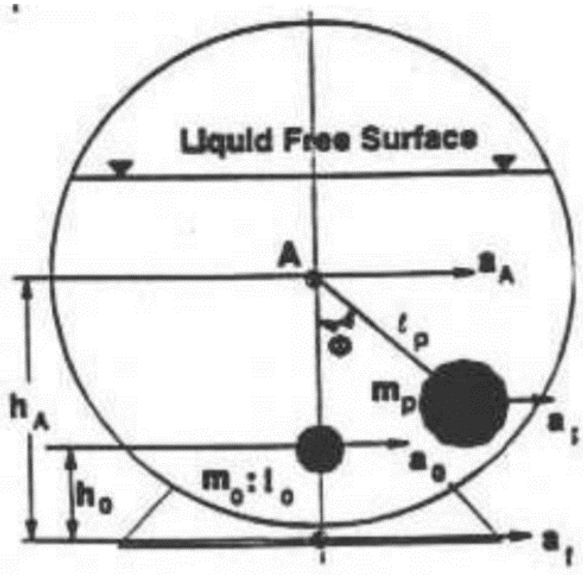

Figure 2.13 Mechanical Analogy of a Cylindrical Fluid-Filled Tank [10]

Gautman and Mucino assumed the sloshing action of the fluid created forces inside the tank body that could be simulated with a mechanical pendulum.

Vesenjak et al. conducted a research study utilizing different FSI models in LS-DYNA to simulate the sloshing of fuel inside a contained box [9]. Lagrangian, Eulerian, ALE and SPH methods were used to simulate the fluid.

Vesenjak et al. modeled a closed container box partially filled with water (60%) and air (40%). The box started at rest and then was subjected to a longitudinal time-dependent acceleration. Both the water and air were modeled with null material (Type 9). Air was included in ALE and Eulerian formulations. Equations of state types Gruneisen and Ideal Gas Law were applied to water and air, respectively. Automatic nodes to surface contact were used in the SPH and Lagrangian models, and constrained Lagrange in solid formulation was used to pair the Eulerian and ALE models.

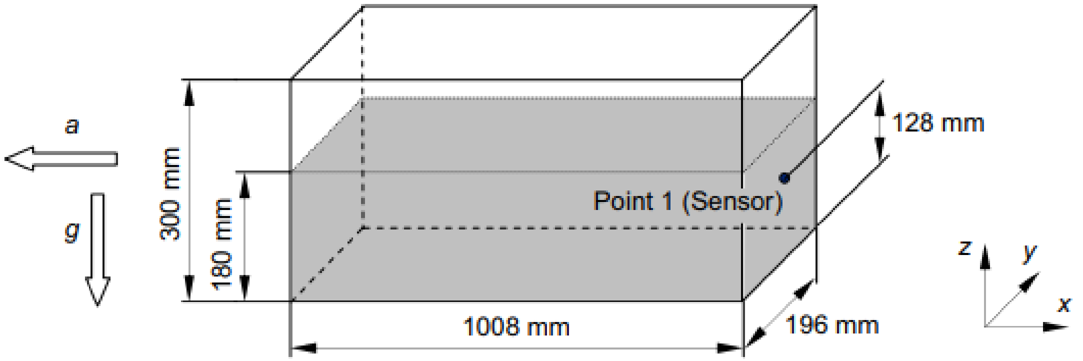

Figure 2.14 Dimensions and Initial Conditions of Plexiglas [9]

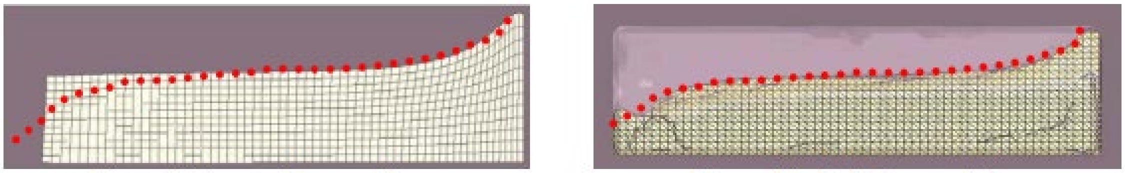

Figure 9: Lagragian model

Figure 10: Eulerian model

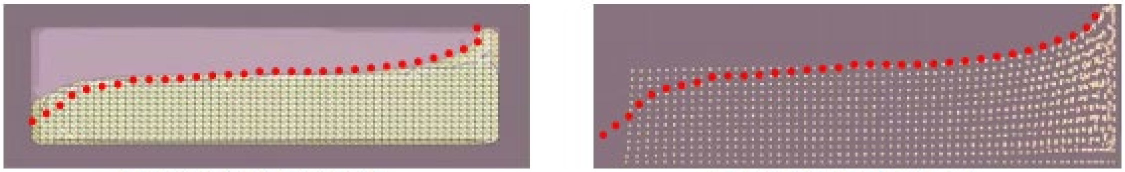

Figure 11: ALE model

Figure 12: SPH model

Figure 2.15 Fluid Model Comparison [9]

The methods were compared by how accurately the fluid model moved inside the box and the pressure of the water. In figure 2.15, the red dotted line is the free surface shape observed in the experiment at the same time instance. From the comparative study it was concluded that the ALE and Eulerian methods were the best for describing the position and form of water, as shown in figure 2.15. The Lagrangian formulation resulted in distorted elements and computational errors while the SPH formulation results were reasonably accurate, but not the best at describing fluid motion.

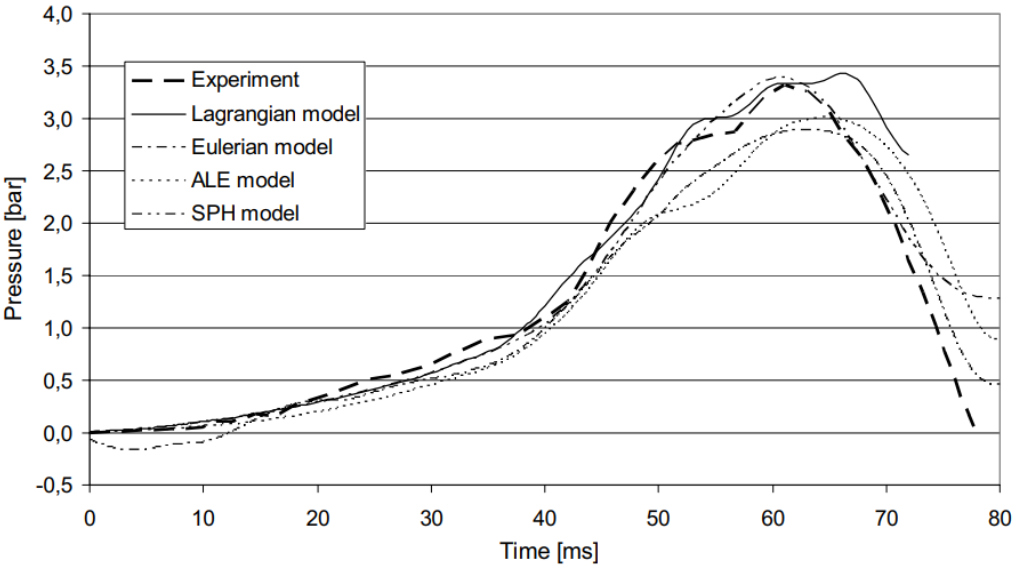

Figure 2.16 Comparison of the Pressure Time Variation at Point 1 [9]

In the pressure comparison in figure 2.16, the Lagrangian and SPH methods showed results more similar to the experimental data than the ALE and Eulerian methods. From the comparison, shown in figure 2.17, the following was concluded: the SPH and Lagrangian model processing time is shorter, but the ALE and Eulerian methods describe fluid motion more accurately.

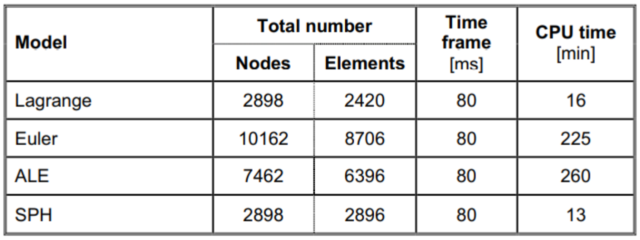

Model	**Total number**		**Time frame** [ms]	**CPU time** [min]
	Nodes	**Elements**		
Lagrange	2898	2420	80	16
Euler	10162	8706	80	225
ALE	7462	6396	80	260
SPH	2898	2896	80	13

Figure 2.17 CPU-time comparison [9]

Xu, Wang and Souli researched different methods to conduct a sloshing tank analysis to design a fuel tank [12]. The authors compared the accuracy between SPH and ALE formulations by creating a detailed finite element model of a rigid tank that contained water and air (void mesh), shown in figure 2.18. For the ALE method, the researchers created three models with different mesh densities from 20,000 to 60,000 hexahedra elements for the fluid mesh. For the SPH formulation, three models with different particle densities were created: SPH1=20,000, SPH2=75,000, and SPH3=120,000 particles. The tank was subjected to a horizontal velocity of $v(t)=0.032\cos(2\pi t/T)$, where T=1.5 sec is the period of horizontal velocity.

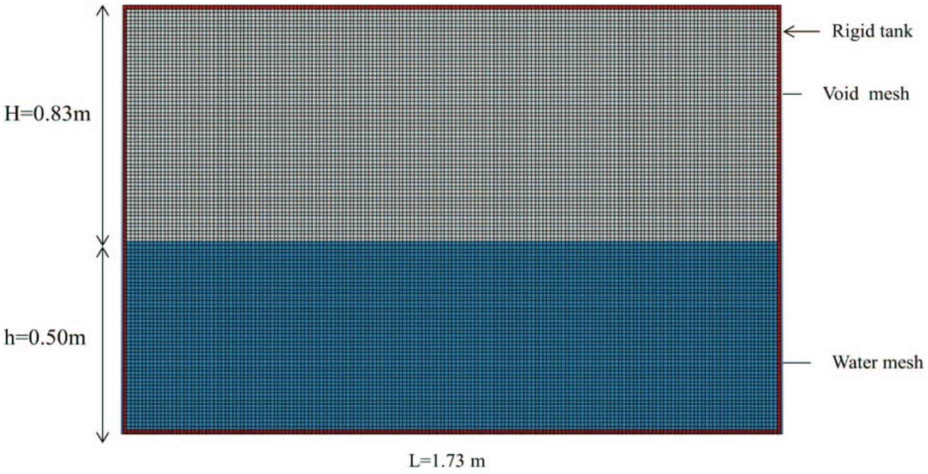

Figure 2.18 Problem description and ALE mesh [12]

For the ALE model, Wang and Souli determined that the three different mesh densities gave the same results. The authors concluded that the 20,000 elements model, shown in figure 2.19, was the most optimal for further investigation due to the similitude with experimental results and because it required less computational time than the other two models. The heights of the peaks from the waves in the simulation are shown in table 2.3.

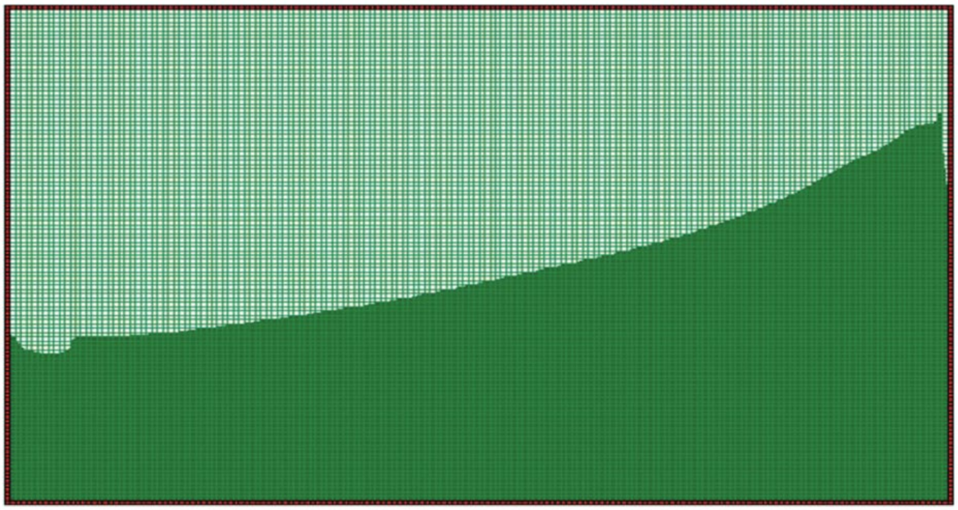

Figure 2.19 Water wave with ALE simulation at time t=9.6 sec [12]

Table 2.3 ALE and experimental data of peak wave amplitudes [12]

High peaks	ALE analysis	Experimental results
first	0.21 m	0. 22 m
second	0.29 m	0.30 m
third	0.32 m	0.35 m

Regarding the SPH models, the authors determined that the model with 20,000 particles did not show a correlation with either the ALE model or the experimental results, so they refined the model. SPH refinement was done by decreasing the particle pacing by a factor of two and four, increasing the number of SPH particles from 20,000 to 75,000 and 120,000. The resultant wave displacement from the simulated model can be observed in figure 2.20, which denotes the time history of the height of the water wave. As the number of particles in the SPH model increased, the correlation with the results of ALE model improved.

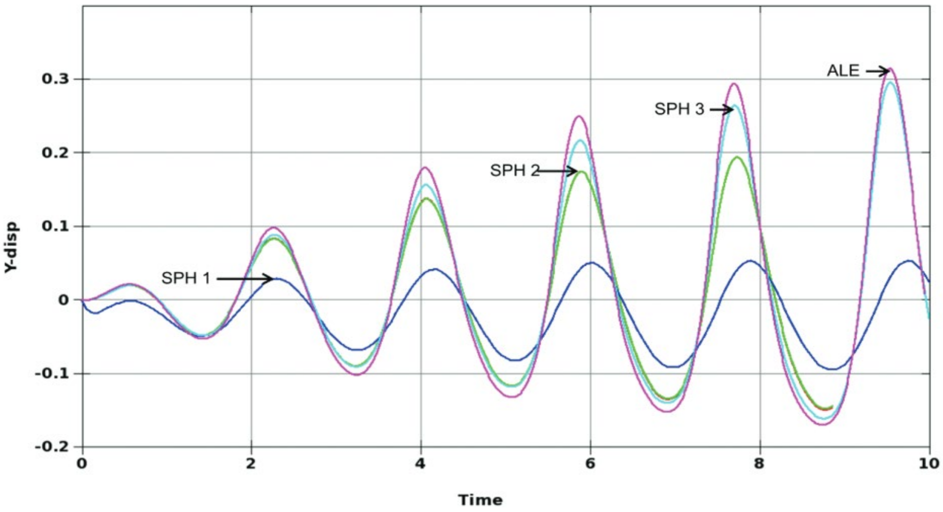

Figure 2.20 Water wave height for ALE and SPH simulations SPH1=20,000 SPH2=75,000 SPH3=120,000 [12]

The authors compared the SPH and ALE methods since SPH provides similar results as ALE formulation. For SPH to provide similar results to ALE, it was determined the SPH method must have a two times finer particle spacing than ALE mesh. From this research, it was concluded the SPH method has the advantage of avoiding re-meshing. The disadvantage is this method needs a finer resolution to achieve the same accuracy as the ALE method.

Han et al. employed the ALE method to analyze the motion of a tank-trailer during a sharp turn [13]. The tank-trailer model was composed of a tractor-tanker and middle swash plate, shown in figure 2.21. Shell elements were used to simulate the vehicle and solid elements were used to represent fluid components.

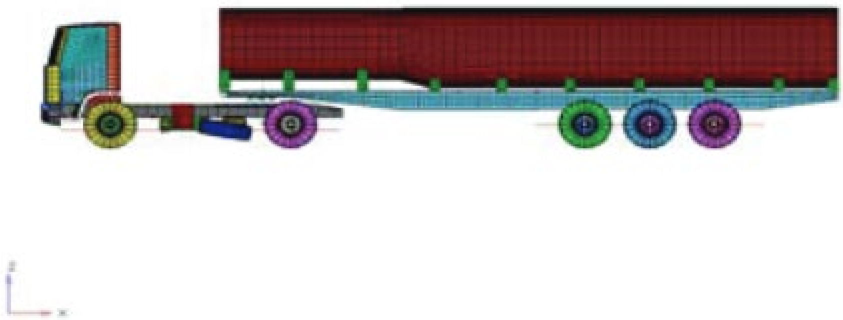

Figure 2.21 Finite element model of tanker semi-trailer [13]

The authors modeled the air and liquid material with null material. The densities used were 1.0E-9 t/mm^3 and 1.0E-12 t/mm^3, respectively. The equation of state used for the liquid and air was linear polynomial:

$$p = C_0+C_1\mu+C_2\mu^2+ C_3\mu^3+(C_4+ C_5+ C_6\mu^6)E \quad (2.1)$$

where:

C_i is the equation coefficient

$\mu = \rho/\rho_0 - 1$

ρ = liquid current density

ρ_0 is the liquid initial density

For this research study, the authors analyzed four variations with tank fill ratios of 0, 0.25, 0.5, and 0.75 during a sharp turn. The study did not evaluate the fluid model used for this research, instead focusing on how the fill ratio of liquid inside the trailer affected the liquid sloshing amplitudes. The authors mentioned that the ALE formulation is superior as it is not restricted by geometrical shape and boundary and load conditions.

Dhole et al. investigated the sloshing inside a fuel tank using nonlinear fluid properties [14]. The authors employed the SPH computational method to simulate the effects of fuel sloshing in the tank structure because dynamic pressure exerted by fuel on baffles can lead to structural failure. The tank shell, baffles, and end plates were meshed with shell elements and the materials were modeled using *MAT_PIECEWISE_LINEAR_PLASTICITY. The meshless SPH method was used to model water since this method requires a lower CPU time than the ALE and Eulerian methods. An Equation of State was defined by the *EOS_TABULATED input card. To define the non-linear behavior of water, volumetric strain and constants variables were defined in the EOS card. The density of water was 1000kg/m^3. A total of 45,743 particles were used for the SPH model.

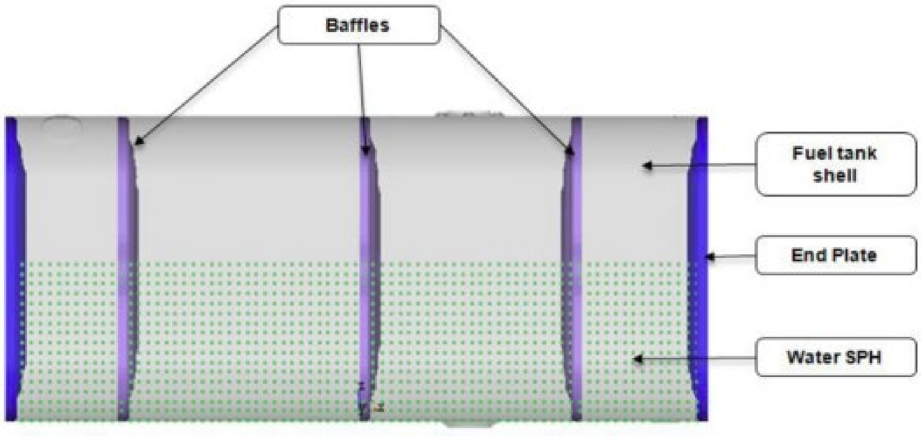

Figure 2.22 FEA Model for Fuel Tank Sloshing [14]

Node to surface contact was defined between water particles and the tank. Boundary conditions were applied to the tank using the *BOUNDARY_PRESCRIBED_MOTION_RIGID card, as shown in figure 2.23, to make the fluid inside the tank slosh. Gravity was applied using *LOAD_BODY_Z.

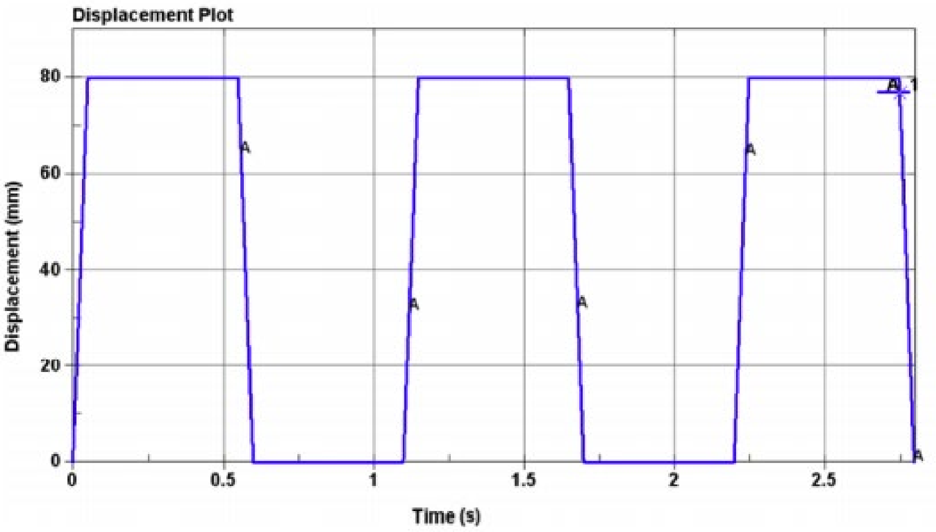

Figure 2.23 Ramp and Hold Input for Fuel Tank Testing [14]

The researchers wanted to evaluate the durability of the fuel tank for defined lifecycle requirements. It was found the center baffle cracked at multiple locations. LS-DYNA model results showed high strain levels at the same cracked areas around the holes of the center baffle as shown in figure 2.24.

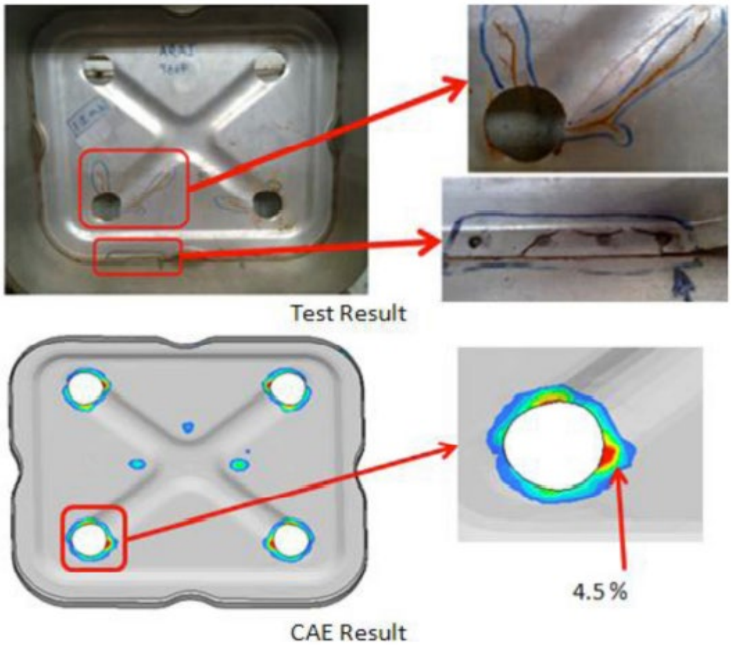

Figure 2.24 Correlation Results-Tank design-01 [14]

Chapter 3 Development of MASH Tank Trailer FEA Model

In this chapter, trailer model subsystems are described based on their function within the trailer. Meshing, element formulation, and material properties are provided. Tabular data discussed in this chapter can be found in Appendix A.

3.1 MASH Criteria for Tractor-Tank Trailer Combination Vehicles

A full-scale crash test is a method used to measure the impact performance of a roadside safety feature in which structural adequacy, occupant risk, and post-impact vehicular response are evaluated to determine if the full-crash test passed or failed. Since 2009, MASH [3] has been the standard testing manual for roadside safety feature evaluation. Prior to MASH, NCHRP Report Nos. 230 [3] and 350 [1] provided guidance for evaluating safety hardware. MASH defines the impact conditions and evaluation criteria for each type of roadside safety hardware. For roadside parapets and barriers, MASH provides six different test levels, TL-1 through TL-6. Each test level represents different vehicle classes and impact conditions for which the barrier must safely contain and redirect errant vehicles. A TL-6 barrier must be able to safely contain and redirect TL-6 vehicles, which include a tractor-van trailer weighing 80,000 lb (36,000 kg) and a tractor-tank trailer weighing 80,000 lb (36,000 kg). Table 3.1 lists the parameters that must be met for TL-6 vehicle selection.

Table 3.1 Recommended Properties of 10000S, 36000V, and 36000T Test Vehicles

Property	1000S (Single-Unit Van Truck)	36000V (Tractor/Van Trailer)			36000T (Tractor/Tank Trailer)		
		Tractor[a]	Trailer[b]	Combination	Tractor[a]	Trailer[c]	Combination
Mass, lb (kg)							
Curb	13,200 ± 2,200 (600 ± 1000)	N/S[d]	N/S[d]	29,000 ± 3,100 (13,200 ± 1,400)	N/S[d]	N/S[d]	29,000 ± 3,100 (13,200 ± 1,400)
Ballast[e]	As Needed	N/A[f]	As Needed	N/A[f]	N/A[f]	As Needed	N/A[f]
Test Inertia	22,046 ± 660 (10,000 ± 300)	N/S[d]	N/S[d]	79,000 ± 1100 (36,000 ± 500)	N/S[d]	N/S[d]	79,000 ± 1100 (36,000 ± 500)
Dimensions, in. (mm)							
Wheelbase (max)	240 (6,100)	200 (5100)	N/S[d]	N/A[f]	200 (5,100)	N/S[d]	N/A[f]
Overall Length (max)	394 (10,000)	N/S[d]	636 (16,155)	780 (19,850)	N/S[d]	N/S[d]	780 (19850)
Trailer Overhang[g] (max)	N/A[f]	N/A[f]	87 (2,200)	N/A[f]	N/A[f]	73 (1,850)	N/A[f]
Cargo Bed Height[i]	49 ± 2 (1,245 ± 50)	N/A[f]	50 ± 2 (1,270 ± 50)	N/A[f]	N/A[f]	N/A[f]	N/A[f]
Center of Mass Location in. (mm)							
Ballast[e] (above ground)	63 ± 2 (1,600 ± 50)	N/A[f]	73 ± 2 (1,850 ± 50)	N/A[f]	N/A[f]	81 ± 4 (2,050 ± 100)	N/S[d]

a Tractor should be a cab-behind-engine model, not a cab-over-engine model
b It is preferable that the trailer structure be of the “semi-monocoque” type construction. It is preferable that a sliding undercarriage (slide axles) be used to attach the trailer tandems to the trailer frame
c It is preferable that a gasoline tank trailer with an elliptical cross section be used
d N/S- Not Specified
e See section 4.2.1.2 for recommended ballasting procedures
f N/A- Not Applicable
g Distance from rearmost part of trailer to center of trailer tandems.
h If trailer is equipped with slide axles, they should be set at rearmost position
i Without ballast

3.2 Tank Trailer Selection

Based on the review of MASH tank trailer specifications, the Midwest Roadside Safety Facility (MwRSF) research team discussed parameters with Liquid & Bulk Tank, Inc. (LBT) to develop an FEA model of a tank trailer similar to the LBT BKZ 5949 elliptical straight-frame structure. This tank trailer consists of four internal, independent tanks connected with a continuous external jacket. The LBT tank structure is shown in figure 3.1.

Each component of the trailer was reviewed and classified as critical or non-critical components. Tank components were defined as critical, and hence were explicitly modeled, if they were part of the tank load-bearing structure, frame, or fluid container. These components included the fifth wheel assembly, tank jacket, bulkheads, baffles, ribs, chassis, suspension system, and frame stiffeners and ribs. Non-structural parts were classified as non-critical and would not affect the dynamic behavior of the tank during impact. Some examples of these components are hoses, pipes, and valves. Components that were classified as non-critical were either removed from the model or represented with simple constraints because they did not have a strong influence on the dynamics, forces, and kinematics of the trailer. Additionally, modeling these components would increase model instabilities without improving accuracy. All structural components, fasteners, and chassis elements were meshed and included in contacts. Critical components were prioritized for accurate geometrical modeling, thicknesses, behaviors, and connections. A total of 134 unique critical components were modeled in the tank trailer model.

A new redefined tractor-tank trailer vehicle model was created for LS-DYNA simulation. The next section provides element descriptions for the modeled critical components of the tank-trailer model. Overall, the tank-trailer compartment had an approximate length of 42 ft – 5 in. (12.9 m), as shown in figure 3.2. The trailer volume capacity was about 9,500 gallons and was divided in four compartments, each having a capacity of 3,500, 1,000, 1,500, and 3,500 gallons, respectively, from front to rear.

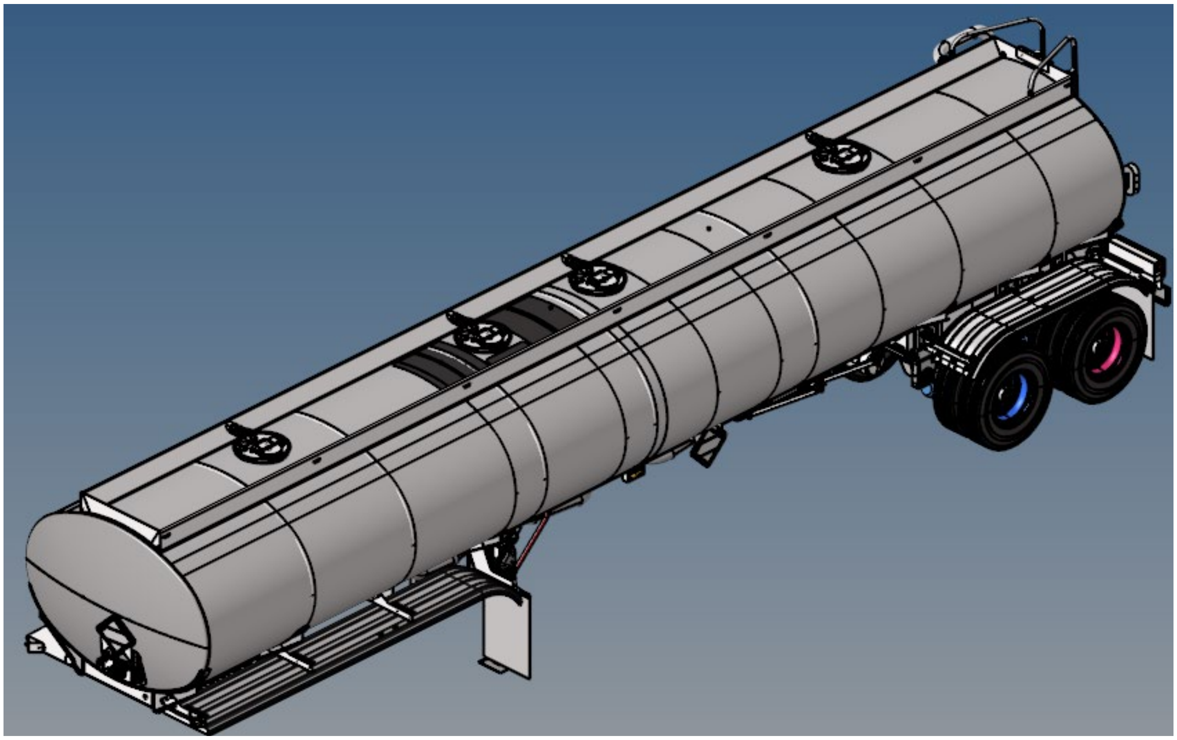

Figure 3.1 BKZ 5949 Trailer Model

BKZ 5949

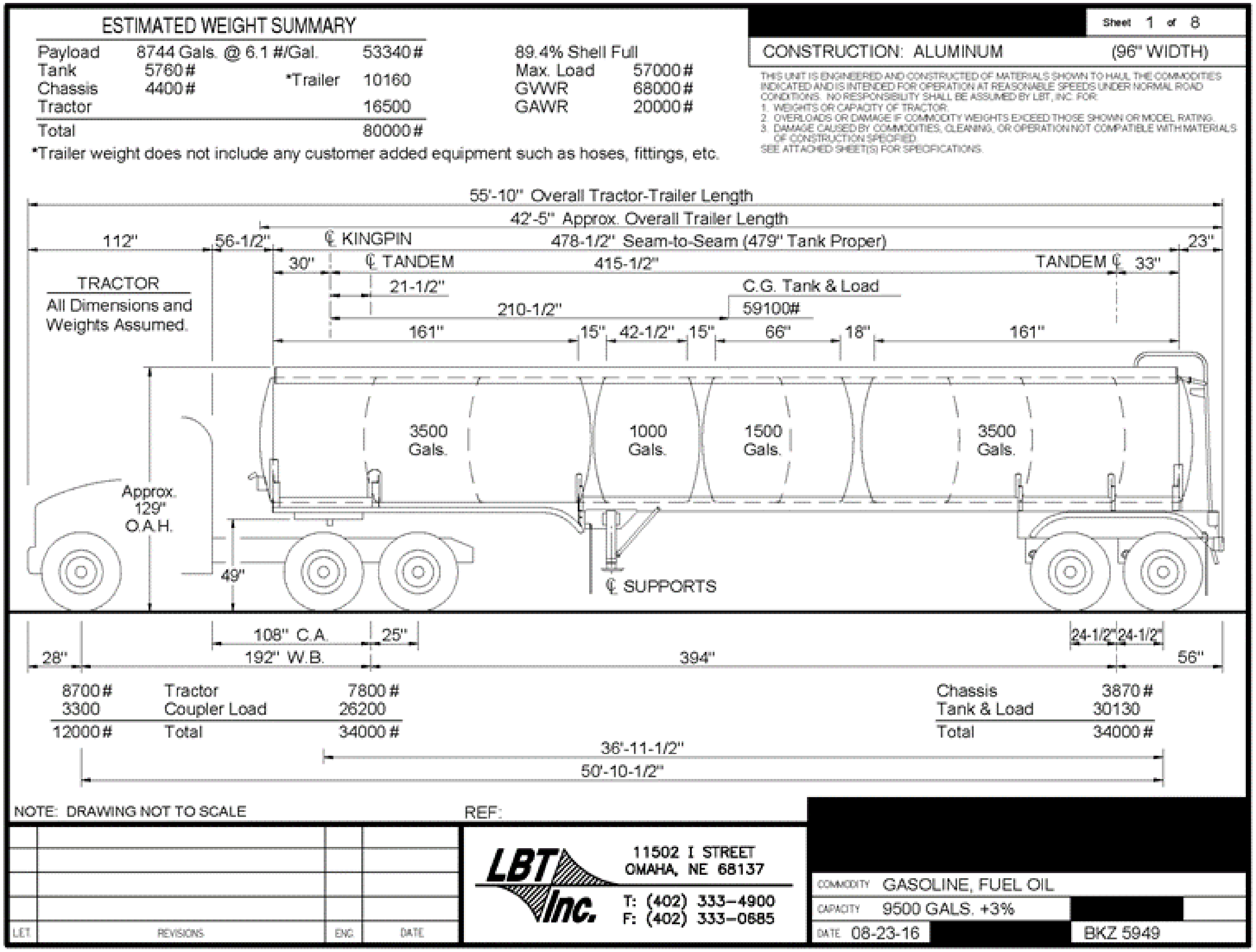

ESTIMATED WEIGHT SUMMARY

Payload	8744 Gals. @ 6.1 #/Gal.		53340#
Tank	5760#	*Trailer	10160
Chassis	4400#		
Tractor			16500
Total			80000#

*Trailer weight does not include any customer added equipment such as hoses, fittings, etc.

89.4% Shell Full

Max. Load	57000#
GVWR	68000#
GAWR	20000#

[redacted]

Sheet 1 of 8

CONSTRUCTION: ALUMINUM (96" WIDTH)

THIS UNIT IS ENGINEERED AND CONSTRUCTED OF MATERIALS SHOWN TO HAUL THE COMMODITIES INDICATED AND IS INTENDED FOR OPERATION AT REASONABLE SPEEDS UNDER NORMAL ROAD CONDITIONS. NO RESPONSIBILITY SHALL BE ASSUMED BY LBT, INC. FOR:

1. WEIGHTS OR CAPACITY OF TRACTOR.
2. OVERLOADS OR DAMAGE IF COMMODITY WEIGHTS EXCEED THOSE SHOWN OR MODEL RATING.
3. DAMAGE CAUSED BY COMMODITIES, CLEANING, OR OPERATION NOT COMPATIBLE WITH MATERIALS OF CONSTRUCTION SPECIFIED.

SEE ATTACHED SHEET(S) FOR SPECIFICATIONS.

8700#	Tractor	7800#
3300	Coupler Load	26200
12000#	Total	34000#

Chassis	3870#
Tank & Load	30130
Total	34000#

NOTE: DRAWING NOT TO SCALE

REF:

LET.	REVISIONS	ENG.	DATE

LBT Inc.
11502 I STREET
OMAHA, NE 68137
T: (402) 333-4900
F: (402) 333-0685

[redacted]

COMMODITY GASOLINE, FUEL OIL

CAPACITY 9500 GALS. +3% [redacted]

DATE 08-23-16 [redacted] BKZ 5949

Figure 3.2 Standard Plan Drawings for Modeled Tank Trailer BKZ 5949

3.3 Model Subsystems

Critical components were defined as the parts from the tank-trailer that are structurally essential for the analysis of impacts consistent with MASH TL-6. The trailer components were separated into three subsystems: (1) chassis frame, (2) suspension, and (3) tank. These components are shown in figure 3.3, comprising the baffles, bulkheads, tank jackets, and chassis frame. These components and tractor model connected to the tank trailer are described in detail in the following sections.

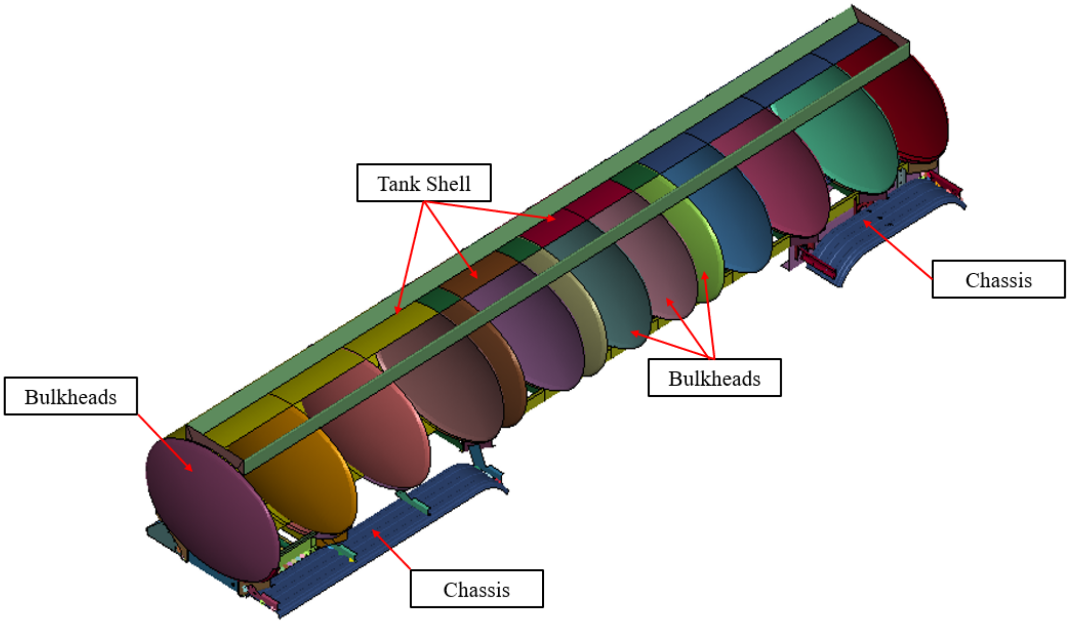

Figure 3.3 Tank and Chassis Components

3.4 Chassis

3.4.1 Components Overview

The chassis frame is used to structurally support the tank, transfer load between the trailer rear axle and the fifth wheel connection at the truck, and increase flexural stability of the trailer.

The chassis system is the conjunction of several components shown in figure 3.4. The components were extracted from a BKZ 4959 CAD model provided by LBT Inc.

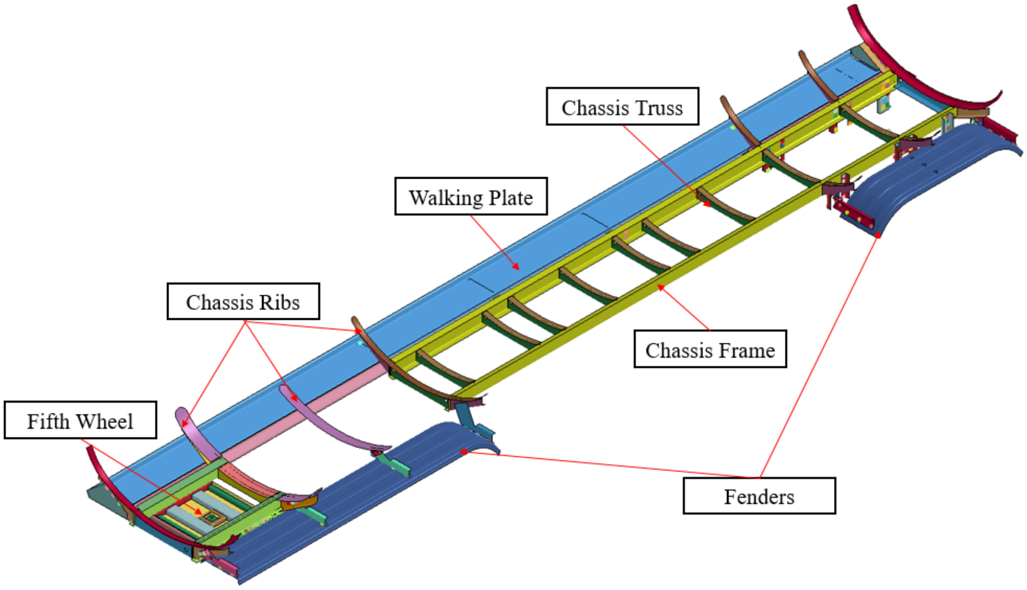

Figure 3.4 Chassis Model

A fifth wheel pin structure is a common method of attaching heavy trailer structures to tractors. The fifth wheel system is critical since it connects the tank to the tractor. At the front of the trailer, a fifth-wheel load frame and shear pin were modeled based on the details provided by LBT Inc. with the fifth wheel components shown in figure 3.5.

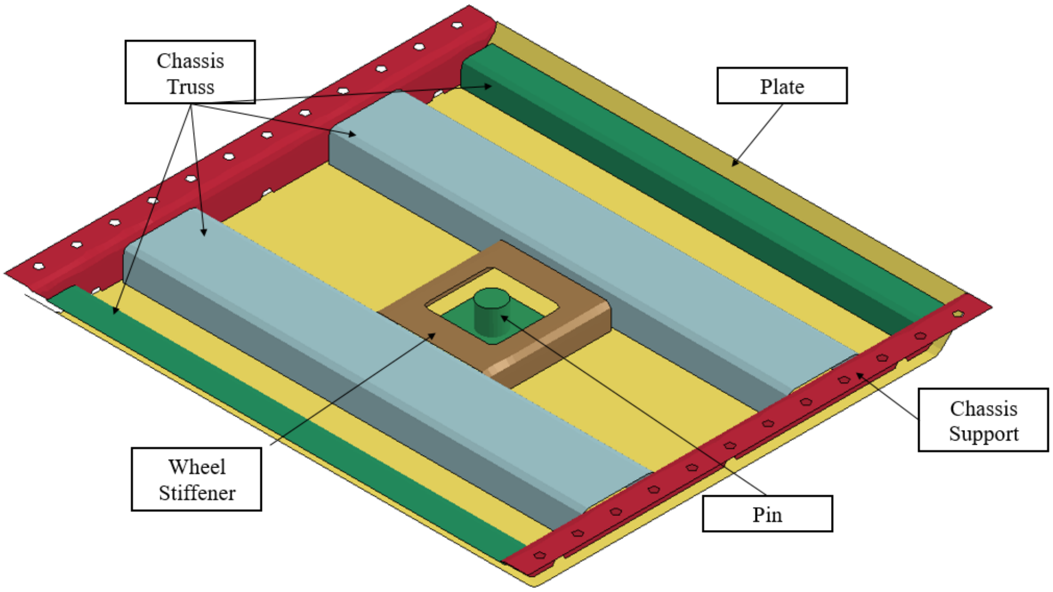

3D

Figure 3.5 Fifth Wheel Components

3.4.2 Meshing and Element Formulation

Most components from chassis system were fully integrated shell elements (ELFORM=16). Other components (lateral and longitudinal ribs) were defined as Belytschko-Tsay (B-T) shell elements (ELFORM=2) because this element formulation is more time efficient. The respective element formulation and thickness for each component can be found in Appendix A. The only component formed from constant stressed solid elements (ELFORM= 1) was the fifth wheel pin. The fifth wheel shear pin was modeled with solid elements to secure to the rib, frame, and strut members of the fifth wheel box. To facilitate meshing, the geometry of the pin was simplified from the original model, as shown in figure 3.6.

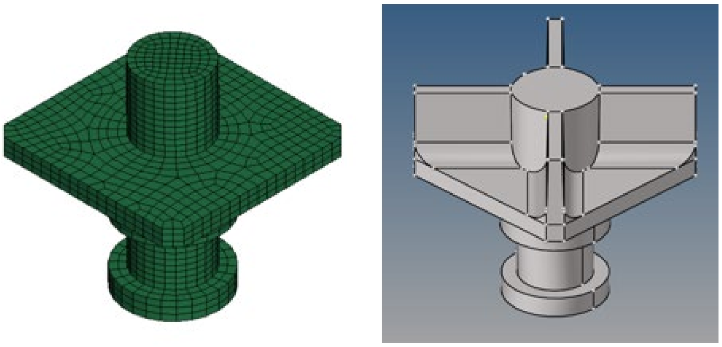

Figure 3.6 Pin Component

3.4.3 Material Overview

This section describes the mechanical properties of different types of aluminum alloys that were applied to the chassis model. Material selection was based on standard guides for structural container specifications for road vehicles, as noted in Aluminum in Commercial Vehicles [15]. Different types of materials were used to model the chassis depending on their function in the model. The materials and properties used in the material sections are shown in table 3.2. The classification of parts with respect to their type of aluminum can be found in table 3.2.

Table 3.2 Aluminum Mechanical Properties for Chassis Components

Material	**Density** (kg/mm^3)	**Young's Modulus (GPa)**	**Poisson Ratio**	**Yield Strength (MPa)**
6005A T5 Al	$2.70(10^{-6})$	69	0.33	250
6060 T6 Al	$2.71(10^{-6})$	68	0.33	170
42000 T6 Al	$2.60(10^{-6})$	70	0.33	220

For the chassis components, the material properties from 6060-T6 Al alloy were used in the vehicle model. This type of aluminum is commonly used for complex cross-sections and has a very good weldability. The 42000 T6 Al material properties were designated for the components that connect different parts to each other. Most of these components consisted of bolted connections. Aluminum 6005A T5 material properties were designated for the L-beam components in the model. This medium strength aluminum alloy is corrosion resistant and used for structural applications, typically used in passenger and commercial vehicles, as well as commercial trailers.

3.4.4 Connections

Researchers extensively referenced the LBT Inc. tank model to identify the best techniques for connecting critical components in the tank model. Different connection types were utilized based on how parts are connected in physical trailers. Welded connections were modeled by either merging the nodes of respective components, using tied node definitions, or defining spot welds. Bolted connections were independently analyzed. When bolt arrangements restricted part rotations and could develop moment in connections, researchers applied nodal rigid bodies to interface components. For bolted connections in which rotation or angular displacements could occur around a bolt, joints or nodal constraints were used to allow relative movement between the connected parts. Connection diagrams are shown in the Appendices to demonstrate the connections for each component in the actual tank-trailer and the LS-DYNA model.

This section details the constraints in the chassis model. Updated connection diagrams are provided to show which contact options and constraints are used for each component. Several components were attached by constraints when the meshing of adjacent components was conducive. Welded components were modeled with spot welds. For example, in figure 3.7 the tank jacket components are connected to the longitudinal ribs by spot welds.

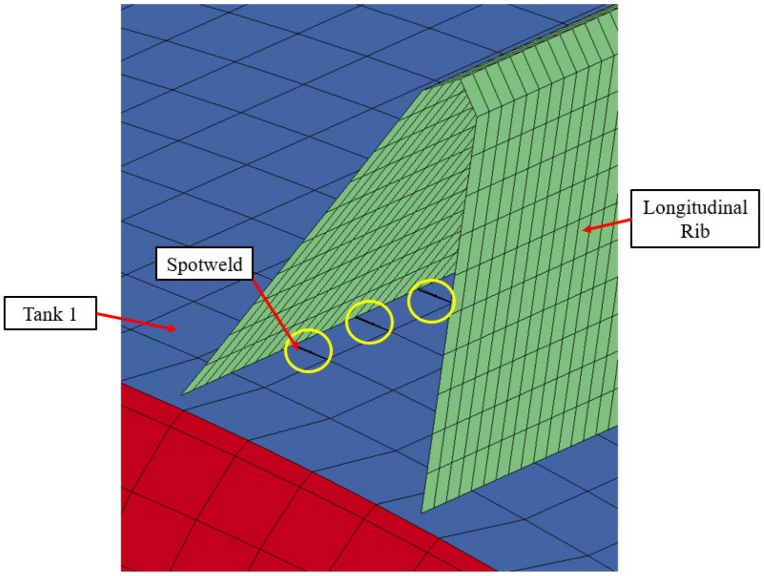

Figure 3.7 Spotweld Constraint

All components bolted on the chassis CAD model from LBT Inc. in the LS-DYNA model were constrained by nodal rigid bodies (CRNB). For example, a chassis rib was attached to a chassis truss using CRNB, as shown in figure 3.8.

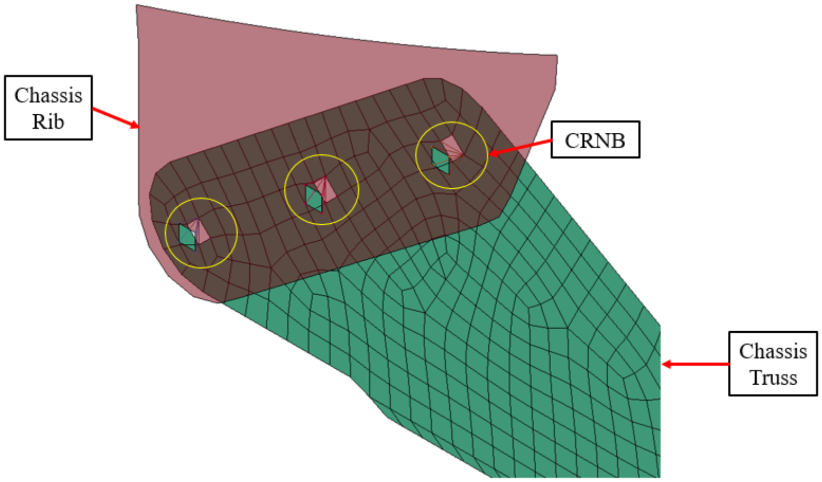

Figure 3.8 CRNB Constraint

In other cases, there was no need to use constraints or contacts to attach components since nodes could be merged without causing meshing distortion or deformation in the model. In figure 3.9 the nodes from the longitudinal rib's edge are aligned and merged with the nodes at the lateral rib's surface.

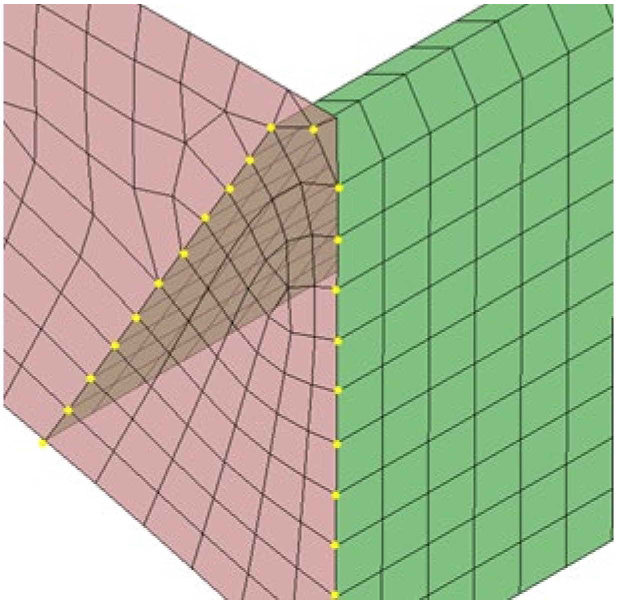

Figure 3.9 Merged Nodes

This section details the different contacts used to attach chassis components. The chassis ribs and frames were attached to the tank components using a CONTACT_TIED_NODES_TO_SURFACE_OFFSET which attached the nodes of the chassis ribs to the tank's surface. This type of contact was used to attach every chassis rib to the tank components, as shown in figure 3.10.

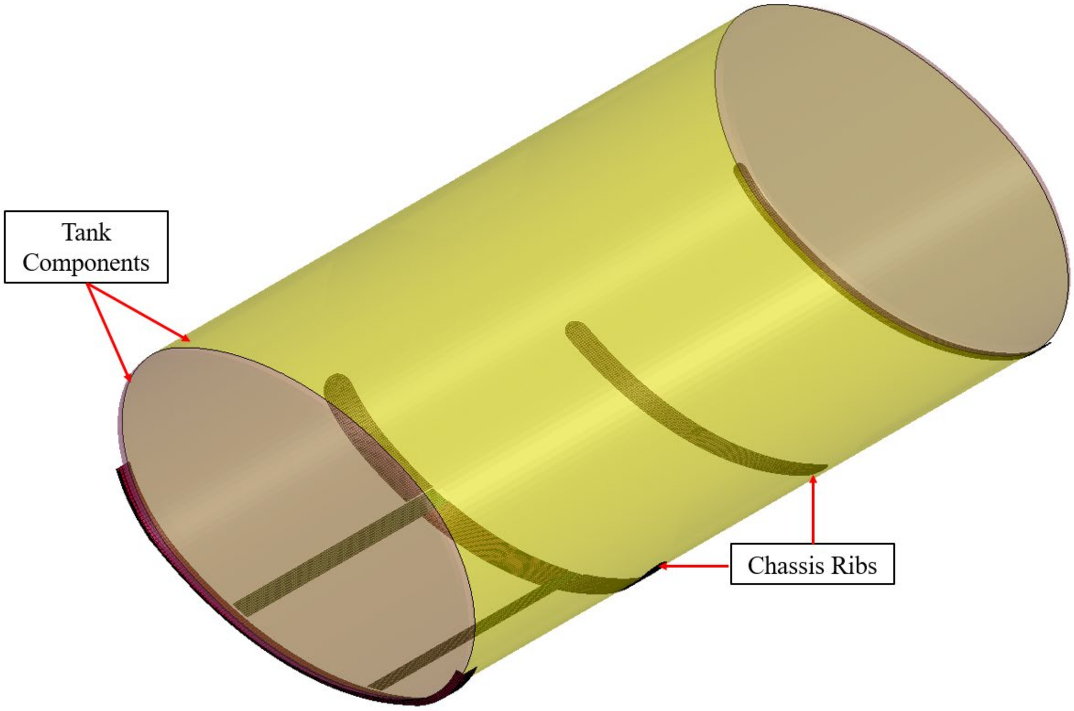

Figure 3.10 Chassis Ribs Constrained to Tank Shell Using Contact Nodes to Surface

Another type of contact defined in the chassis model was TIED_SHELL_EDGE_TO SURFACE_OFFSET. This type of contact was used to define the contact between the surface and the edge of the chassis frame components, as shown in figure 3.11, where the edges of the chassis ribs are attached to the surface of a frame.

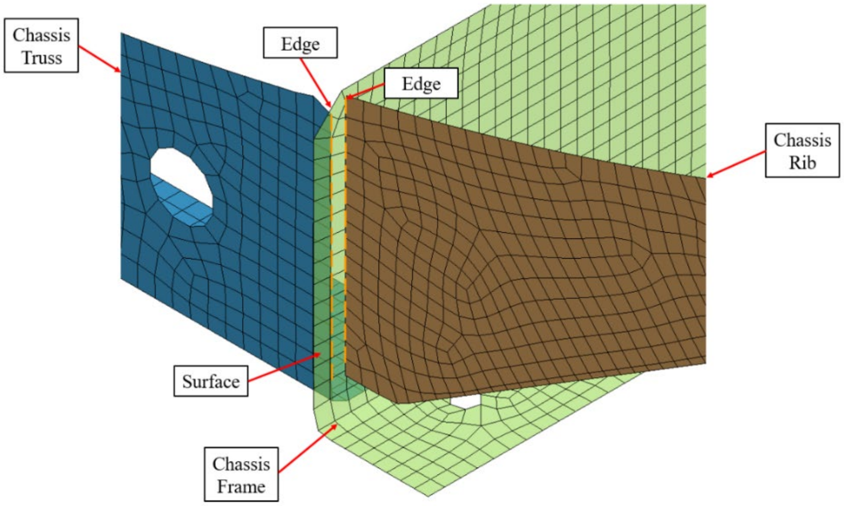

Figure 3.11 Contact Edge to Surface Offset

The fifth wheel components are shown in figure 3.12. These components were used in the model to attach the trailer to the tractor model. The components from the trailer's fifth wheel were connected using TIED_SHELL_EDGE_TO_SURFACE contacts. The edges from the chassis truss support and wheel stiffener were attached to the plate's surface.

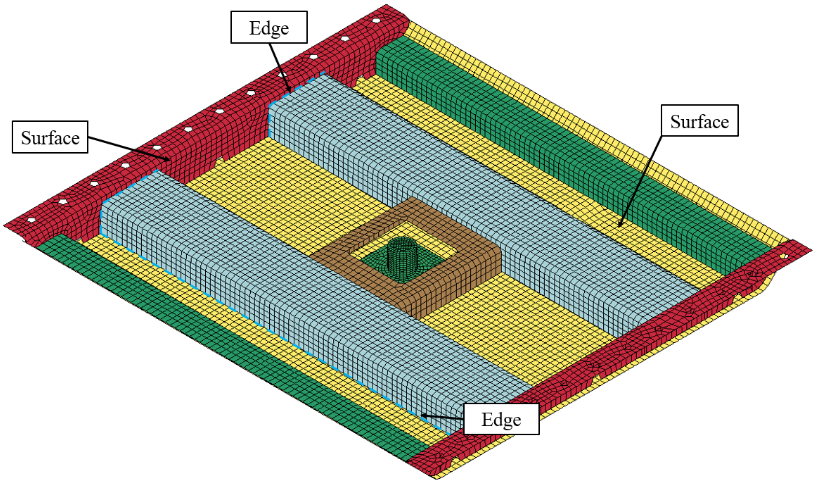

Figure 3.12 Fifth Wheel Edge to Surface Contact

3.4.5 Fifth Wheel to Tractor Connection

The fifth wheel components are shown in figure 3.5. This system was used in the model to attach the trailer to the tractor model. The components used to attach the fifth wheel from the trailer to the tractor are shown in figure 3.13. The constraint used to model the attachment between the fifth wheel pin and hitch was an extra node set. The pin's nodes from the bottom surface were attached to the hitch's surface.

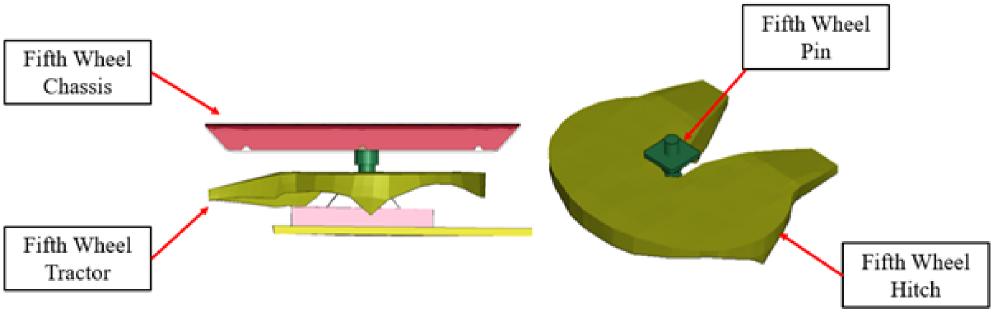

Figure 3.13 Fifth Wheel Constraint

3.5 Suspension Modeling

3.5.1 Component Overview

The suspension of the trailer system was reviewed and compared to existing vehicle and trailer models. It was observed that the TL-6 model had very similar structure to a van-based trailer, including air ride suspension, trailing arm assembly, dual axle support, and height. This was conducive to adapting the model of the trailer from an existing van-type (box) trailer and modifying the suspension to match the geometry, connections, and stiffness of the tank trailer vehicle. The modified TL-5 suspension system, which was used in the TL-6 tank trailer model, is shown in figure 3.14.

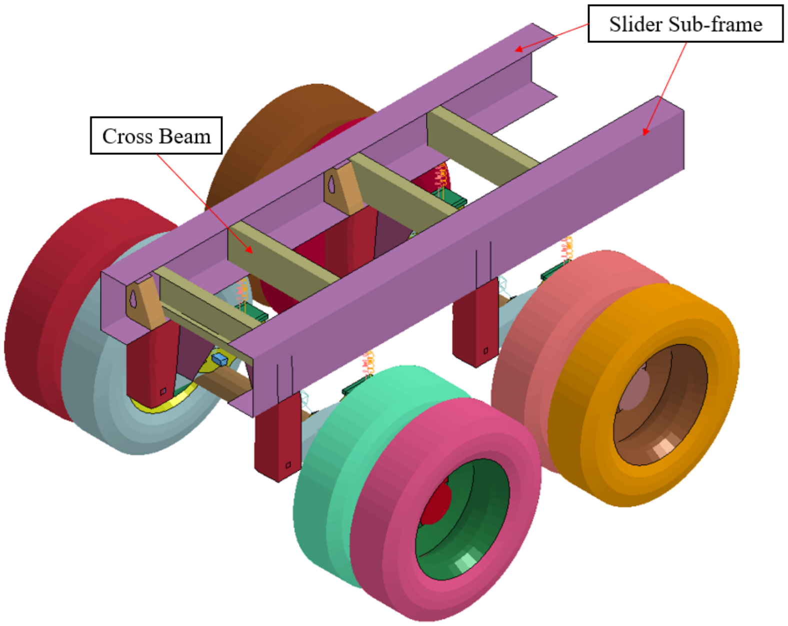

Figure 3.14 Suspension-System Components

3.5.2 Meshing and Element Formulation

Most of the components from the suspension and wheel system are fully integrated shell elements (ELFORM=16). The components that were a constant-stress solid element were the suspension pivot, air bag supports and accelerometer. The rear shock absorber, air ride spring and air ride damper were modeled with discrete elements.

3.5.3 Connections

The main components used to model the connection between the trailer and the suspension were the chassis frame, suspension frame, bumper mounting bracket and suspension mounting. The mountings were constrained to the frames by CRNB, as shown in figure 3.15, to represent the bolted connection.

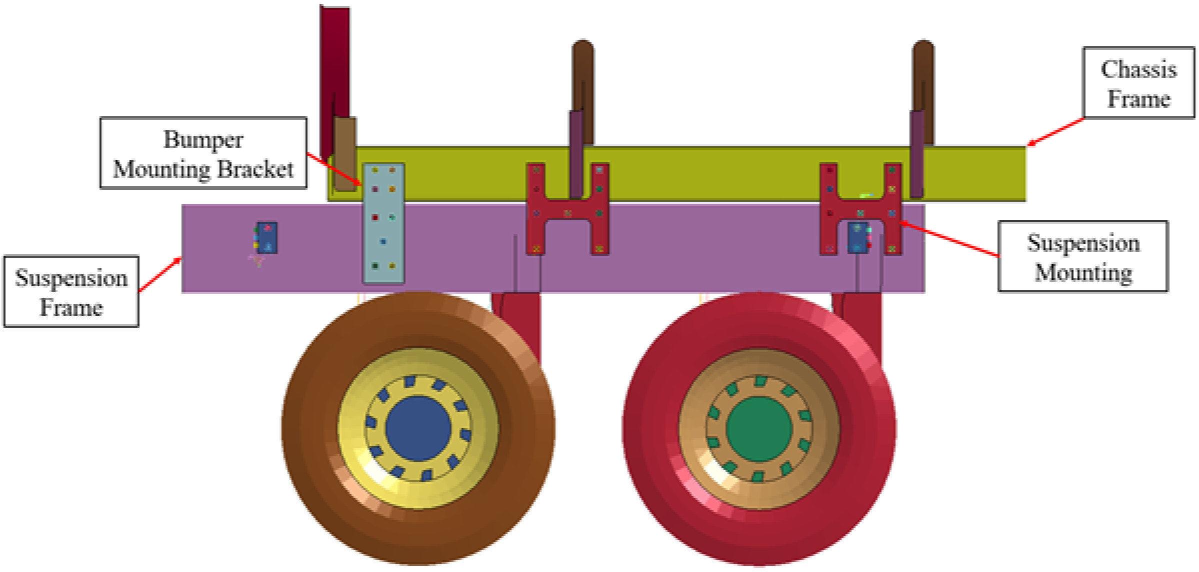

Figure 3.15 Suspension to Chassis Constraints

3.6 Tank Modeling

3.6.1 Components Overview

The tank structure consisted of an exterior elliptical aluminum skin (shell) which was welded to the tank end caps and baffles to provide intermediate lateral stiffness and control end-to-end sloshing behaviors. These tank components were the only parts that directly interacted with the fluid. The modeled tank structure is shown in figure 3.16. The tank shell was modeled in five parts, one for each tank compartment and one for the connecting skin between tanks. The tank shell is shown in figure 3.17.

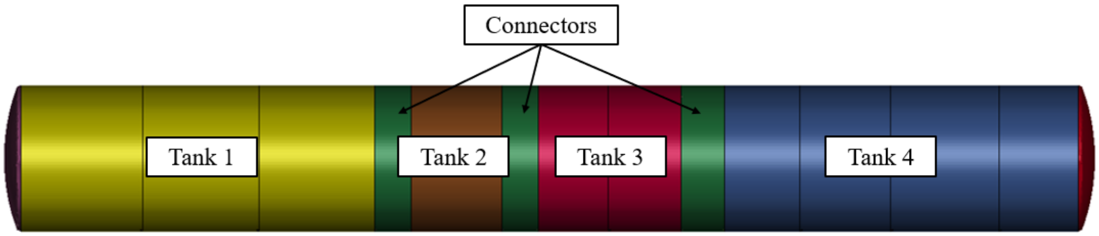

Figure 3.16 Tank Components

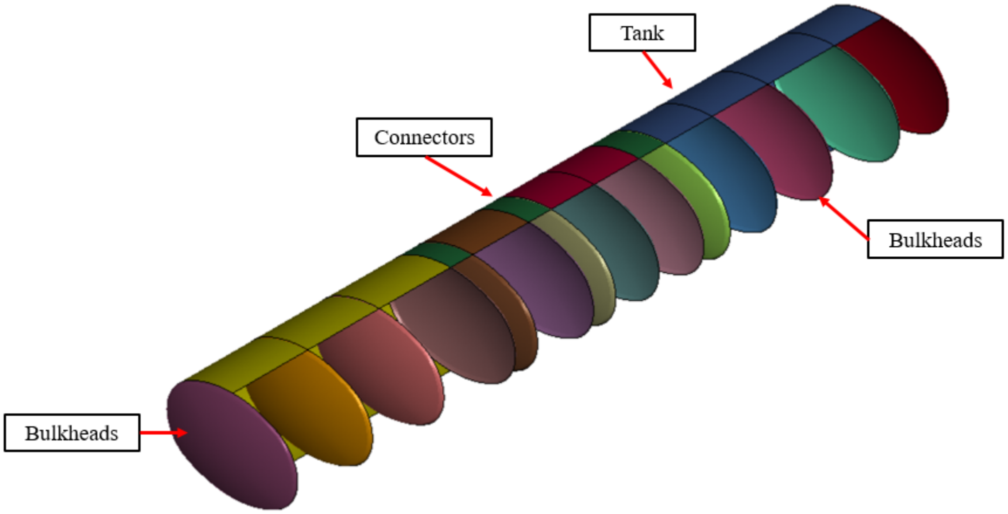

Figure 3.17 Tank and Bulkheads

3.6.2 Tank Meshing

The meshing consisted of a uniform distribution where the tank's shell components were aligned with bulkheads and baffles. The components' mesh was attached by merging the nodes at the edges of the bulkheads and tank shell.

The tank's shell components were modeled as fully integrated B-T shell elements, which is computationally efficient due to the reduced number of integration points used. The bulkheads were meshed to be consistent with the tank shell and utilized the same node and element pattern on the surfaces, although the elliptical surfaces for bulkheads and baffles varied slightly. As a result, the meshes for all bulkhead structures were consistent throughout the tanks from front to rear. The average element edge size of the baffle and bulkhead structures was approximately 25 mm. The bulkhead is shown in figure 3.18.

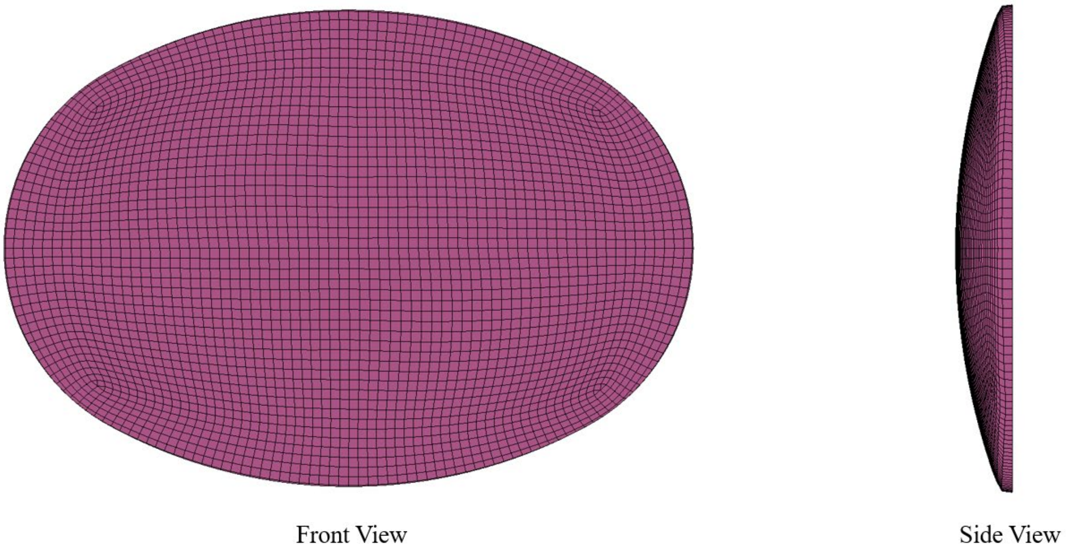

Figure 3.18 Bulkhead and Modified Baffle Mesh

It should be noted that the baffle geometries were simplified for this model. Baffles are flow direction panels designed to support tube bundles and direct the flow of fluids, as shown in figure 3.19. Early models which included baffle openings frequently resulted in numerical instabilities during fluid engagement with the baffle edges. The baffles were simplified for this model by using the mesh of the bulkheads and reducing the thickness of the components to be equal to the baffle thicknesses, which reduced model complexity and increased stability.

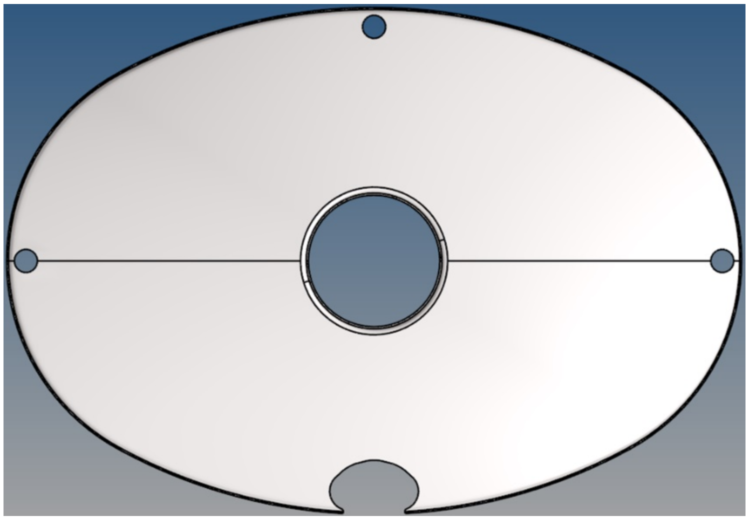

Figure 3.19 LBT Inc. (BKZ 5949) Baffle Geometry

3.6.3 Material Overview

This section details the mechanical properties of different types of aluminum alloys that were applied to the tank model. Two materials and properties were used as shown in table 3.3. The classification of parts with respect to their type of aluminum can be found in Appendix A.

Table 3.3 Aluminum Mechanical Properties

Material	**Density** (kg/mm^3)	**Young's Modulus (GPa)**	**Poisson Ratio**	**Yield Strength (MPa)**
5454-O Al	$2.69(10^{-6})$	69	0.33	100
5454-H32 Al	$2.69(10^{-6})$	69	0.33	200

The type of aluminum alloy for the baffles and bulkheads is 5454-O Al, as provided by tank description documents from LBT Inc. This type of aluminum is commonly used in welded structures such as pressure vessels and has a very good corrosion resistance. Material properties were approximated based on ASTM specifications and estimated yield and ultimate stresses.

5454-H32 Al alloy was selected to represent the material properties of the outer shell in the model. This material has high corrosion resistance and heat treatment and fabrication techniques can alter strength from medium to high with a high fatigue strength. The alloy has a high strength at high temperatures (65-170 degrees Celsius) compared to similar alloys.

3.6.4 Connections

The tank connections are composed of only the bulkhead, and the tank jacket. As described in section 6.2, the nodes for both components need to be the aligned as shown in figure 3.20. Thus, the connection of the components was achieved through merged nodes on the edges.

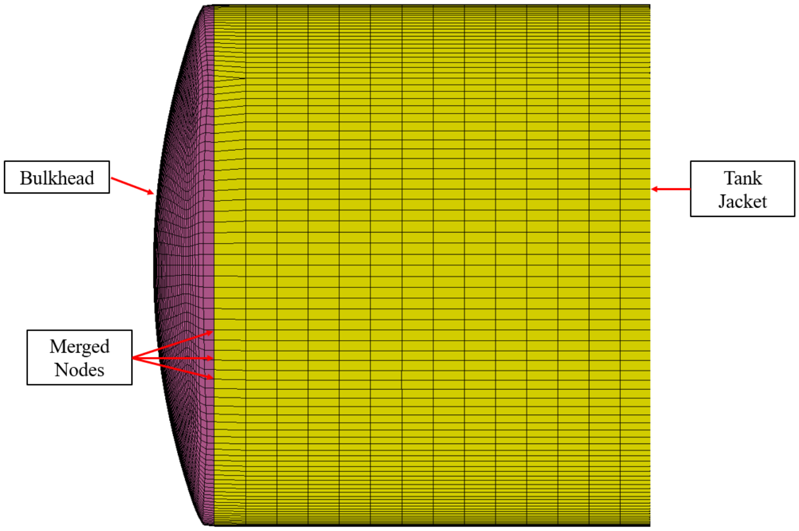

Figure 3.20 Bulkhead and Tank Merged Nodes

3.7 Tractor Modeling

3.7.1 Model Overview

Tractor model was extracted from an existing TL-5 tractor-van trailer truck model, originally developed by a research team at UT-Battelle's Oak Ridge National Laboratory and the University of Tennessee at Knoxville and modified by Dr. Chuck Plaxico of Roadsafe, LLC and Dr. John Reid of MwRSF. The truck model is shown in figure 3.21. The rear tandem axle was shifted forward to accommodate the differences between the tank trailer and van body trailer wheelbases. The tank model was attached to the original tractor at the fifth wheel plate.

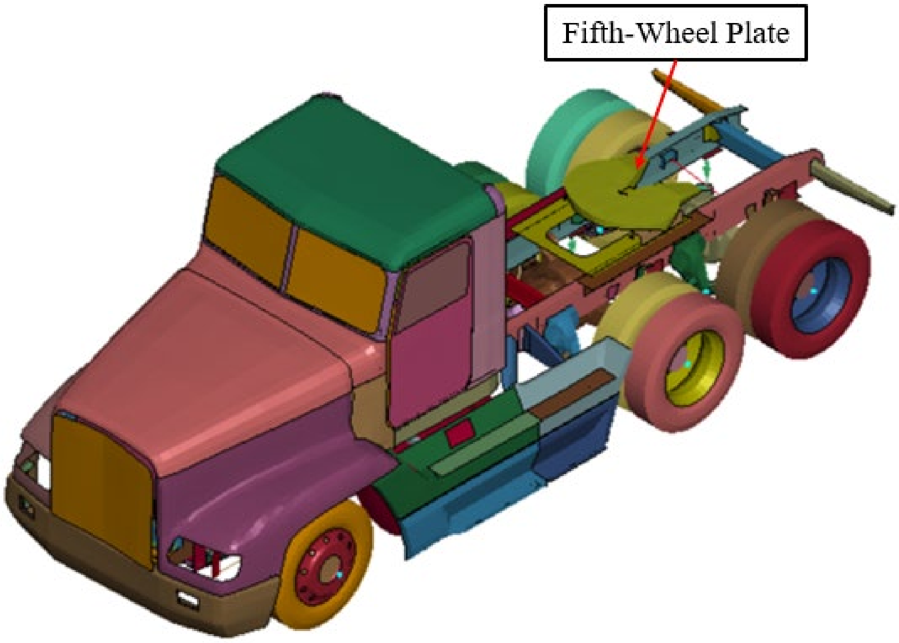

Figure 3.21 Tractor Model

3.8 Model Simplifications

As discussed, some non-structural components were likely to contribute to simulated numerical instabilities, including snag. These numerical instabilities were unlikely to affect trailer behavior but could hamper the stability and accuracy of the model if these components contributed to non-physical behaviors. As such, these components were not modeled during this effort. These components included hoses, wires, gaskets, light structures, and some tubing structures. Future applications of this model could include these components if the need arises. The comparison between the BKZ 5949 model from LBT Inc. and the current LD-DYNA trailer model is denoted in figure 3.22 through figure 3.27.

The highly detailed components are the parts of the model that have a complex geometry, including spigots and valves, molded components, bolts, and taillight structures, which are shown in figure 3.27. The final trailer model is shown in figure 3.28.

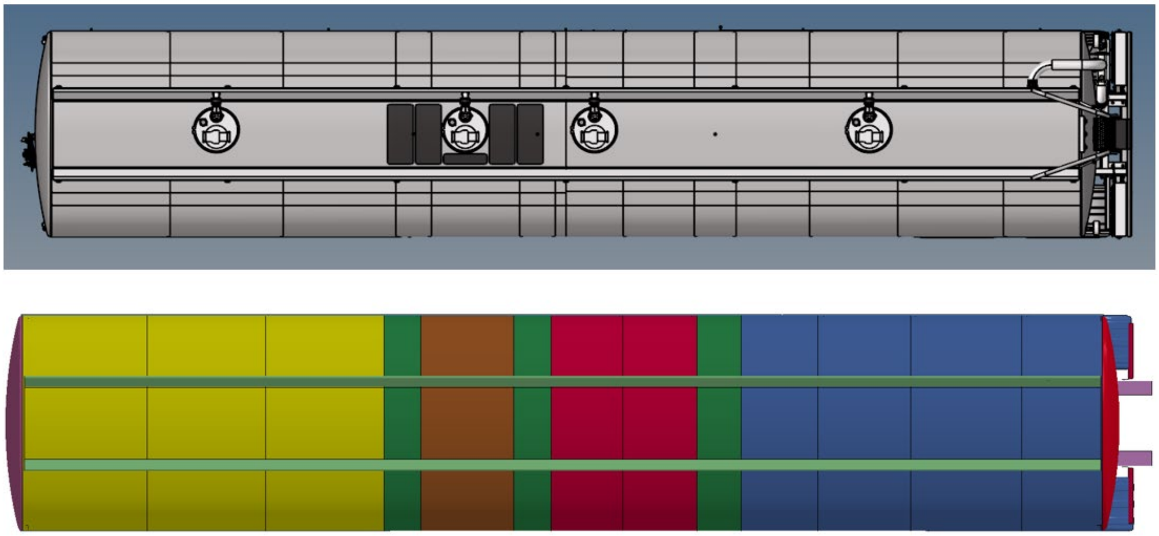

Figure 3.22 LBT Inc. Trailer Model Top View (Top) and LS-DYNA Model Top View (Bottom)

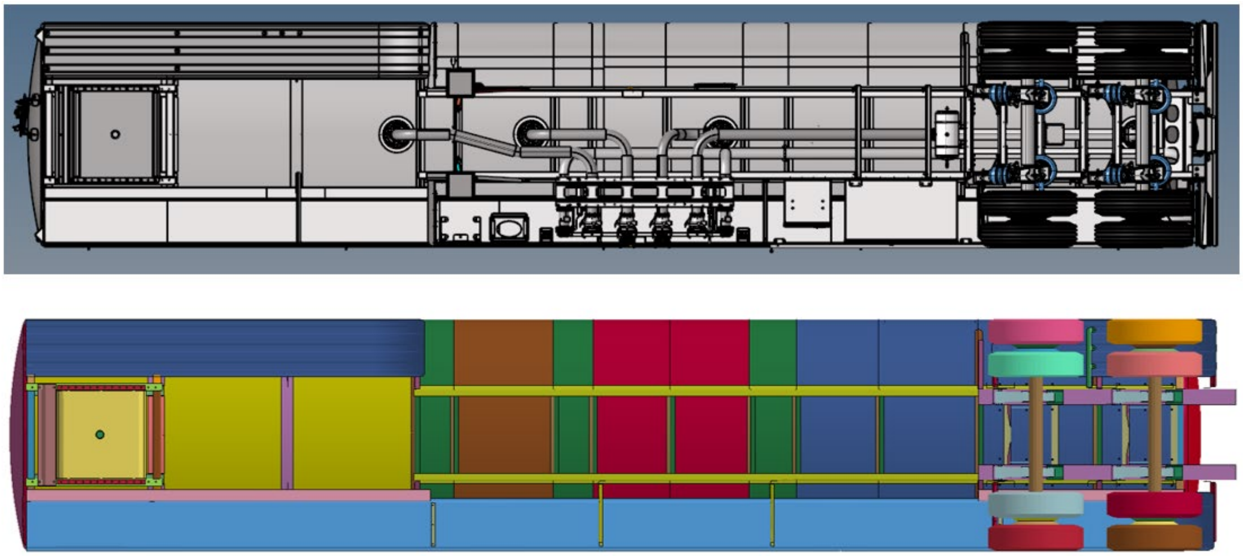

Figure 3.23 LBT Inc. Trailer Model Bottom View (Top) and LS-DYNA Model Bottom View (Bottom)

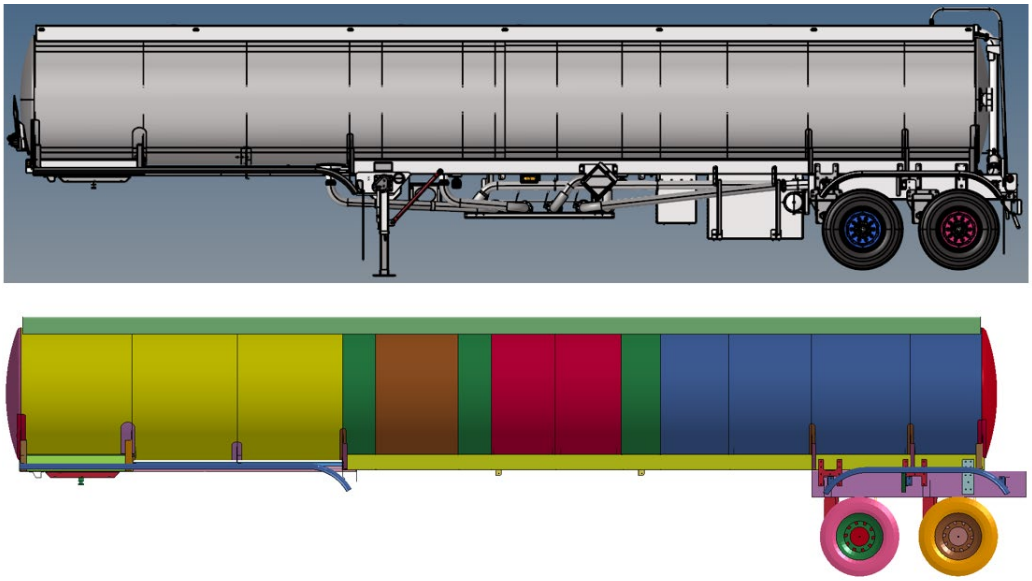

Figure 3.24 LBT Inc. Trailer Model Right View (Top) and LS-DYNA Model Right View (Bottom)

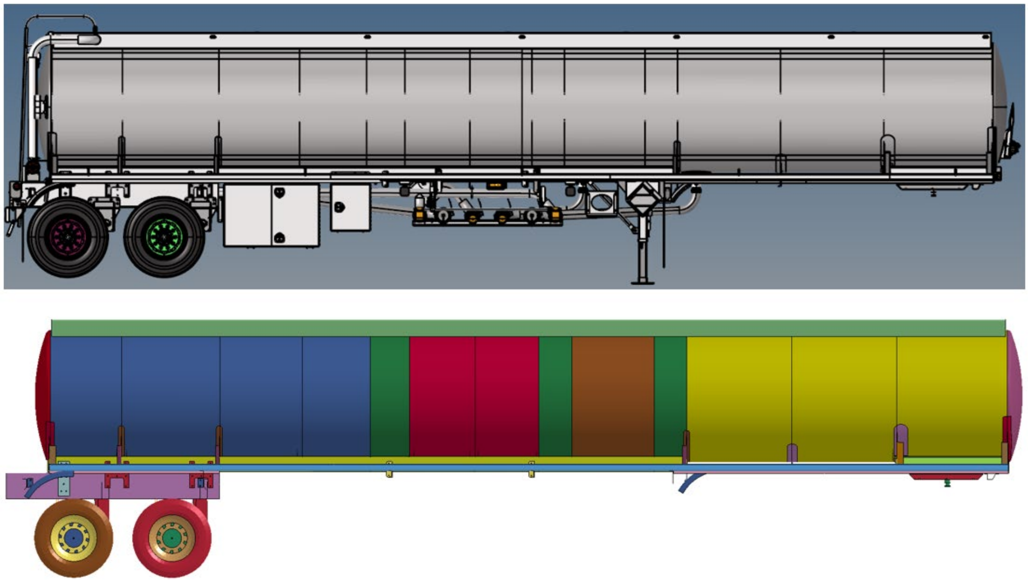

Figure 3.25 LBT Inc. Trailer Model Left View (Top) and LS-DYNA Model Left View (Bottom)

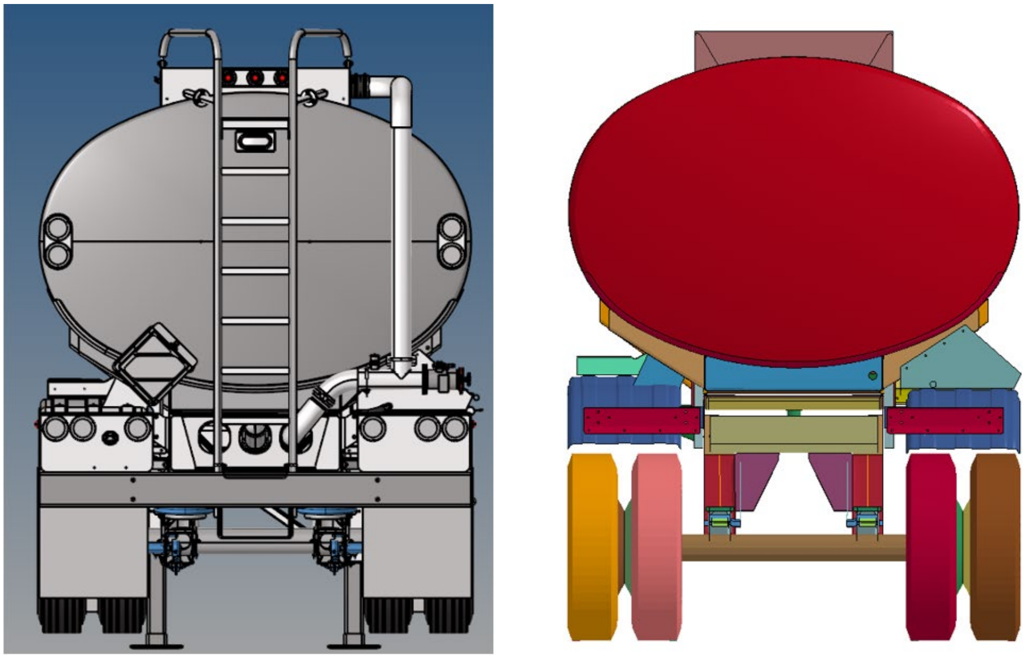

Figure 3.26 LBT Inc. Trailer Model Back View (Left) and LS-DYNA Model Back View (Right)

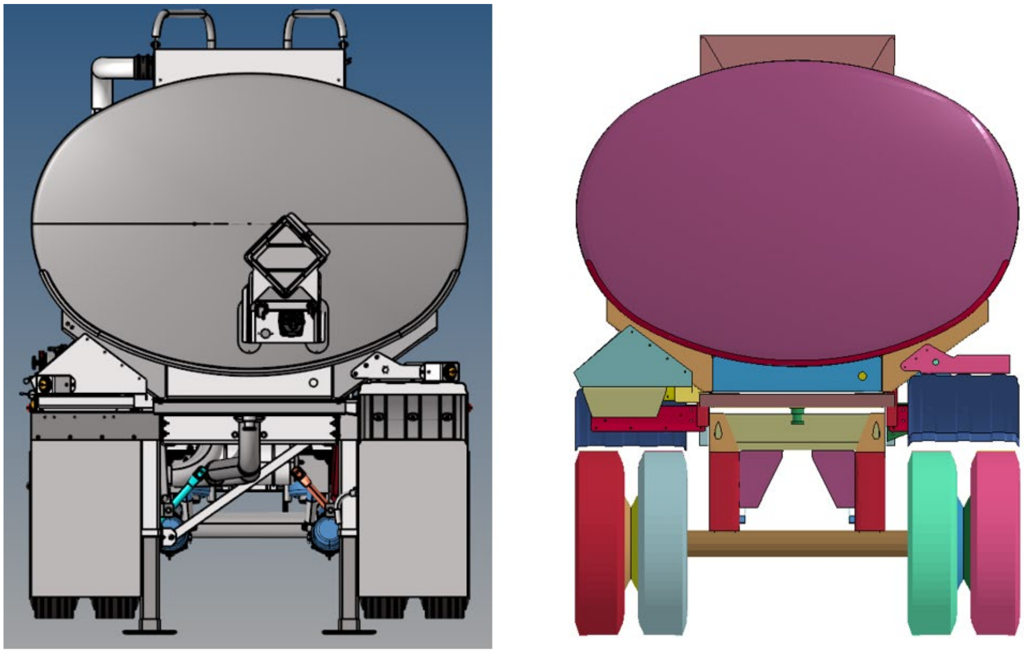

Figure 3.27 LBT Inc. Trailer Model Front View (Left) and LS-DYNA Model Front View (Right)

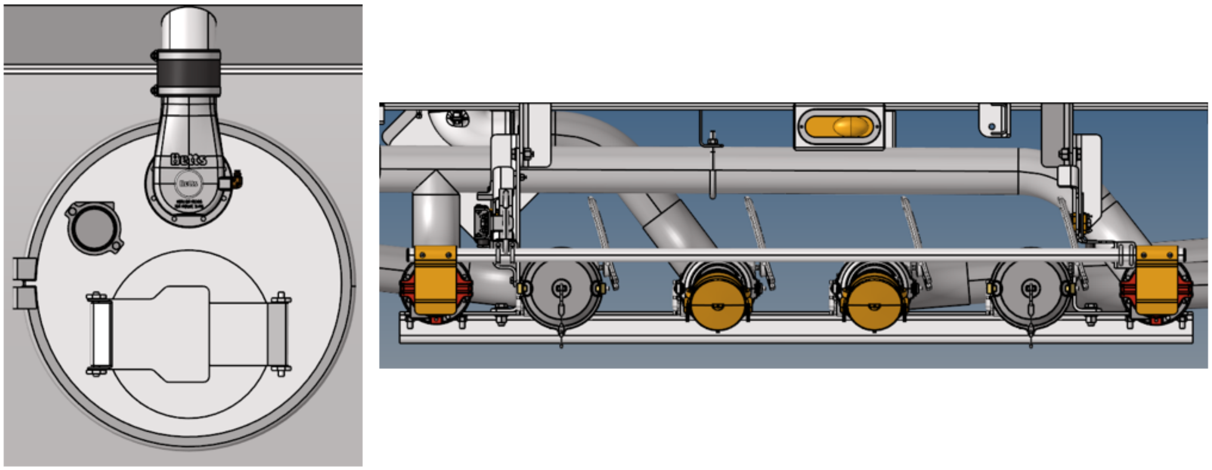

Figure 3.28 Non-Critical Component with Explicit Geometry

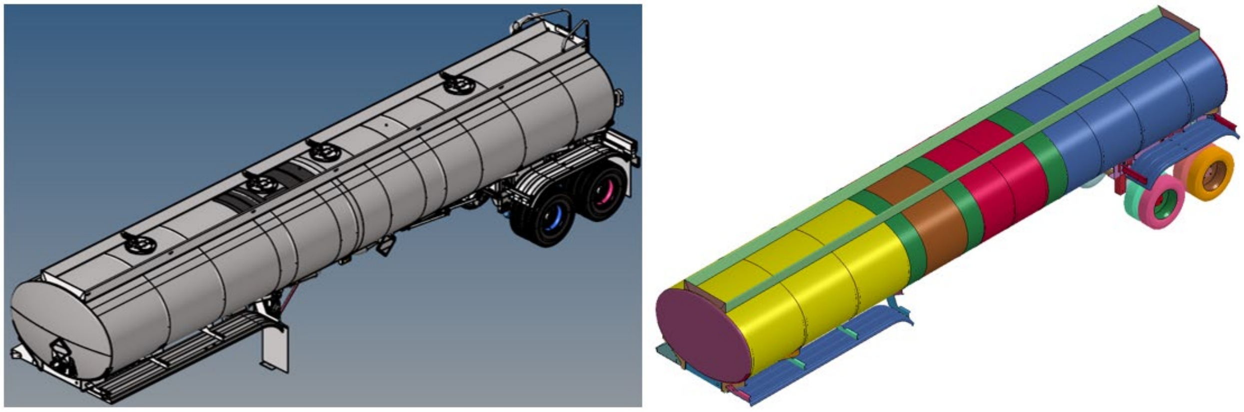

Figure 3.29 Trailer (Left) and Trailer After Clean-Up (Right)

Chapter 4 Overview of Finite Element Models Fluid

Before evaluating the simulations of the stability, forces, and reactions of the truck-tank trailer combination vehicle impacting potential designs for the TL-6 barrier, researchers first evaluated potential fluid models to represent the fluid ballast in the tank trailer. This chapter explores two computational methods that can be used to model fluid structure interaction (FSI) in LS-DYNA. The fluid was analyzed inside a TL-6 trailer's tank model with multiple compartments. Each FSI method will be discussed in terms of meshing and element formulation, material overview, and simulation results. The objective of this study is to compare both methods and determine whether they are appropriate for general fluid modeling. Parameters explored for this comparison are kinetic energy, internal energy, and computational efficiency.

4.1 Simulation Conditions

To test the fluid with both modeling techniques, a boundary prescribed motion was applied to the tank's nodes. This prescribed motion consisted of implementing an initial velocity to the nodes in the form $v = 30\sin(t)$, providing a small sloshing behavior. The sinusoidal input is shown in Figure 4.1 and lasted 15 ms with 1-ms time steps. The integrated position of the tank was calculated and is shown in figure 4.2. Gravity was also added to the model.

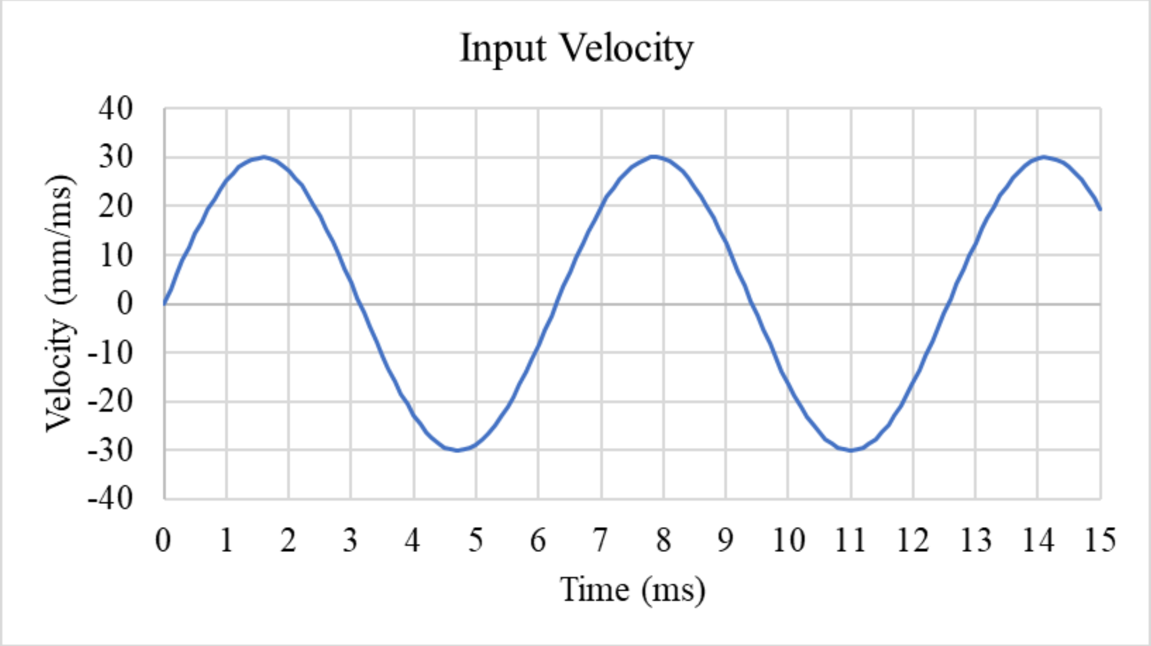

Figure 4.1 Sinusoidal Velocity Input Curve for Simulated Tank Movement

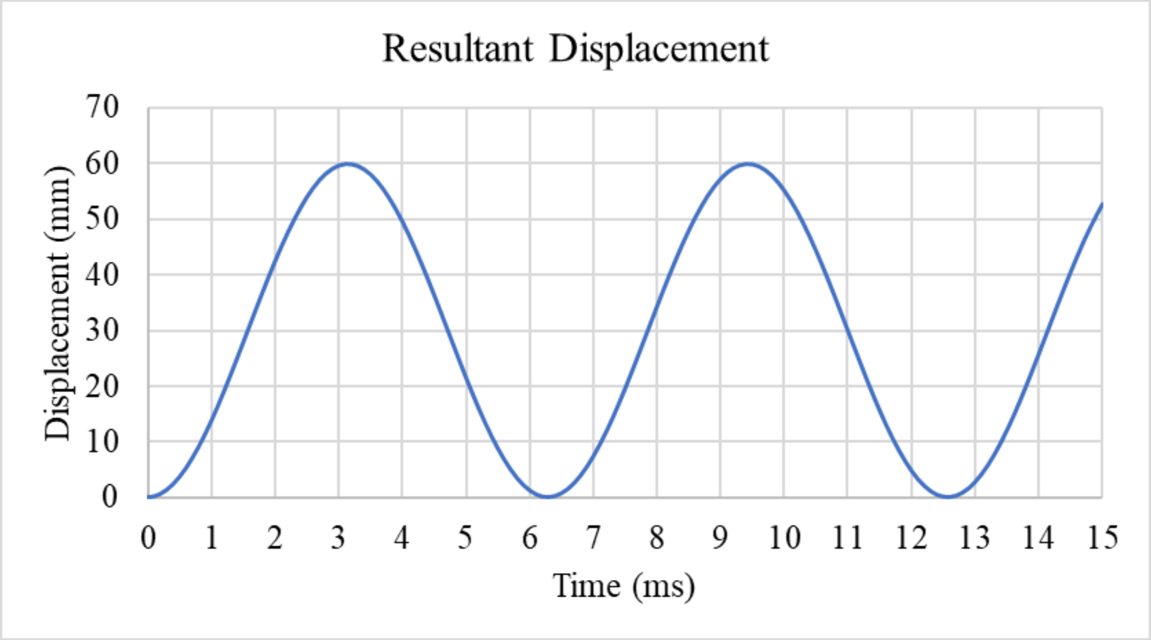

Figure 4.2 Tank Displacement for Simulated Tank Movement

4.2 Lagrangian Formulation

Lagrangian formulations are commonly used to deal with the deformation of structural parts in LS-DYNA. In Lagrangian formulation, nodes are connected to each other with a material medium. As a result, the mesh follows the material. In general, this method is applied to structural elements that have a high stiffness.

To approximate a fluid model using a Lagrangian model, approximated water material properties were applied to a solid element mesh representing the water ballast using a *MAT_ELASTIC_FLUID material formulation. The Young's modulus was replaced with a low bulk modulus, and the yield stress was set to nearly zero. Thus, Lagrangian fluid model representation is a computationally efficient means of representing the fluid behavior. This fluid model is only applicable when significant fluid mixing does not occur, as the intersection of non-connected fluid meshes can result in numerical instabilities.

4.2.1 Meshing and Element Formulation

For the Lagrangian formulation, the ten fluid components consisted of solid elements with a constant stress solid element formulation (ELFORM=1). The mesh of one fluid compartment is shown in figure 4.3. The mesh size of the fluid is about 20 mm per element and was modeled as a half-elliptical shape matching the tank's dimensions.

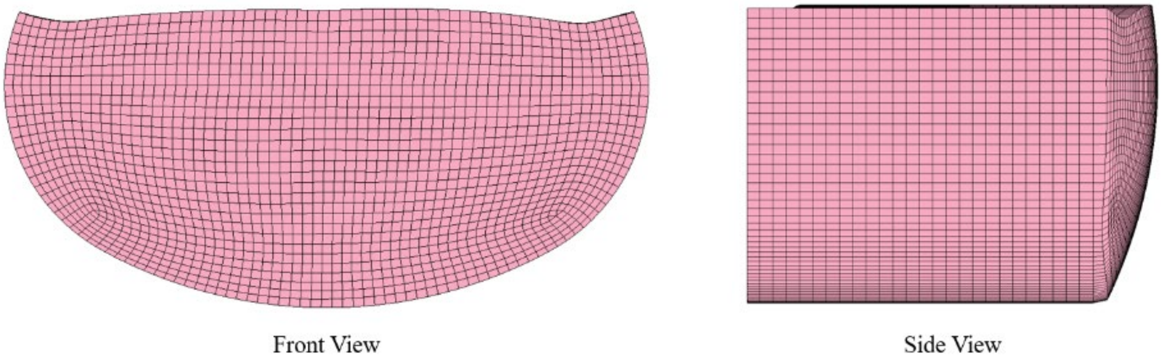

Figure 4.3 Lagrangian Fluid Meshing

4.2.2 Material Selection

The materials consisted of the tank material and fluid material. The fluid was simulated with the properties of water at room temperature (20°C), denoted in table 4.1. The fluid material was modeled using MAT_ELASTIC_FLUID.

Table 4.1 Material Properties for Water in Lagrangian Formulation

Property	Water
Density (kg/mm^3)	1.0E-6
Poisson's Ratio	0.2
Bulk Modulus (GPa)	2.15

4.2.3 Model Connections and Organization

The contact between the fluid and tank components is critical because their contact behavior can lead to instabilities. CONTACT_AUTOMATIC_SINGLE_SURFACE was used for the interaction between tank shell, bulkheads, and fluid components. An illustration of the tank components with the fluid meshes is shown in figure 4.4.

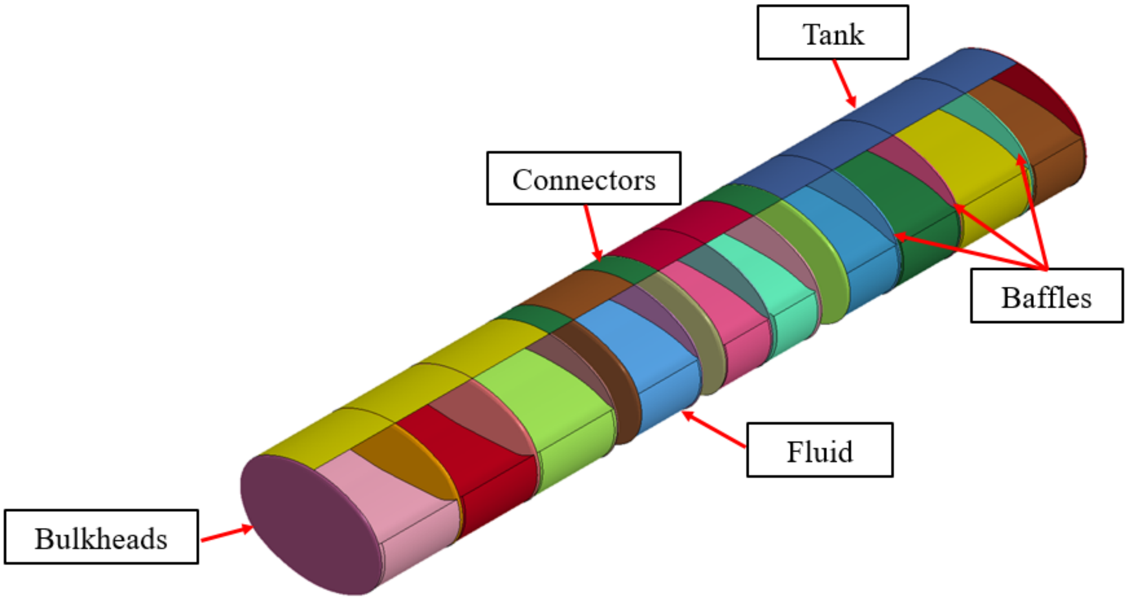

Figure 4.4 Fluid-Tanker Connections

To perform an energy analysis on the fluid model, the mass of each fluid was obtained and plotted with its corresponding container location as shown in figures 4.5 and 4.6. The mass distribution was also ordered from lower to higher mass, as shown in figure 4.7.

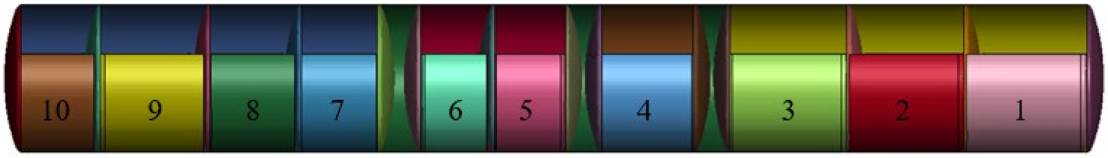

Figure 4.5 Tank Container Numbering

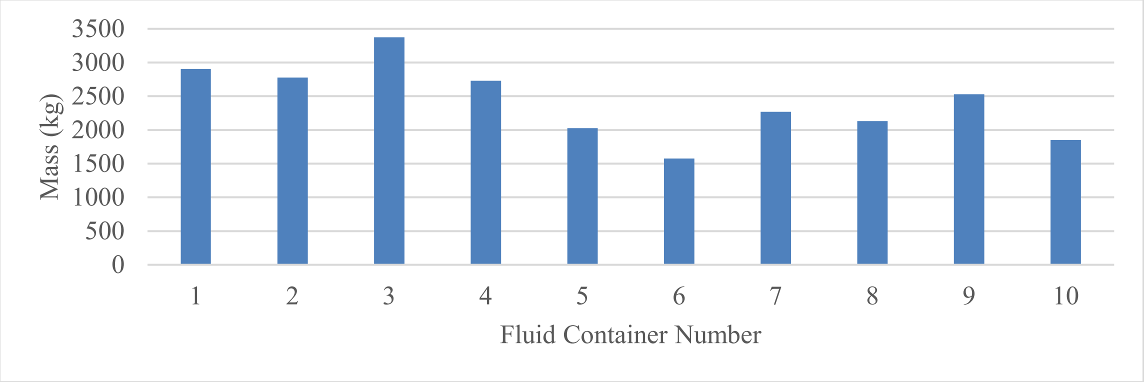

Figure 4.6 Container Mass Distribution

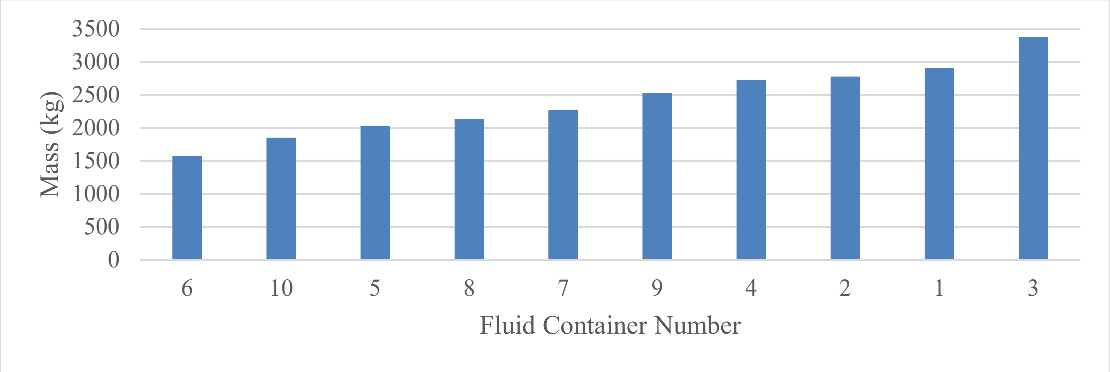

Figure 4.7 Containers Mass Distribution Ordered

4.2.4 Results and Data Analysis

Sequential images of simulation results are shown in figure 4.8. Results indicated the fluid component completely separated from the walls of the tanks during movement and behaved as a “sticky” body. Some sloshing occurred in the vessels. No element penetration from the fluid to the tank occurred.

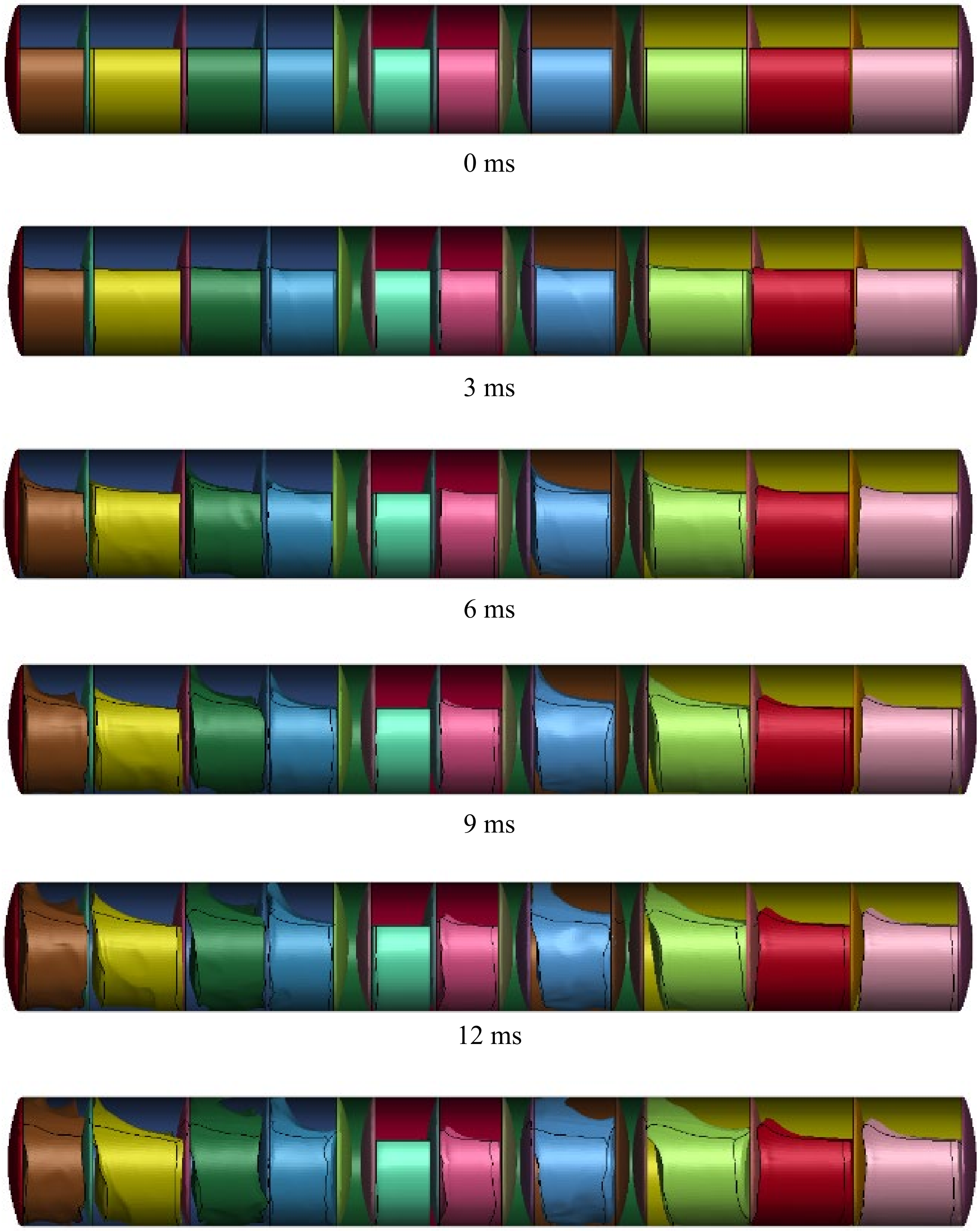

0 ms

3 ms

6 ms

9 ms

12 ms

15 ms

Figure 4.8 Lagrangian Fluid Sloshing Sequential Images

The internal and kinetic energies of the tank-fluid models were extracted to compare the fluid models. Internal energy of the complete system is shown in figure 4.9. This energy shows a fast increase of internal energy followed by a convergence at 6 ms, staying at around 500 kJ. The kinetic energy, found in figure 4.10, shows a sudden increase followed by an oscillatory behavior matching the sinusoidal input velocity. The fluid kinetic energy resembled the sinusoidal tank energy behavior after 2 ms.. Further analysis and comparison of the modeled ballast energy is shown later in comparison with the ALE fluid model.

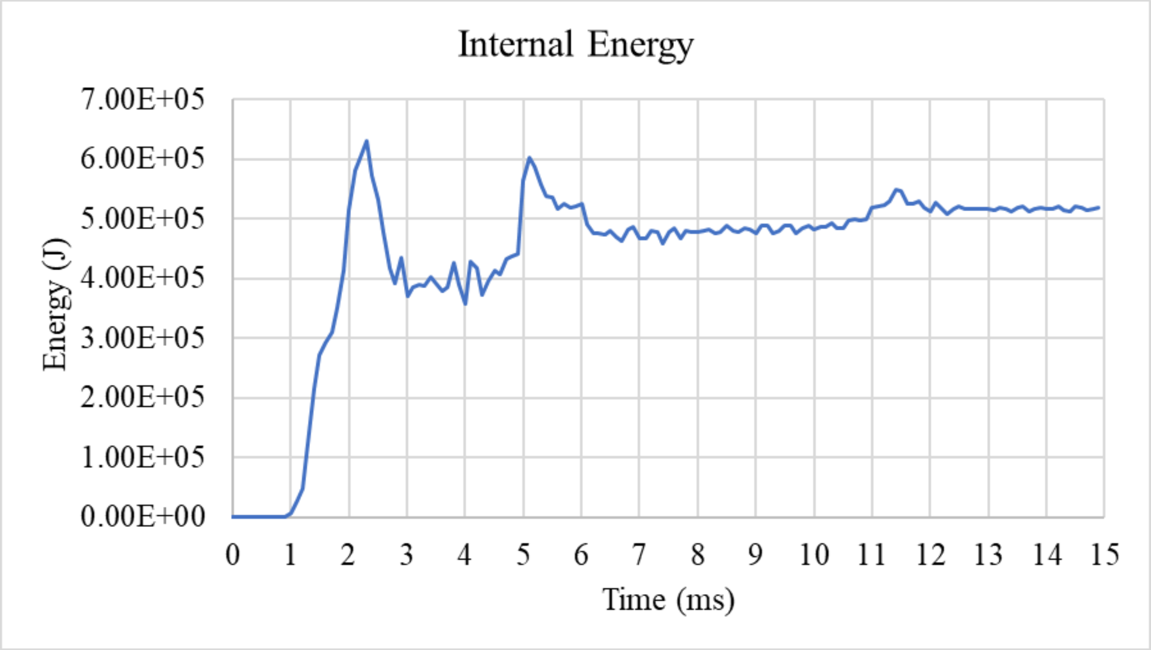

Figure 4.9 Internal Energy of Lagrangian Mode

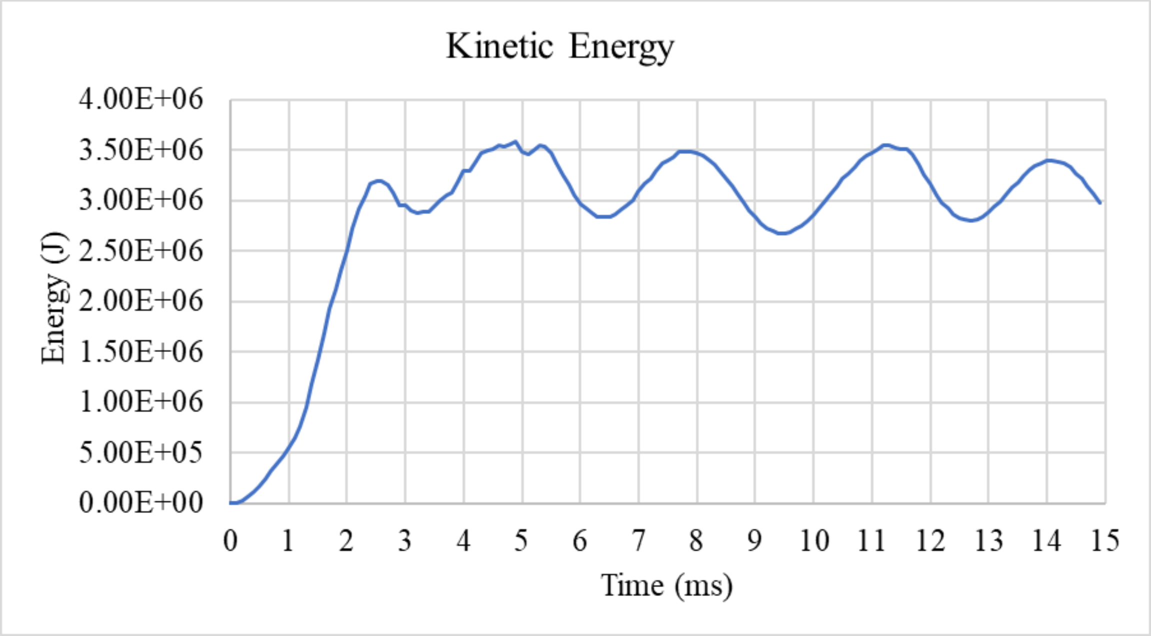

Figure 4.10 Kinetic Energy of Lagrangian Model

4.3 Arbitrary Lagrangian-Eulerian Formulation

The second method is denoted as a combination of the Lagrangian formulation with a Eulerian formulation, known as the Arbitrary Lagrangian-Eulerian (ALE) method. In ALE, a structural and a fluid part are created. This differs from the Lagrangian method which only requires one fluid part. The Lagrangian material part deals with the deformation of an outer structural part that surrounds the Eulerian part simulating the fluid movement (water and/or air). With this method, the motion of the Eulerian mesh is independent from the Lagrangian material's mesh. This permits higher strain rates with conventional material stiffness that increases stability and reduces mesh distortion of the fluid, thus obtaining higher accuracy but longer computational times.

4.3.1 Meshing and Element Formulation

The fluid component from the Lagrangian method was used in the ALE method. The air part was generated from the previously created water component by copying and rotating the water elements 180 degrees to match the tank's jacket shell. Fluid parts consisted of solid elements with 1-point ALE multi-material element formulation (ELFORM=11). The mesh of an example ALE fluid component is shown in figure 4.11. The mesh size of the fluid is same as the Lagrangian, or about 20 mm per element.

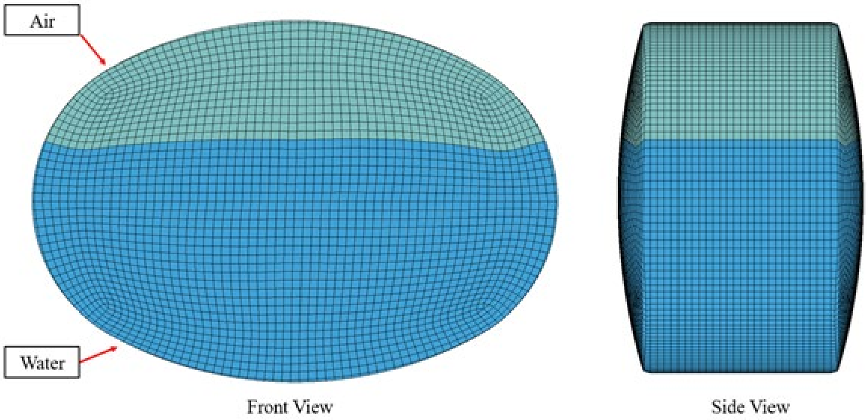

Figure 4.11 ALE Fluid Components

To create an ALE computational model, a second component is needed in each of the fluid components. This component, called the fluid container, is shown in figure 4.12 and does not represent a physical component of the actual tank-trailer. This component is needed for ALE implementation only. The fluid container is made of shell elements with negligible thickness but matches some of the material properties of the tank's shell. The location of the container is in between the tank's jacket and the fluid model, similar to an internal skin. The container is given negligible thickness to prevent any physical changes the ALE modeling could cause to allow comparison with the Lagrangian model. The meshing for this container is aligned with the fluids' surface meshing. The nodes from the fluids' surface are constrained to the nodes of the container's inner surface to allow the fluid components to move along with the tank components.

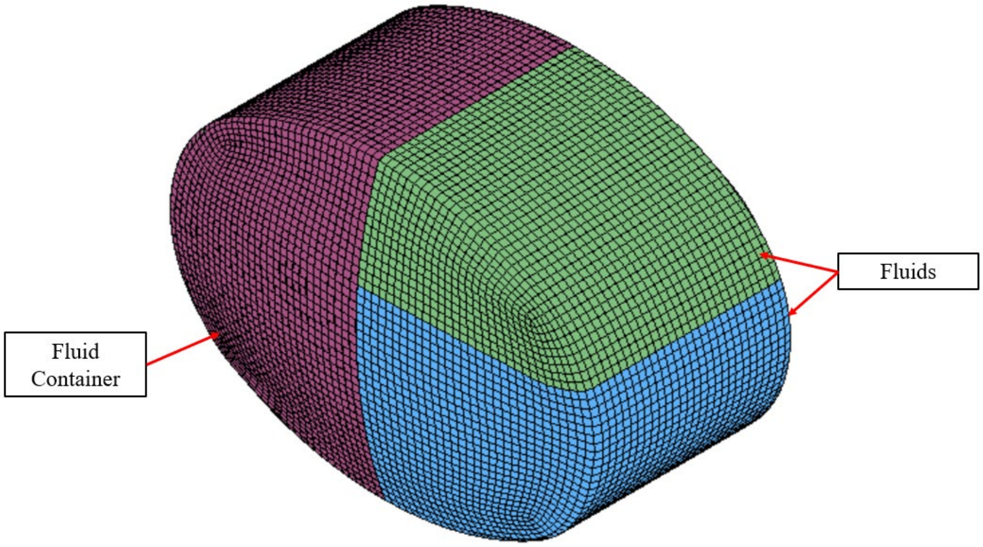

Figure 4.12 Fluid Container within ALE Tank-Fluid Model

4.3.2 Material Selection

For ALE, material properties of water and air at room temperature (20°C) were used as listed in table 4.2. For ALE, both fluid materials are modeled using *MAT_NULL. This computational method requires an Equation of State (EOS) to accurately simulate material behavior of water and air. In this model, the *EOS_LINEAR_POLYNOMIAL keyword is used, but multiple EOS keywords are available. The EOS parameters are also denoted in table 4.2.

Table 4.2 Material Properties ALE

Material Property	Water	Air
Density (kg/mm^3)	1E-6	1.25E-9
Pressure Cutoff (GPa)	-1E-4	0.0
Viscosity Coefficient (GPa·ms)	8.9E-10	1.75E-11
Equation of State	Water	Air
C0, C1, C2, C3, C4, C5, and C6	0	0
Internal Energy	0	0
Initial Relative Volume	1	1

4.3.3 Model Connections

Similar to Lagrangian modeling, the contact between the fluid and tank components is critical. The fluid mesh was constrained to the container using a constrained Lagrange in solid definition. This constrained command provides the coupling mechanism for modeling FSI. The fluid container was established as the slave part and the fluid components as the master part set. A CONTACT_TIED_NODES_TO_SURFACE was defined to establish a contact between the nodes of the fluid container and the surface of tank components. The tank component numbering was the same as for the Lagrangian model, and the weights per tank were approximately the same in the ALE fluid model as in the Lagrangian fluid model.

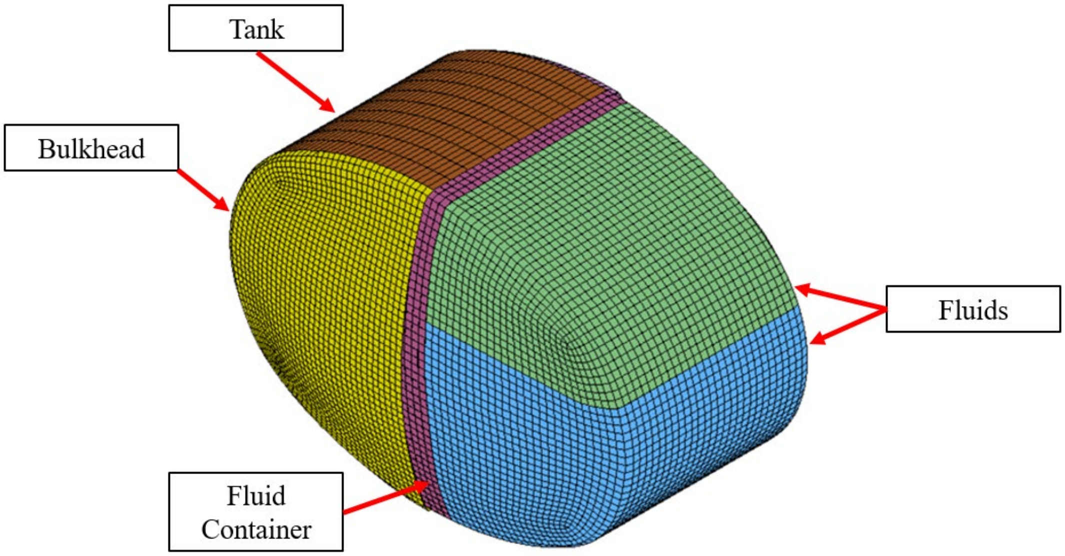

Figure 4.13 Fluid-Tanker Connections

4.3.4 Results and Data Analysis

ALE simulation results with sequential images are shown in figure 4.13. Results indicated the fluid component sloshed inside the tank with no shooting nodes or warpage, and no element penetration from the fluid into the tank occurred. It was also noted the sloshing behavior was smoother than in the Lagrangian model and created waves. The fast movement of the ALE fluid-filled tanks caused the water models to slosh upward through the top of the tank, creating voids on the boundaries and middle of the tank and leading to the appearance of “clouding” as shown in figure 4.14. However, the fluid mass per tank section remained unchanged throughout the analysis.

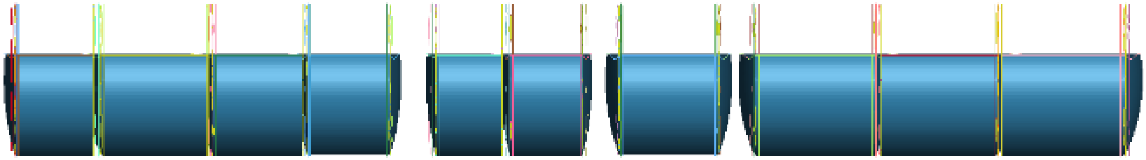

0 ms

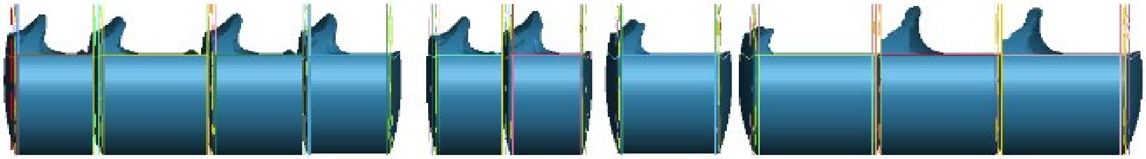

3 ms

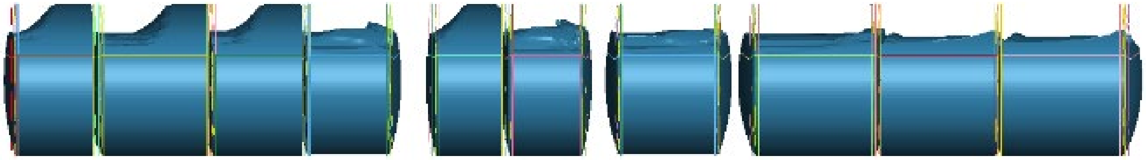

6 ms

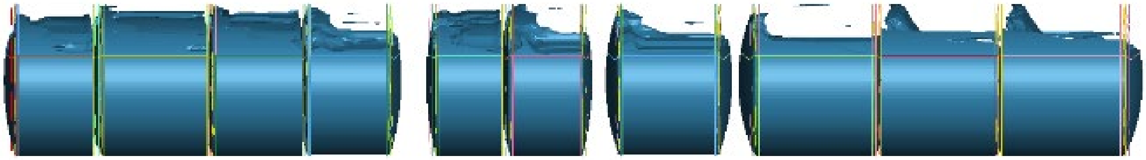

9 ms

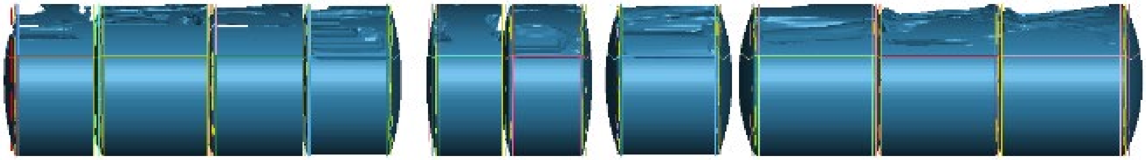

12 ms

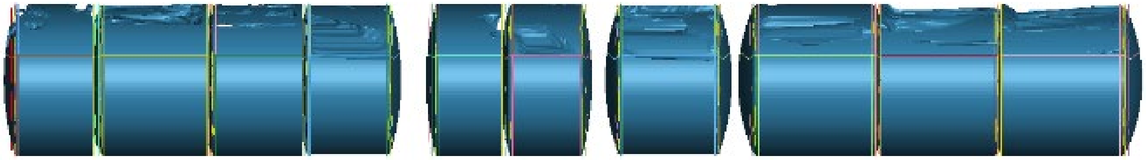

15 ms

Figure 4.14 ALE Model Sequential

To compare fluid models, the internal and kinetic energies of the tank-fluid models were extracted. The internal energy of the complete system is shown in figure 4.15. This energy showed a constant increase throughout the simulation time. The kinetic energy is shown in figure 4.16, and indicated an oscillatory behavior matching the sinusoidal input velocity. These results were explored further to compare both fluid computational models.

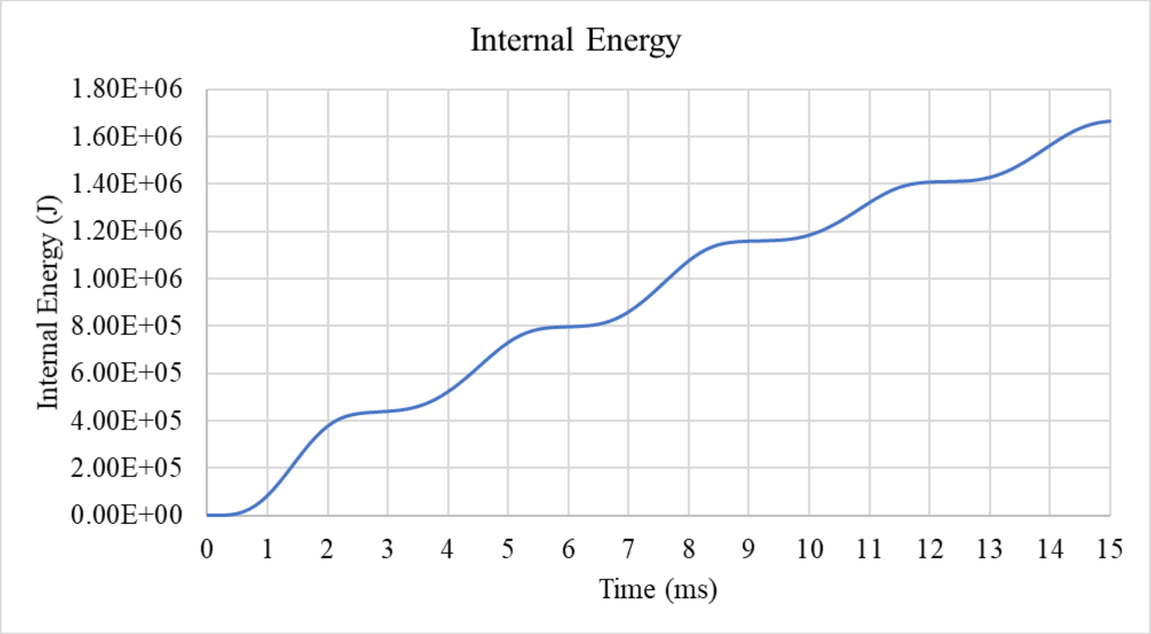

Figure 4.15 Internal Energy of ALE Mode

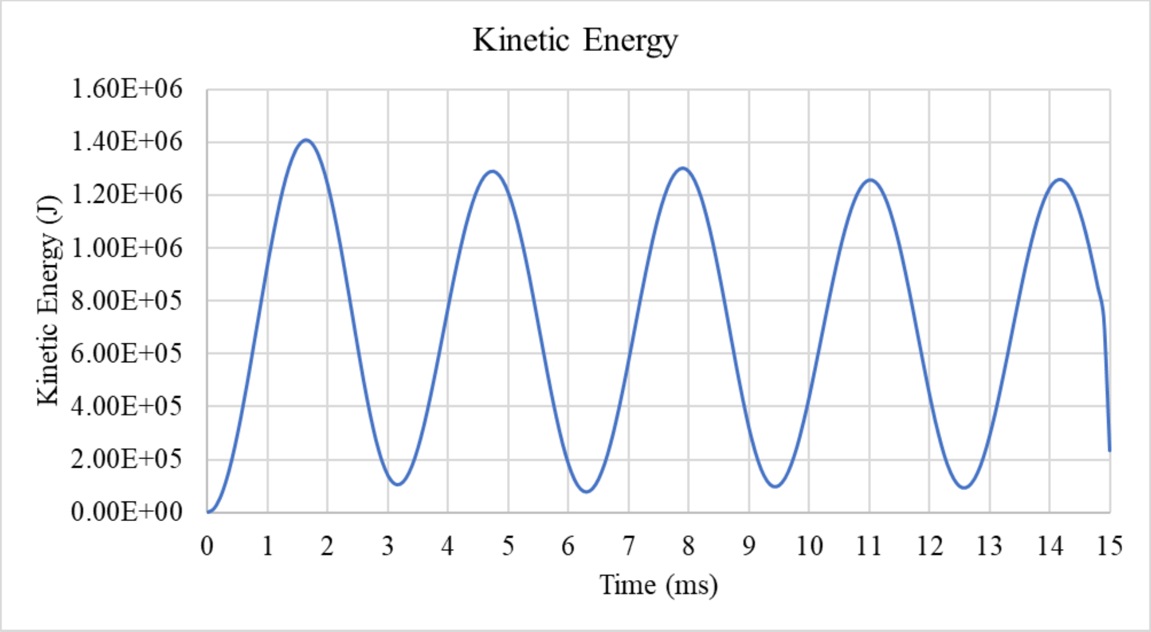

Figure 4.16 Kinetic Energy of ALE Model

4.4 Fluid Model Comparisons

In this section, the previous modeling results are compared and discussions and recommendations are given for future modeling of fluids using the Lagrangian or ALE methods.

4.4.1 Computational Comparisons

The model size and required CPU times for each computational method are listed in table 4.3 to illustrate the required computational effort and efficiency of solving the model with different approaches.

Table 4.3 CPU-Time Comparison

Model	**Total Number**		**Time Frame(ms)**	**CPU Time (min)**	**No. CPU**
	Nodes	**Elements**			
Lagrangian	554,082	516,994	15	23	32
ALE	784,394	832,074	15	57	32

4.4.2 Result Comparisons

For both Lagrangian and ALE techniques, the internal energy was plotted and compared as shown in figure 4.17. When using the Lagrangian method, the internal energy plateaus at approximately 500 kJ while the ALE energy increased linearly. The quasi-steady state result of internal energy in the Lagrangian simulation was attributed to the fluid not having enough time to follow the tank's motion, which caused the fluid to absorb less energy than the ALE model. As seen in figure 4.5, gaps form between the fluid and the bulkheads whereas these gaps are not present in ALE modeling, shown in figure 4.14. From this data, the Lagrangian fluid can be seen more as "slime" rather than a fluid, which cannot deform as a fast as a normal fluid would. This causes "bouncing" that removes contact in between the bulkheads and the fluid. However, the ALE simulations produced high-velocity waves near the baffles and bulkheads and "sprayed" water around the interior of the tanks. The ALE fluid was always in touch with the bulkheads, and the bulkheads have the prescribed velocity. As the fluid evacuated from the centers of the tanks and moved to the tank boundaries, the kinetic energy increased to reflect the additional mass momentum transfer throughout the events, but trended toward a quasi-steady sinusoidal behavior toward the end of the simulation. As a result, both of the models had some strengths, but some weaknesses in this high-speed vibration simulation.

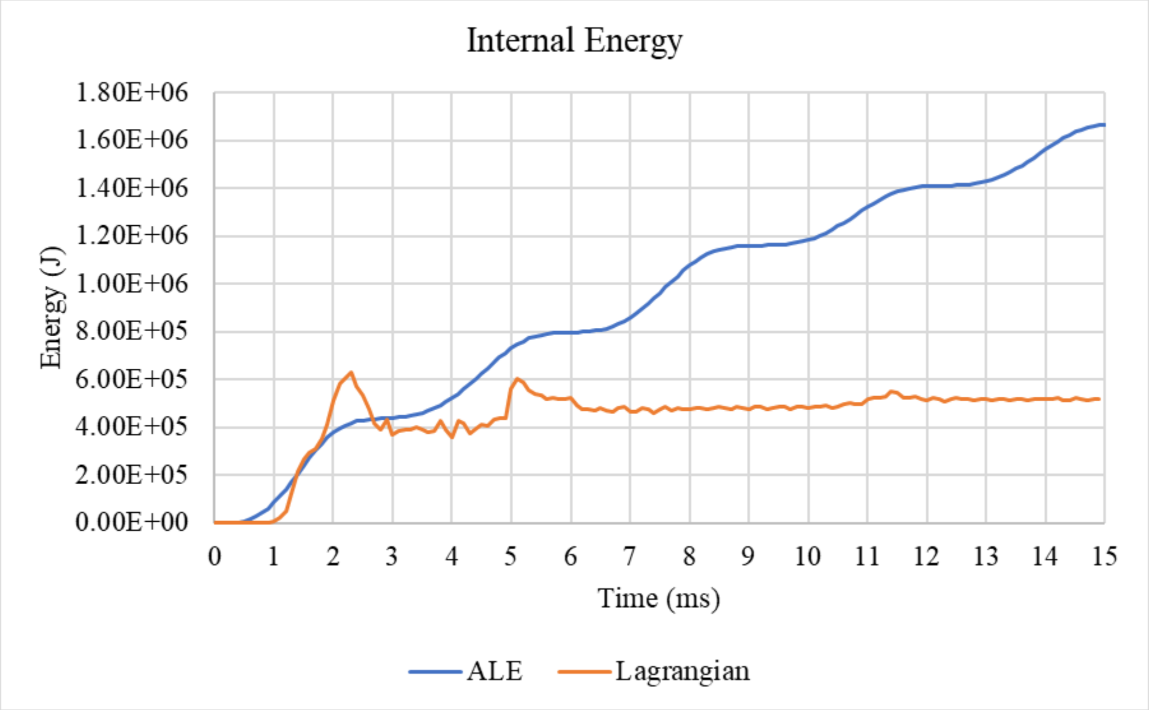

Figure 4.17 Internal Energy for ALE and Lagrangian Simulations

The kinetic energies of both methods are shown in figure 4.18. The total kinetic energy is higher in the Lagrangian model than in ALE. This difference is attributed to the same reason as the internal energy behavior. The Lagrangian method does not deform fast enough, which causes the fluid to have a semi-solid behavior during the initial velocity impulse. This creates the initial kinetic energy jump shown in the Lagrangian model. After the first impulse, the prescribed velocity on the tank pushes the fluid in a “bouncing” rather than sloshing behavior, which maintains the higher velocity compared to that of the ALE fluid. In the case of ALE, the fluid deforms fast enough to adapt to the volume of the tank and can maintain contact with the bulkheads, thus the interaction of the bulkheads and ALE fluid produces a slower velocity during the actual sloshing, which is more representative of a fluid-like behavior.

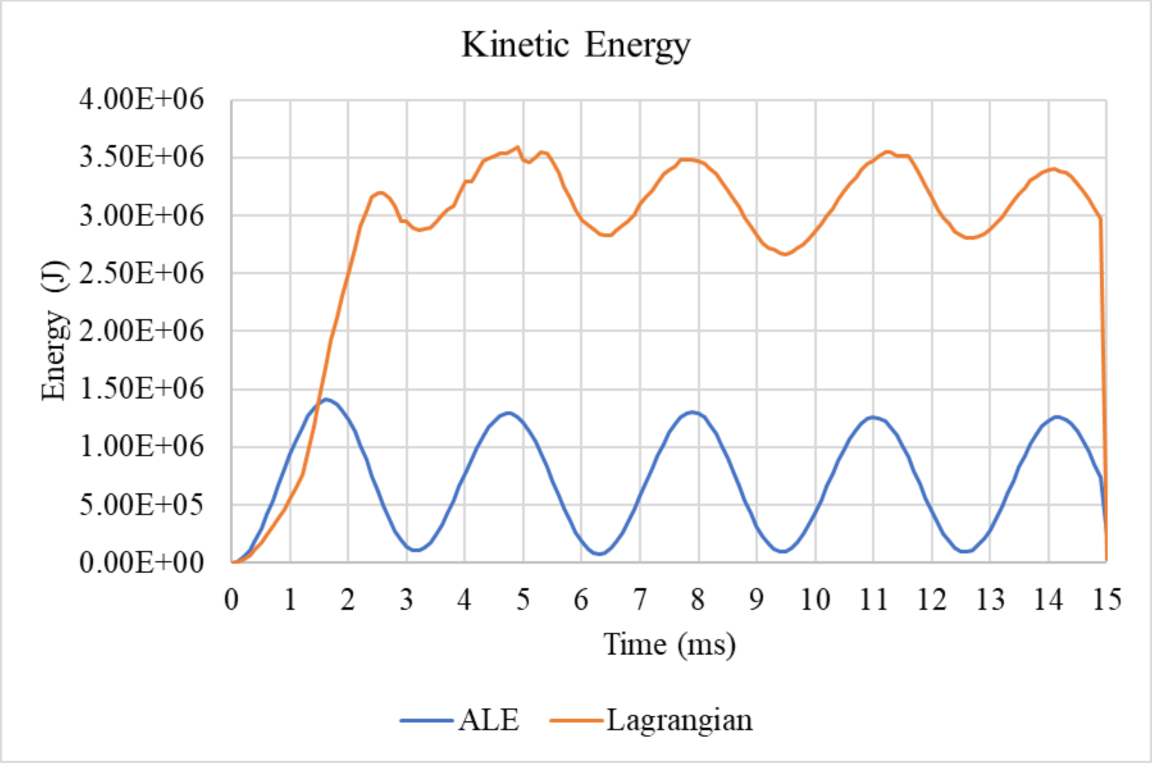

Figure 4.18 Kinetic Energy for ALE and Lagrangian Simulations

4.4.3 Discussions and Recommendations

In terms of visual representation, ALE provided a more fluid-like behavior following the tank’s movement at high speeds, whereas the Lagrangian fluid model showed a gel-like behavior by resisting flow near the boundaries of the tank. Likewise, the movement of the water to the boundaries of the tank model, pushing the air to the interior cavity, is believed to be a more realistic behavior than the Lagrangian “slime” result as it suggests the low viscosity and density of water relative to the fast tank movement.

After comparing both computational methods, it can be concluded that ALE offers a more accurate modeling technique with better results than the Lagrangian method. However, this modeling technique is more computationally expensive, as noted in table 4.3, and requires extra modeling techniques to achieve. ALE requires special attention and considerations of how the container is meshed as the mesh must be consistent with the fluid for implementation. Also, for better results, it is recommended the container also matches the tank’s mesh. An aspect that increases ALE modeling difficulty is the use of Equations of State. Instabilities were often found for most Equation of State types and it will be recommended to explore others and how their parameters affect implementation into the trailer model. Multiple combinations of ALE parameters can be explored and compared with Lagrangian parameters as well to determine better combinations.

Results of slower sloshing models are not shown in this report. Some additional investigative work was also completed to investigate low-speed wave modes, but the models did not show significant differences. However, some errors were observed in those models and for consistency were not discussed here. Further research into low-speed fluid behaviors and fluid reactions to impact is recommended.

In conclusion, if the complexity of the model is not high, ALE may provide a better overall representation. For models where complexity is high and time is a priority, the Lagrangian method offers reliable results. Due to time constraints and issues related to initial velocity and containment of the ALE fluid model in the tank, which were not resolved during the course of this research study, researchers proceeded with the Lagrangian fluid model. However, results of this fluid research were applied toward full vehicle model results to understand and accommodate numerical instabilities which were encountered.

Chapter 5 TL-6 Vehicle Model Validation

In this chapter the model validation is described to verify that the data obtained from the TL-6 vehicle model was reliable. To validate the TL-6 vehicle model, the angular displacements, longitudinal and lateral accelerations, and wall forces from the TL-6 vehicle model were compared to those from a simulated version of the full-scale Instrumented Wall (1988) crash test [16]. The instrumented wall consisted of five independent reinforced concrete wall segments which measured 120 in. long by 90 in. tall (3,048 mm x 2,286 mm), and sixteen load cells were placed behind the walls [16]. Three of the walls were instrumented with three accelerometers arranged in a triangular pattern on the back face of the wall segment [16]. The last wall segment, at the furthest upstream, was instrumented with one accelerometer at the c.g. of the wall.

The crash test, shown in figure 5.1, consisted of a tractor-tank trailer impacting the 90 in. (2,286-mm) tall barrier at a speed and angle of 54.8 mph (88.2 km/h) and 16 degrees, respectively. The test vehicle was equipped with four accelerometers located at the rear tandem of the tractor, on the tractor in front of the trailer, and in two places on the trailer.

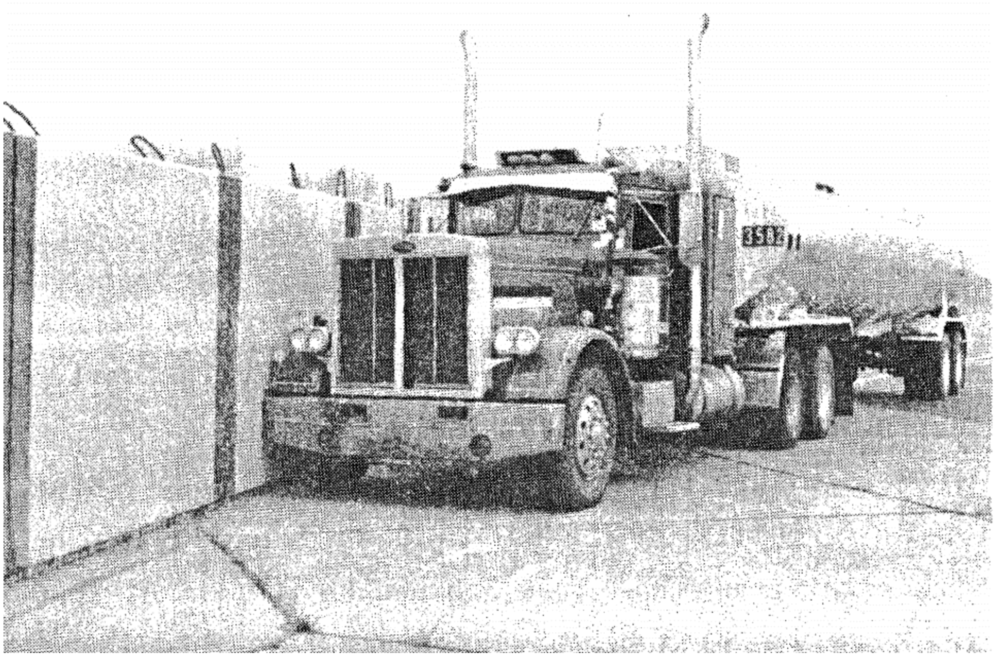

Figure 5.1 Vehicle before Test 2 [16]

5.1 Dimensions and Weight

Both computational methods were utilized with the TL-6 vehicle model and compared with existing data from Instrumented Wall Test to determine which computational method produced more accurate results and stability.

The Lagrangian fluid components were successfully implemented into the vehicle model. Unfortunately, the ALE fluid components were unable to be implemented into the vehicle model due to instabilities such as out of range forces and out of range velocities. These instabilities were caused by the type of initial velocity used (*INITIAL_VELOCITY_GENERATION) and the material property of water (cutoff pressure). Recommendations for how to fix these instabilities are discussed in Chapter 7.

The weight and dimensions of the trailer model needed to be verified. According to table 2.1, which lists the MASH TL-6 crash test criteria, the weight of a TL-6 vehicle must be approximately 79,366 lb (36,000 kg). Table 5.1 denotes the weight of the tractor-trailer as provided by LBT Inc. The weight of the LS-DYNA vehicle model was 2,639 lb (1,197 kg) lighter than the LBT Inc. model due to the removal of components from the original trailer.

Table 5.1 Vehicle Model Mass

Mass	**LBT Inc. Model**	**Lagrangian Model**	**ALE Model**
Vehicle	12,093 kg	10,896 kg	10,896 kg
Fluid	24,195 kg	24,165 kg	24,213 kg
Total	36,288kg	35,061 kg	35,109 kg

Consistent with the methods used by Whitfield [1], the simulated barrier had sixteen small, instrumented rigid walls, as shown in figure 5.2, that were created using *RIGIDWALL_PLANAR_FINITE. The walls were used to simulate the sixteen load cells placed behind four wall sections in the full-scale crash test. The simulated rigid wall panels were 60 in. (1,524 mm) long and 45 in. (1,130 mm) tall. A chamfer with a width of 1.5 in. (36 mm) and a total length of 140 ft (43 m) was placed above the rigid wall cells in the simulation. The simulated Instrumented Wall crash test is shown in figure 5.3. One additional larger rigidwall was added downstream from the sixteen smaller walls, to allow investigation of the vehicle stability and redirection length after impact.

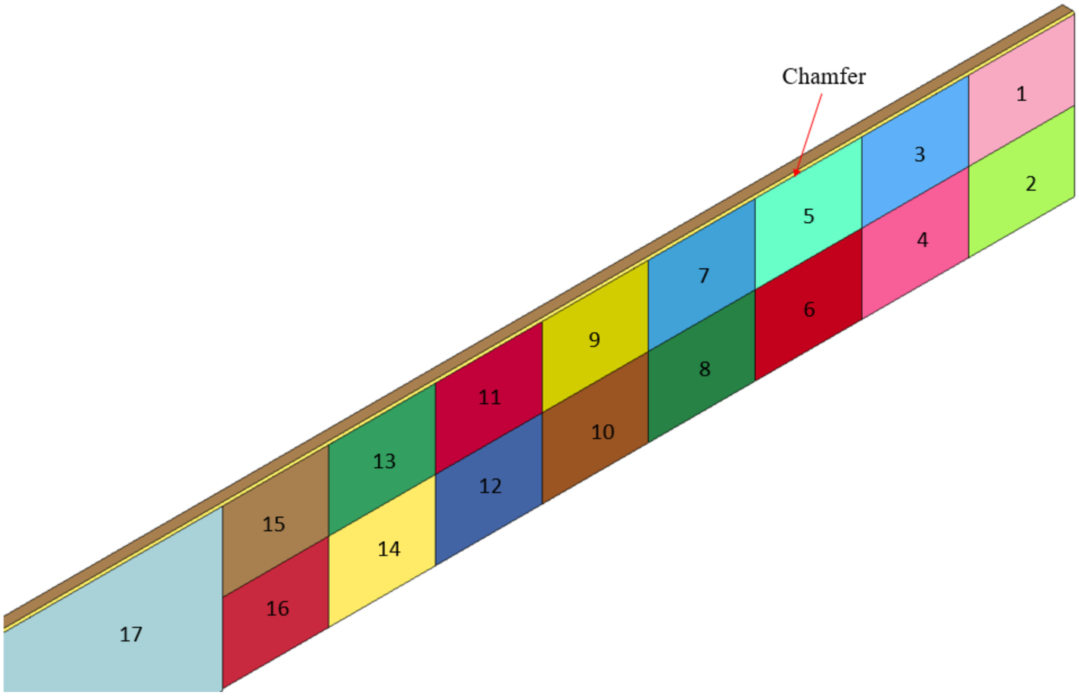

Figure 5.2 Rigid Wall Layout

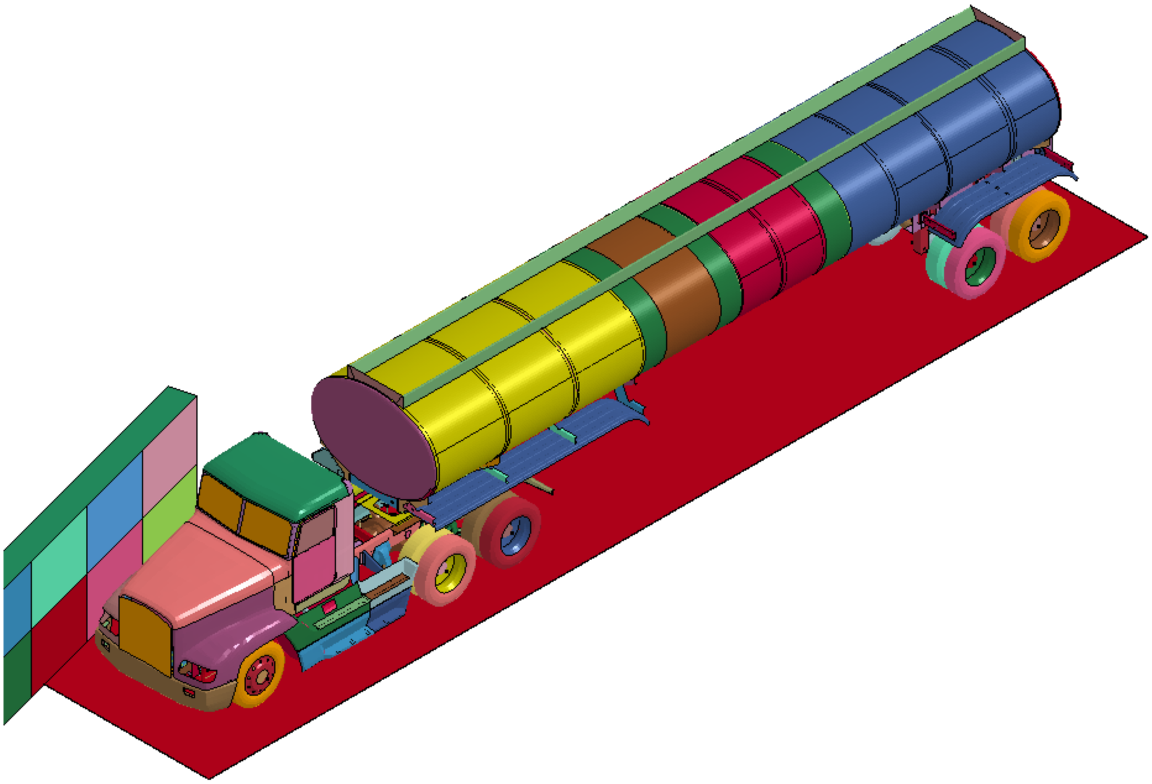

Figure 5.3 Instrumented Wall Simulation

5.2 Vehicle Angular Displacement

For the rigid wall model, the *DATABASE_RWFORCE key was used to record the forces on the rigid walls. Similarly, to the Instrumented Wall test data, a 50-ms moving average was applied to the obtained wall forces.

For the TL-6 vehicle, accelerometers were located at the c.g. of the tractor, at the rear tandem of the tractor, and the rear tandem of the trailer. The accelerations and rotational velocities at the x, y, and z axes were extracted from the accelerometers. This set of data was processed to obtain the angular displacements (roll, yaw, and pitch), and accelerations (lateral and longitudinal).

Angular displacements were recorded in the full-scale crash test at the c.g. of the tractor. The angular displacements were compared between the simulation and full-scale crash test, as shown in figure 5.4. Most of the angular data compared favorably, although the angular displacements of the tested vehicle were larger and occurred earlier during the impact event than comparable angular displacements of the simulated truck-tank trailer combination vehicle.

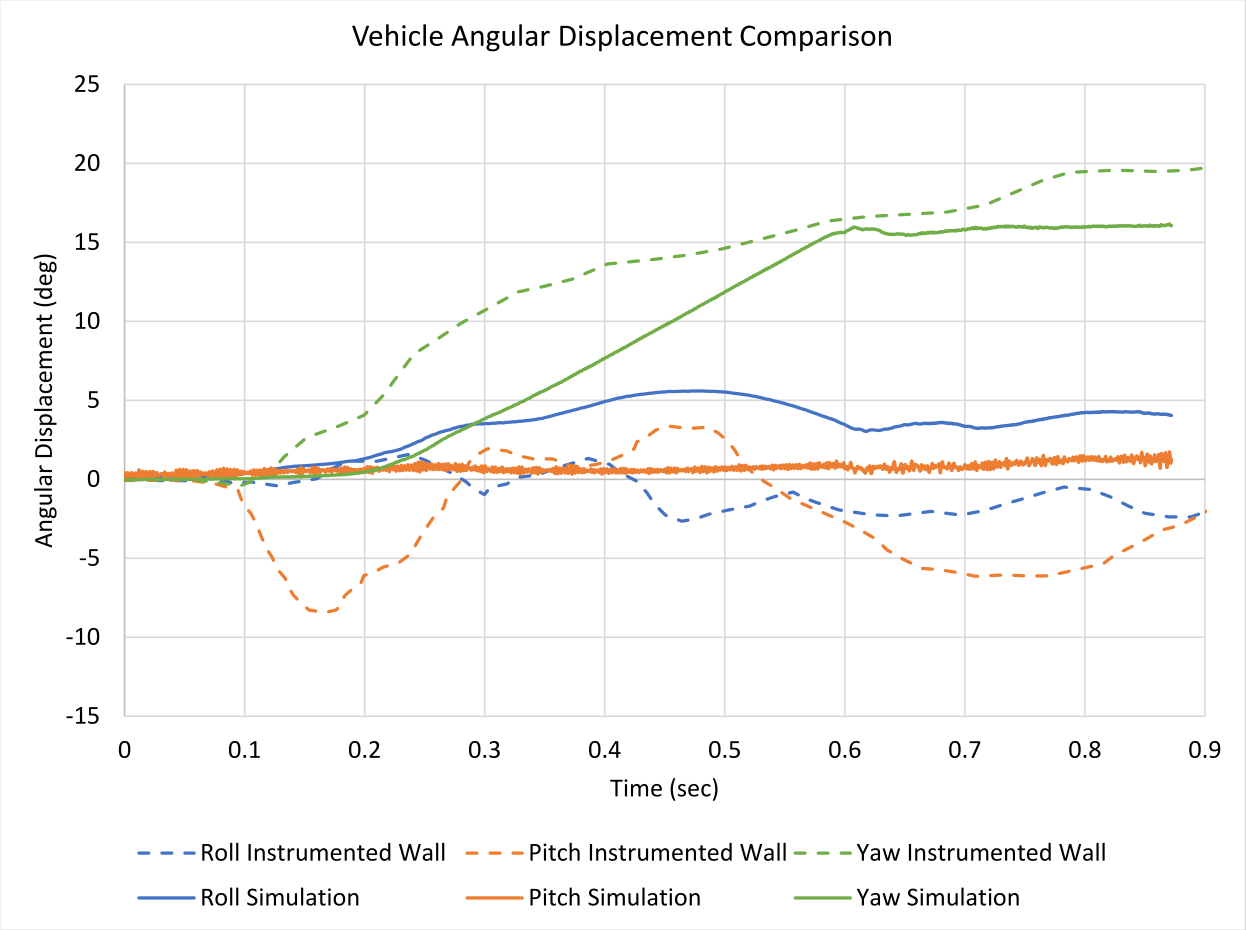

Figure 5.4 Angular Displacement Comparison

5.3 Accelerations

The accelerations were extracted from the tractor's accelerometer and compared to the accelerometer data from Instrumented Wall crash test. The extracted accelerations were filtered using a 0.05-sec moving average. The extracted accelerations are shown in figures 5.5 and 5.6.

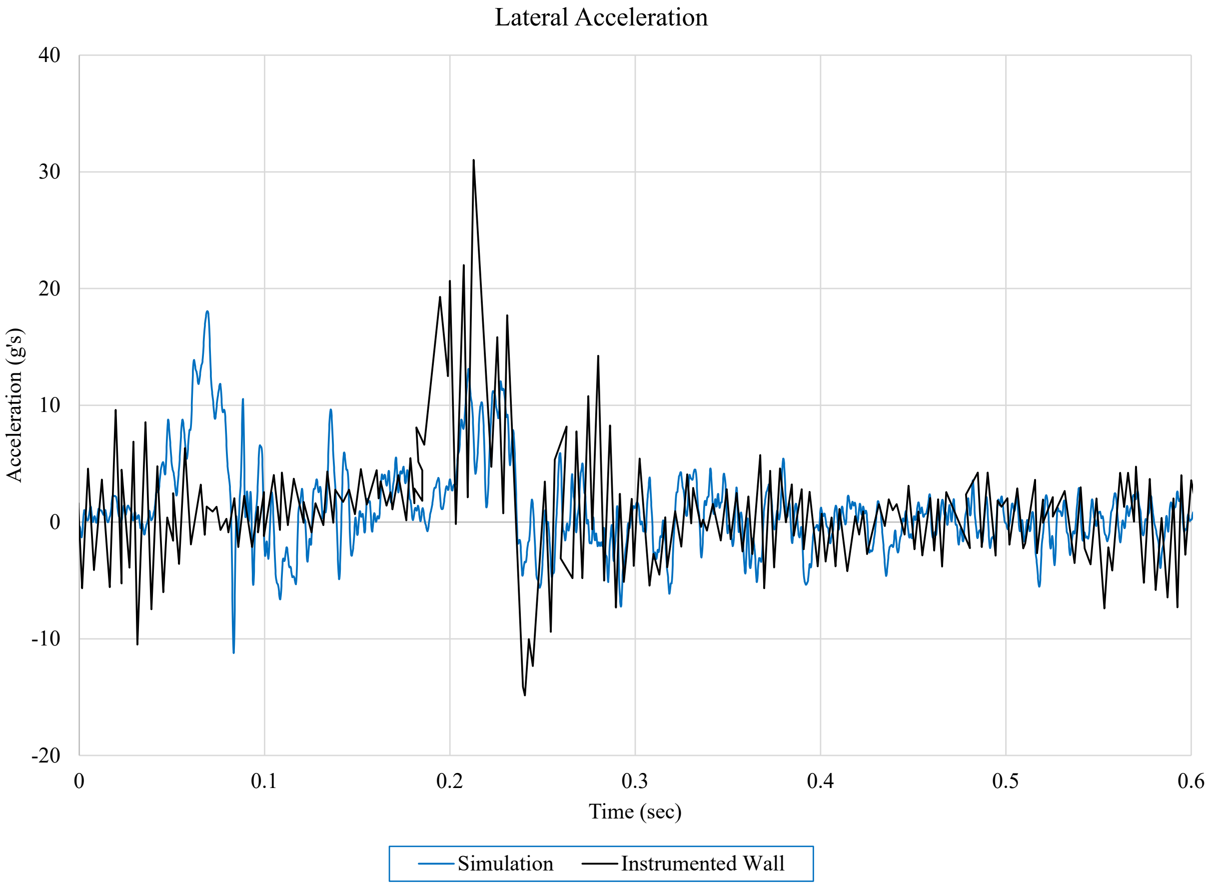

Figure 5.5 Lateral Acceleration

Lateral acceleration traces for the test and the simulation were similar. In both cases, the first major peak indicated the time the tractor impacted the barrier, and the second major peak indicated the tractor's rear tandem wheels impacting the barrier. The front of the tank trailer also struck the barrier at approximately the same time. The main difference was found in the time it took for the tank to impact the barrier after the initial tractor impact. In the Instrumented Wall test, the tank's tail slap into the barrier took approximately 0.04 sec longer than in the simulation impact. However, this difference could be attributed to differences in the vehicle and tank geometries. The largest 0.05-sec average acceleration in the Instrumented Wall test was reported as 12.3 g as compared to 8.7 g in the simulation. Overall, the general trend of the two tests was similar, but the magnitude and timing were shifted.

The longitudinal accelerations from the tractor's c.g. were also obtained for both the test and the simulation, as shown in figure 5.7. This graph shows trends similar to those seen in the lateral acceleration. Increased accelerations during the tractor and front trailer impact occurred in the full-scale test compared to the simulation. The largest 0.05-sec average acceleration in the full-scale test was 2.1 g versus 1.0 g in the simulation data.

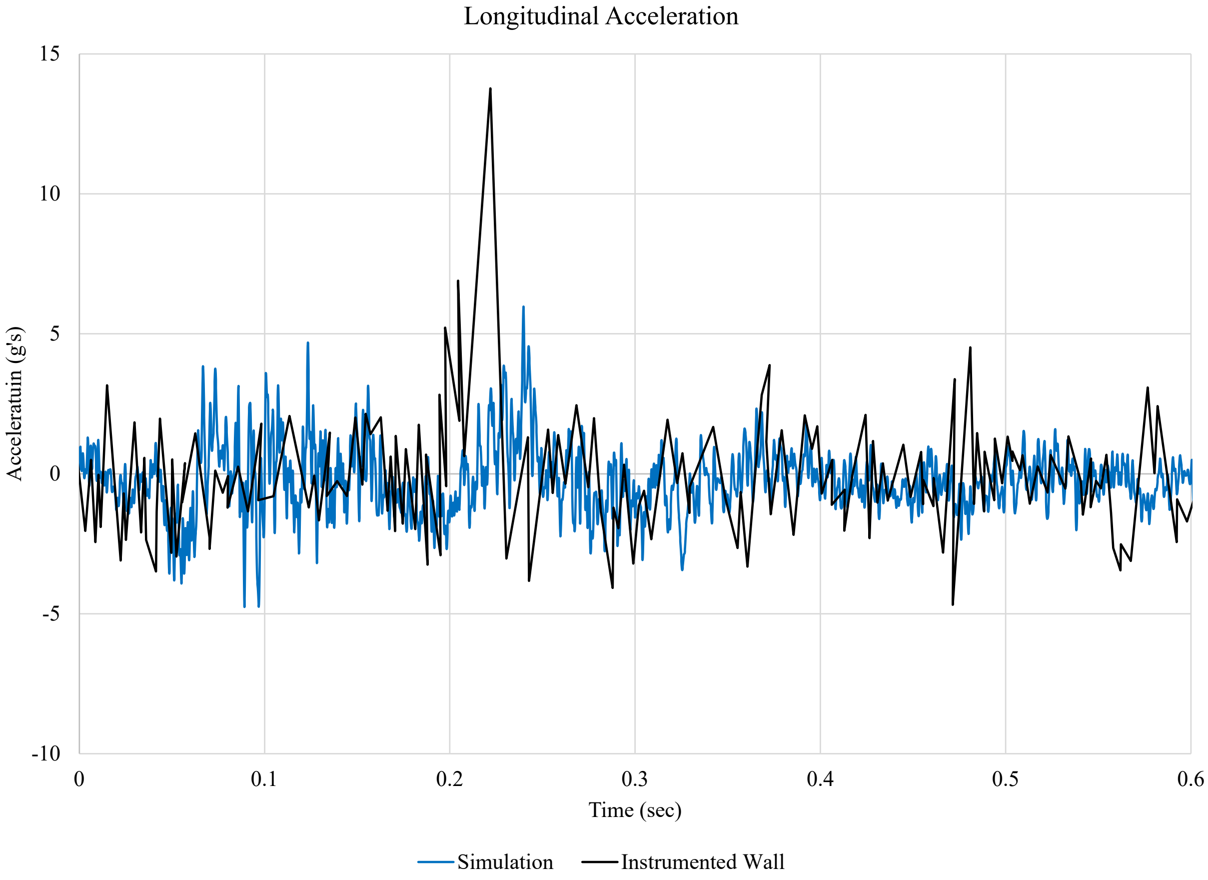

Figure 5.6 Longitudinal Acceleration

5.4 Barrier Forces

The simulated wall forces were extracted from the rigidwalls and filtered using a 0.05-sec average to match the filtering performed on the Instrumented Wall test data. The forces from the rigidwalls were summed to obtain the total loading, as shown in figure 5.8. Four peaks are shown in the graph, representing the first impact from the tractor, trailer's front, and trailer's tandem (two peaks).

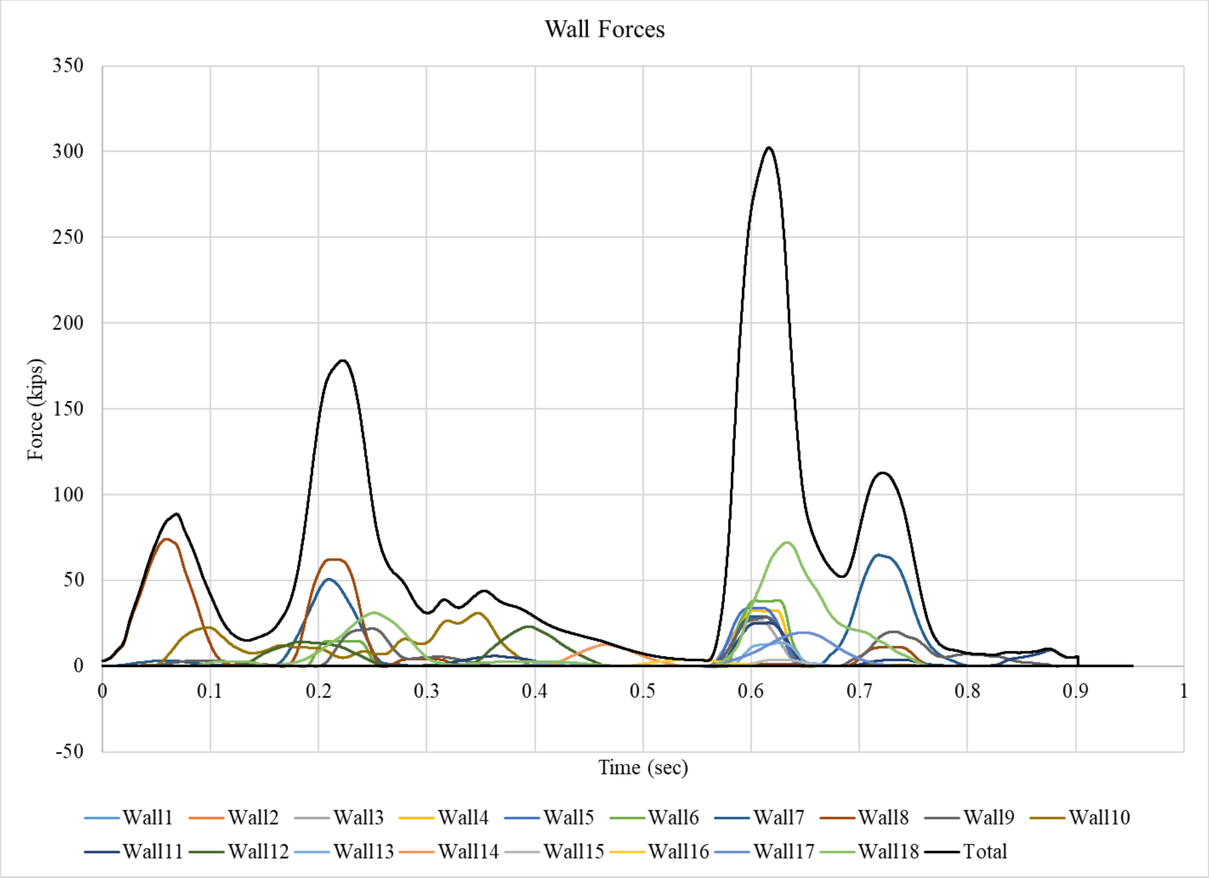

Figure 5.7 Wall Forces, 90 in. (2,286-mm) Barrier

The total forces from the Phase I (Whitfield), Phase II (Vasquez), and Instrumented Wall simulations are graphed in figure 5.8. The most important aspect was the magnitude of the load being imparted onto the barrier. The first peak load in the Instrumented Wall test was 91 kips as compared to 104 kips in the Phase I simulation and 90 kips in the Phase II simulation. The second peak loadings were 212 kips, 149 kips and 178 kips for the Instrumented Wall, Phase I, and Phase II simulations, respectively. Lastly, the largest load, the rear tandem, exerted 408 kips in the Instrumented Wall test, 160 kips in the Phase I simulation, and 302 kips in Phase II simulation.

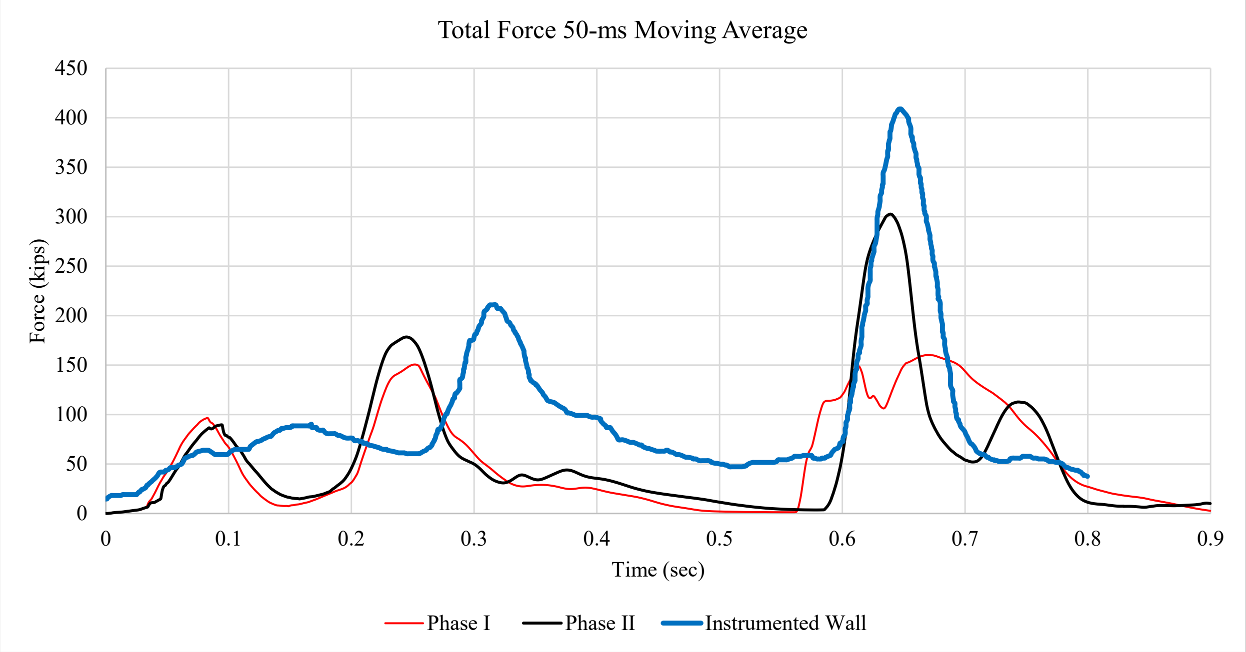

Figure 5.8 Total Wall Forces

Chapter 6 Investigation of Optimized Barrier Height

6.1 Minimum Barrier Height Study

A barrier study was conducted to determine which barrier height meets the safety standards for MASH TL-6. The accelerations, rotational velocities, and wall forces were extracted and analyzed. Barrier heights ranged from 50 in. (1,270 mm) to 90 in. (2,286 mm) at 5 in. (127-mm) increments. Rigidwall sizes in the barrier height evaluation study were identical to those used in the model verification simulation, but the heights of the walls were reduced to reflect the barrier height changes. The model layout can be seen in figure 6.1. In total, ten simulations of the MASH TL-6 vehicle model impacting different barrier heights at 50 mph (80.5 km/h) and an angle of 15 degrees were run. Example sequential images of four different heights, 50, 62, 70, and 90 in. (1,270, 1,575, 1,778, and 2,286 mm) are shown in figure 6.3 through figure 6.5, respectively.

The extracted x, y, and z rotational velocity data was used to calculate the Euler roll, pitch, and yaw. The normal forces from the sixteen smaller rigid walls and one larger rigidwall were extracted, and a 50-ms average was applied. Results of the impact force investigation are shown in figure 6.6.

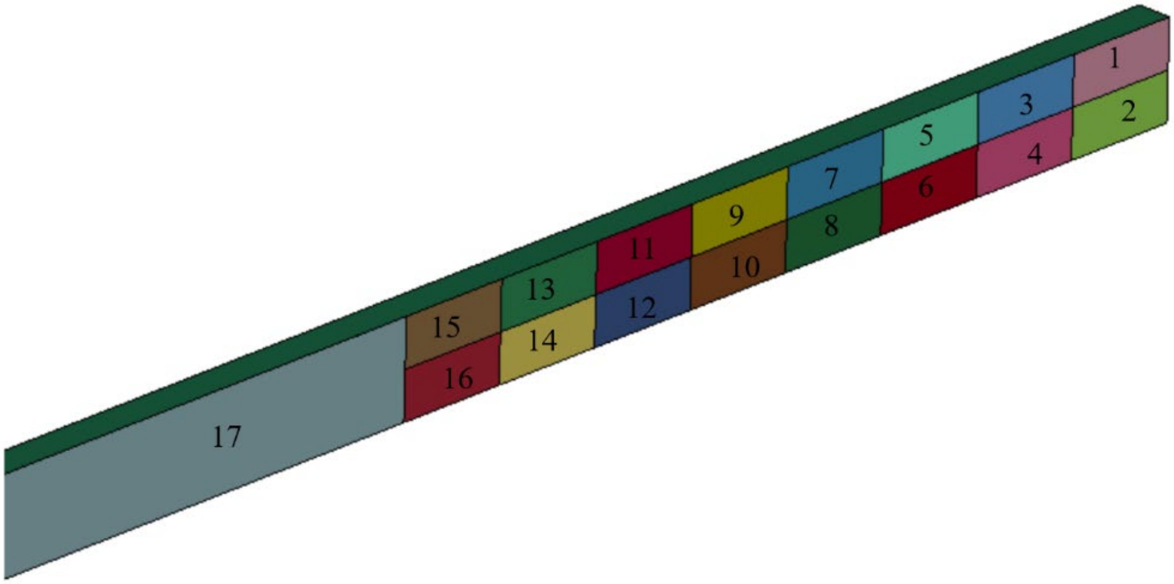

Figure 6.1 Rigid Wall Model

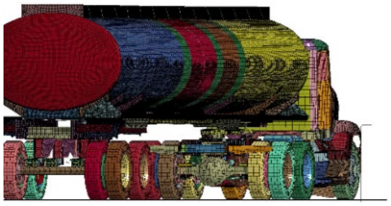

100 ms

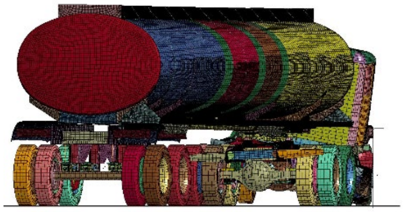

200 ms

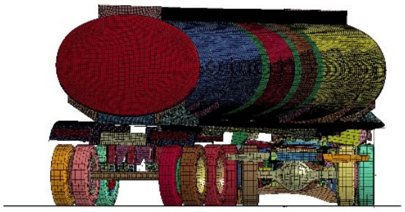

300 ms

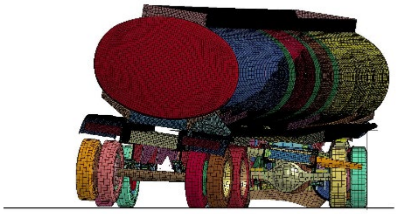

400 ms

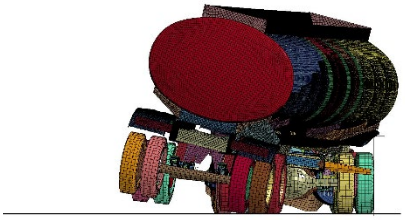

500 ms

600 ms

700 ms

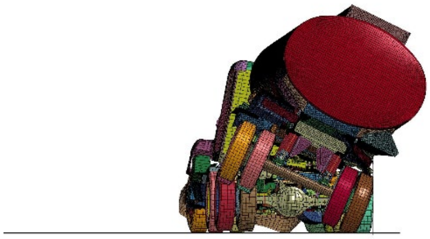

800 ms

900 ms

1000 ms

Figure 6.2 50 in. Tall Barrier Sequential Images

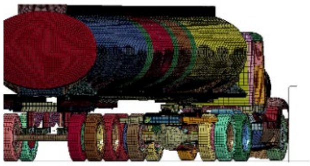

100 ms

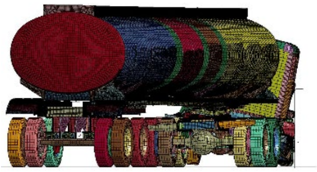

200 ms

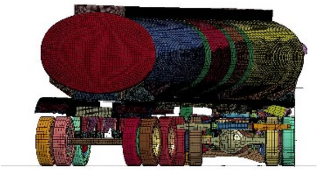

300 ms

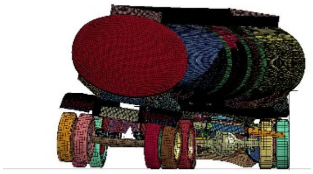

400 ms

500 ms

600 ms

700 ms

800 ms

900 ms

Figure 6.3 62 in. Tall Barrier Sequential Images

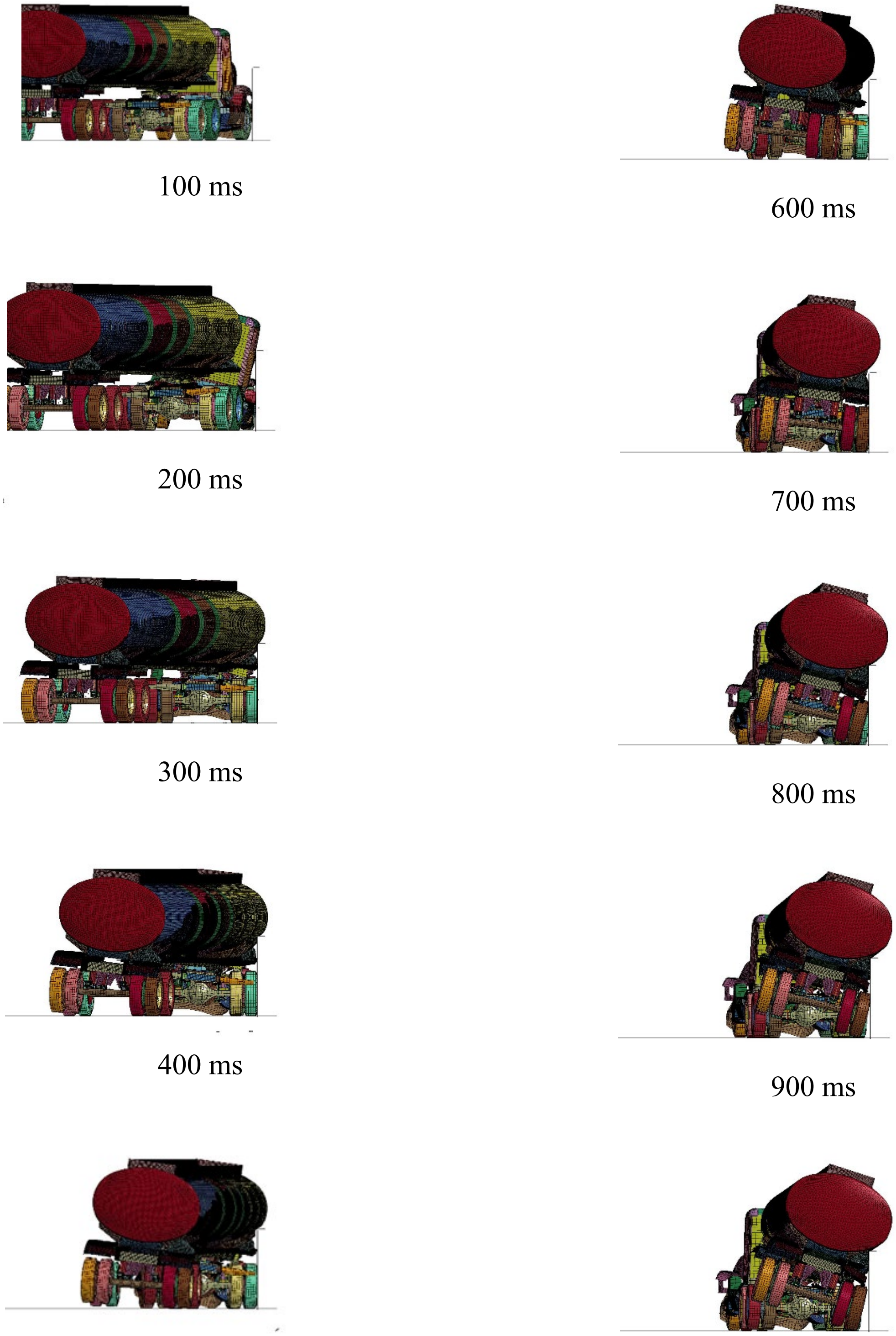

100 ms

600 ms

200 ms

700 ms

300 ms

800 ms

400 ms

900 ms

500 ms

1000 ms

Figure 6.4: 70 in. Tall Barrier Sequential Images

100 ms

200 ms

300 ms

400 ms

500 ms

600 ms

700 ms

800 ms

900 ms

Figure 6.5 90 in. Tall Barrier Sequential Images

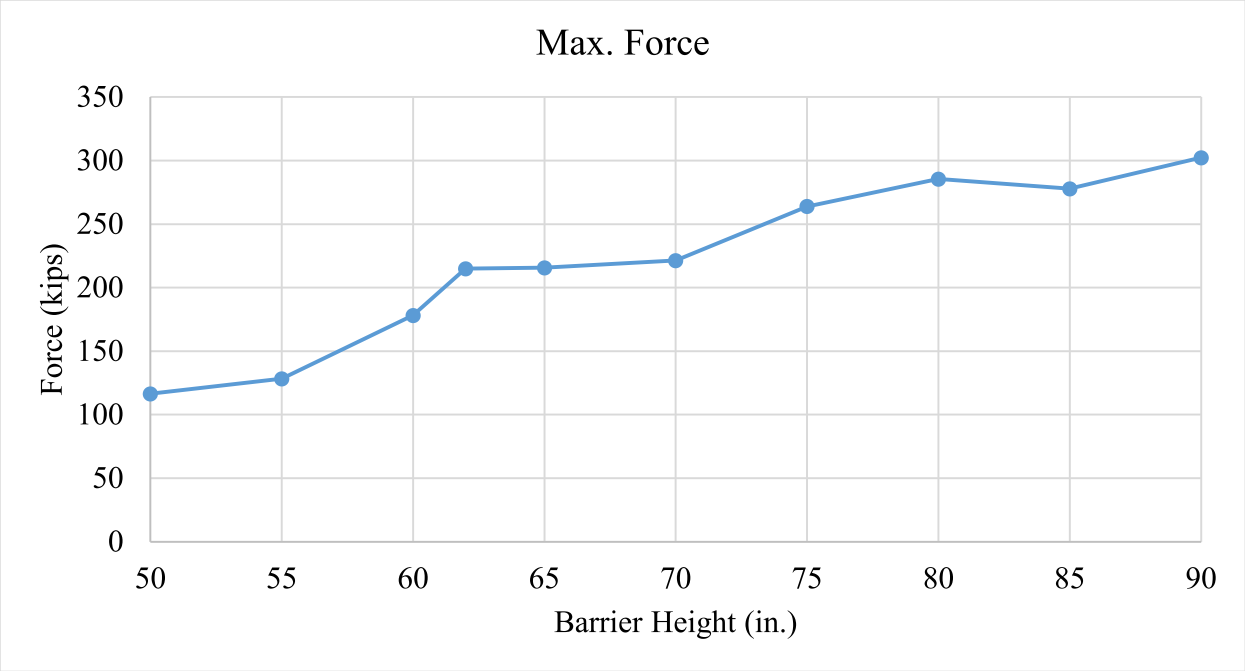

Figure 6.6 Maximum Force Summary of MASH TL-6 Vehicle Model Impact with Rigid Walls at Different Heights

6.2 Barrier Height Study Roll

The x, y, and z-accelerations and rotational velocities were measured at the rear tandem of the trailer. These data sets were exported from each barrier height simulation and processed to obtain the Euler roll angles. The results through 900 ms after the time of impact are shown in figure 6.6. Barriers with a height of 50 in. to 90 in. have a similar rolling behavior from the beginning until reaching 0.3 sec. The highest rolling angle happens at 0.9 sec for barriers less than 85 in. tall, but for 85 and 90 in. barriers, the max trailer roll angle occurred before the secondary contact between the trailer rear axles and the wall. During that frame of time, it can be concluded as the height of barrier increases, the lower the rollover generated in the trailer.

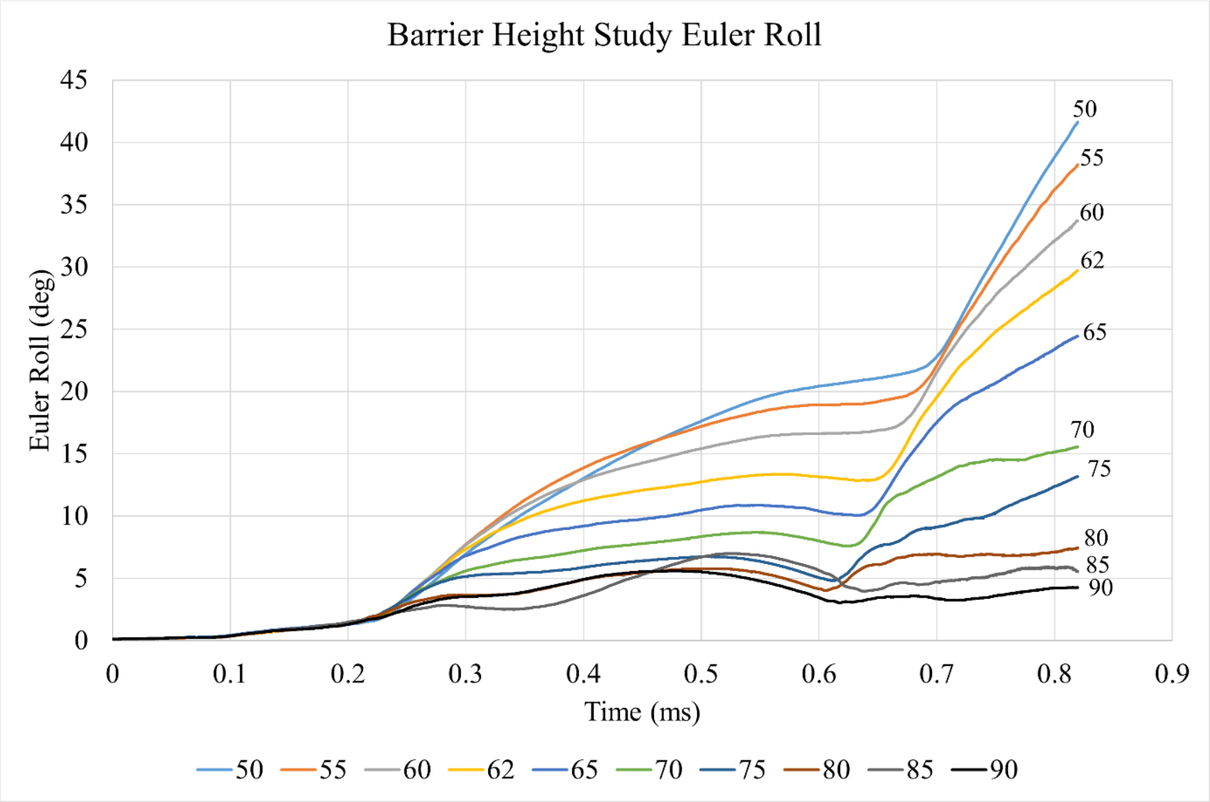

Figure 6.7 Euler Roll Study

The maximum trailer roll for each barrier height is shown in figure 6.7. The maximum roll change between the 65 and 75 in. tall barriers was a substantial decrease of 11.92 degrees. Similar to figure 6.6, the maximum roll angle decreased as the barrier height increased. The difference in maximum roll for barrier heights from 80 to 90 in. is minimal compared to other barrier heights.

Simulation data used a similar cutoff time to compare data with meaningful snapshots. Some of the models experienced numerical instabilities at approximately 900 ms, whereas other models were able to run for additional time. Results are only shown for 900 ms for all models for purposes of comparing results, but it was noted in Phase I (Whitfield) simulations the maximum vehicle roll displacement did not occur until approximately 1.1 s after impact. Thus, the maximum roll angle displacements are compared as indicators and may not reflect the maximum total angular displacement of the tank trailer during an impact.

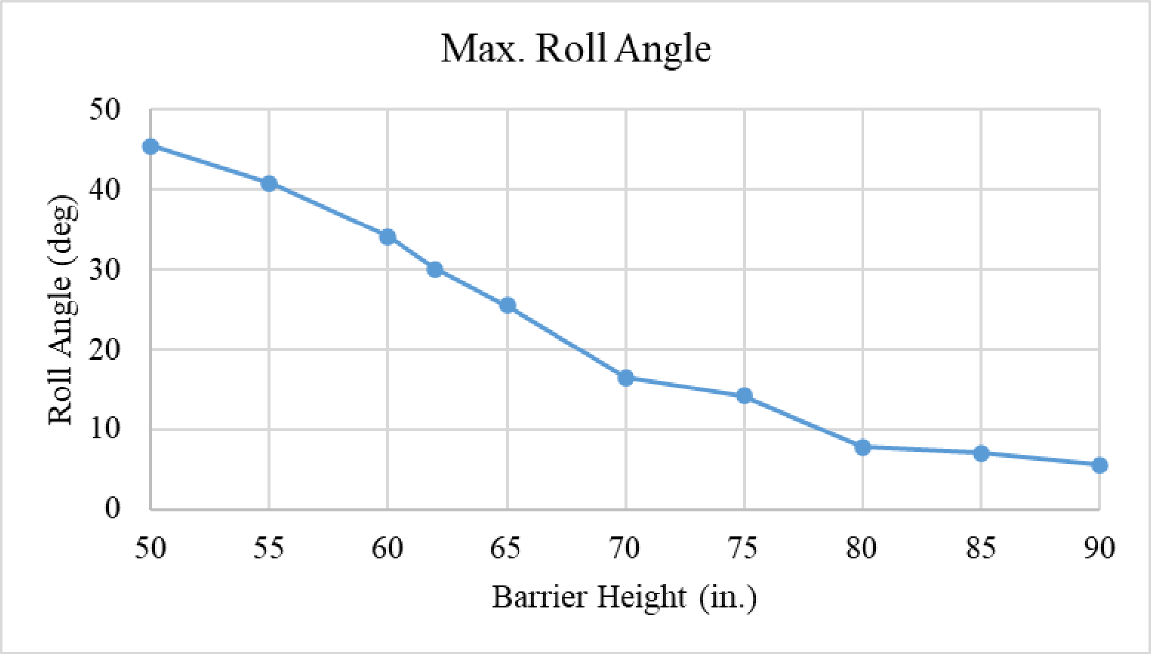

Figure 6.8 Barrier Height Study Maximum Roll Angle at 0.9 s

To illustrate the changes in maximum roll, the instant of maximum roll for barrier heights of 50 to 90 in. is shown in figures 6.8 through 6.17, with time noted in seconds. The simulation results suggest that a minimum barrier height of 70 in. is recommended due to the large decrease in roll from 65 to 70 in., the magnitude of the maximum roll (13 deg.), and the general shape of the roll vs. time graph. This initial recommendation was somewhat conservative due to the limitations of the model.

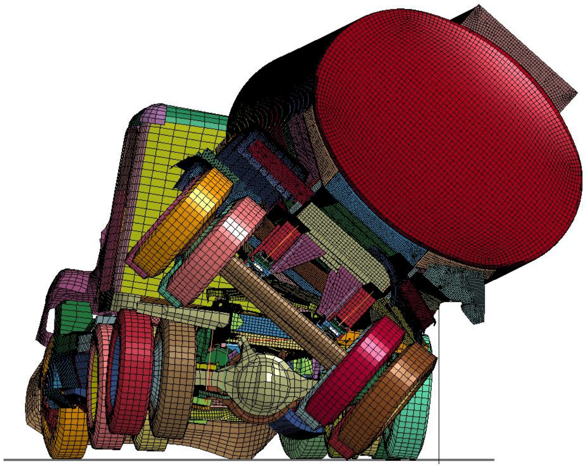

Figure 6.9 50 in. Barrier Maximum Roll at 900 ms

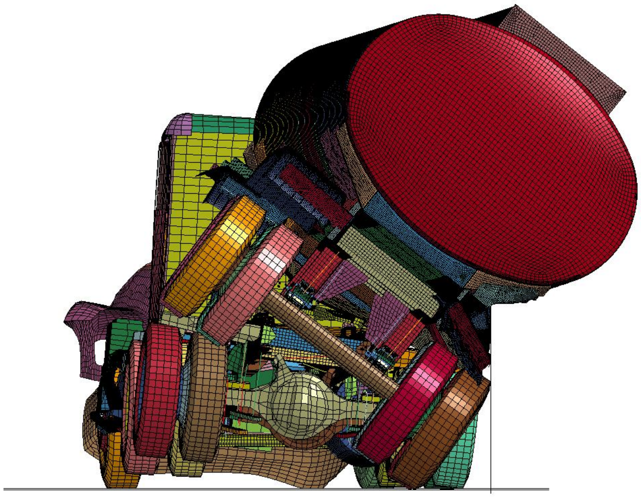

Figure 6.10 55 in. Barrier Maximum Roll at 900 ms

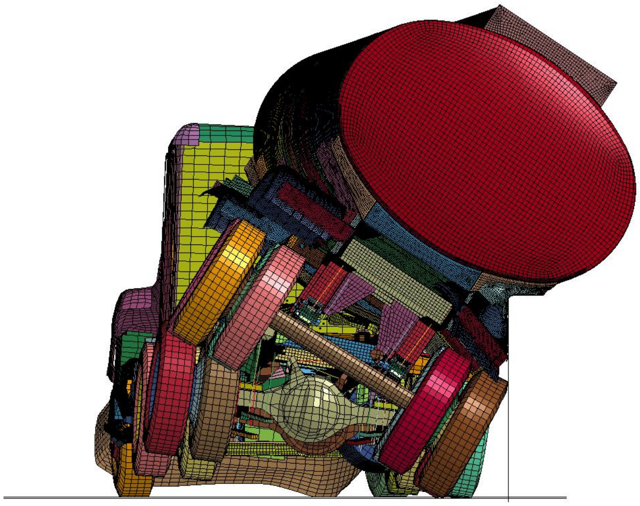

Figure 6.11 60 in. Barrier Maximum Roll at 900 ms

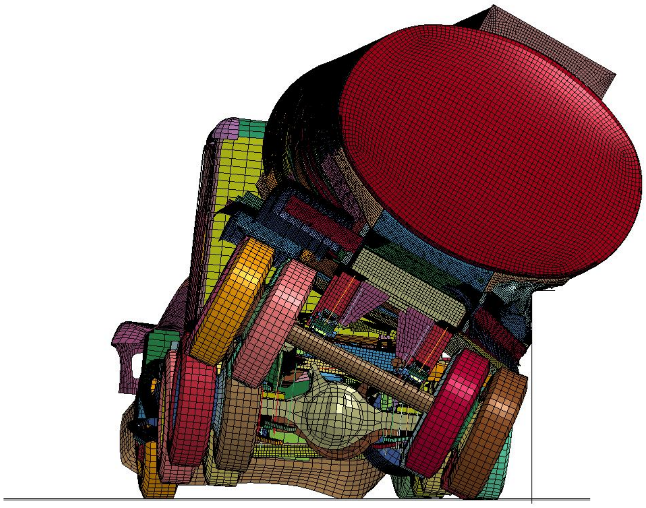

Figure 6.12 62 in. Barrier Maximum Roll

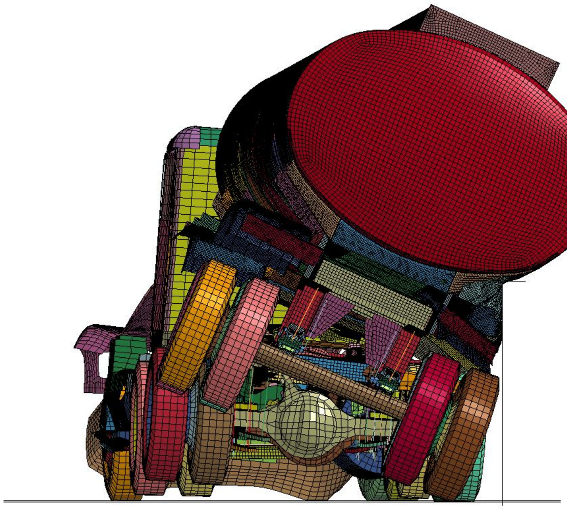

Figure 6.13 65 in. Barrier Maximum Roll at 900 ms

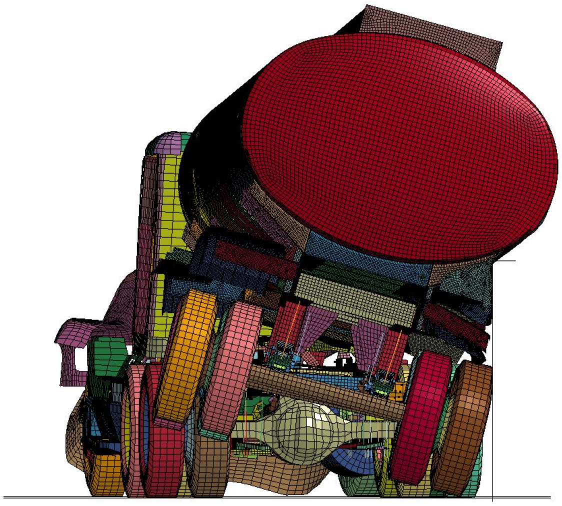

Figure 6.14 70 in. Barrier Maximum Roll at 900 ms

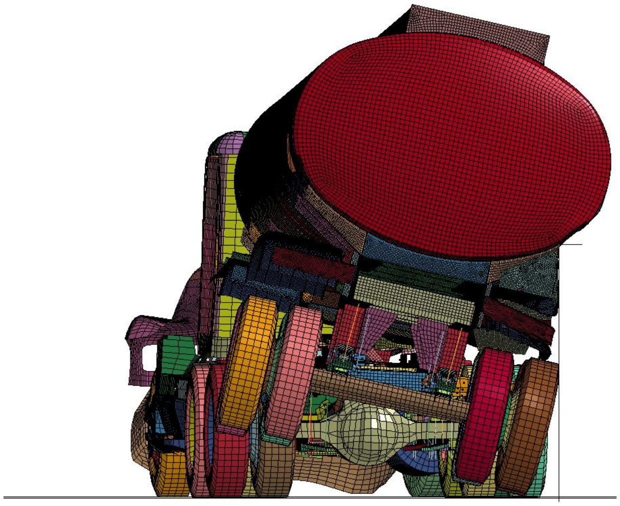

Figure 6.15 75 in. Barrier Maximum Roll at 900 ms

Figure 6.16 80 in. Barrier Maximum Roll at 900 ms

Figure 6.17 85 in. Barrier Roll Angle at 900 ms

Figure 6.18 90 in. Barrier Roll Angle at 900 ms

6.3 Zone of Intrusion

The zone of intrusion is the region measured vertically and laterally from the face of a barrier system where vehicle impact occurred to the farthest point of the vehicle behind the barrier. A schematic of a TL-6 vehicle's zone of intrusion is shown in figure 6.18, which was identical to the method used in Phase I (Whitfield). To estimate the minimum TL-6 barrier height, the location of the point of maximum lateral overhang of the trailer, both laterally and vertically, was identified. This study provided an indication of the risk an impacting truck tank-trailer combination vehicle would impose on structures located behind the front face of the barrier. The data was extracted from the following simulated barrier heights: 50, 55, 60, 62, 65, 70, 75, 80, 85 and 90 in., which will be discussed in this section.

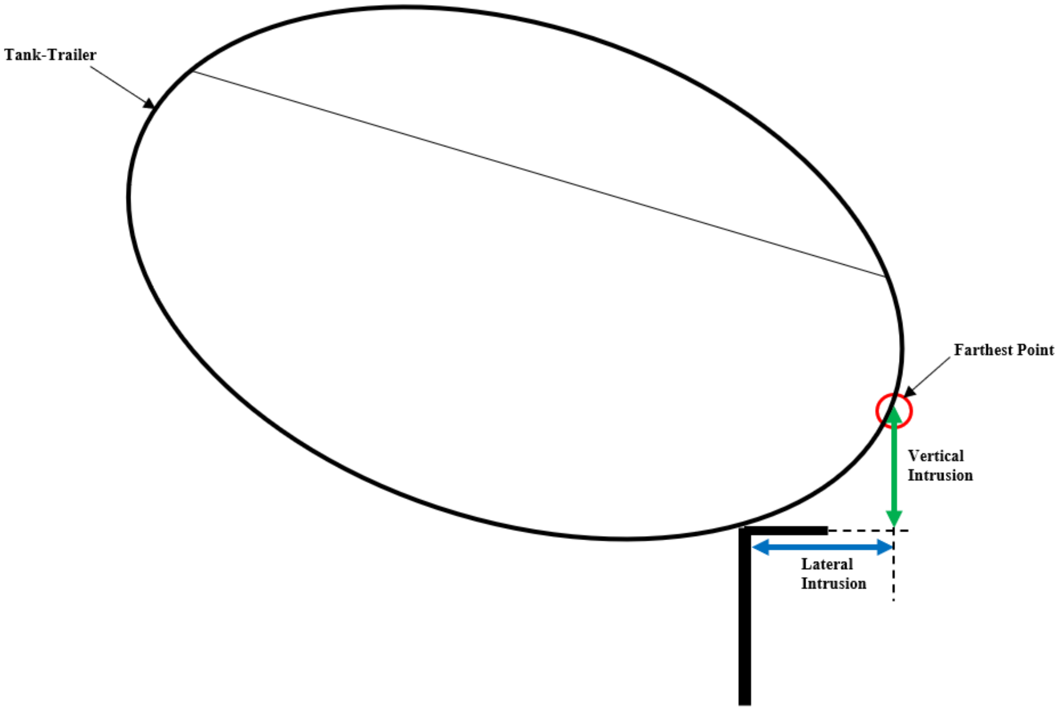

Figure 6.19 Zone of Intrusion Measurement Schematic

The lateral intrusion is the distance from the front face of the barrier to the farthest edge of the tank. The lateral intrusion for each barrier height is denoted in figure 6.19. As the barrier height increased, the tank trailer experienced less lateral intrusion behind the leading top edge of the barrier. The largest change in lateral intrusion occurred between 65 and 70 in.

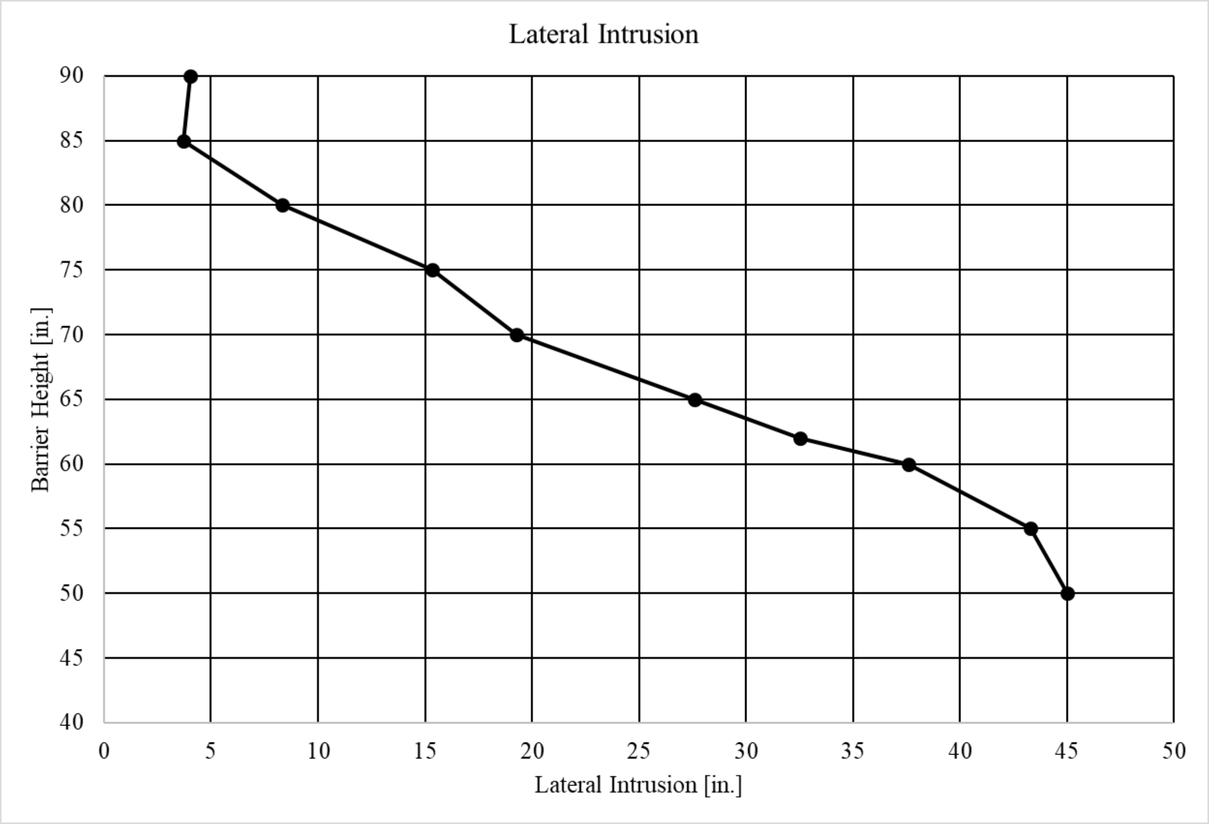

Figure 6.20 Lateral Intrusion as a Function of Barrier Height

Vertical intrusion is shown figure 6.20 to illustrate the vertical height from the ground to the top of the barrier and the distance from the barrier's top to the farthest extent of the tank behind the rigid wall. For barrier heights between 50 and 75 in., the vertical intrusion of the tank trailer vehicle increased as the height of the barrier increased; however, between 75 and 90 in., the vertical height of tank trailer intrusion remained approximately constant at 100 in.

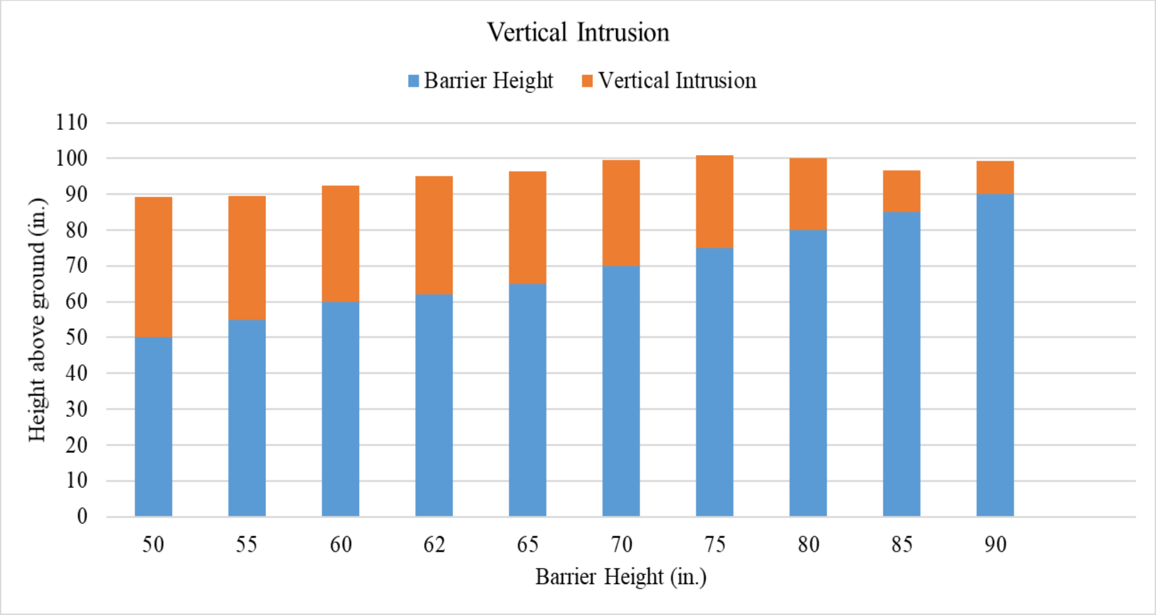

Figure 6.21 Barrier Height and Vertical Intrusion

Next, the vertical position above the ground vs. the lateral position behind the front face was plotted, as shown in figure 6.21. The 50 and 55 in. barrier heights resulted in higher lateral displacement for the tank in addition to reduced heights at the point of maximum extension. For locations such as around bridge piers where protection of the pier from direct impact with a tank truck trailer may be critical, lateral and vertical intrusion values can inform the optimal offset between the bridge pier and the barrier front face. For areas with constrained space, taller barriers may be used to optimize the space limitations with construction cost.

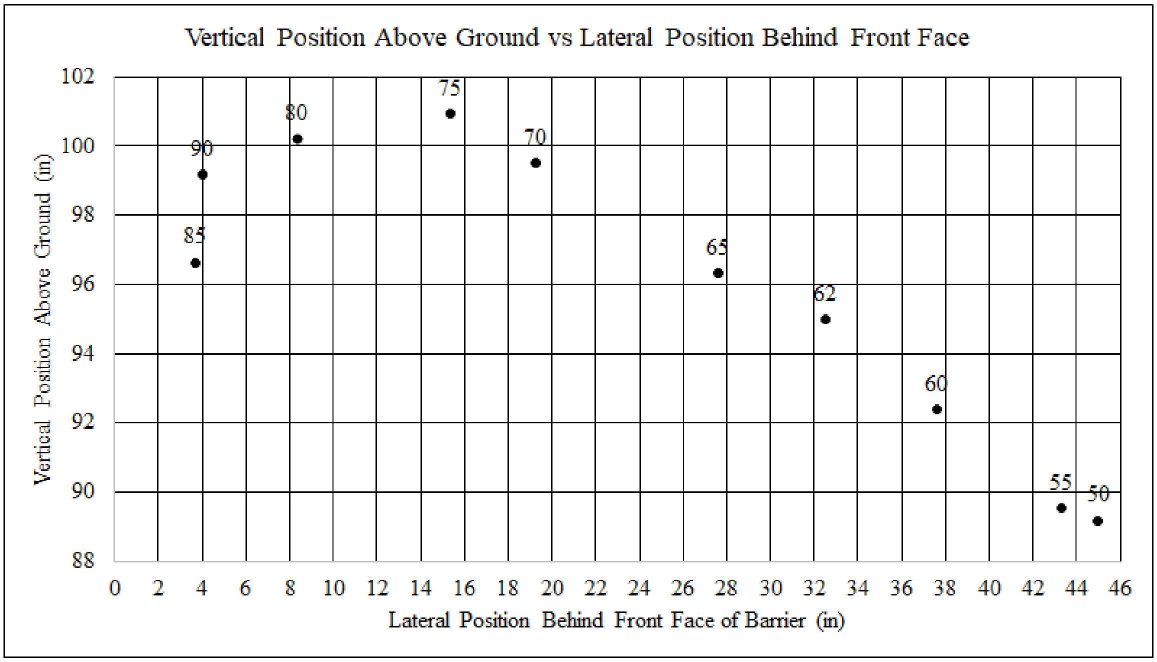

Figure 6.22 Vertical and Lateral Intrusion

As mentioned in Section 6.2, the lateral intrusion data at the trailer's maximum rolling angle was extracted from the model through 900 ms after impact. As the barrier height increases, the maximum roll and lateral intrusion decrease, as shown in figure 6.22. The lateral intrusion and maximum roll angle had a quasi-linear relationship for barriers between 50 and 80 in. tall.

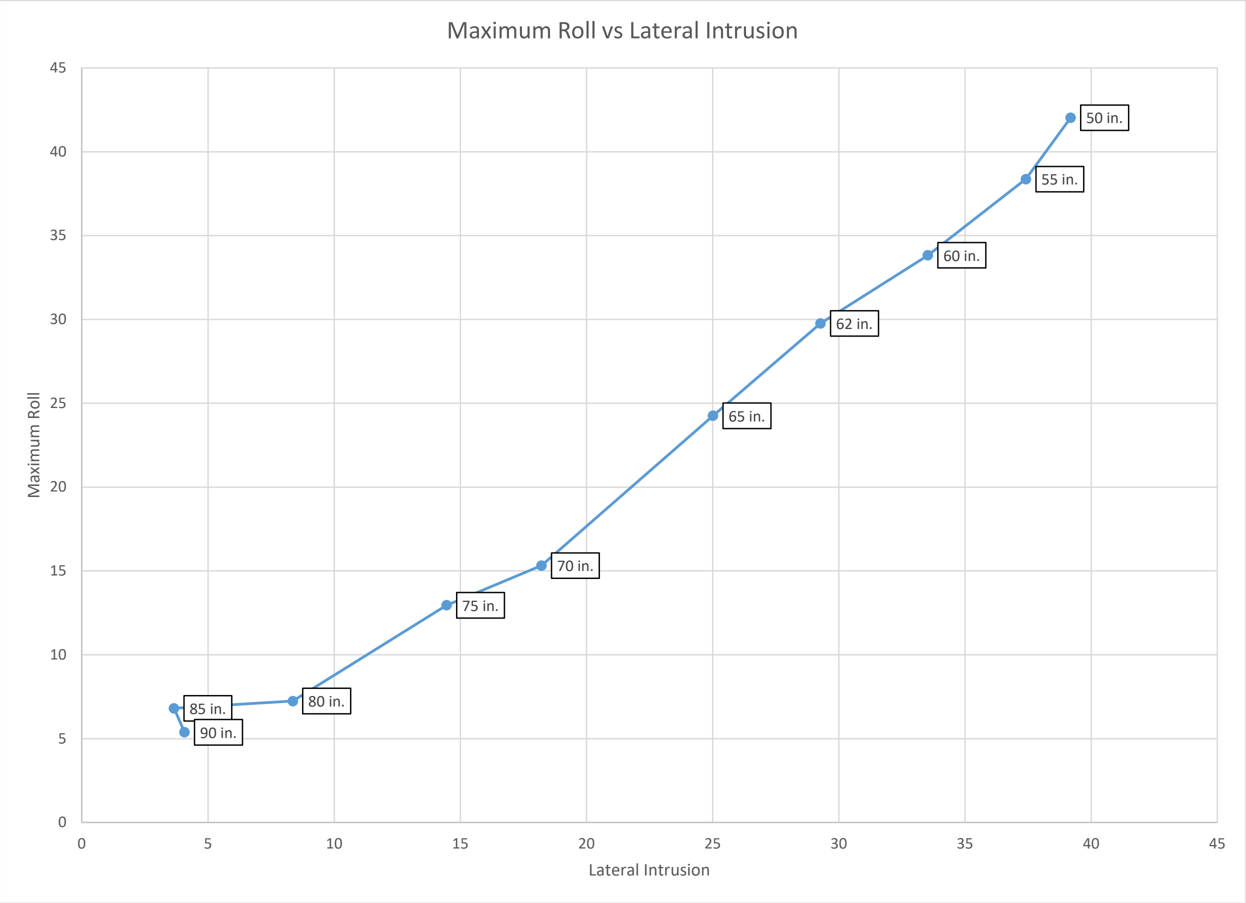

Figure 6.23 Maximum Roll vs. Lateral Intrusion

6.4 Barrier Height Forces

The shear capacity of the barrier was critical for when designing the barrier to handle the full capacity of the TL-6 vehicle impact. Shear forces are carried through the barrier and applied to the foundation, such as a bridge deck or subgrade reinforced structure.

The forces exerted onto the barrier from the truck during impact were extracted and filtered with a 50-ms average from the barrier rigidwalls. The forces from each rigidwall were summed and the total forces for each barrier height, ranging from 50 in. to 90 in., were plotted for comparison, as shown in figure 6.23. The impact forces were distinct but behaved similarly. The first impact happened at 0.08 sec, when tractor impacted rigid wall number 8. From 0.08 sec to 0.40 sec only the tractor impacted the rigid wall. At approximately 0.22 sec, the rear axle of the truck and the front end of the tank trailer contacted the barrier. During this time, the behavior of the different barrier height models diverged; lower barrier heights experienced lower forces at approximately 0.22 sec, because the trailer impact was both delayed and the magnitude was reduced due to the initiation of tank trailer roll displacement. Between 0.60 sec and 0.76 sec, the trailer's rear axle and back end impacted the barrier, at which time the highest impact forces were observed. Lower barrier heights experienced trailer rear axle contact much later in the impact event than taller barriers, but were likewise coupled with reduced overall force. It is believed that due to the reduced redirection force on the front of the truck and the extended impulse at the back of the trailer, that the trailer yaw rate and rotational speed were reduced, leading to lower "tail slap" forces. Remarkably, the "tail slap" force for the 50 in. barrier height was less than the impact force during the truck rear wheel impact, and occurred much later in the event.

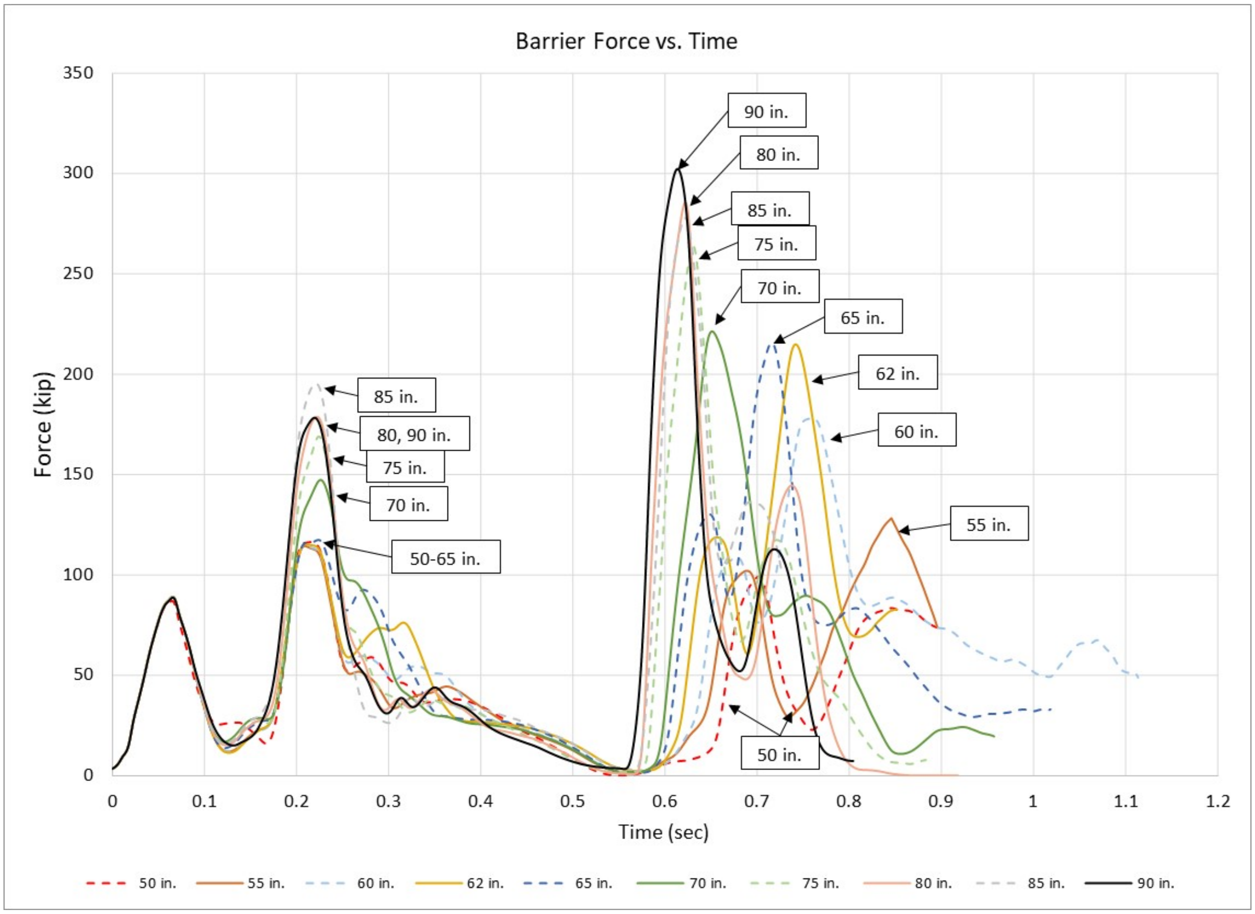

Figure 6.24 Barrier Forces

The maximum force vs. barrier height is shown in figure 6.24. The impact forces increased as the barrier height increased. Barriers with a height of 50 to 60 in. caused the lowest impact force on the barrier and showed considerably similar peak loads. When the barrier height increased from 60 in. to 62 in. the maximum impact force increased abruptly. The 90 in. tall barrier had the largest maximum force.

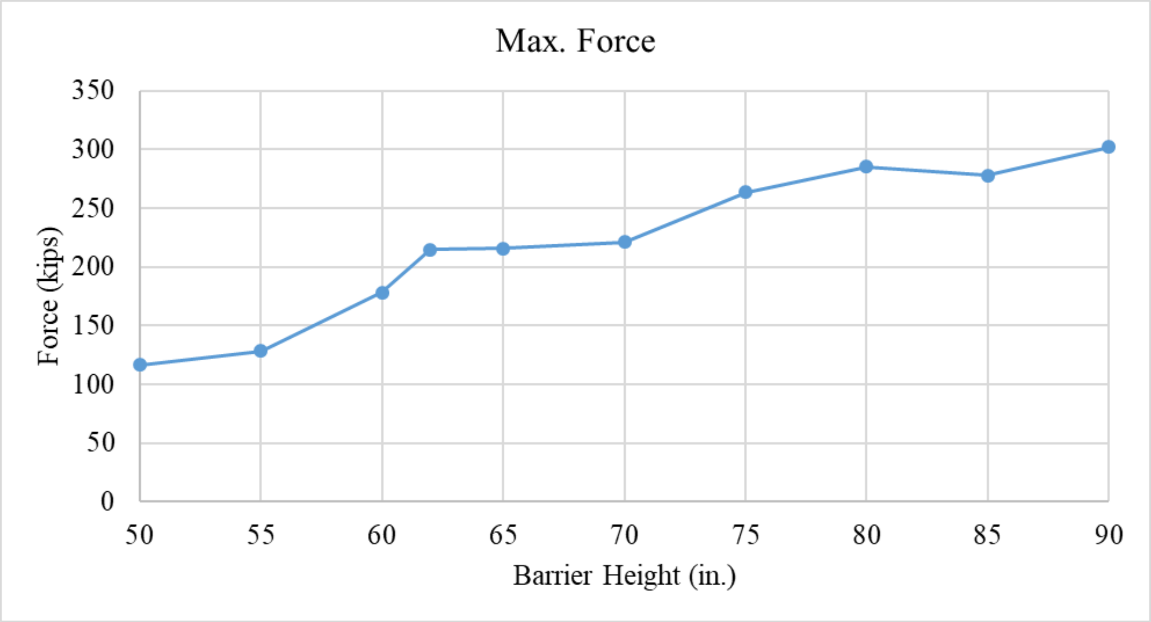

Figure 6.25 Peak Barrier Shear Forces

6.4.1 Barrier Forces for Every 5-ft Section

The forces acting on every upper and lower rigidwall were summed to determine the maximum instantaneous and 50-ms average shear forces through the base of the barrier acting during the simulations. The wall forces for every 5 ft section of the barrier are plotted in figures 6.25 through 6.28. It should be noted that the chamfer was treated differently than the vertical wall forces. For all vertical walls, only the normal component of force was extracted for a shear force estimate. However, the chamfer normal is oriented at an angle to the vertical barrier face. Therefore, the chamfer normal force was multiplied by the cosine of 45 degrees to vectorize the applied force into vertical and horizontal components. Only the horizontal force was considered for this analysis.

For the 50 in. tall rigidwall simulations, the initial impact load was carried primarily at walls 7 and 8 when the tractor impacted the barrier 20 ft upstream from the beginning of the barrier with a force of 76 kips, as shown in figure 6.25. At approximately 0.18 sec, the front of the trailer impacted walls 7 and 8 with a force of 69 kips. From 0.18 sec to 0.55 sec the trailer's front end was in contact with the barrier. At 0.66 sec the tank's back end impacted walls 7 and 8 with a force of 62 kips. The trailer also contacted walls 5, 6, 9, and 10 until 0.80 sec, but walls 7 and 8 received the highest loads.

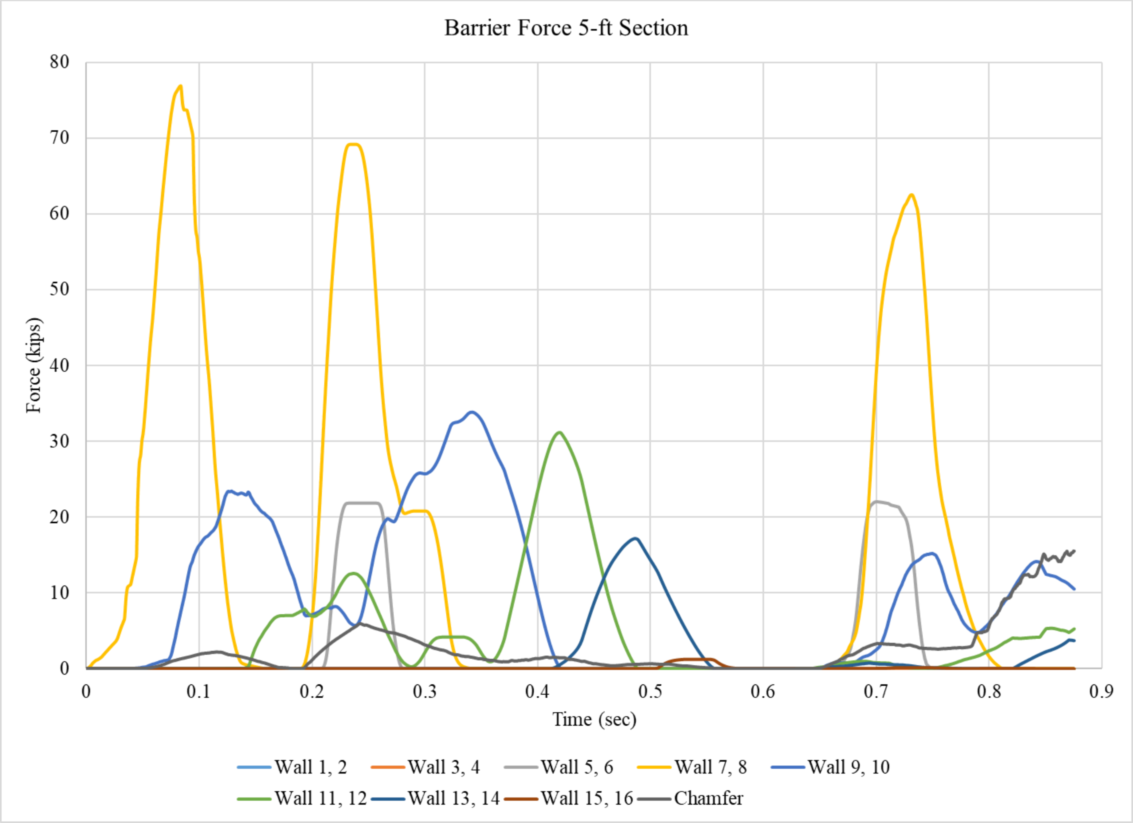

Figure 6.26 5-ft Section Barrier Force on 50 in. Barrier

For the 62 in. barrier height, which was recommended during the Phase I (Whitfield) research study, the initial load was generated at walls 7 and 8 when the tractor impacted the barrier 20 ft upstream from the beginning of the barrier with a force of 78 kips, as shown in figure 6.26. At approximately 0.18 sec the trailer's front end impact walls 7 and 8 with a force of 80 kips. From 0.18 sec to 0.55 sec the trailer's front end was in contact with the barrier. At 0.66

sec the tank's back end impacted walls 7 and 8 with a force of 40 kips. The trailer also contacted walls 5 and 6 as well as the chamfer until 0.80 sec, however, walls 7 and 8 received the largest load at the begging of the simulation (0 sec to 0.30 sec). At the end of the simulation, when trailer's back end impacted the barrier, the chamfer received the largest load of 99 kips. This occurred during the trailer roll against the barrier top edge.

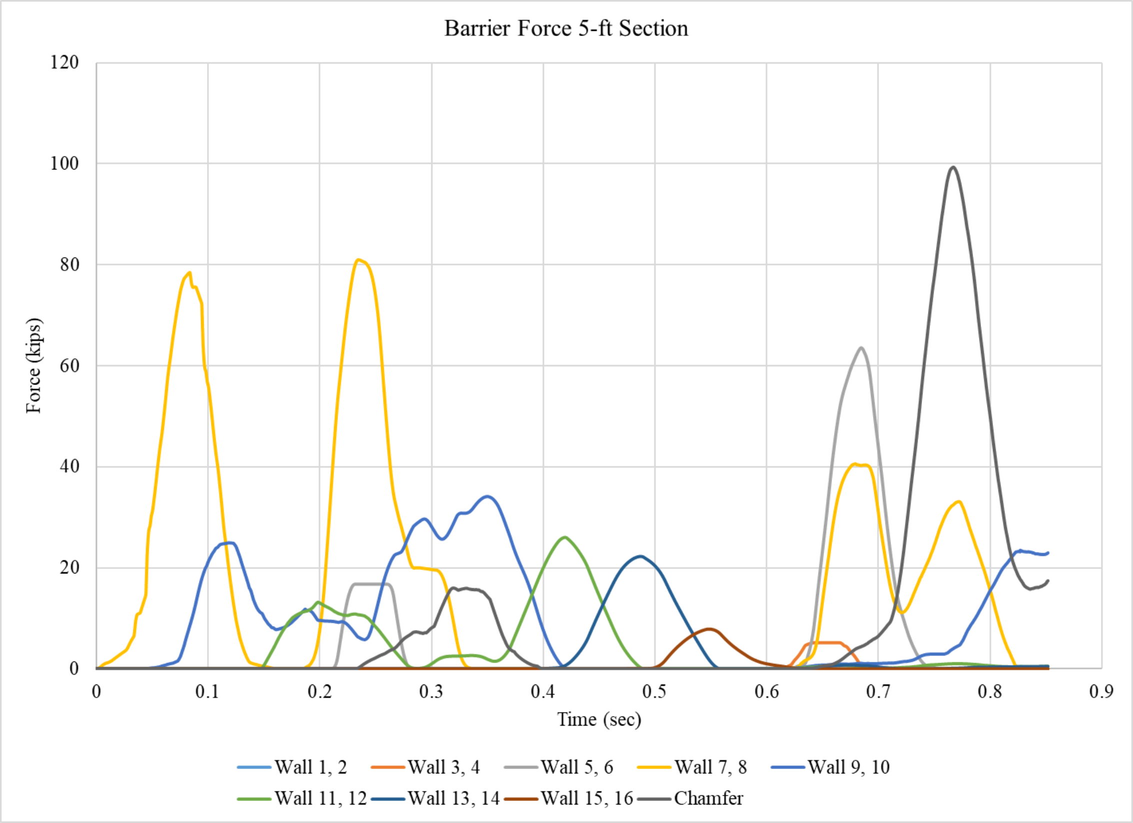

Figure 6.27 5-ft Section Barrier Force on 62 in. Barrier

For the 70 in. barrier simulations, the initial load was generated at walls 7 and 8 when the tractor impacted the barrier 20 ft upstream from the beginning of the barrier with a force of 81 kips, as shown in figure 6.27. At approximately 0.18 sec the trailer's front end impacted walls 7 and 8 with a force of 82 kips. From 0.18 sec to 0.55 sec the trailer's front end was in contact with the barrier. At 0.66 sec the tank's side impacted walls 3 and 4 with a force of 22 kips. The trailer also contacted walls 5, 6, 7, 8, and the chamfer until 0.80 sec. Walls 5 and 6 received a maximum loading of 75 kips. Walls 7 and 8 received the largest load at the begging of the simulation (0 sec to 0.3 sec). At the end of the simulation, when trailer's back end impacted the barrier, the chamfer received the largest load of 112 kips. This occurred during the trailer roll against the barrier top edge.

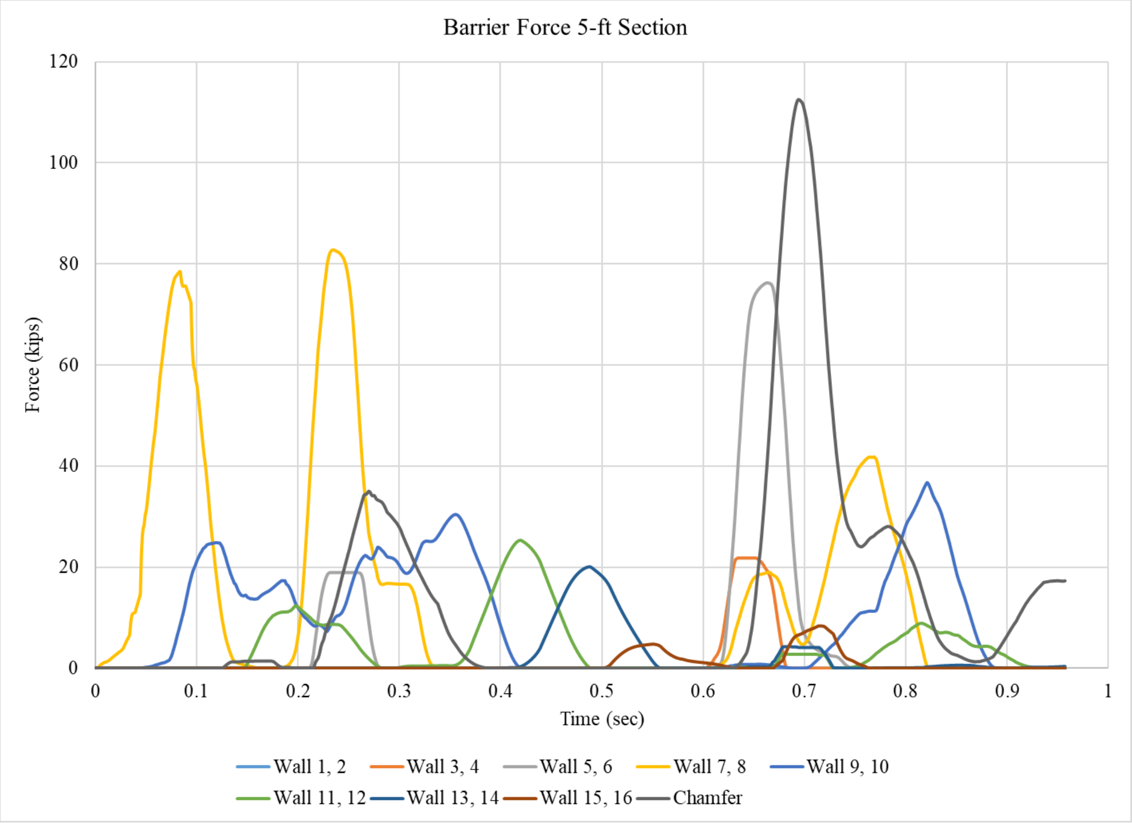

Figure 6.28 5-ft Section Barrier Force on 70 in. Barrier

Figure 6.28 shows that the initial load was generated at walls 7 and 8 when the tractor impacted the barrier 20 ft upstream from the beginning of the barrier with a force of 78 kips. At approximately 0.18 sec the trailer's front end impacted walls 7 and 8, reaching a force of 112 kips at 0.23 sec. Times from 0.18 sec to 0.55 sec corresponded to the trailer's front end impacting the barrier. At 0.58 sec the tank's side impacted walls 3 and 4, and at 0.63 sec reached a force of 58 kips. From 0.58 sec to 0.70 sec, tank contacted the chamfer and walls 5 through 14, of which walls 5 and 6 received the largest load at 75 kips. At 0.68 sec the tank's tail impacted walls 7 through 12, generating a force of 76 kips for walls 7 and 8, 21 kips for walls 9 and 10, and 4 kips for walls 11 and 12.

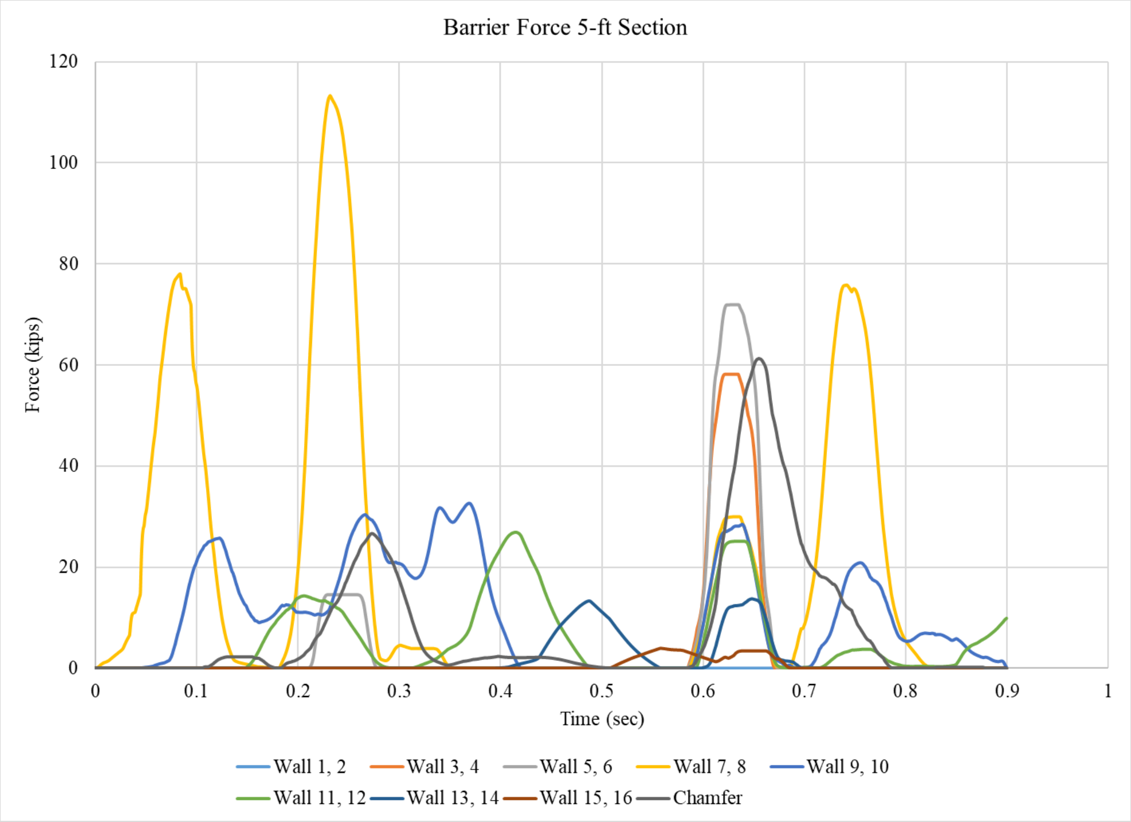

Figure 6.29 5-ft Section Barrier Force on 90 in. Barrier

A conservative estimate of the maximum force was generating by assigning 100% of the chamfer load to each 5 ft long, vertical barrier segment. This conservative estiamte of impact force would provide a factor of safety for shear design of controlled lengths. The peak rigidwall shear load with the additional chamfer load added is shown in figure 6.29. Four peaks were observed: the first peak occurred when the tractor impacted the barrier, and all barrier heights had a similar impact force. The second peak was generated by the tractor's rear end and trailer's front end impacting the barrier at approximately 0.20 sec. The maximum loading at the second peak occurred around 0.25 sec. The loading at that moment is similar for barriers 50 through 65 in. tall while the loading for barriers between 70 and 90 in. tall was higher, due to the trailer bulkhead contact with the barrier. The trailers's front end contacted the barrier until 0.60 sec. From 0.60 sec to 0.70 sec the trailer's side contacted the barrier, loading different walls. At 0.70 sec the tank's back end impacted the barrier, and at about 0.75 sec the trailer's back generated its peak load.

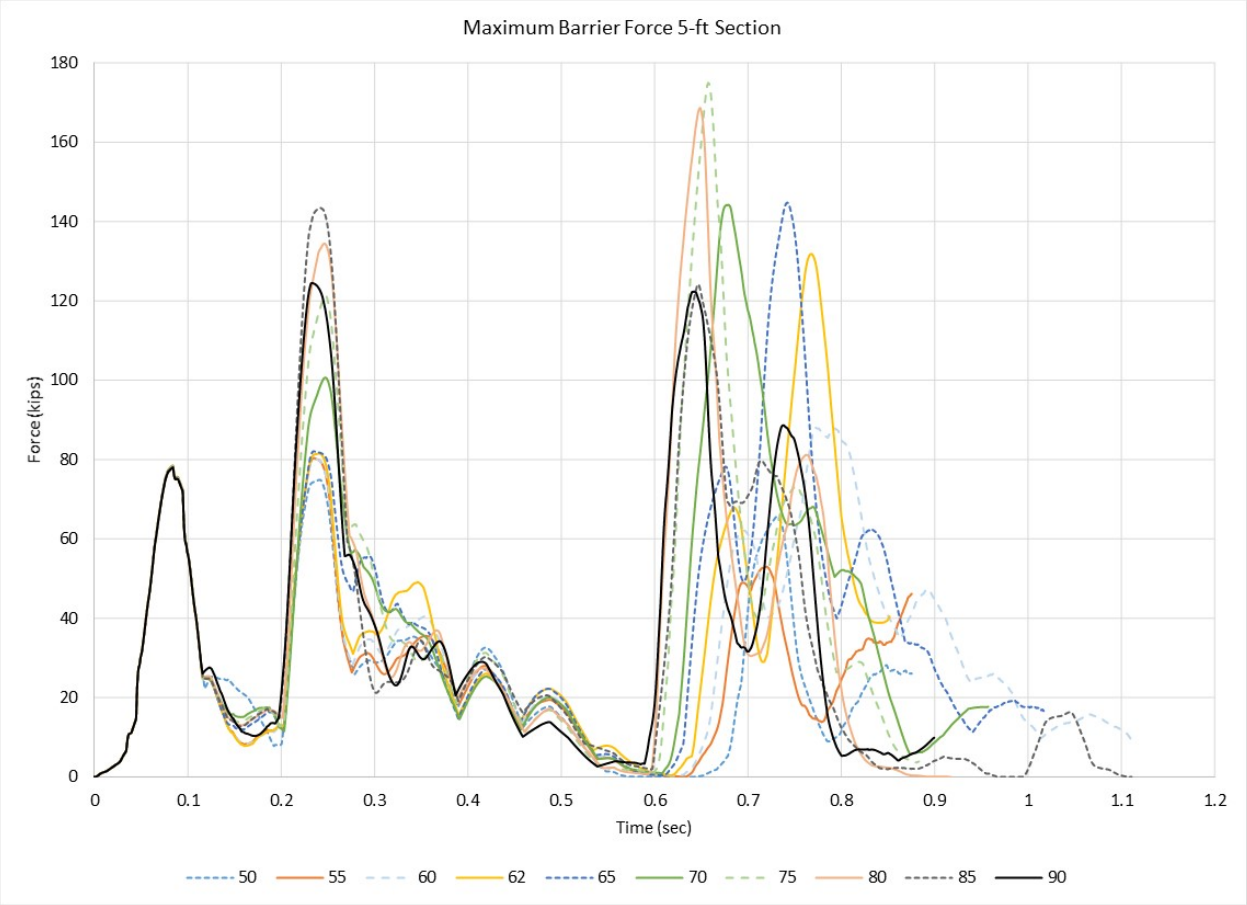

Figure 6.30 Maximum Force for a 5-ft Section by Barrier Height

The maximum force vs. barrier height is shown in figure 6.30. As barrier height increases, the maximum loading increases, except for barrier heights of 70, 80, 85, and 90 in. Barriers with a height from 50 to 60 in. caused the lowest impact forces on the barrier and showed considerably similar peak loading. When the barrier height increased from 60 in. to 62 in. the maximum impact force increased abruptly. The 75 in. tall barrier had the largest maximum force.

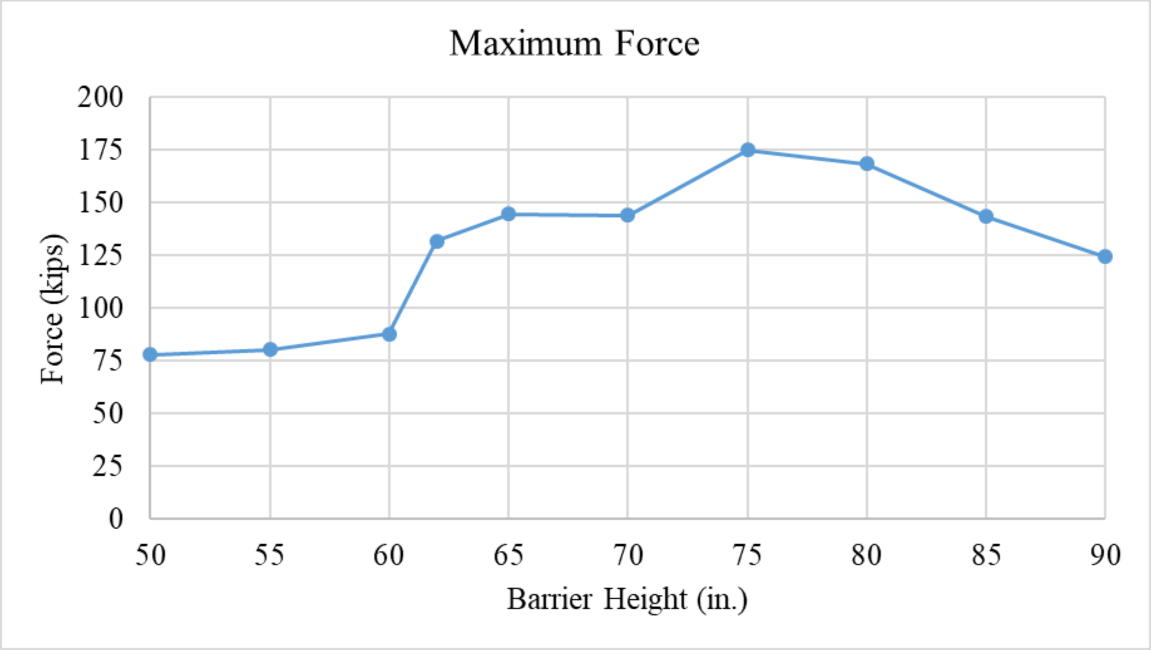

Figure 6.31 Maximum Force Acting on 5-ft Long Barrier Segment vs. Barrier Height

This analysis indicates as the barrier height increased, the barrier forces increased. At barrier heights of 50, 55, and 60 in., the peak force was significantly lower because the tank remained mostly above the top barrier surface, causing the tank to ride on top of and press down on the rail, and the barrier shear forces were principally applied to the chassis. As the barrier height increased, the peak shear loading increased as well, but the shear loading was applied over a longer length of barrier, resulting in a reduction of peak 5 ft barrier length force between 75 and 90 kip.

6.4.2 Barrier Forces for Every 10-ft Section

Results of the 5 ft length maximum forces indicated that, for some wall heights, the times of maximum force resulted in force being applied across spans longer than only 5 ft. Although designing a barrier with a capacity over a 5 ft length consistent with what is shown in figure 6.30 is likely to be sufficiently strong, researchers also investigated how consecutive pairs of 5 ft rigidwall forces may alter the anticipated force distributions for barrier design. Researchers summed contact forces for adjacent pairs of 5 ft vertical wall strips and plotted results. Note that the result provided forces over 10 ft long average lengths, such that overlaps occurred in the dataset when the same 5 ft vertical strip was used in the sum or forces for 10 ft lengths.

Barrier shear forces over 10 ft lengths are shown for the 50 in. tall barrier in figure 6.31. The first load was generated at walls 7 through 10 when the tractor impacted the barrier 20 ft upstream from the beginning of the barrier with a force of 85 kips. At approximately 0.19 sec the trailer's front end impacted walls 7 through 10, reaching a loading of 75 kips at 0.23 sec. In the simulation results, 0.18 sec to 0.60 sec corresponded to the trailer's front end impacting the barrier. At 0.65 sec the tank's side impacted walls 3 through 6 reaching a force of 22 kips at 0.68 sec. From 0.65 sec to 0.80 sec, the tank contacted the chamfer and walls 5 through 14. During that impact, walls 5 through 8 received the largest loading of 82 kips and the remaining walls experienced a smaller force of approximately 22 kips. Based on the results of figure 6.31, the peak forces during impact were concentrated on wall panels 7 and 8; only minor differences were observed between the sum of panels 5, 6, 7, and 8 compared to the sum of 7, 8, 9, and 10. In contrast, the sum of panels 3, 4, 5, and 6 as well as the sum of 9, 10, 11, and 12 were much, much lower than for the contributions of panel nos. 7 and 8.

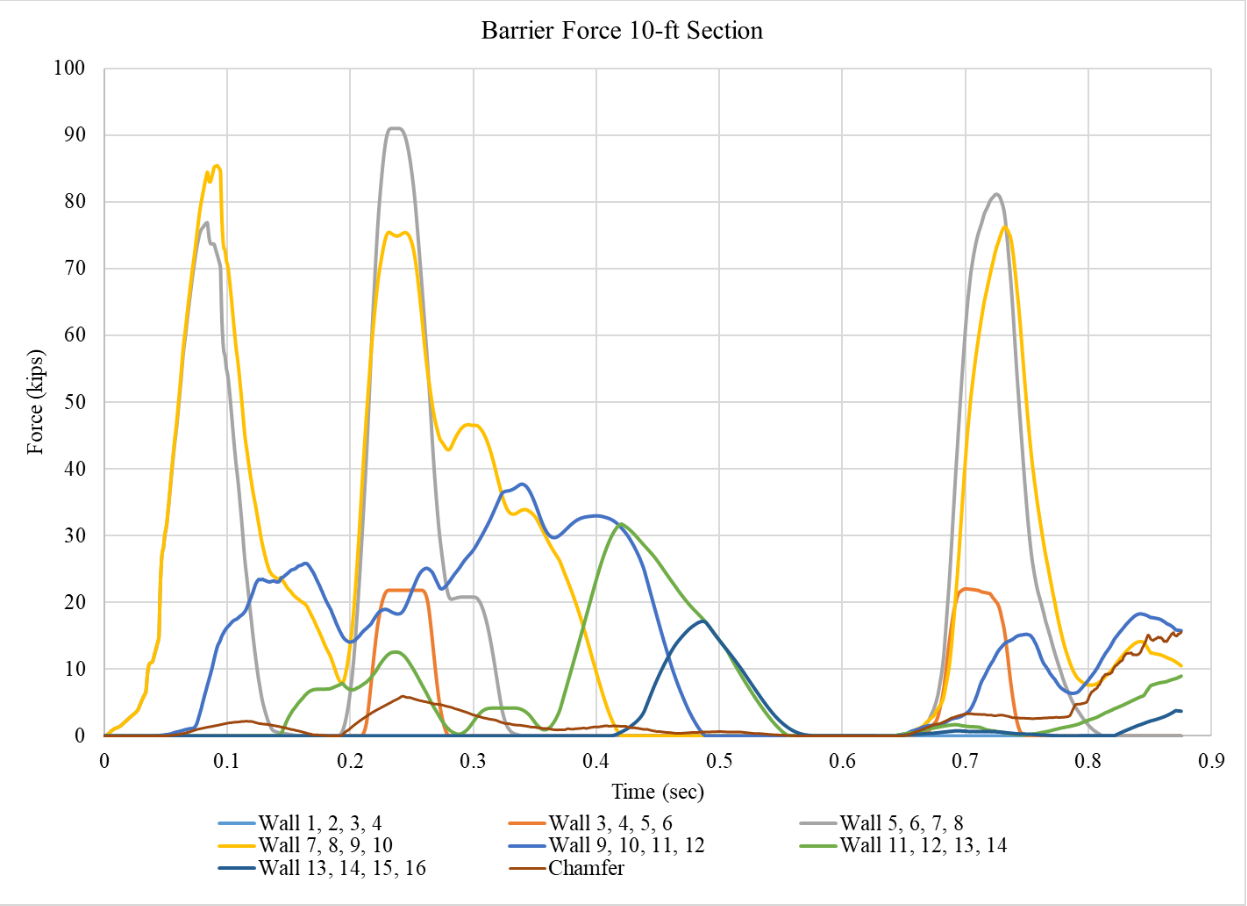

Figure 6.32 Barrier Shear Force Acting on 10-ft Section Length, 50 in. Barrier Height

Barrier forces for the 62 in. barrier height recommended in the Phase I (Whitfield) study are shown in figure 6.32. The first loading was generated at walls 7 through 10 when the tractor impacted the barrier 20-ft upstream from the beginning of the barrier with a force of 88 kips. At approximately 0.18 sec the trailer's front end impacted walls 5 through 10, reaching a force of 88 kips (walls 7 through 10) and 98 kips (walls 5 through 8) at 0.23 sec. In the simulation results, 0.25 sec to 0.60 sec corresponded to the trailer's front side impacting the barrier. At 0.60 sec the tank's backside impacted walls 7 through 10, reaching a force of 41 kips at 0.68 sec. From 0.60 sec to 0.70 sec, the tank contacted walls 3 through 10, during which walls 3 through 6 received a load of 64 kips, walls 5 through 8 had 103 kips and walls 7 through 10 had a load of 42 kips.

Most of the impact of the trailer's tail was received by the chamfer with a maximum load of 99 kips. For the initial impact, the load was very concentrated at wall panel nos. 7 and 8, just as with the 50 in. barrier results; however, trailer "tail slap" forces were distributed across the vertical panels 5, 6, 7, and 8 between 0.65 and 0.7 sec before the trailer rolled onto the chamfer.

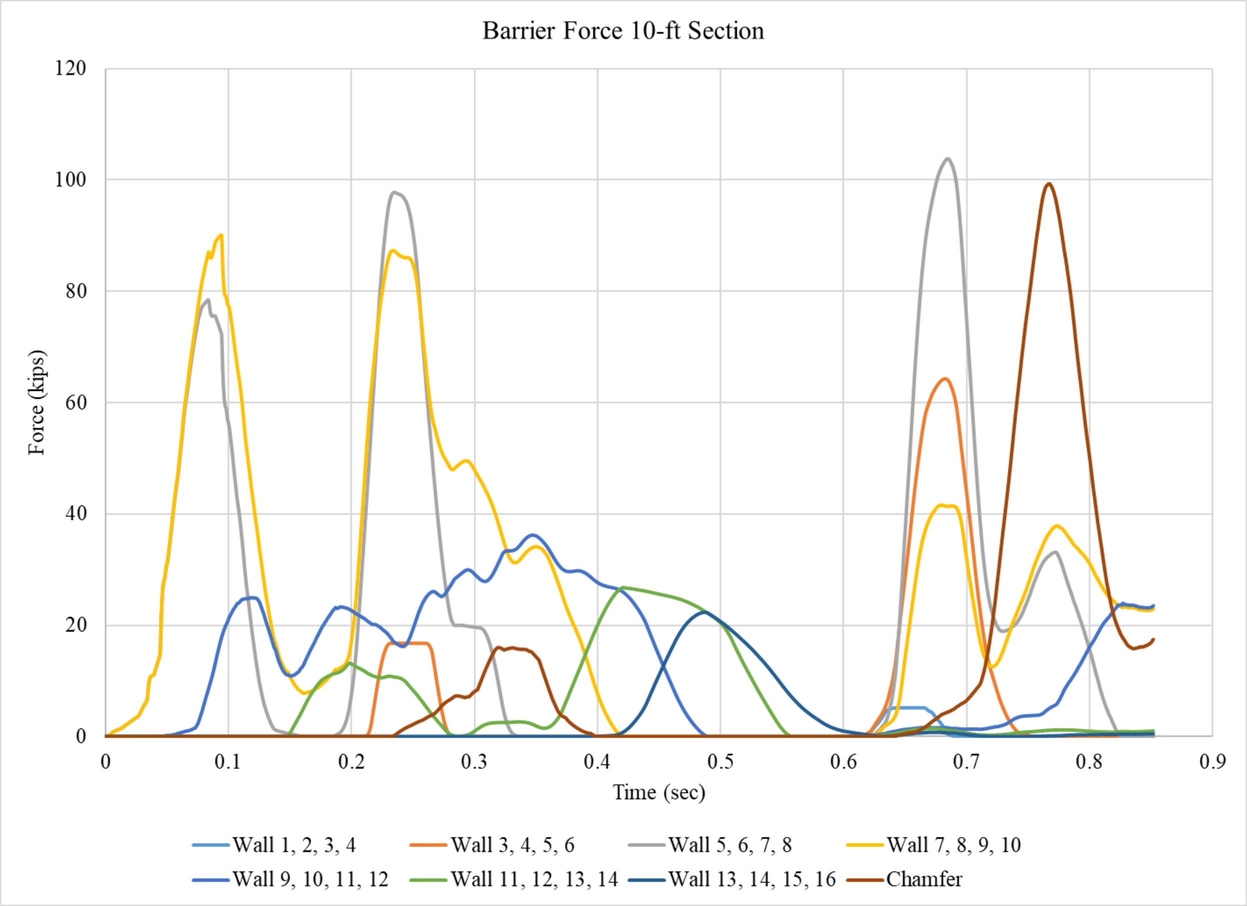

Figure 6.33 62 in. Barrier Force 10-ft Section

The impact forces for the 70 in. barrier height for 10 ft barrier segments are shown in figure 6.33. The first load was generated at walls 7 through 10 when the tractor impacted the barrier 20 ft upstream from the beginning of the barrier with a force of 90 kips, which was very similar to simulations with lower heights. At approximately 0.20 sec the trailer's front end impacted walls 7 through 10 and 5 through 8, reaching loads of 92 kips and 102 kips, respectively, at 0.25 sec. In the simulation results, 0.27 sec to 0.60 sec corresponded to the trailer's front side contacting the barrier. At 0.60 sec the tank's back side impacted walls 3 through 8, reaching a force of approximately 92 kips at 0.65 sec. The 70 in. barrier forces were highly concentrated on wall panels 5 and 6, with much less load distributed to wall panels 3, 4, 7, and 8. However, as with the 62 in. barrier, as the tank rolled onto the top of the barrier, the loading applied to the chamfer from the tank became the predominant source of redirective shear force acting on the tank trailer starting at approximately 0.67 to 0.72 sec. At 0.70 sec the tank's tail impacted walls 5 through 16, generating a load of 50 kips for walls 7 through 10, 41 kips for walls 5 through 8, and 44 kips for walls 13 through 16.

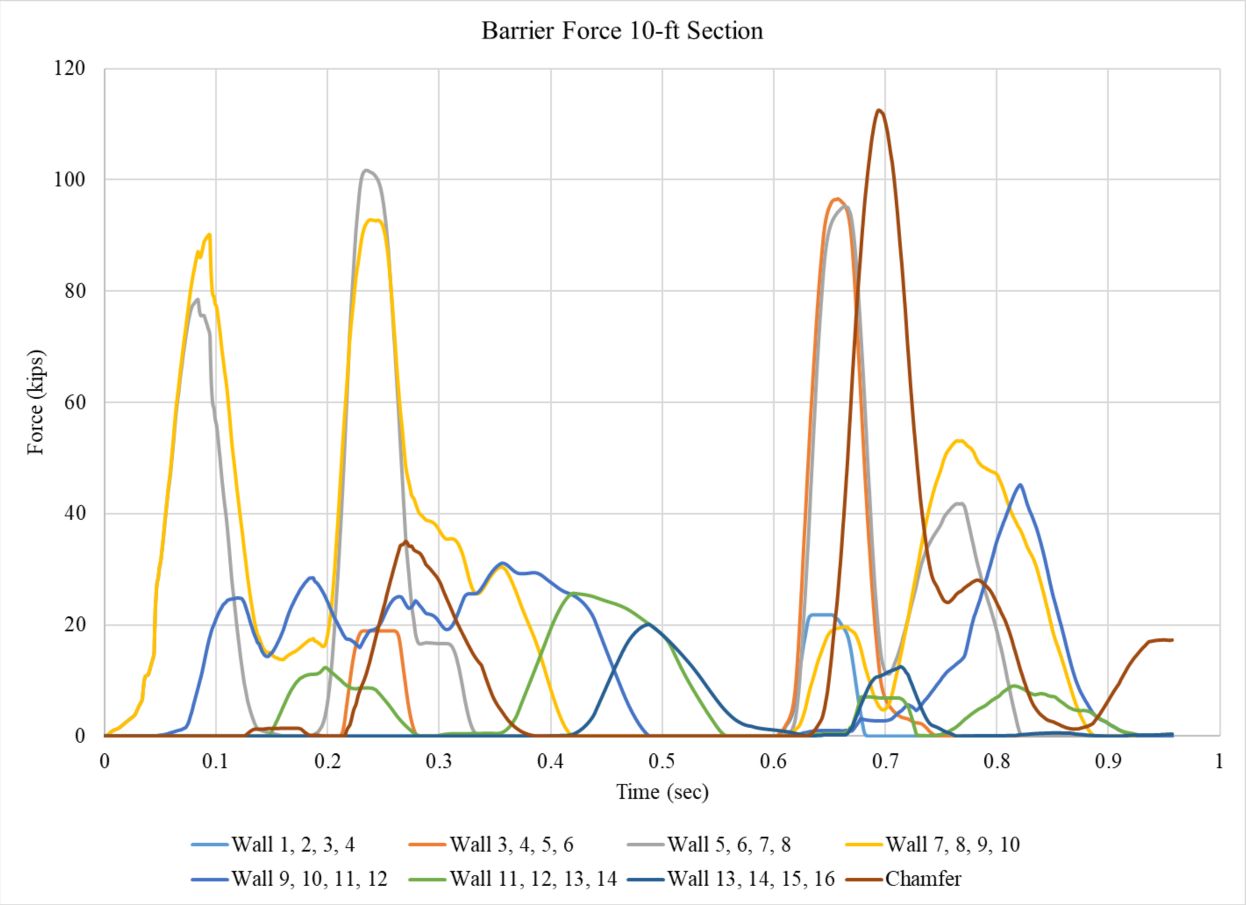

Figure 6.34 70 in. Barrier Force 10-ft Section

The shear forces acting on 10 ft long segments of the 90 in. tall barrier are shown in figure 6.34. Results of the impact loading were similar in behavior and magnitude to shorter barrier heights for the first 0.50 sec, but diverged considerably during “tail slap”. At 0.60 sec the tank’s side impacted walls 3 through 16, reaching forces of 18 kips (walls 13 through 16), 38 kips (walls 11 through 14), 52 kips (walls 9 through 12), 58 kips (walls 7 through 10), 102 kips (walls 5 through 8), and 132 kips (walls 3 through 6) at 0.64 sec. The peak load was concentrated at the wall segment nos. 5 and 6, but wall segments 7 and 8 also experienced large lateral loads. However, as shown in figure 6.34, the lateral load was distributed across the entire tank trailer contact with the barrier and was much less concentrated than for lower barrier heights. The tank trailer also contacted the barrier chamfer between 0.60 sec to 0.90 sec, with a peak load of 61 kips. Surprisingly, the tank trailer appeared to rebound partially, with minimal load between 0.67 and 0.69 sec, before re-engaging with a concentrated load at wall segment nos. 7 and 8.

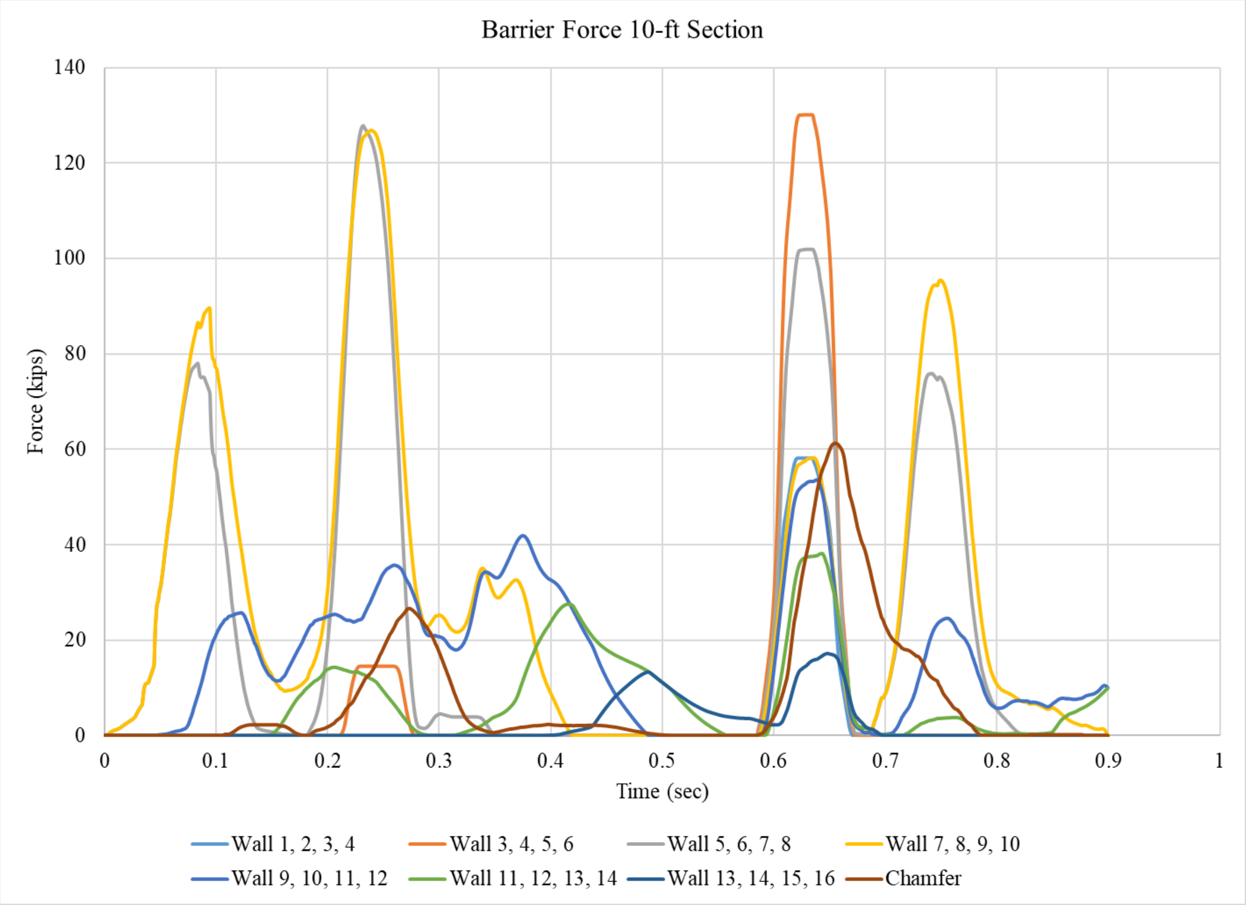

Figure 6.35 90 in. Barrier Force 10-ft Section

As with the maximum 5 ft long barrier shear forces, the chamfer load was added to each 10 ft long segment to generate a conservative estimate of peak shear force and the maximum was force throughout the barrier event is shown in figure 6.35. Four peaks can be seen in the graph. The first peak occurrs when the tractor impacted the barrier; all barrier heights had a similar loading. The second peak was generated by the trailer's front end impacting the barrier at about

0.20 sec. The maximum load at the second peak occurred at around 0.25 sec. The load at that moment remained similar for barriers 50 to 65 in. the loading for barriers 70 to 90 in. Note the 80 and 85 in. tall barriers recieved a larger load than the 90 in tall barrier. The trailers's front end remained in contact with the barrier until 0.60 sec. From 0.60 sec to 0.70 sec the trailer's side contacted the barrier, loading different walls. At 0.70 sec the tank's back end impacted the barrier, and at about 0.75 sec generated its peak load.

It was noted that the peak 10 ft long barrier forces were much lower than the peak barrier forces from the sum of all wall panels, which was shown in figure 6.24. Results indicate that although concentrated forces did occur to certain narrow wall panels, the barrier shear capacity required to contain the vehicle could be much lower and still successfully contain the vehicle, because contact was distributed along the entire length of the trailer and part of the tractor at peak "tail slap" load.

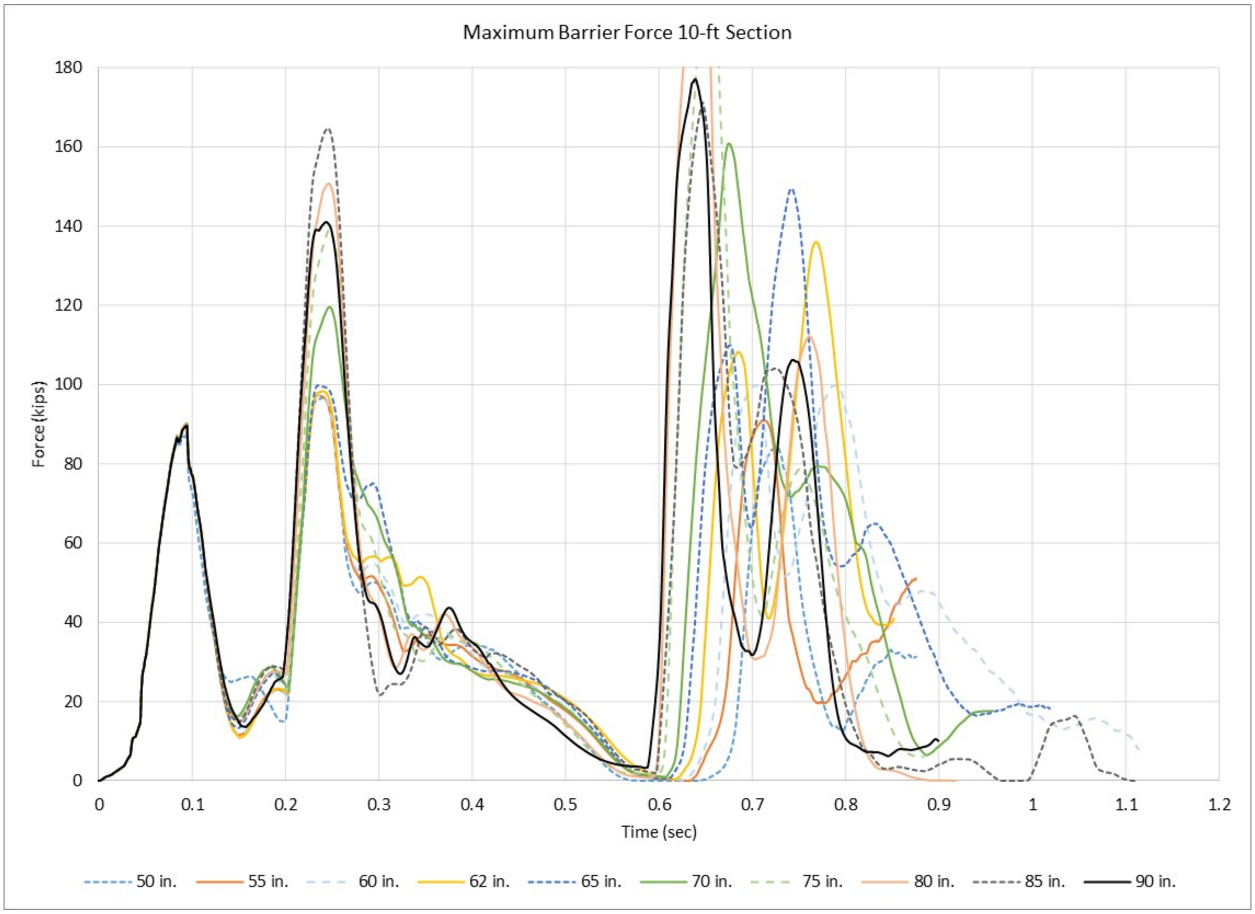

Figure 6.36 Maximum Force 10-ft Section

The maximum force vs. barrier height were tabulated and summarized in figure 6.36. Overall, as the barrier height increased, the maximum loading increased. Barriers with a height of 50 to 60 in. caused the lowest impact force on the barrier and showed similar peak loading. Significant changes in lateral shear loads acting on narrow longitudinal barrier lengths occurred between barrier heights of 60 and 80 in., but for barriers of 85 and 90 in., the shear forces were distributed along the length of the trailer. The 80 in. tall barrier had the largest maximum force.

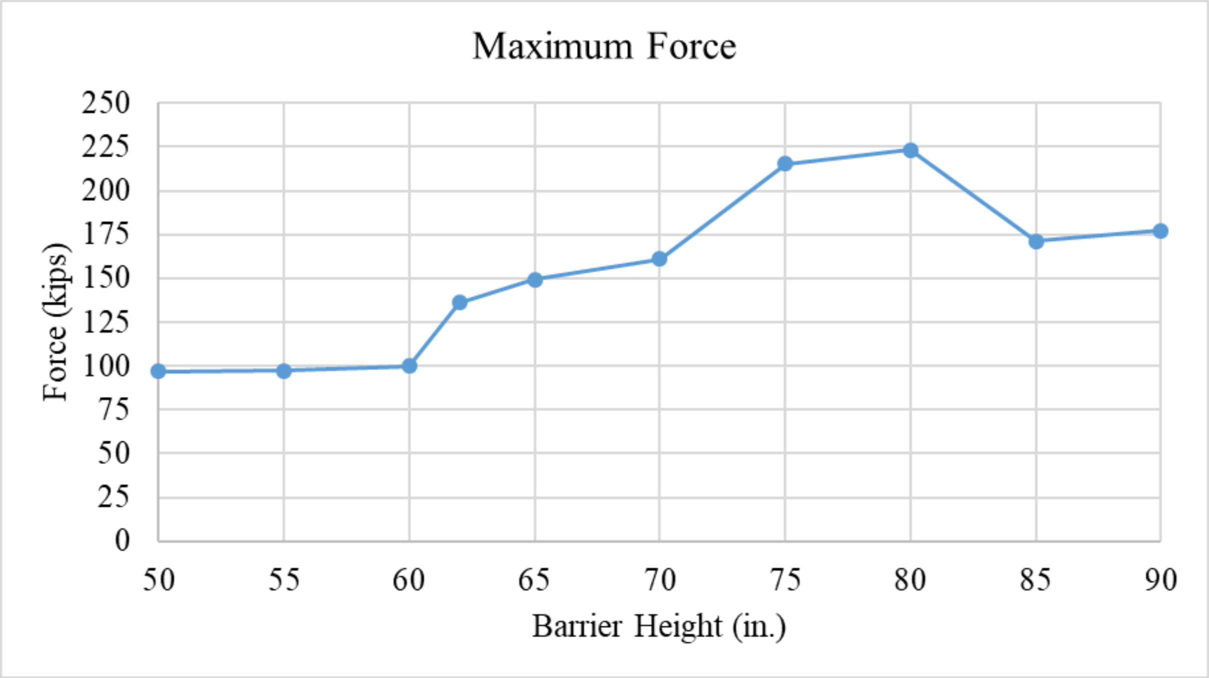

Figure 6.37 Maximum Force Acting on 10-ft Long Barrier Section

6.5 Barrier Moments

Another critical factor which affects barrier design is the moment generated by the impact force. Barriers must be designed with enough moment capacity to transmit moment to the foundation or bridge deck support, prevent rotation or damage to the foundation or bridge deck connection, and resist flexural loads in the barrier upstream and downstream from the point of impact.

The total longitudinal moment generated by the vehicle's impact, which is experienced at the foundation of the barrier, was calculated by discretizing the applied force locations. Impacts on the lower wall panels were primarily associated with wheel and axle loads, whereas the impacts experienced at the upper panels were primarily applied by the truck body, tank chassis, and tank jacket. For a conservative analysis, it was assumed that all forces acting on the lower rigidwalls in the model were attributable to the wheels, and all forces acting on the upper rigid walls were attributable to the truck, tank chassis, and tank jacket. Further, it was assumed that wheel forces acted at the nominal height of the center of the wheel, and the truck, tank chassis, and tank jacket impact forces acted at the top impact-side edge of the barrier (i.e., top edge of the upper rigidwall). These forces were multiplied by their respective heights from the point of reference to where the force is being applied.

$$M_o = \sum F_T \cdot h_b + \sum F_W \cdot h_w \tag{6.1}$$

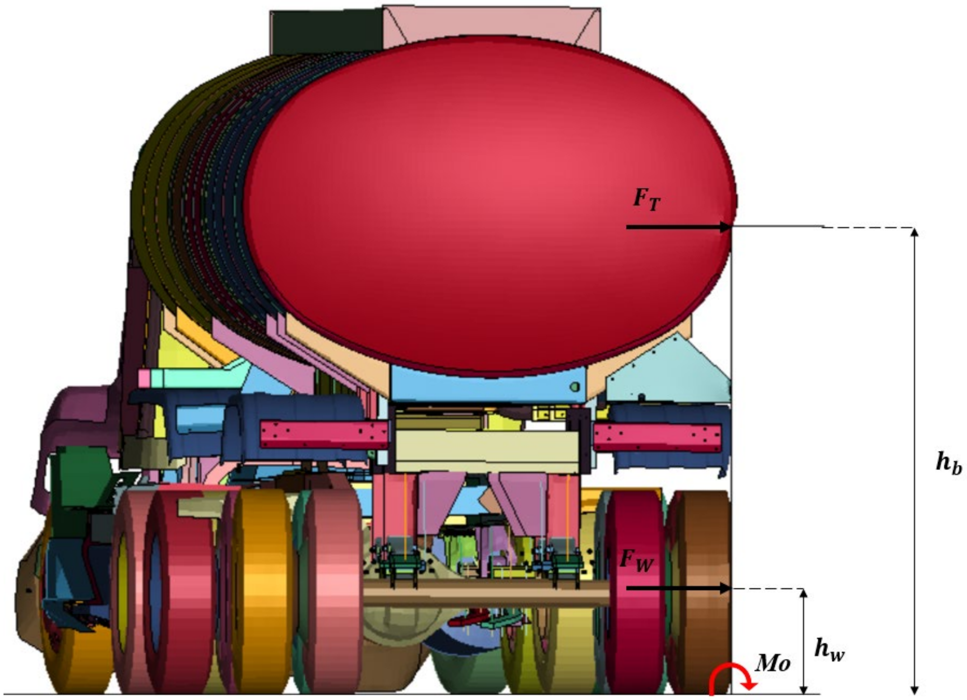

Figure 6.38 Moment Free Body Diagram

The total moments applied to the barrier during impact were calculated using Equation 6.1, and results are shown in figure 6.38. The first moment loading reflects the initial impact of the tractor, which occurred between 0 ms and 0.20 sec. The second spike in moments occurred in conjunction with the tractor rear axle and trailer front end impacting the barrier, spanning from 0.25 sec and ending at 0.40 sec. The moment spike was associated with the trailer's rear axle and tank impact with the rigidwalls, which occurred between 0.65 sec and 0.85 sec. On the first part of the graph, the moments show as the barrier height increased, the moment increased.

As expected, the first peak moment was the smallest, as the majority of the redirection load was applied by the lower rigidwall on the wheels of the tractor. The peak moment for all barrier heights was approximately the same, at approximately 190 kip-ft. The second peak moment was strongly affected by barrier height due to the tank impact with the barrier surface. Note that the 85 in. barrier, which located the barrier's impact side top chamfer at the center of the tank, had the highest moment due to the 45 degree angled chamfer contact on the tank body. The third moment spike was the largest for all barrier heights event.

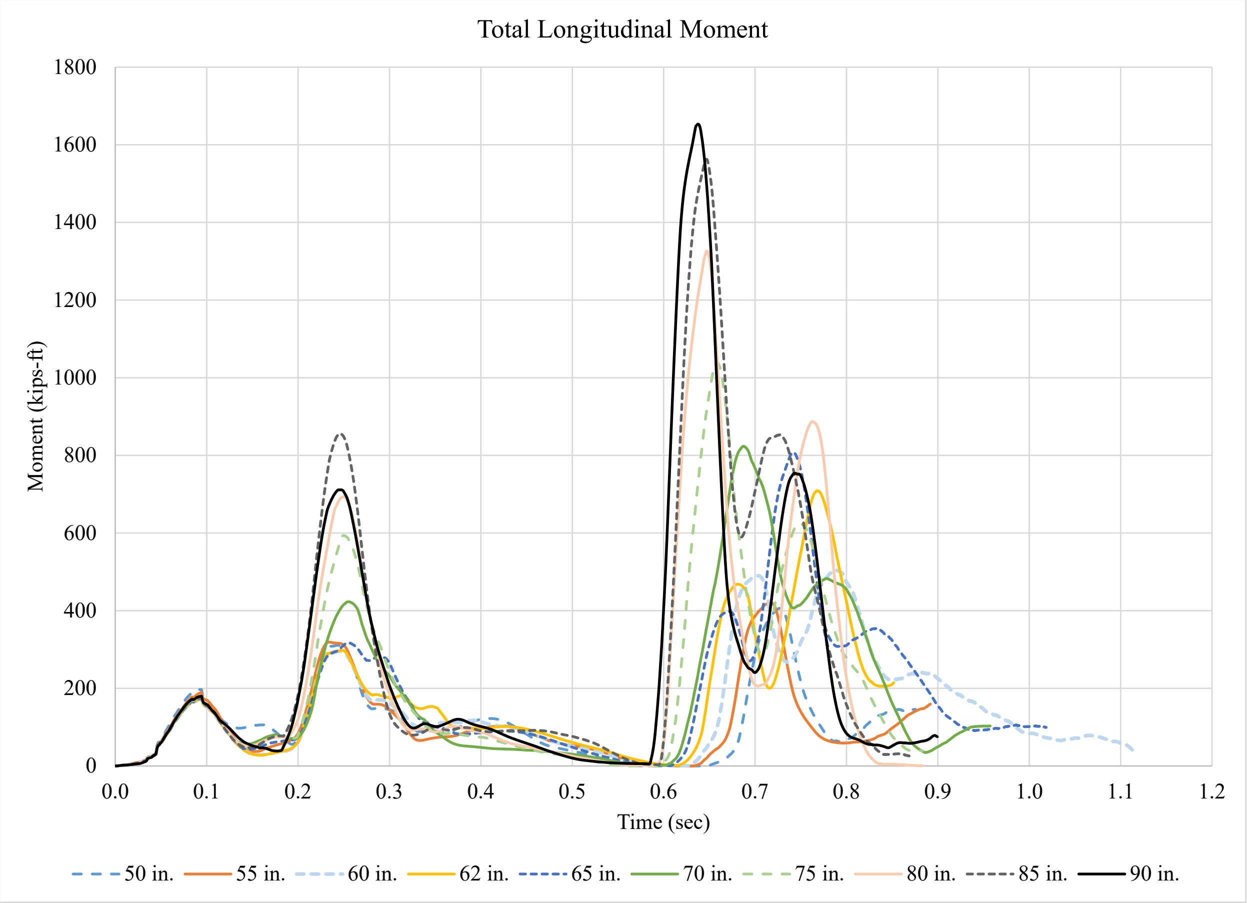

Figure 6.39 Total Barrier Moment Comparison

The maximum total longitudinal moment developed during impact and calculated at the barrier foundation is summarized for each barrier height in figure 6.39. The graph shows that the moment generally increased as the barrier height increased. This was because the distance from the foundation to the loading point on the trailer, which corresponded to the maximum lateral load in the model, increased. All of the barriers with top heights of 60 in. or less experienced a peak moment less than 600 kip-ft. When the vehicle model impacted a 62 in. tall barrier, the moment increased because at that height, the trailer tank impacted the front, chamfered face of the barrier which caused a larger load at a higher height. The moment for the 65 and 70 in. tall barriers remained similar. After increasing the barrier height from 70 in., the barrier moment increased as the barrier height increased.

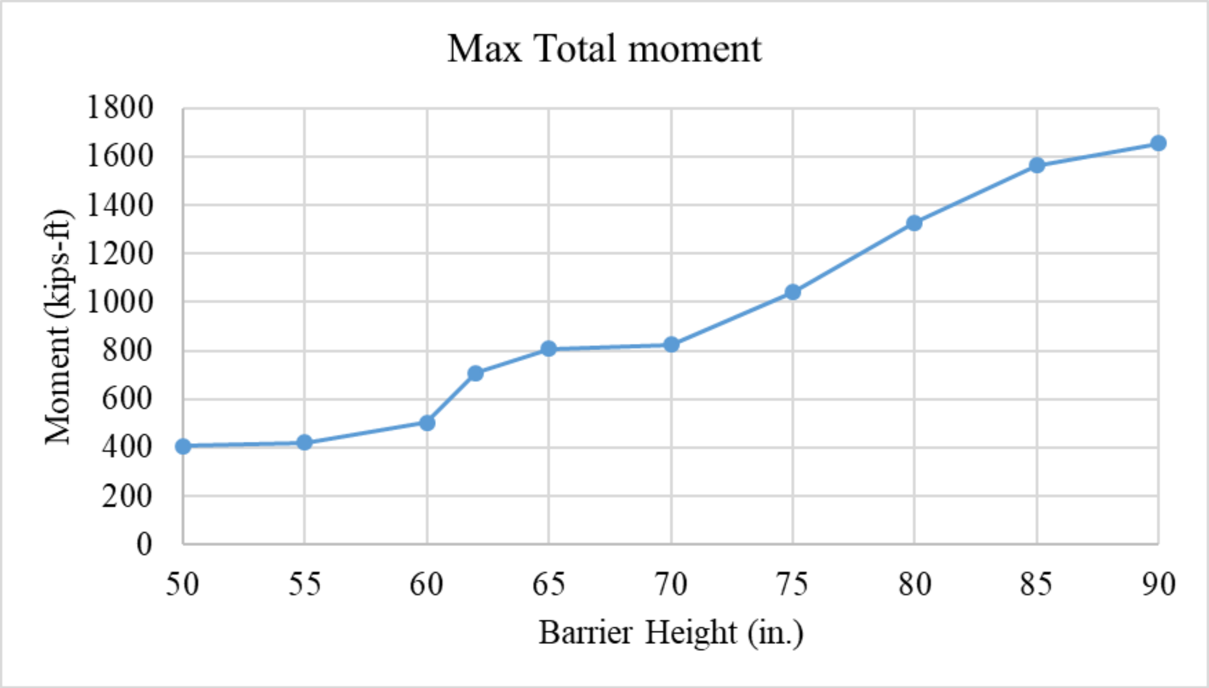

Figure 6.40 Barrier Height Max. Total Moment

6.5.1 Barrier Moment for Every 5-ft Section

The total longitudinal moment at the barrier foundation is useful for understanding the load behavior of the structure, and the peak moment acting on shorter segments of barriers is needed to design the proper capacity along the entire length of the barrier. Thus, the longitudinal moments were calculated using the results of the 5 ft rigidwall force analysis.

The moments along consecutive 5 ft sections of barrier with 50, 62, 70, and 90 in. barrier heights are plotted in figures 6.40 through 6.43. For each barrier height, the timing and shape of the moment-time curves were similar. For the 50 in. tall barrier, the first moment was generated at walls 7 and 8 when the tractor impacted the barrier 20 ft upstream from the beginning of the barrier with a peak moment of 160 kip-ft. At approximately 0.19 sec the tractor rear tandem axle and the trailer's front side impacted walls 7 and 8, and at 0.23 sec reached a moment of 175 kips. At 0.65 sec the tank's back side impacted walls 7 and 8, reaching a moment of 260 kip-ft at 0.73 sec. From 0.65 sec to 0.80 sec, the tank contacted the chamfer and walls 5 through 14, in which walls 5 and 6 had a peak moment of 90 kip-ft and walls 9 and 10 had a peak moment of 60 kip-ft. At 0.78 sec the tank's tail end impacted walls 9 and 10 and the chamfer reaching loads of about 65 kip-ft for both.

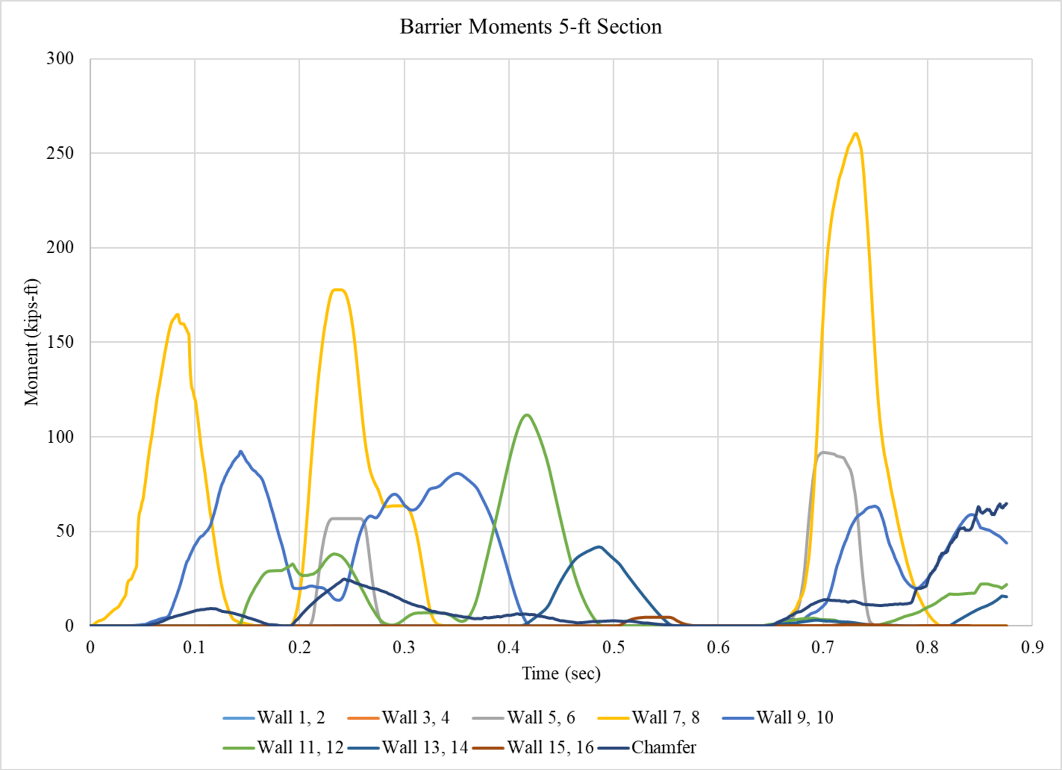

Figure 6.41 50 in. Barrier Moment 5-ft Section

Results from the 62 in. tall barrier moment calculation are shown in figure 6.41. The first moment was generated at walls 7 and 8 when the tractor impacted the barrier 20 ft upstream from the beginning of the barrier with a peak moment of 145 kip-ft. At approximately 0.19 sec the tractor's back end and the trailer's front end impacted walls 7 and 8, reaching a peak moment of 220 kip-ft at 0.24 sec. At 0.64 sec the tank's side impacted walls 5 through 8, resulting in peak moments of 155 kip-ft (walls 5 and 6) and 255 kip-ft (walls 7 and 8) at 0.67 sec. From 0.70 sec to 0.85 sec, the tank rolled onto the chamfer and the trailer loaded against walls 5 through 14, resulting in a peak moment of 155 kip-ft on wall nos. 7 and 8 and the chamfer receiving the largest moment of 510 kip-ft.

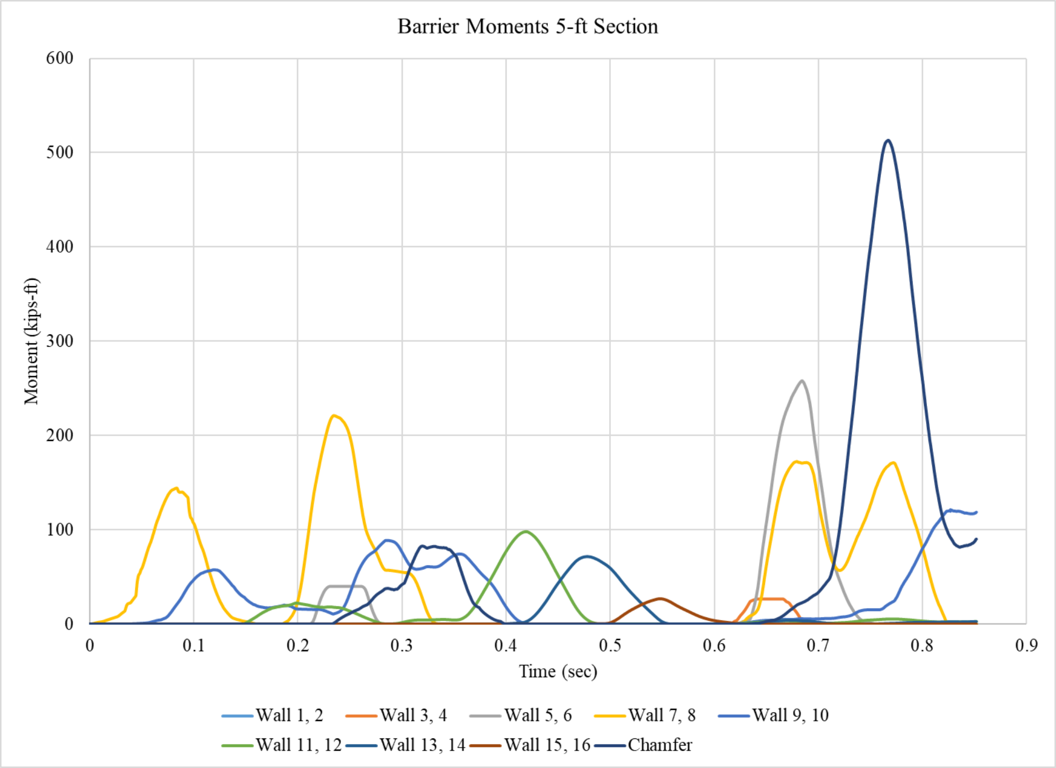

Figure 6.42 62 in. Barrier Moment per 5-ft Section

The moment calculation for the 70 in. tall barrier is shown in figure 6.42. The first moment was generated at walls 7 and 8 when the tractor impacted the barrier 20 ft upstream from the beginning of the barrier with a peak moment of 150 kip-ft. At approximately 0.19 sec the tractor's back end and the trailer's front end impacted walls 7 and 8, resulting in a peak moment of 200 kip-ft at 0.23 sec. At 0.64 sec the tank chassis and rear axle impacted walls 3 through 8, resulting in a peak moment of 90 kip-ft for walls 3 and 4 and 200 kip-ft for walls 5 and 6 about 0.67 sec. From 0.70 sec to 0.90 sec, the tank trailer rolled onto the chamfer and loaded against walls 5 through 14 during which the chamfer received the largest moment of 650 kip-ft.

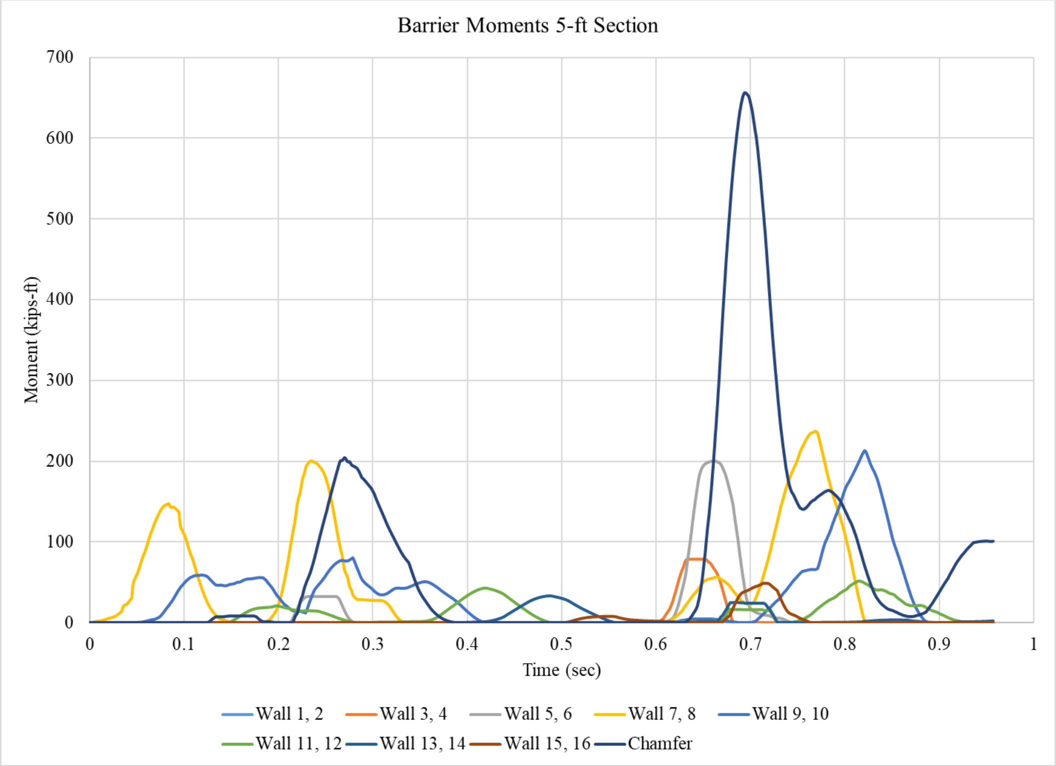

Figure 6.43 70 in. Barrier Moment per 5-ft Section

The moment calculation results for the 90 in. tall barrier are shown in figure 6.43. The first moment was generated at walls 7 and 8 when the tractor impacted the barrier 20 ft upstream from the beginning of the barrier with a moment of 150 kip-ft. At approximately 0.18 sec the tractor's back end and the trailer's front end impacted walls 7 and 8, resulting in a peak moment of 490 kip-ft at 0.24 sec. At 0.60 sec the tank trailer chassis and tank jacket impacted walls 3 through 14 with a peak moment of 250 kip-ft at walls 3 and 4, 320 kip-ft at walls 5 and 6, 180 kip-ft at walls 11 and 12, and 95 kip-ft at walls 13 and 14, respectively. From 0.65 sec to 0.80 sec, the tank shifted laterally and partly rolled against the chamfer and walls 7 through 10, resulting in peak moments of 500 kip-ft on walls 7 and 8 and 150 ft-kips at walls 9 and 10, respectively. The chamfer peak moment was 460 kip-ft at 0.67 sec.

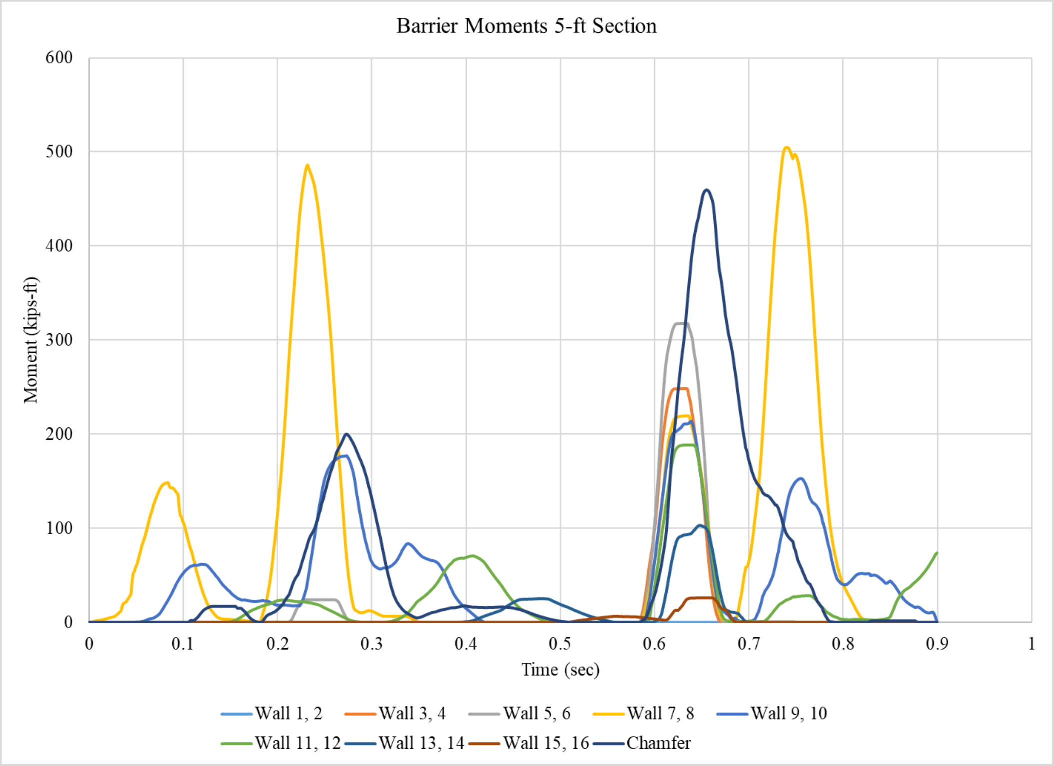

Figure 6.44 90 in. Barrier Moment per 5-ft Section

The maximum moment generated at each instant in time was plotted for every barrier height and is summarized in figure 6.44. Similar to the method used to conservatively estimate peak shear force, the maximum moment was determined based on the Equation 6.2:

$$M_{Max} = \max_{walls\ 1-16}(moment\ on\ 5ft\ long\ wall\ section) + M_{chamfer} \qquad (6.2)$$

As a result, the chamfer moment was added to the maximum of the moments of the 5 ft long barrier segments. Results exhibited similar characteristics to the moment-time plots: the first peak was related only to the impact of the tractor front end, followed by the impact of the tractor back end and trailer front end, a peak load from the trailer jacket and rear axle, and a secondary large moment spike resulting from the trailer rolling against the top edge of the barrier. Somewhat surprisingly, the maximum moment over a 5 ft continuous length of barrier was higher for 65, 70, 75, and 80 in. barrier heights than the 90in. barrier height. This occurred because the lower barrier heights experienced very concentrated back-end “tail slap” impact forces particularly near the top edge of the barrier, whereas the yaw rotation and trailer engagement with the 85 and 90in. barriers was much more distributed along the length of the barrier. The 62 in. barrier height also experienced a large peak moment during the secondary impact, as the trailer leaned onto the chamfer edge. Barrier heights lower than 62 in. experienced much lower moments because more of the trailer leaned on the top surface of the barrier in a vertical compression mode during trailer rotation, resulting in less lateral load and a lower peak moment. Thus, a 62 in. barrier height was determined to be a critical height for evaluating the peak moment and barrier strength as well as vehicle stability.

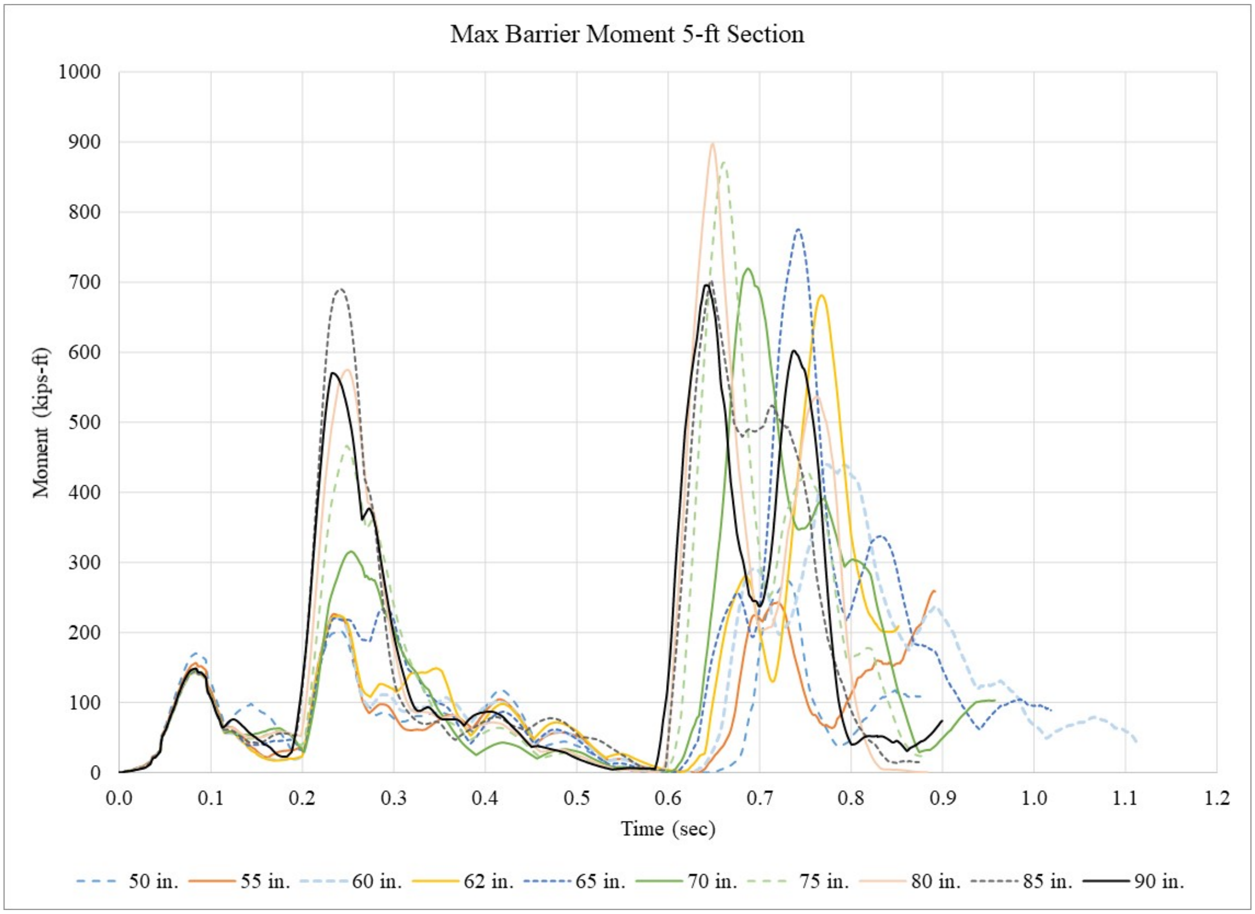

Figure 6.45 Maximum Moment per 5-ft Section

The largest moment experienced in a 5 ft barrier section was summarized and shown in figure 6.45. The 80 in. tall barrier had the largest maximum moment on a 5 ft section, which indicated that the trailer "tail slap" impact had the most concentrated loading at the 80 in. barrier height. A slight reduction in the peak moment at the 70 in. barrier height was associated with less of a concentrated impact on a specific 5 ft panel, and part of the peak "tail slap" load was distributed to multiple panels. As well, the yaw behavior of the trailer was slower for the 70 in. barrier height, which resulted in a longer distribution of forces during "tail slap".

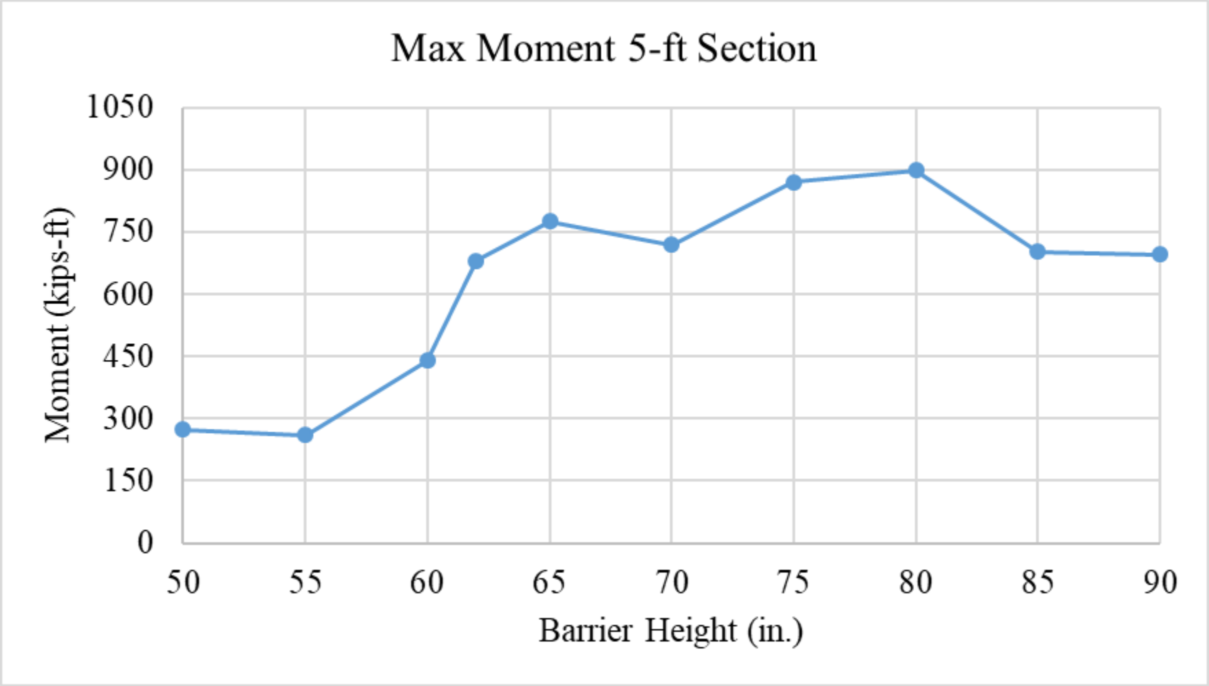

Figure 6.46 Maximum Moment per 5-ft Section

6.5.2 Barrier Moment for Every 10-ft Section

The analysis was repeated using 10 ft barrier segments (pairs of 5 ft wall segments added together) to evaluate how concentrated the tail slap loads were. Results of the 10 ft peak moment estimates are shown in figures 6.46 through 6.49. Overall, shorter barriers resulted in more concentrated moments that did not span across multiple segments, whereas taller barriers distributed moments along multiple 10 ft barrier segments. Results indicated the taller barriers more effectively distributed the tank trailer impact moment along the length of the trailer, but also experienced larger moments compared to shorter barrier segments.

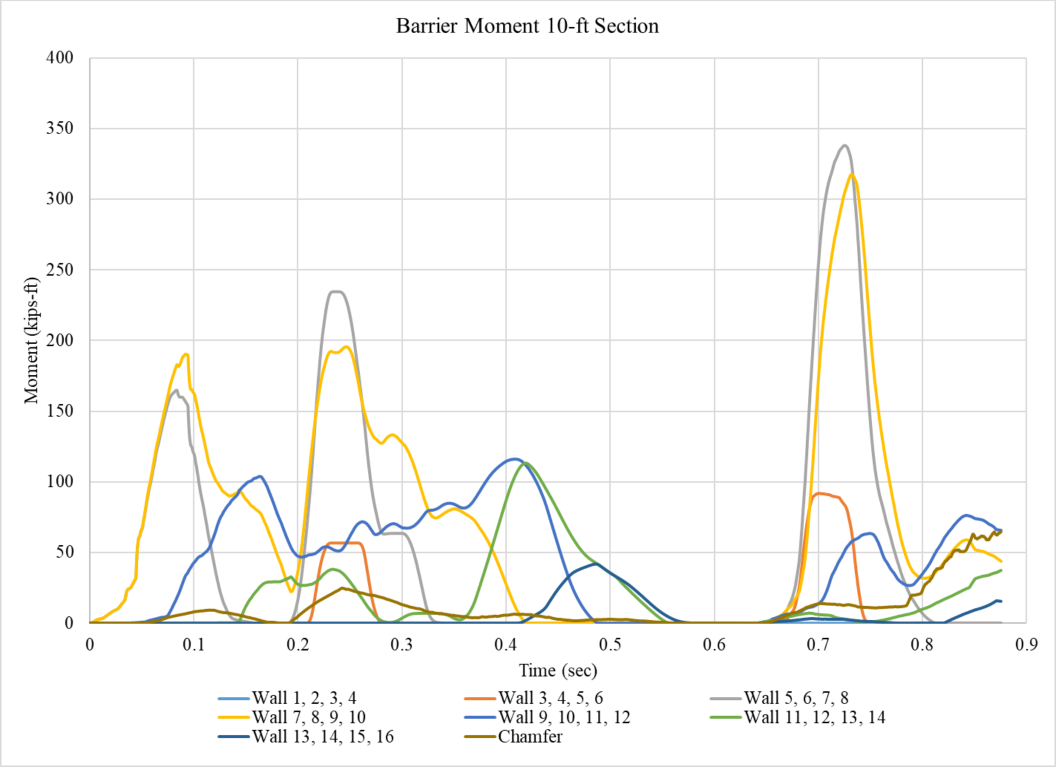

Figure 6.47 50 in. Tall Barrier Moment per 10-ft Section

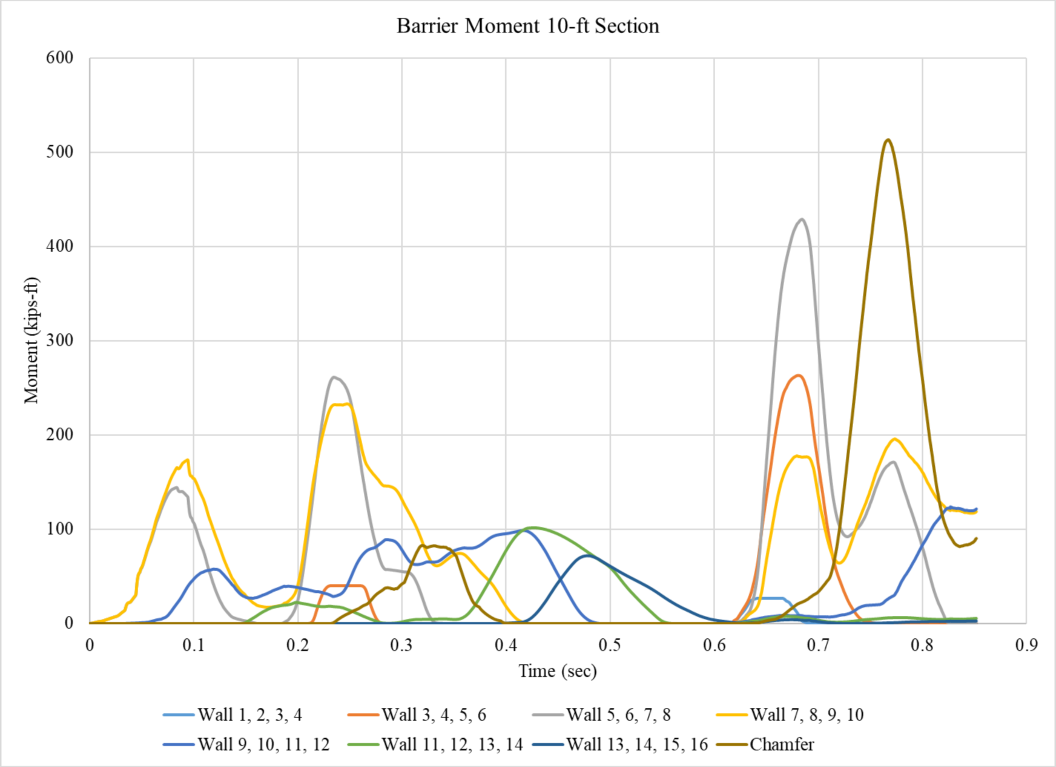

Figure 6.48 62 in. Tall Barrier Moment per 10-ft Section

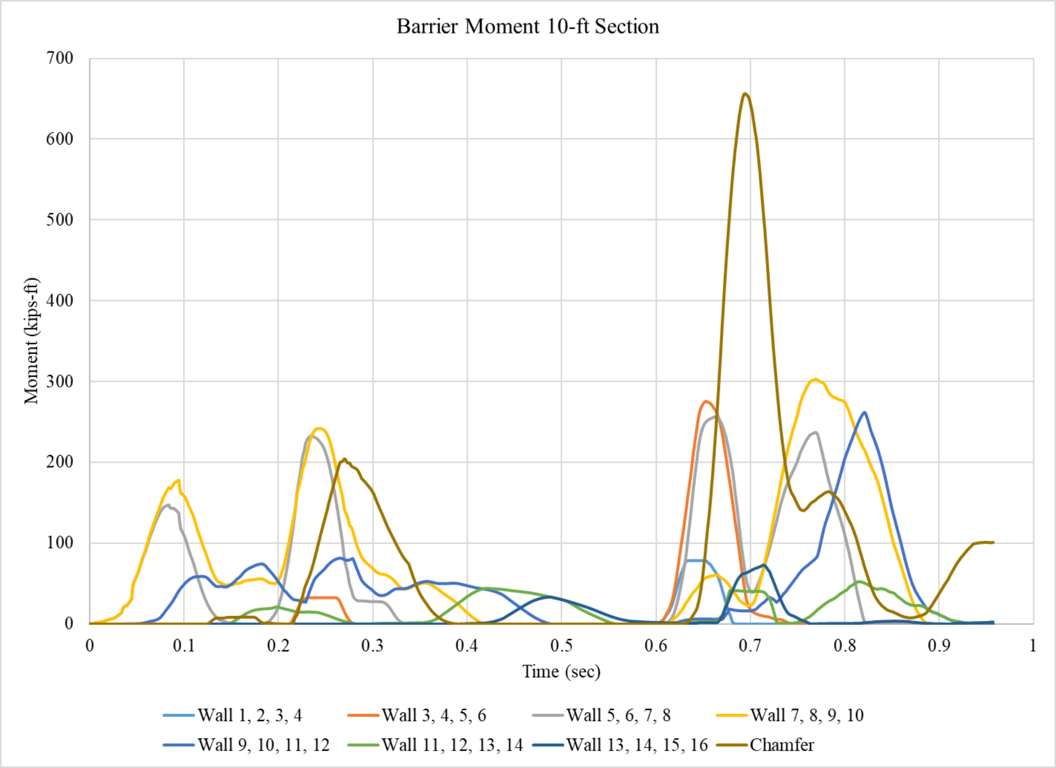

Figure 6.49 70 in. Tall Barrier Moment per 10-ft Section

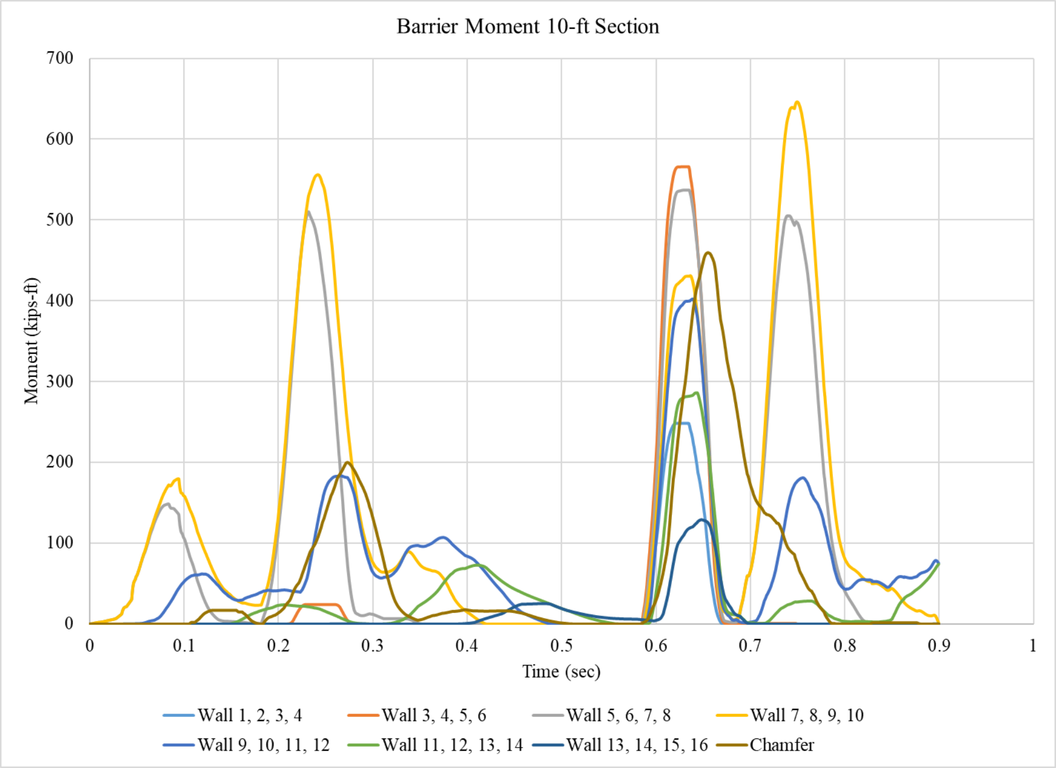

Figure 6.50 90 in. Tall Barrier Moment per 10-ft Section

The maximum moment for each barrier height was also estimated using Equation 6.2, modified for 10 ft long barrier segments. The maximum moment at every wall section was plotted in figure 6.50. Four peaks can be seen in the graph. The first peak was associated with the initial tractor impact with the barrier; all barrier heights had a similar moment as the load was primarily applied at the height of the vehicle's impacting front wheel. The second peak was generated by the tractor's back and the trailer's front end impacting the barrier at about 0.20 sec. The maximum moment at the second peak strongly influenced by barrier height, although surprisingly the 85 in. barrier height had the highest moment. The trailers's front end remained in contact with the barrier until 0.60 sec. The highest peak moment was associated with the near-simultaneous impact of the rear tank trailer axle and tank jacket against the barrier, between 0.60 and 0.68 sec (for different barrier heights), and the tank jacket remained in contact with the barrier through 0.80 sec.

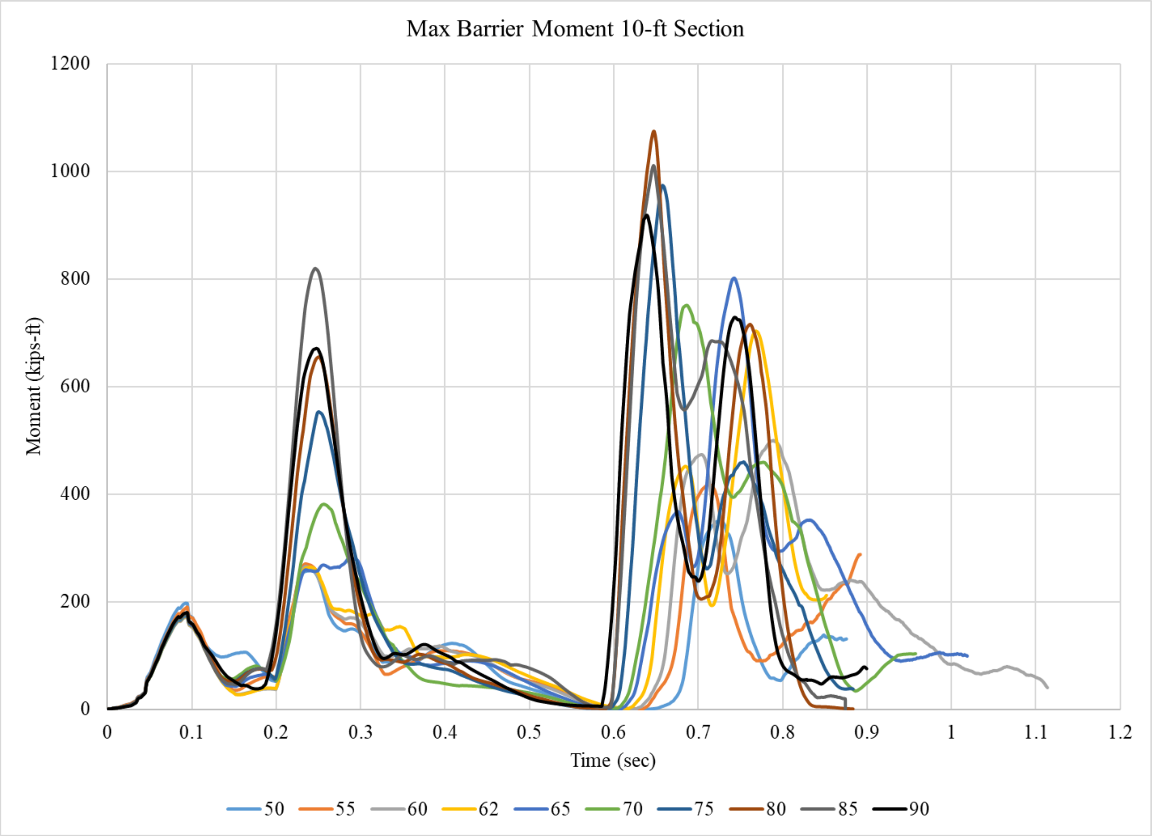

Figure 6.51 Maximum Moment per 10-ft Section

A summary of the maximum moment vs. barrier height for 10 ft long barrier segments is shown in figure 6.51. Overall, results indicated as the barrier height increased, the maximum moments increased with some exceptions: 70, 85, and 90 in. Barriers with a height of 50 to 60 in. caused the lowest impact moment on the barrier, although the abrupt increase in moment at 62 and 65 in. barrier heights were associated with concentrated tank jacket and chassis contact during "tail slap" and against the barrier top chamfer.

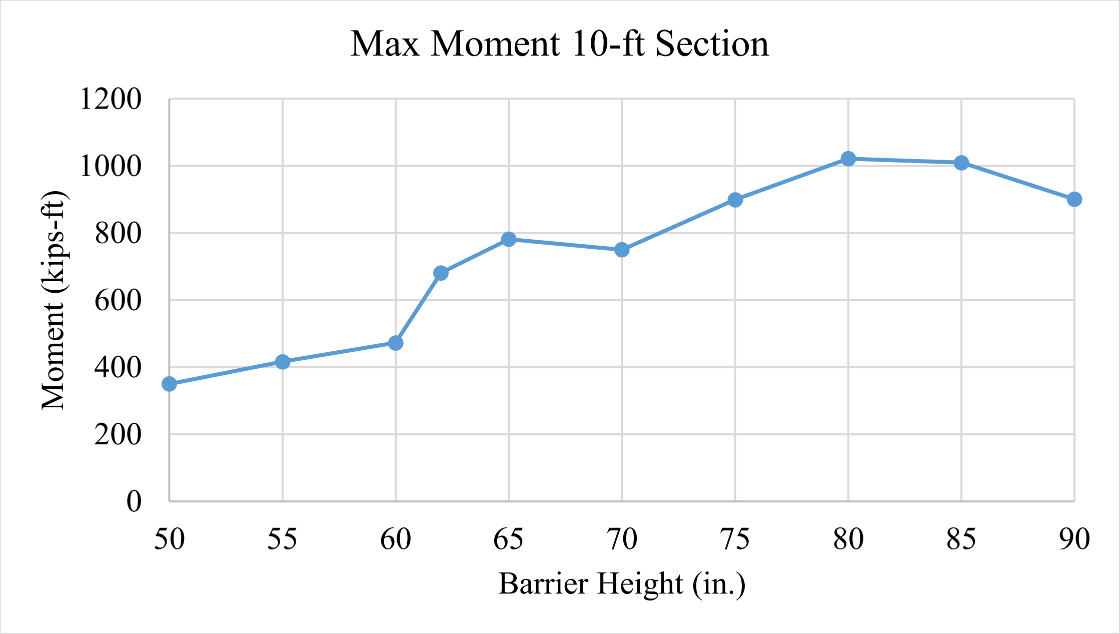

Figure 6.52 Maximum Moment per 10-ft Section

The 10 ft long barrier segment, maximum moment estimation was used to evaluate what portion of the total barrier maximum moment occurred in concentrated regions of impact, as opposed to distributed along the length of the barrier. Results of the 10 ft long barrier segment maximum moments were similar to the 5 ft long barrier segment maximum moments, indicating that large, concentrated shear forces and moments are developed at different barrier heights. However, the yaw behavior of the vehicle after impact had a strong effect on how concentrated the peak load (and therefore moment) was during “tail slap”. Barriers above 80 in. tended to reduce the severity of “tail slap” by distributing contact along the entire side of the tank trailer, whereas barriers between 62 and 75 in. tall produced very concentrated collisions at the rear axle of the trailer and were associated with the maximum moments at both 5 ft and 10 ft segment lengths considered.

6.6 Considerations for the Design of Barrier Capable of Containing MASH TL-6 Vehicle

During this research effort, the design of the barrier capable of containing and redirecting a MASH TL-6 vehicle was not performed. Instead, the critical design data which were needed when designing the barrier were presented. Results suggested the barrier height had a strong effect on concentrated shear force and longitudinal moment generation. Increased shear and moment demand will increase the design capacity of the barrier and may require additional reinforcement, weight, and cost. Therefore, the solution which provides sufficient containment (lateral ZOI need) at the lowest cost should be selected as needed. The recommended barrier configuration to be evaluated for full-scale crash testing will be determined in the next phase of the MATC research project.

Numerical simulation is a valuable tool for investigating potential outcomes of dynamic impact events, particularly with large non-linearities such as material plasticity, fluid reactions, and joint connections. However, numerical simulation results are also limited based on the accuracy of model calibration, modeling techniques, component reactions, connection modeling methods, and other features. Simulation predictions are consistently viewed with caution in the roadside safety industry due to the large and propagating effects of potentially small deviations in the analysis. For example, the tractor front axles did not include a fracture or release condition allowing disengagement from the truck body; although it was not believed to have a strong influence on barrier loading or moment, the post-impact trajectory of the truck may alter the duration and location of the point of maximum loading on the barrier, as well as the roll angle displacement of the truck-tank trailer combination. As well, a sliding fifth wheel connection was modeled which connected the trailer to the truck and the latch connection to the fifth wheel approximated the connection as a joint. Some large truck testing with tractor-van trailer vehicles has resulted in significant damage to the fifth wheel connection and large rotations of the van trailer relative to the truck body, which were not considered in this analysis. Failure of the fifth wheel connection could result in the trailer disengaging from the truck and altering the estimated lateral intrusion and trailer stability.

As a result, barrier design configurations are considered preliminary until improved model calibration with full-scale crash testing can be conducted. Full-scale crash testing is anticipated in the next phase of this research effort. Although simulation results with the highest barrier heights resulted in reduced moment and shear load estimates, researchers conservatively assumed the minimum shear and moment capacities of the barriers should be equal to the maximum of shear and moment capacities at each simulation value or for any barrier of lower height. The resulting barrier design recommendations are shown in table 6.1.

Table 6.1 Recommended Capacities of Barriers Designed to Contain MASH TL-6 Vehicle

Barrier Height (in.)	Minimum Shear Capacity (kip)		Minimum Moment Capacity (kip-ft)		Maximum Lateral Encroachment (in.)
	5- ft Section	10-ft Section	5- ft Section	10-ft Section	
50	78.2	96.7	273	351	45.0
55	80.4	97.4	273	417	43.3
60	88.1	99.9	440	473	37.6
62	131.9	136.0	681	681	32.5
65	144.8	149.5	775	782	27.6
70	144.8	160.9	775	782	19.3
75	175.0	215.5	871	900	15.4
80	175.0	223.4	898	1022	8.3
85	175.0	223.4	898	1022	4.0*
90	175.0	223.4	898	1022	4.0

*ZOI revised to reflect 4.0 in. lateral encroachment estimated from 90 in. barrier

Chapter 7 Tank Trailer Model Refinement

The detailed tank-trailer model was constructed to provide an improved representation of real tank-trailers to obtain the general behavior of a real/physical tank trailer. More critical components from the preliminary model were included. The tank trailer model created in Whitfield [1] was revised and used to investigate the required capacities of barriers in this study. This chapter outlines the differences between the real truck-tank trailer combination vehicle and the simulated vehicle, concerns with the numerical model, and potential revisions that can be implemented to make the model more accurate.

7.1 Fluid Model

For the fluid component, solid elements with the properties of water at room temperature were used to simulate the sloshing of water inside the tank. The solid elements were given an element formulation of 1, and constant stress solid elements and material were modeled using MAT_ELASTIC_FLUID. The element formulation and material model experienced large deformations and negative volumes when the elements sloshed back on top of other elements. An illustration of elements deforming on top of others is shown in figure 7.1. This resulted in early and error terminations in the simulation before reaching termination time.

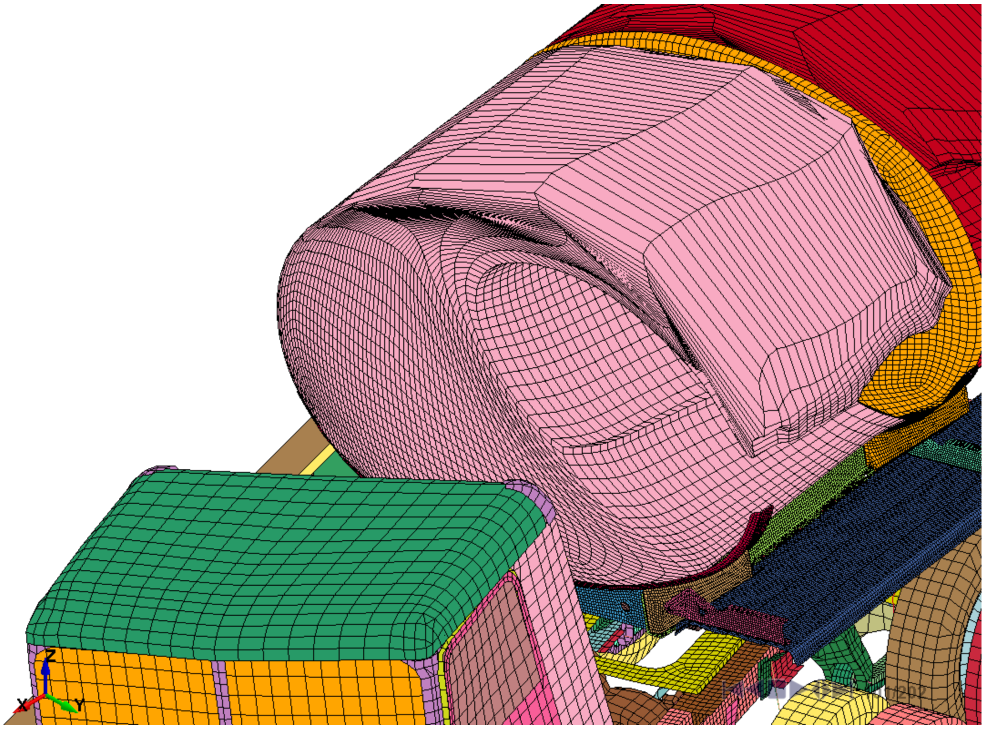

Figure 7.1 Fluid Mesh Deformation

As concluded in Section 4.4.2, the ALE computational method is more suitable for simulating the behavior of sloshing fluid than the Lagrangian method. Although an ALE containerized fluid model was developed and successfully simulated, implementation into the full TL-6 model was time-consuming and presented additional challenges. Therefore, the Lagrangian model was used during this study and implemented to fulfill the project objectives within available time and budget constraints. It is recommended that the ALE implementation be completed as its formulation will likely be correlated with improved model stability and may result in a more accurate estimation of tank wall pressure and internal fluid reaction.

7.2 Tank Re-meshing

One significant issue for implementing the ALE fluid model into the TL-6 vehicle model was that the meshing of tank components did not match the meshing of fluid components. As a result, an extra component was required to ensure the compatibility between the two interfaces.

This component is the fluid container, which has a mesh that matches the mesh of the fluid's surfaces. Shell elements are the best option to model the tank structure since this type meshing requires a lower CPU time to process simulations. Tank components also absorb most of the barrier impact and suffer more deformation than other components.

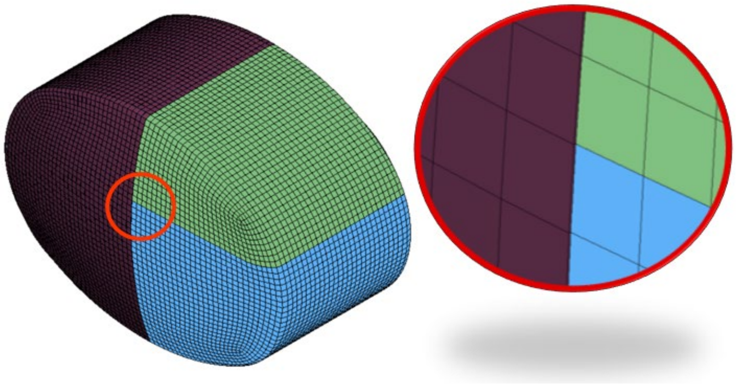

Figure 7.2 Tank Meshing

7.3 ALE Fluid Model

Use of the existing ALE model as a base model is recommended since it showed a consistent fluid behavior. For further investigation, more detailed research is recommended regarding the type boundary condition that can be applied to the ALE method. Researchers were unable to overcome some errors in the model specific to the ALE fluid condition, including application of the initial velocity causing out of range velocities and resulting in error termination. Further investigation may be warranted to improve the initial velocity of the fluid in the tank model for a stable interaction with the barrier. An area recommended for further research is the equation of state (EOS) for the ALE method since different types of EOS can be used to model more accurate fluid behavior.

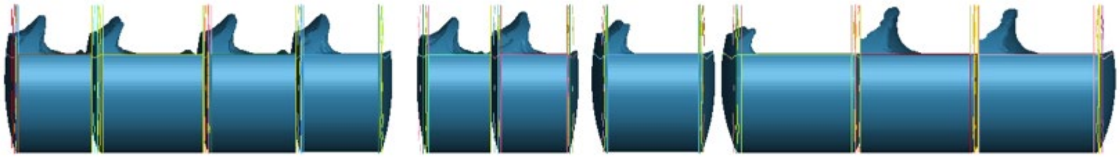

Figure 7.3 ALE-Method Fluid Sloshing Inside Tank

7.4 Baffles

Recall that simplified models of baffles were used in the simulation to prevent fluid contact instabilities with the Lagrangian fluid mesh. More detailed baffle models may be used if ALE fluid models are adopted, as shown in figure 7.4. In tank-trailer vehicles, the manufacturers are required to have baffles to direct the flow of fluid. A model of the trailer, which depicts the baffles and bulkheads, is shown in figure 7.5. These baffles add strength and stability to the tank while also limiting the sloshing of liquids within the tanks. The LBT Inc. tank-trailer, which was similar to the MASH-specified vehicle, has six baffles within the tank’s compartments. Further refinements of the tank model could utilize more realistic baffles, which include flow orifices, as it may affect fluid flow calculations and could affect the lateral stiffness of the tank.

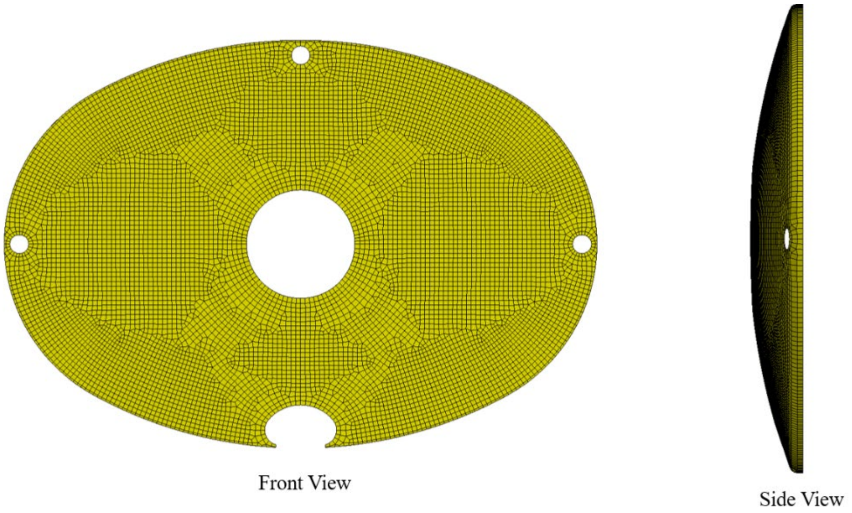

Figure 7.4 Potential Re-mesh of Baffle Component with Fluid Flow Orifices

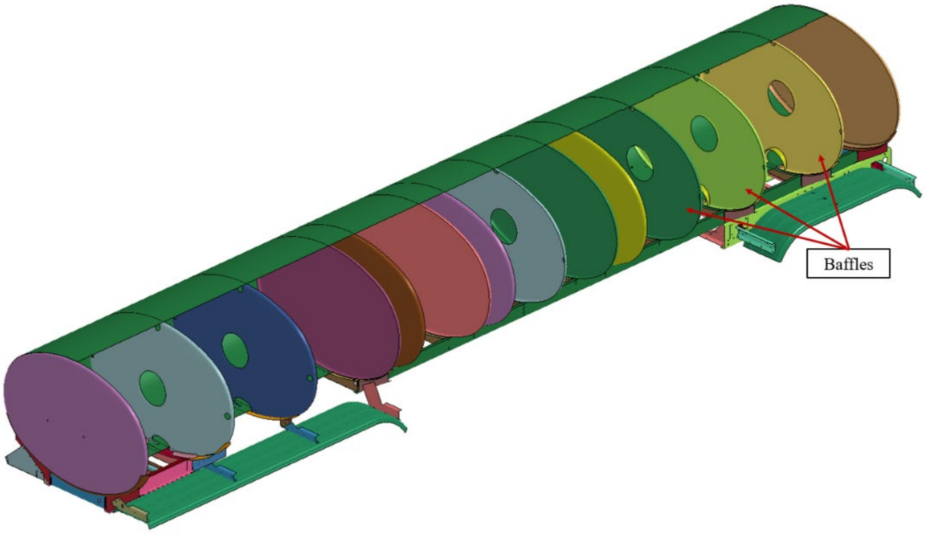

Figure 7.5 Potential Re-mesh of Tank-Trailer Structure Including Baffles with Fluid Flow Orifices

Chapter 8 Summary and Conclusion

The objective of this research project was to replicate the dynamic behavior of a truck-tank trailer vehicle using representative dimensions, properties, and inertias of the trailer/fluid ballast combination. This model was employed to develop a new, cost-effective, MASH TL-6 barrier.

A literature review on FSI methods to model fluid was completed to review and compare Lagrangian, Eulerian, ALE, and SPH methods. The literature review determined that the ALE method would most accurately represent the position and movement of fluid inside the tank-trailer. The researchers decided to use the ALE and Lagrangian methods for a comparative study to decide which computational method was going to be used for the trailer model.

A TL-6 vehicle model was created. The trailer model was reviewed and components were classified as critical or non-critical components. The non-critical components were removed to simplify the trailer model. The only components that were kept structurally supported the tank and connected the tractor to the tank-trailer. The baffles were removed the from tank-trailer and substituted with bulkheads to keep the model simple and avoid any type of interaction between fluids from different compartments as this fluid interaction may have increased the complexity of the fluid structure interaction.

The critical components were meshed and component thickness and element formulations were applied. Materials for trailer components were selected; aluminum was used for this model. The mechanical properties were implemented into the TL-6 trailer model. The tractor and suspension system were extracted from an existing TL-5 vehicle model and implanted into TL-6 vehicle model because of similarities with the LBT, Inc. BKZ 5949 trailer model. A real life trailer model was reviewed to select which type of constrains and contact would be used in the vehicle model.

A review of the vehicle model was conducted to verify the tank's components, connections, and material properties were working properly. After verifying the tank model fluid components were created for the Lagrangian and ALE computational methods, both fluid components were implemented into the tank model. Contacts and constraints were created to model the interaction between the fluid components and the tank's surface. Both computational methods successful showed the fluid sloshing inside the tank. An analysis of the results found that the ALE computational method showed a more accurate sloshing fluid behavior than the Lagrangian method. The ALE method also required a higher computational time than the Lagrangian method, which might cause the trailer model to have a lower time-step due to the size of model and the amount of elements when using ALE. The Lagrangian method did not show accurate fluid behavior, but required lower computational time. For models where complexity is high and time is a priority, the Lagrangian method offers reliable results. For these reasons, both methods were implemented into a TL-6 vehicle model, however, the Lagrangian method was successfully implemented into the vehicle model while the ALE method was not. This was due to out-of-range forces and velocities in the model caused by boundary conditions applied in the fluid component and the pressure cutoff in the fluid material. Therefore, the study continued using the Lagrangian method.

A model verification of the updated TL-6 vehicle model was completed to check that the vehicle model was showing reasonable results. The model verification was done by comparing Phase II simulation results with test data from the full-scale Instrumented Wall crash test. The simulation consisted of the TL-6 model moving at a constant velocity of 22 mph impacting a 90 in. tall rigid wall barrier. The TL-6 vehicle model did not accurately represent the impact loads and accelerations from the Instrumented Wall test due to the differences in the 1968 test vehicle and the preliminary vehicle model, which was created from the geometry of a newer tractor and trailer.

The researchers used the Lagrangian fluid model with a smoother and more refined mesh to overcome some fluid reaction issues. The TL-6 model was then used to simulate crash tests on rigid vertical walls ranging in height from 50 to 90 in. The results from the simulations (roll, lateral and vertical intrusion, forces, general behavior of the vehicle, and others) were analyzed to evaluate the relationship between barrier height and impact loads. The recommended configurations of barriers to contain a MASH TL-6 vehicle based on barrier heights are shown in table 8.1.

Table 8.1 Recommended Capacities of Barriers Designed to Contain MASH TL-6 Vehicle

Barrier Height (in.)	Minimum Shear Capacity (kip)		Minimum Moment Capacity (kip-ft)		Maximum Lateral Encroachment (in.)
	5- ft Section	10-ft Section	5- ft Section	10-ft Section	
50	78.2	96.7	273	351	45.0
55	80.4	97.4	273	417	43.3
60	88.1	99.9	440	473	37.6
62	131.9	136.0	681	681	32.5
65	144.8	149.5	775	782	27.6
70	144.8	160.9	775	782	19.3
75	175.0	215.5	871	900	15.4
80	175.0	223.4	898	1022	8.3
85	175.0	223.4	898	1022	4.0*
90	175.0	223.4	898	1022	4.0

*ZOI revised to reflect 4.0 in. lateral encroachment estimated from 90 in. barrier

Comparisons were made between the vehicle simulations performed using a simplified vehicle model from Phase I (Whitfield) and the detailed truck and tank-trailer combination vehicle modeled during Phase II (Vasquez). The Phase II model included bulkheads in the tank compartments and had a more detailed chassis and tank. Additionally, the bulkheads in the front and back of the Phase II model were concave and the model was taller than the Phase I vehicle. This difference in geometries can be observed in figures 8.1 and 8.2. Since the Phase II model had bulkheads, the dynamic forces generated by fluid sloshing were distributed individually for each compartment and not as a whole, like in Phase I. This caused barrier forces and maximum roll angles to behave differently than in the Phase I results. The vertical and lateral intrusions were higher than in the Phase I results because the Phase II model was taller.

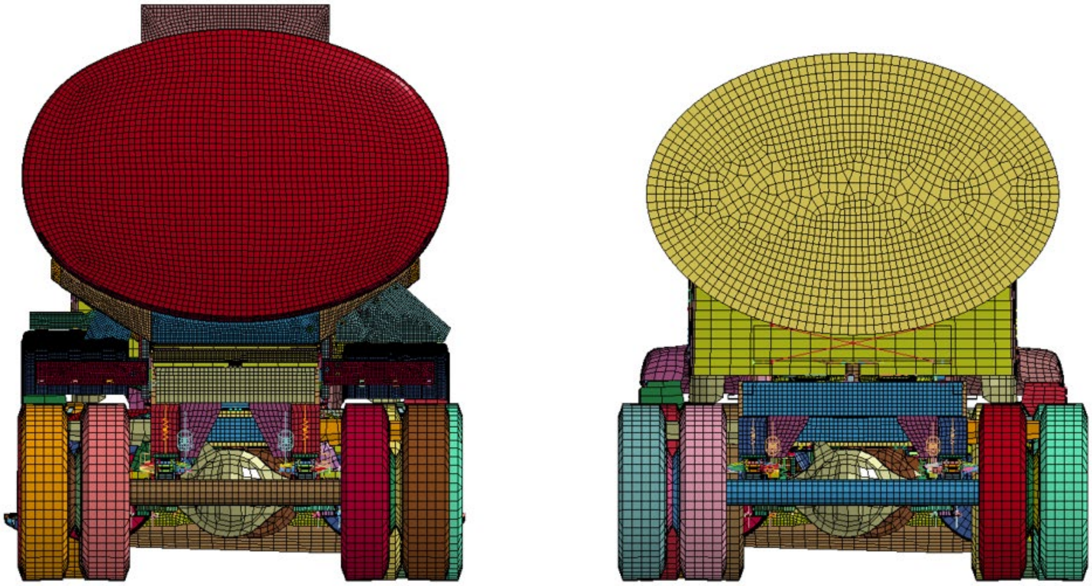

Figure 8.1 Phase II Model (Left) and Phase I Model (Right)

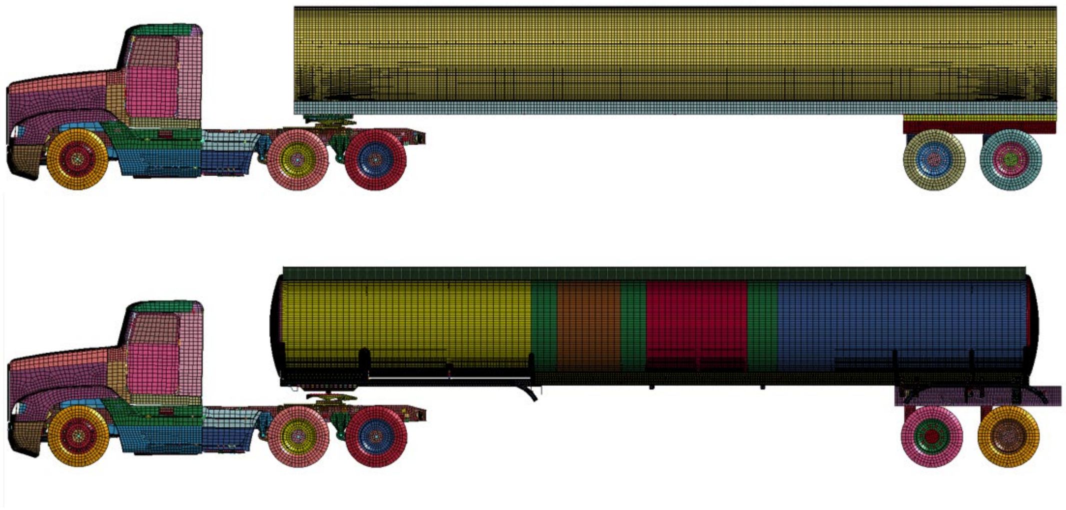

Figure 8.2 Phase I Model (Top) Phase II Model (Bottom)

The fluid model in the TL-6 model should be updated to more accurately reflect the behavior and loading generated by fluid sloshing, including: (1) ALE fluid model implementation in the TL-6 vehicle model, (2) more research about the equation of state that can be used to simulate fluid using the ALE method, (3) re-meshing the tank components to match the tank's mesh to the fluid mesh to simplify the model and improve the constraint between fluid and tank, (4) include baffles int tank model to accurately simulate fluid sloshing and dynamic forces generated by fluid; and (5) have the Lagrangian ballast model inside the tank as a backup in case the ALE fluid model gets complicated.

References

1. Whitfield, D.L., Investigation of a Tractor-Tank Trailer Roadside Containment Barrier, University of Nebraska, 2018.

2. Ross, H.E., Sicking, D.L., Zimmer, R.A., and Michie, J.D., Recommended Procedures for the Safety Performance Evaluation of Highway Features, National Cooperative Highway Research Program (NCHRP) Report 350, Transportation Research Board, Washington, D.C., 1993.

3. Manual for Assessing Safety Hardware (MASH), Second Edition, American Association of State Highway and Transportation Officials (AASHTO), Washington, D.C., 2016.

4. Michie, J.D., Recommended Procedures for the Safety Performance Evaluation of Highway Appurtenances, National Cooperative Highway Research Program (NCHRP) Report 230, Transportation Research Board, Washington, D.C., March 1981.

5. Federal Highway Administration (FHWA), Truck and Truck-Tractor Registrations – 2018, https://www.fhwa.dot.gov/policyinformation/statistics/2018/mv9.cfm Accessed: September 04, 2020.

6. Allison E. and Mandler B., Transportation of Oil, Gas, and Refined Products, Petroleum and the Environment, Part 15/24, American Geoscience Institute, 2018

7. Ibrahim R.F., Liquid Sloshing Dynamics Theory and Applications, Cambridge University Press, 2006

8. Smith and Stojko, The Application of Fluid Structure Interaction Techniques Within Finite Element Analyses of Water-Filled Transport Flasks.

9. Vesenjak et al., Simulation of Fuel Sloshing – Comparative Study.

10. Aquaro, M., Mucino, V., Gautam, M., & Salem, M. (1999). A Finite Element Modeling Approach for Stability Analysis of Partially Filled Tanker Trucks. SAE Transactions, 108, 452-460. Retrieved November 17, 2020, from http://www.jstor.org/stable/44723069

11. Vesenjak M., Müllerschön H., Hummel A., Ren Z., Simulation of Fuel Sloshing-Comparative Study. LS-DYNA Anwendeforum, Bamberg 2004

12. Xu J., Wang J., Souli M., SPH and ALE formulations for sloshing tank analysis. Int. Jnl. Of Multiphysics Volume 9, Number 3, 2015

13. Han D., Shen B., Zhou W., Zhang X., Qiang L., The Study of Semi-trailer's Steering Stability on the Fluid-Structure Interaction. Procedia Environmental Sciences, Volume 12, Part B, 2012, from: https://doi.org/10.1016/j.proenv.2012.01.391.

14. Dhole A., Raval C., Shrivastava R., Fluid Structure Interaction Simulation of Automotive Fuel Tank Sloshing using Nonlinear Fluid Properties. SAE Technical Paper 2015-26-0240, 2015

15. Aluminum in Commercial Vehicles, European Aluminum Association, 2013. https://european-aluminium.eu/media/1295/aluminium-in-commercial-vehicle_en.pdf

16. Mak K.K, Beason W.L., Hirsch T.J., and Campise W.L, Oblique Angle Crash Test of Loaded Heavy Trucks into an Instrumented Wall, Report No. DOT HS 807 256, Texas Transportation Institute Texas A&M University, 1988.

17. Hirsch, T.J., and Fairbanks, W.L., Bridge Rail to Restrain and Redirect 80,000 lb Tank Trucks, Report No. FHWA/TX-84/911-1F, Texas Transportation Institute, Texas A&M University, January 1984.

18. Hirsch, T.J., Analytical Evaluation of Texas Bridge Rails to Contain Buses and Trucks, Report No. FHWATX78-230-2, Study 2-5-78-230, Texas Transportation Institute, Texas A&M University, August 1978.

19. Plaxico, C., and Kennedy–Battelle, J., Enhanced Finite Element Analysis Crash Model of Tractor-Trailers (Phase A), Report No. #DTRT06G-0043, 2007.

20. Plaxico, C., and Kennedy–Battelle, J., Enhanced Finite Element Analysis Crash Model of Tractor-Trailers (Phase C), Report No. #DTRT06G-0043, September 2010.

21. Simunovic, S., Bennett, R., and Zisi., N., Enhanced Finite Element Analysis Crash Model of Tractor-Trailers: Website and User's Manual, Report No. DTRT06G-0043, June 2009.

Appendices

Appendix A Tank-Trailer Description

Table A.1 Tank Components

Baffles, Bulkheads and Shell							
Part ID	**Component ID Geometry (Hypermesh)**	**Name**	**Element Type**	**Element Thickness**	**Element Size**	**Material ID**	**Section ID**
12000100	20	Baffle_1	Shell	6.3	19	6300002	6300012
12000101	503	Baffle_2	Shell	4.7	19	6300002	6300003
12000102	552	Baffle_3	Shell	4.7	19	6300002	6300003
12000103	17	Baffle_4	Shell	4.738	19	6300002	6300003
12000104	506	Baffle_5	Shell	6.3	19	6300002	6300002
12000105	508	Baffle_6	Shell	4.7	19	6300002	6300003
12000104	25	Bulkhead_1	Shell	6.35	19	6300002	6300002
12000105	514	Bulkhead_2	Shell	4.7	19	6300002	6300003
12000106	505	Bulkhead_3	Shell	4.7	19	6300002	6300003
12000107	2902	Bulkhead_4	Shell	4.7	19	6300002	6300003
12000108	555	Bulkhead_5	Shell	4.7	19	6300002	6300003
12000107	558	Bulkhead_6	Shell	4.7	19	6300002	6300003
12000108	559	Bulkhead_7	Shell	4.7	19	6300002	6300003
12000109	30	Bulkhead_8	Shell	6.35	19	6300002	6300008
12000001	1	Outer Shell	Shell	5.588	19	6300003	6300019
12000002	9		Shell	5.588	19	6300003	
12000003	2		Shell	5.588	19	6300003	
12000004	10		Shell	5.588	19	6300003	
12000005	4		Shell	5.588	19	6300003	

Table A.2 Fifth Wheel Components

Fifth Wheel							
Part ID	**Component ID Geometry (Hypermesh)**	**Name**	**Element Type**	**Element Thickness**	**Element Size**	**Material ID**	**Section ID**
10000020	75	Fifth Wheel Pin	Solid		6	6300005	45
10000021	71	Fifth-Wheel-1	Shell	7.9	12	6300005	6300006
10000022	72	Fifth-Wheel-2	Shell	4.8	12	6300005	6300007
10000023	74	Fifth-Wheel-3	Shell	7.9	12	6300005	6300006
	565		Shell	7.9	12		6300006
10000024	73	Fifth-Wheel-4	Shell	6.3	12	6300005	6300002
	564		Shell	6.3	12		
10000025	76	Fifth-Wheel-5	Shell	4.8	12	6300005	6300007
	566		Shell	4.8	12		

Table A.3 Chassis Components

Chassis Frame							
Part ID	**Component ID Geometry (Hypermesh)**	**Name**	**Element Type**	**Element Thickness**	**Element Size**	**Material ID**	**Section ID**
10000014	43	Beam_1	Shell	7.9	12	6300004	6300006
	56		Shell	7.9	12		
10000015	35	Beam_2	Shell	4.8	12	6300004	6300007
	516		Shell	4.8	12		
	529		Shell	4.8	12		
	532		Shell	4.8	12		
	534		Shell	4.8	12		
	535		Shell	4.8	12		
	536		Shell	4.8	12		
	537		Shell	4.8	12		
	538		Shell	4.8	12		
	542		Shell	4.8	12		

Table A.4 Chassis Components

Chassis Frame							
Part ID	**Component ID Geometry (Hypermesh)**	**Name**	**Element Type**	**Element Thickness**	**Element Size**	**Material ID**	**Section ID**
10000016	45	Beam_3	Shell	6.4	12	6300004	6300008
10000017	44	Beam_4	Shell	9.5	12	6300004	6300010
10000018	32	Bulk_Support	Shell	6.4	12	6300005	6300008
	33		Shell	6.4	12		
10000019	105	Fender	Shell	1.9	12	6300005	6300009
	305		Shell	1.9	12		
	365		Shell	1.9	12		
10000026	53	Rail	Shell	7.9	12	6300005	6300006
	54		Shell	7.9	12		6300006
10000027	46	Tank_Support 1	Shell	7.9	12	6300005	6300006
	47		Shell	7.9	12		6300006
	55		Shell	7.9	12		6300006
	57		Shell	7.9	12		6300006
10000028	50	Tank_Support 2	Shell	4.8	12	6300005	6300007
	52		Shell	4.8	12		
	525		Shell	4.8	12		
	526		Shell	4.8	12		
	527		Shell	4.8	12		
	549		Shell	4.8	12		
10000029	48	Tank_Support 3	Shell	9.5	12	6300005	6300010
	49		Shell	9.5	12		
10000030	51	Tank_tkg	Shell	5.6	12	6300005	6300011
10000051	18	TKE	Shell	6.3	12	6300005	6300002
	504		Shell	6.3	12		
	507		Shell	6.3	12		
	509		Shell	6.3	12		
	513		Shell	6.3	12		
	553		Shell	6.3	12		

Table A.5 Chassis Components

Chassis Frame							
Part ID	**Component ID Geometry (Hypermesh)**	**Name**	**Element Type**	**Element Thickness**	**Element Size**	**Material ID**	**Section ID**
10000031	373	TKE1	Shell	4.7	12	6300005	6300003
10000032	41	TKG1	Shell	6.4	12	6300005	6300008
	522		Shell	6.4	12		
1000033	58	TKG2	Shell	6 side, 7.9 middle	12	6300005	6300014
	68		Shell	6.2 side, 7.9 middle	12		
	560		Shell	6.2 side, 7.9 middle	12		
	561		Shell	6.2 side, 7.9 middle	12		
	562		Shell	6.2 side, 7.9 middle	12		
10000034	69	TKG3	Shell	5.6	12	6300005	6300011
	70		Shell	5.6	12		
	563		Shell	5.6	12		
10000035	64	TKG4	Shell	6.4	12	6300005	6300008
	556		Shell	6.4	12		
10000036	352	TKG5	Shell	4.7	12	6300006	6300003
	1917		Shell	4.7	12		
10000037	355	TKG6	Shell	6.4	12	6300005	6300008
	356		Shell	6.4	12		
10000038	359	TKG7	Shell	3.2	12	6300005	6300015
	360		Shell	3.2	12		
	362		Shell	3.2	12		
10000041	42	TKG8	Shell	9.5	12	6300006	6300010
	524		Shell	9.5	12		
10000047	354	TKG11	Shell	3.2	12	6300005	6300015
	1918		Shell	3.2	12		
	1919		Shell	3.2	12		
	3236		Shell	3.2	12		
10000040	2990	TKG13	Shell	4.7	12	6300005	6300003
1000050	114	TKG14	Shell	4.7	12	6300005	6300003
	2996		Shell	4.7	12		

Chassis Frame							
10000039	115	TKG15	Shell	6.3	12	6300005	6300002

Appendix B Chassis-Tank Connection Diagram

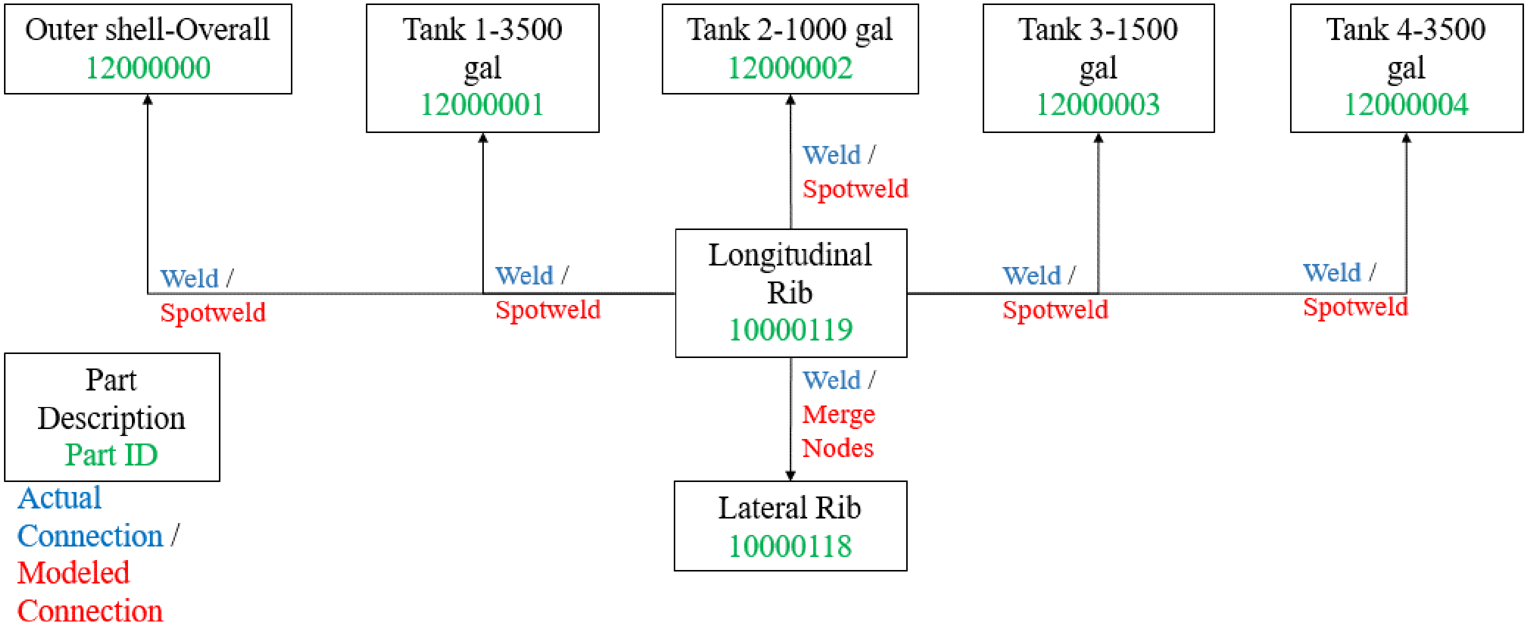

Figure B.1 Soil Strength, Initial Calibration Tests

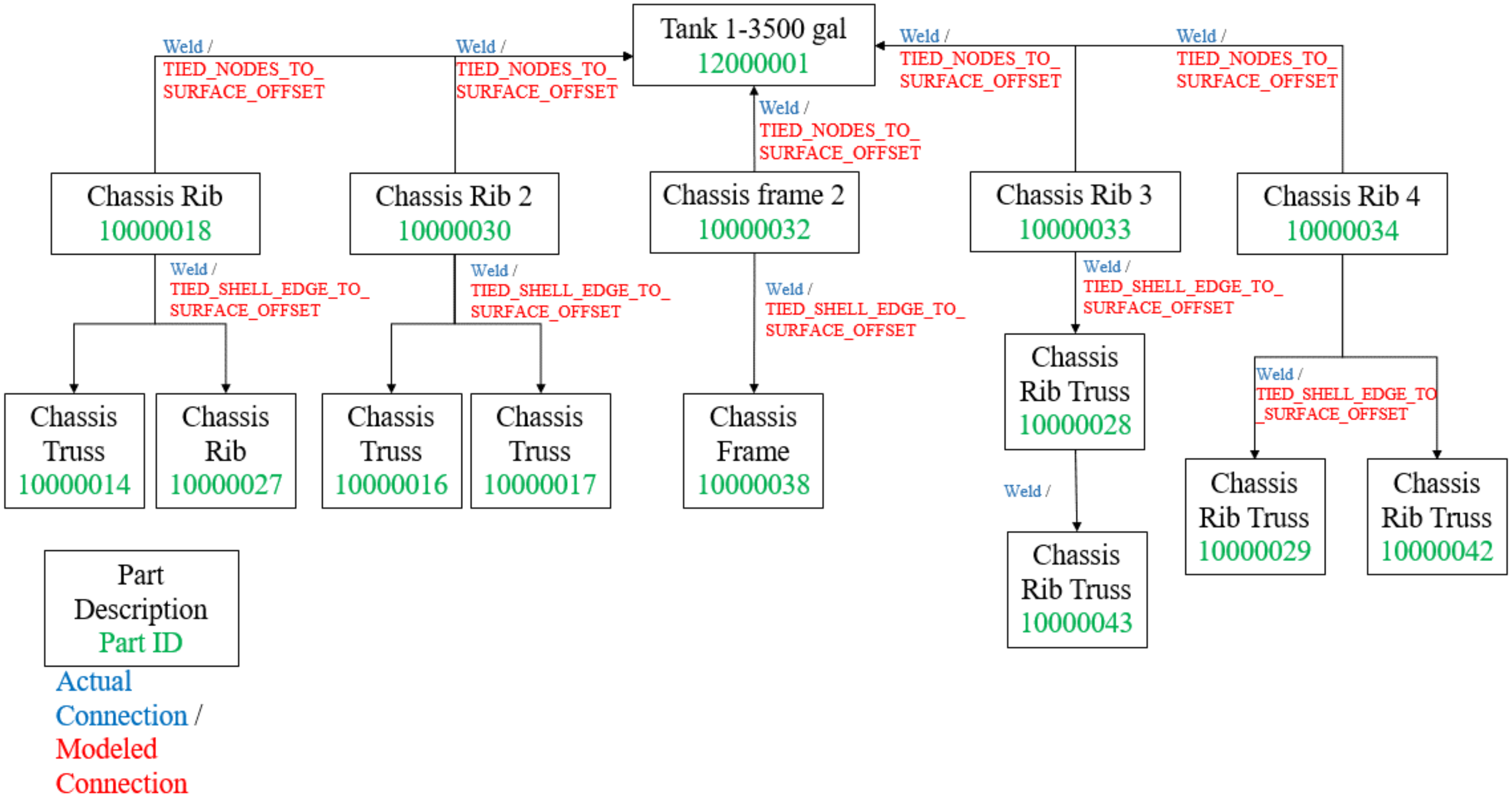

Figure B.2 Chassis to Tank-1 Connection Diagram

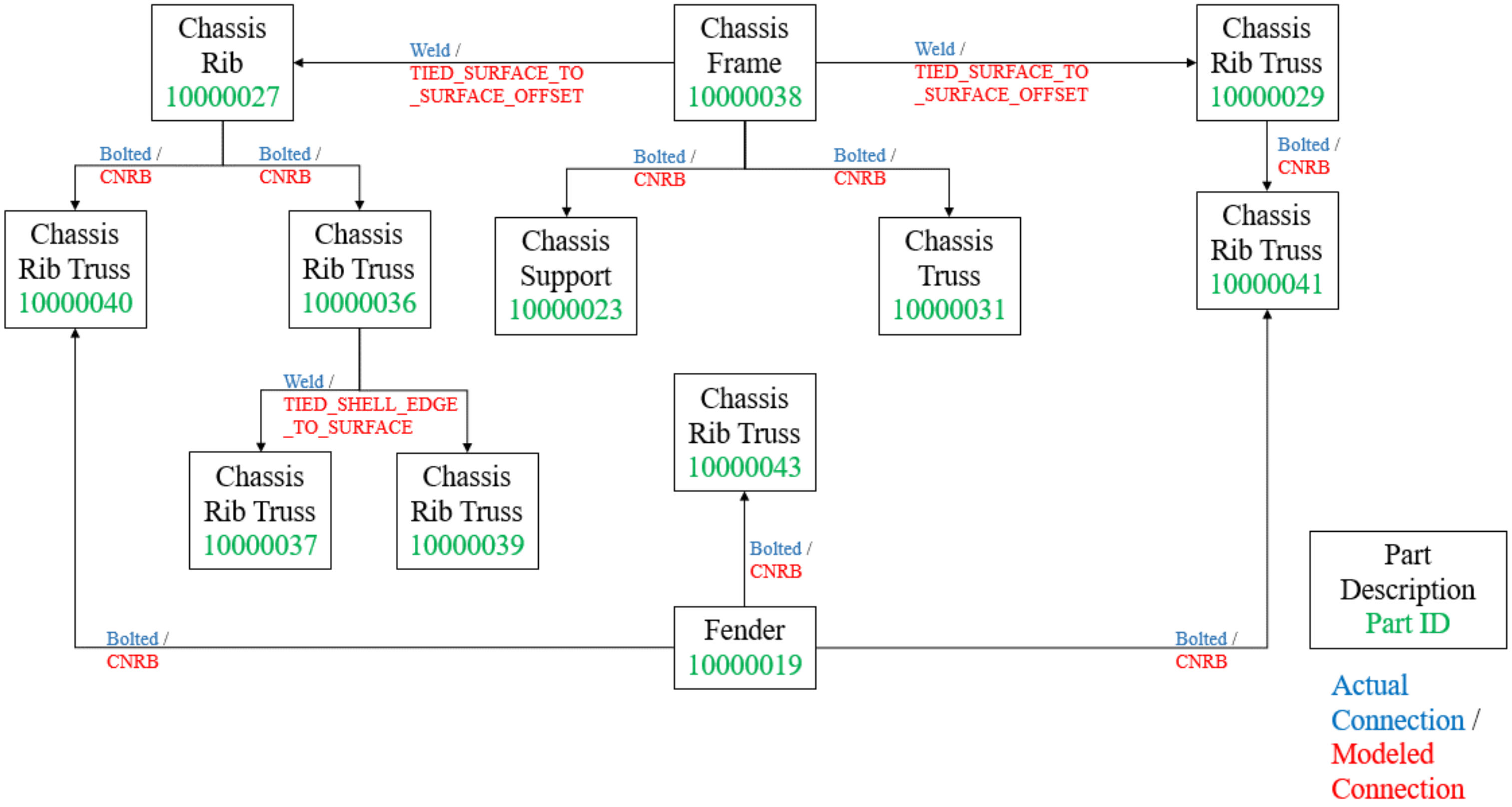

Figure B.3 Chassis Connection Diagram

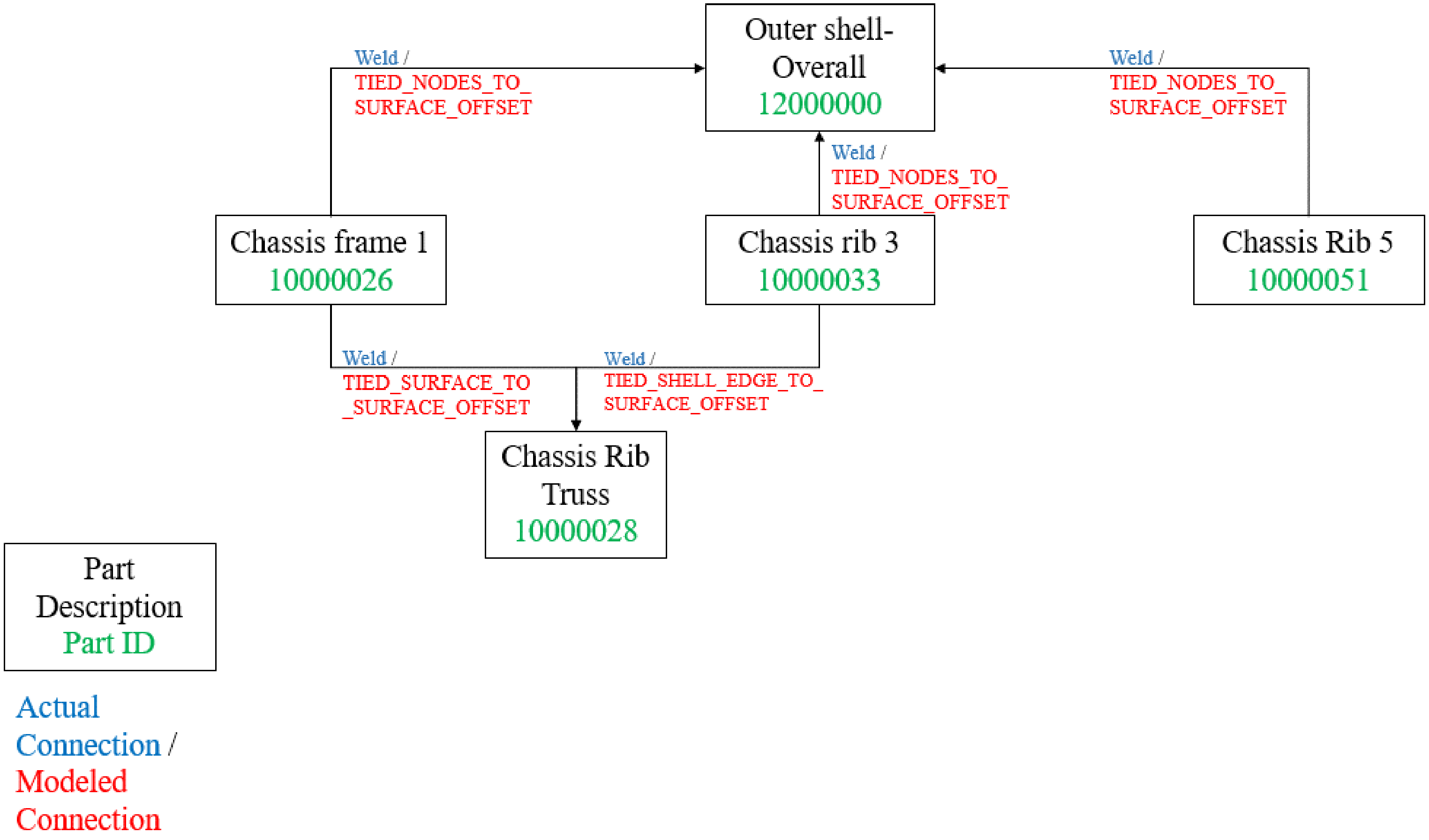

Figure B.4 Overall-Tank to Chassis Connection Diagram

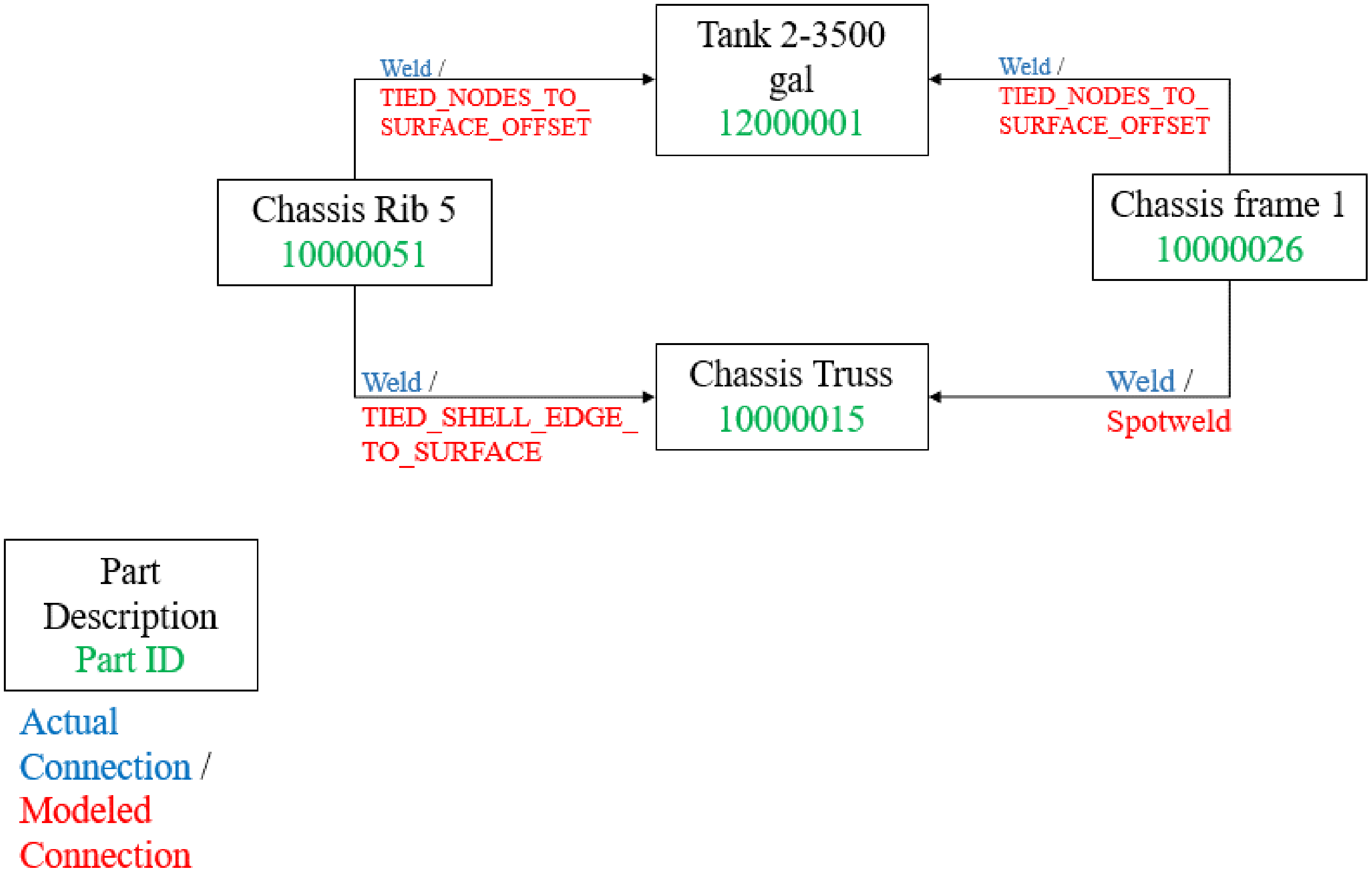

Figure B.5 Chassis to Tank-2 Connection Diagram

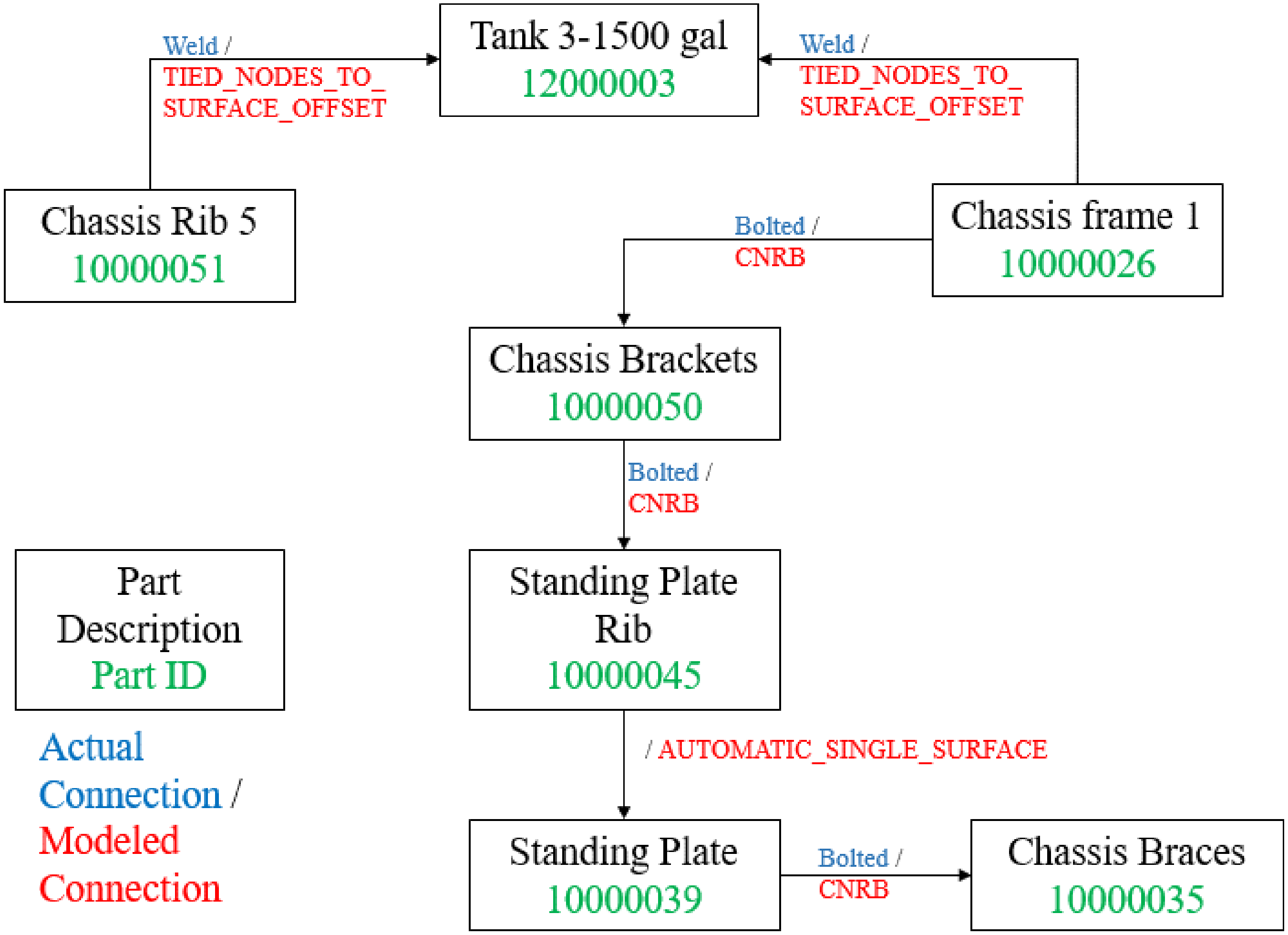

Figure B.6 Chassis to Tank-3 Connection Diagram

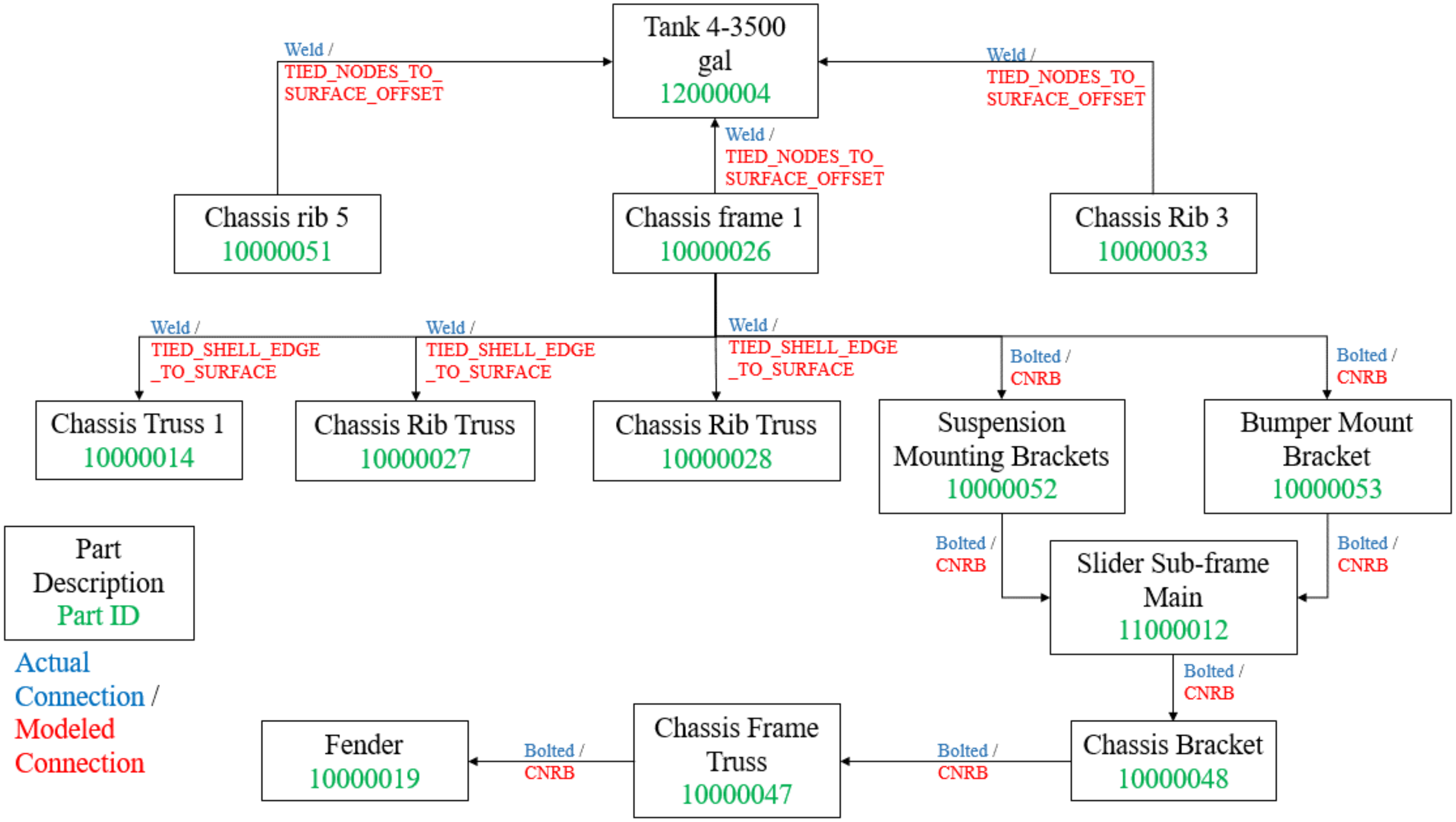

Figure B.7 Chassis to Tank-4 Connection Diagram

Appendix C Fifth Wheel-Tractor Connection Diagram

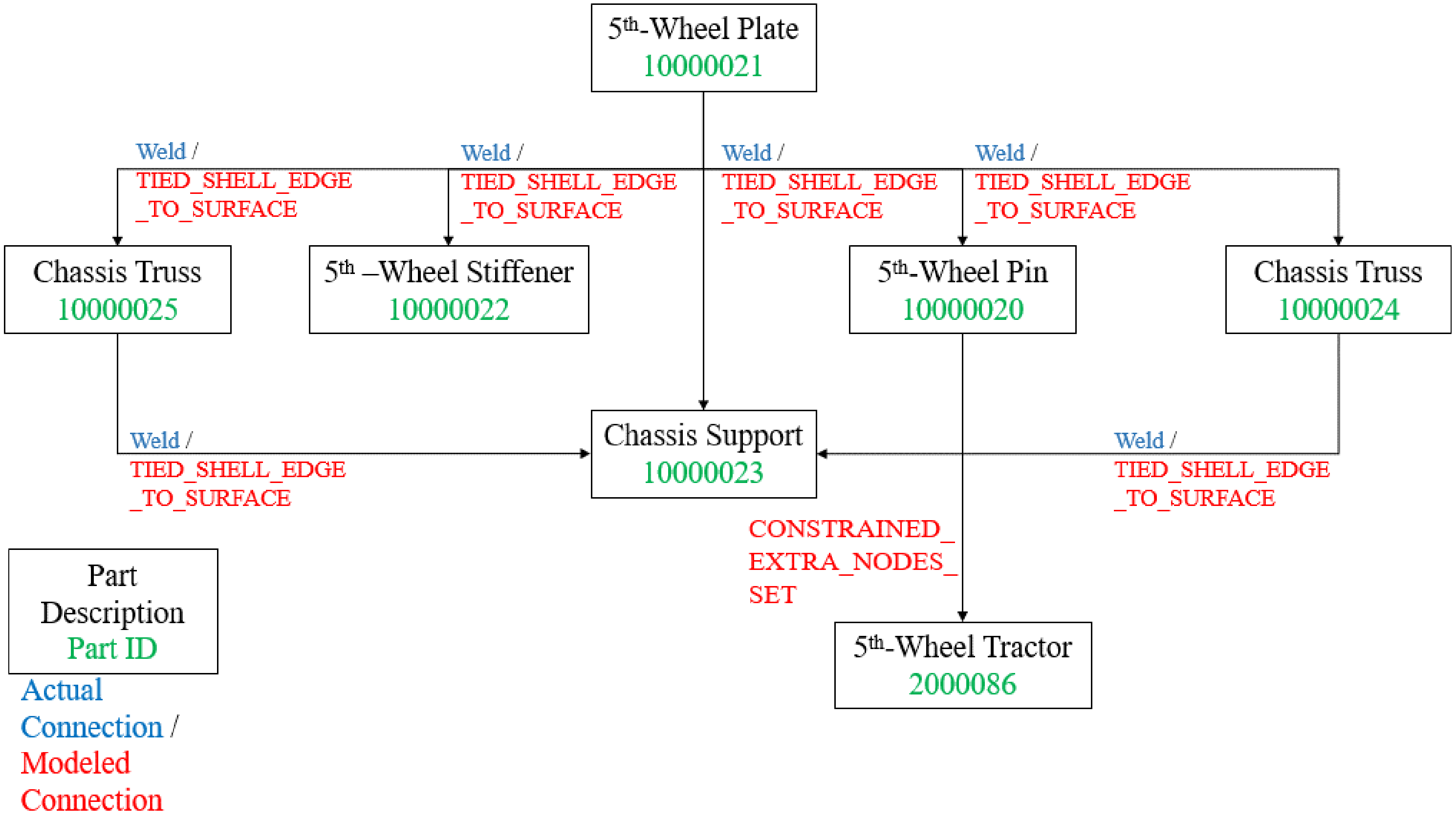

Figure C.1 Fifth-Wheel Connection Diagram

Appendix D Lagrangian Tank-Fluid Connection Diagram

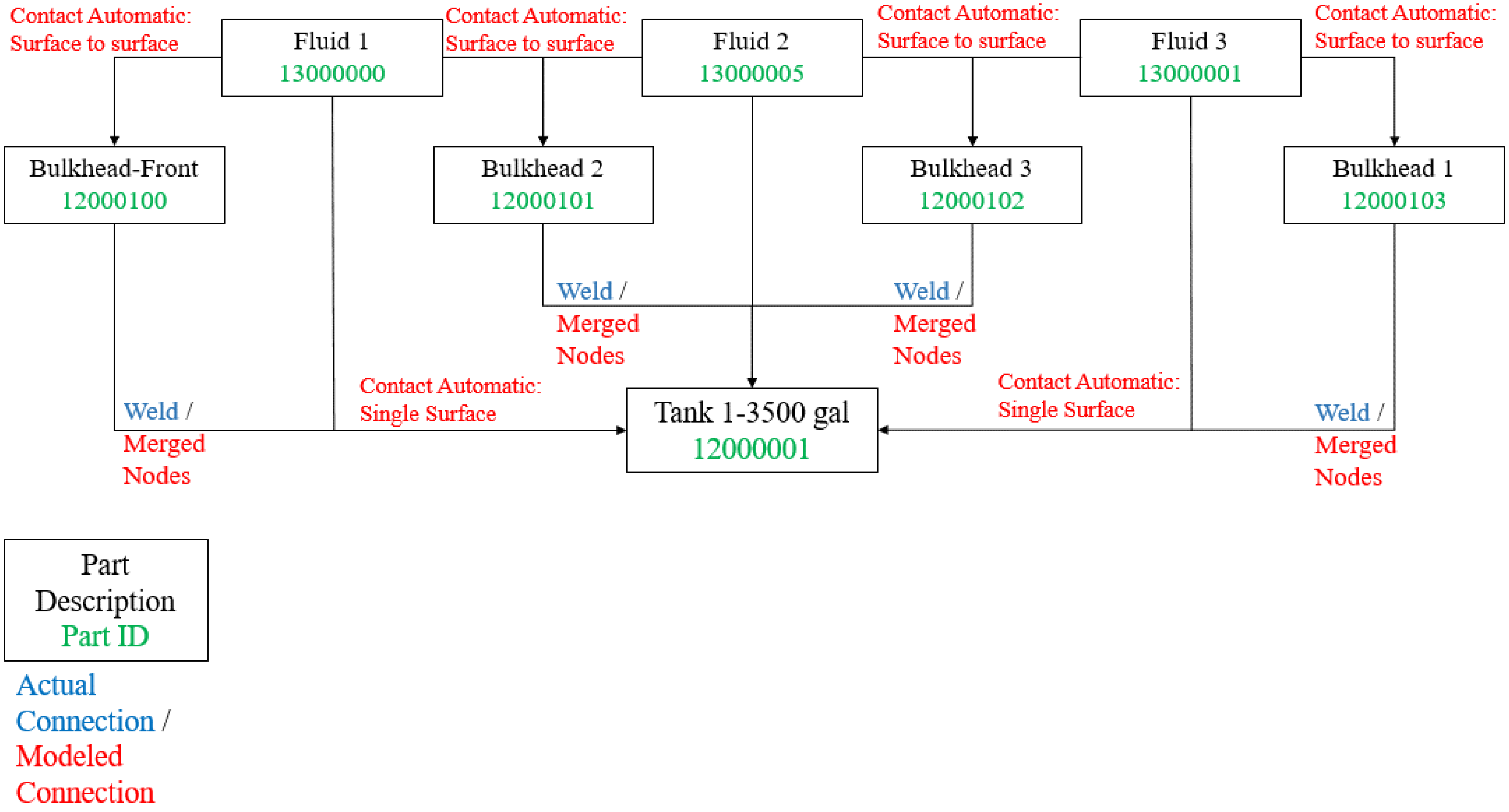

Figure D.1 Lagrangian Fluid to Tank Connection Diagram

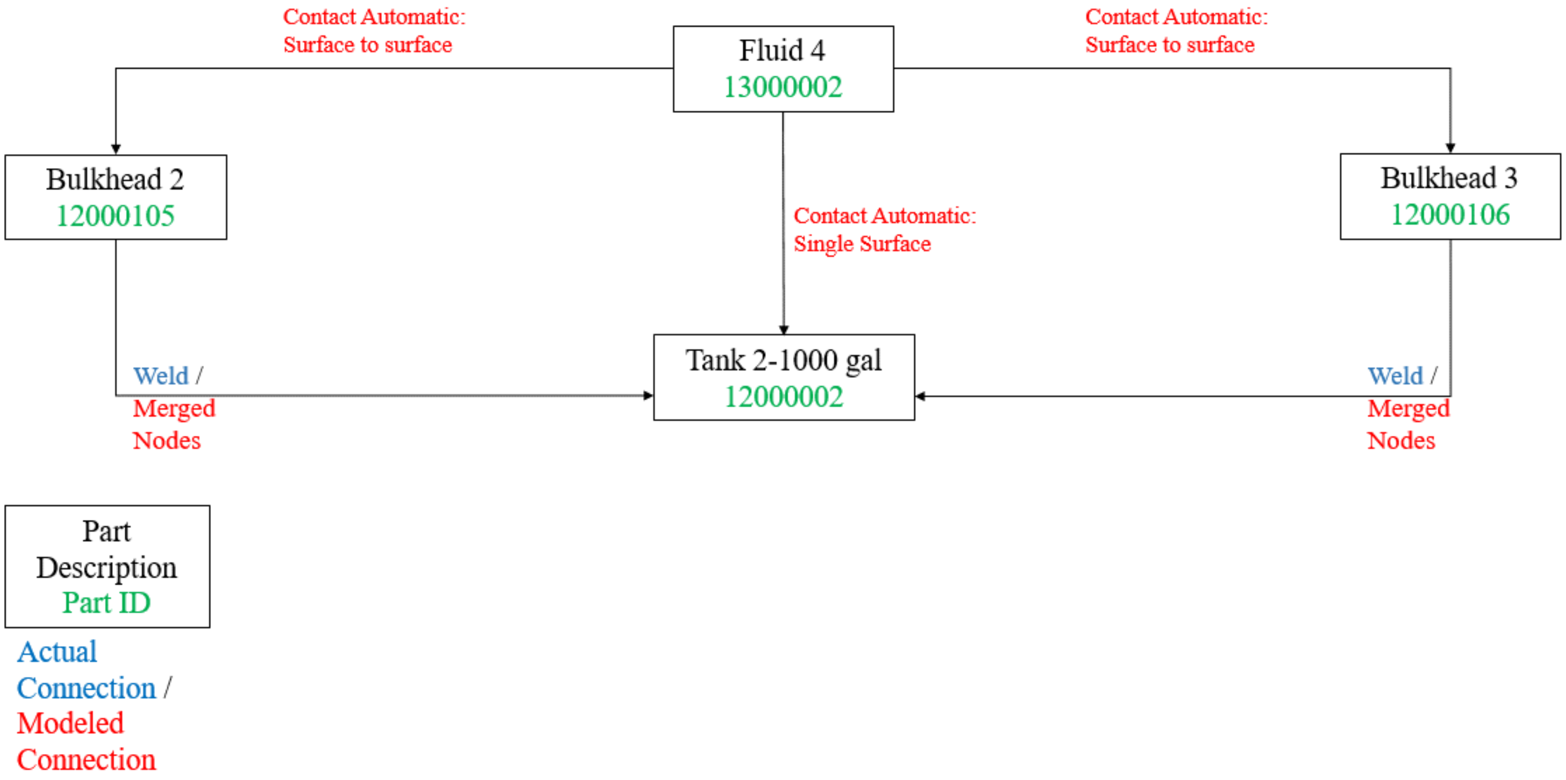

Figure D.2 Lagrangian Fluid to Tank Connection Diagram

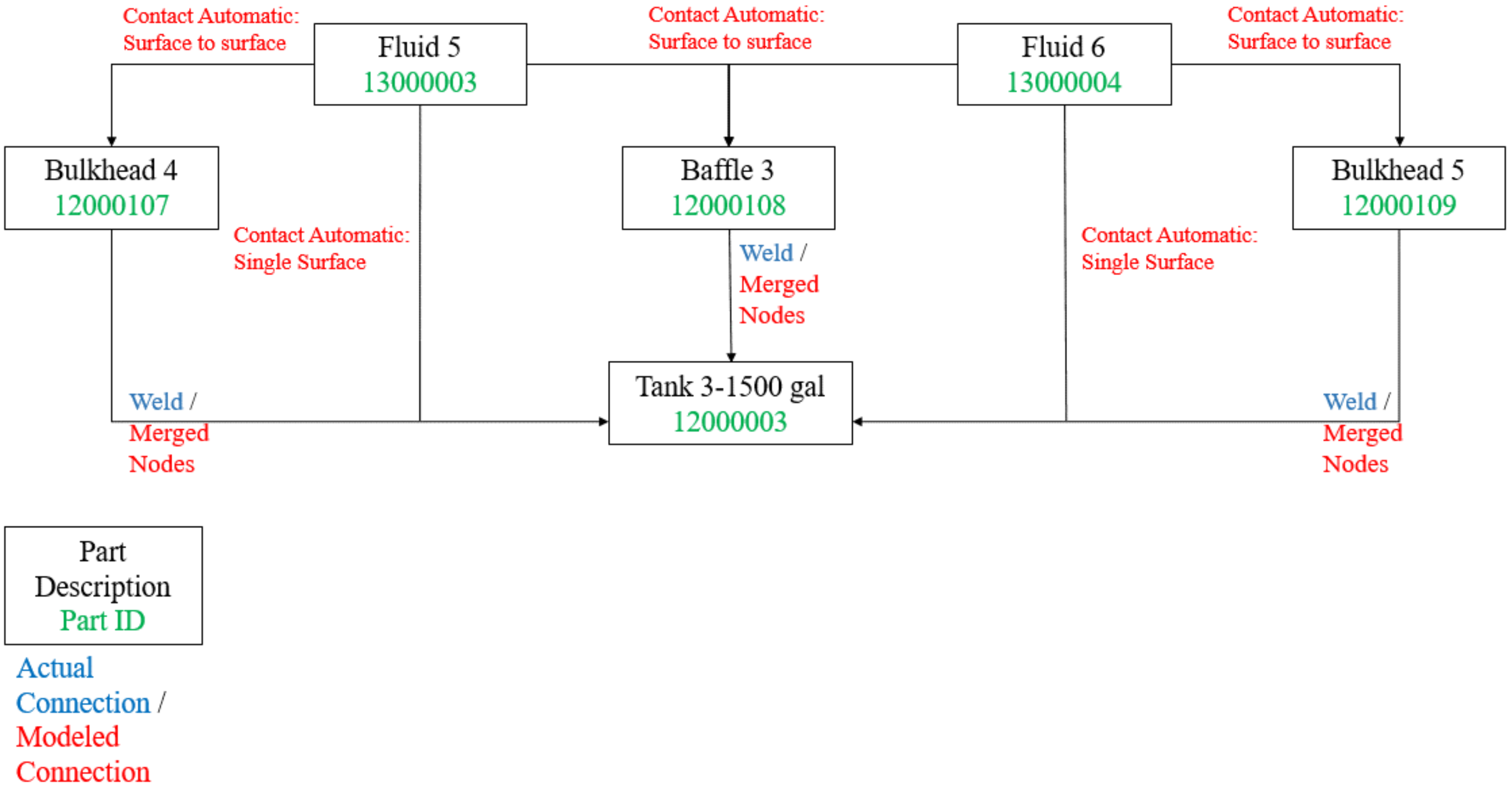

Figure D.3 Lagrangian Fluid to Tank Connection Diagram

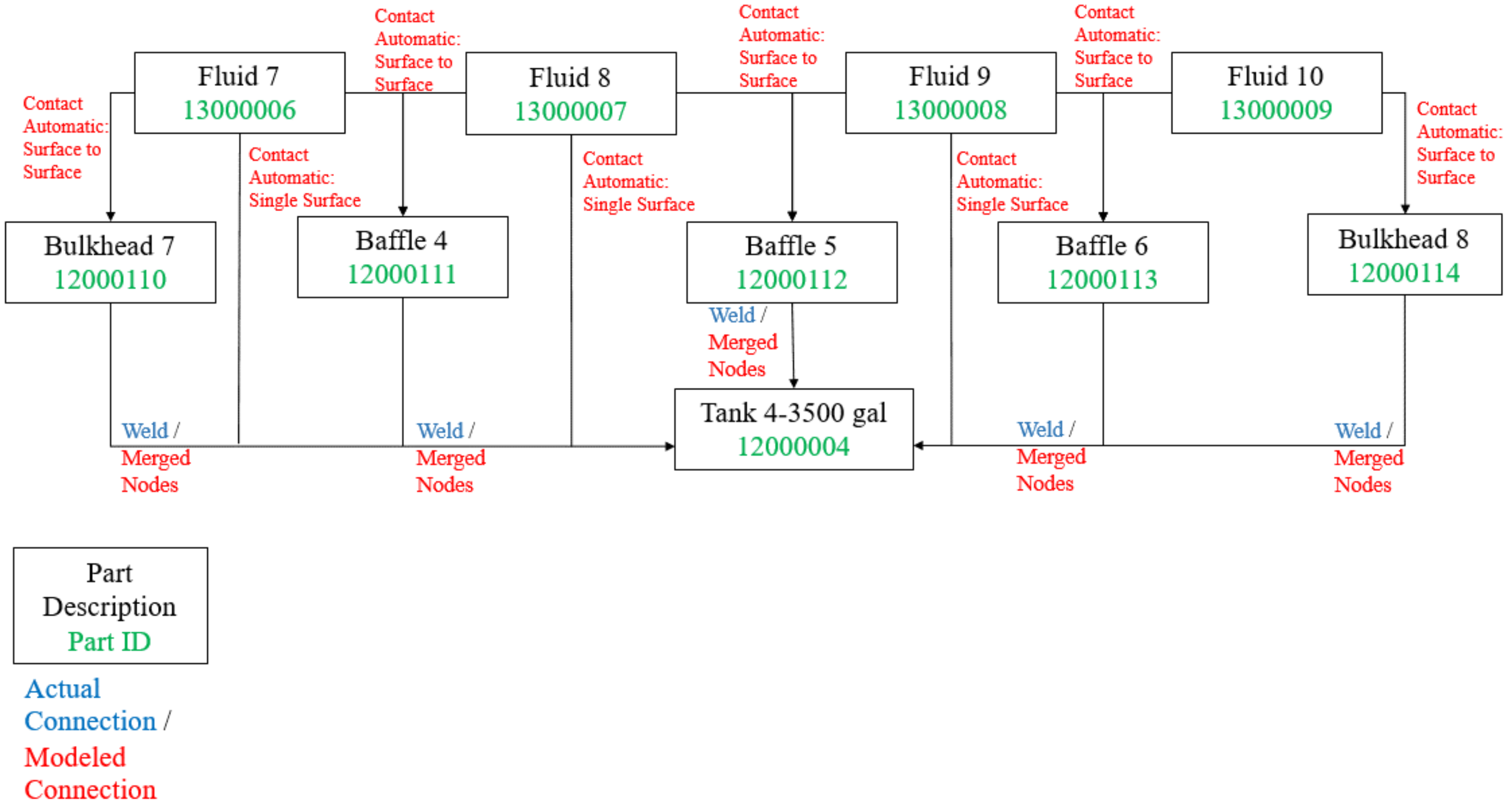

Figure D.4 Lagrangian Fluid to Tank Connection Diagram

Appendix E ALE Tank-Fluid Connection Diagram

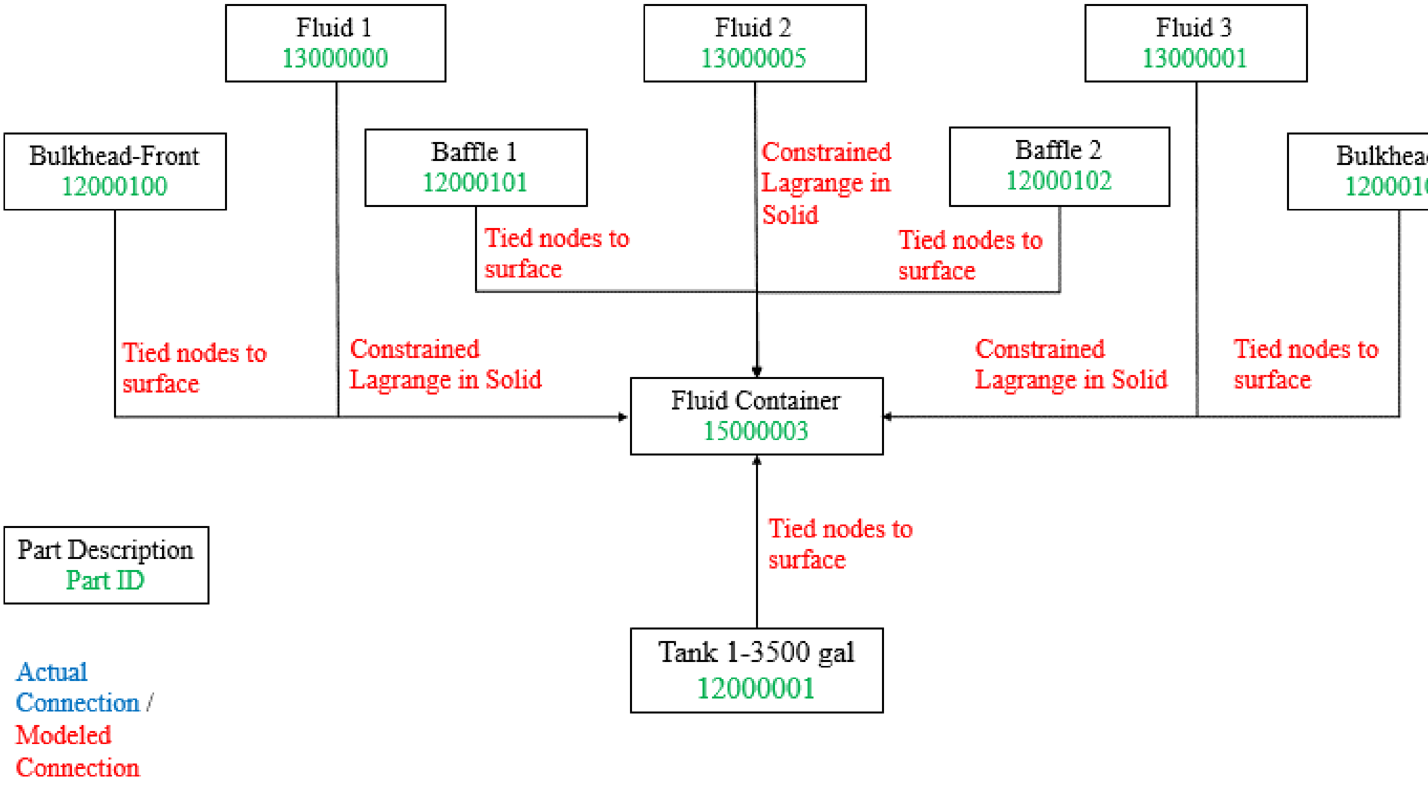

Figure E.1 ALE Fluid to Tank Connection Diagram

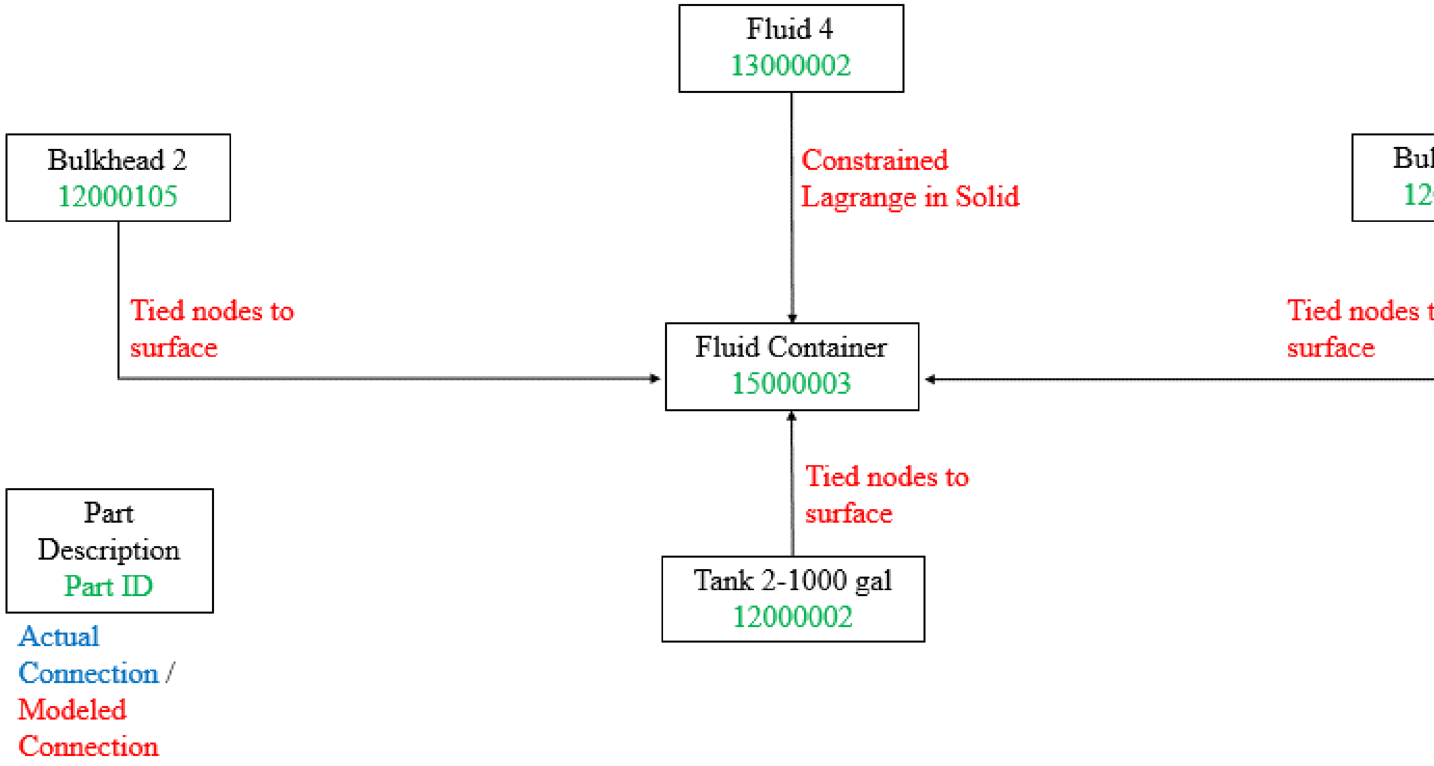

Figure E.2 ALE Fluid to Tank Connection Diagram

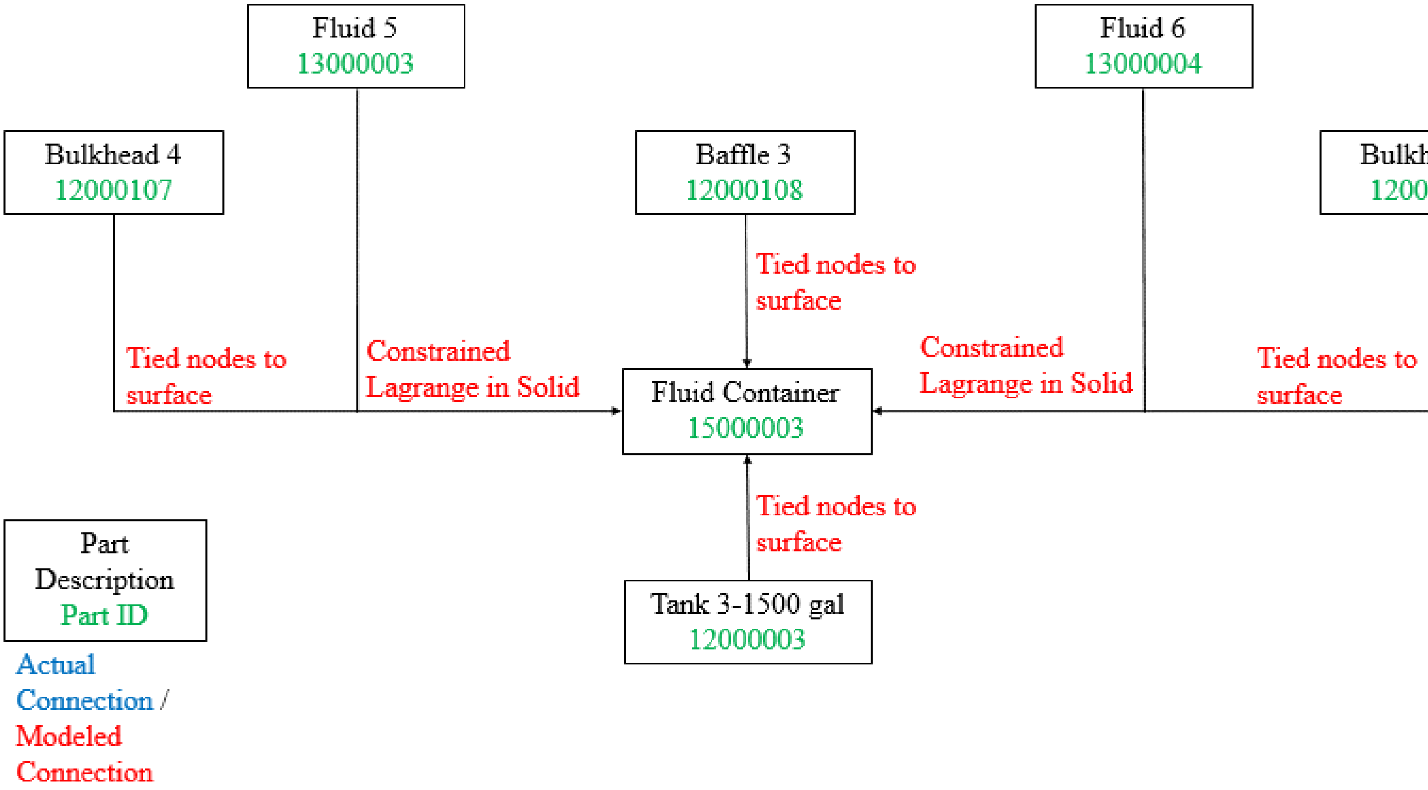

Figure E.3 ALE Fluid to Tank Connection Diagram

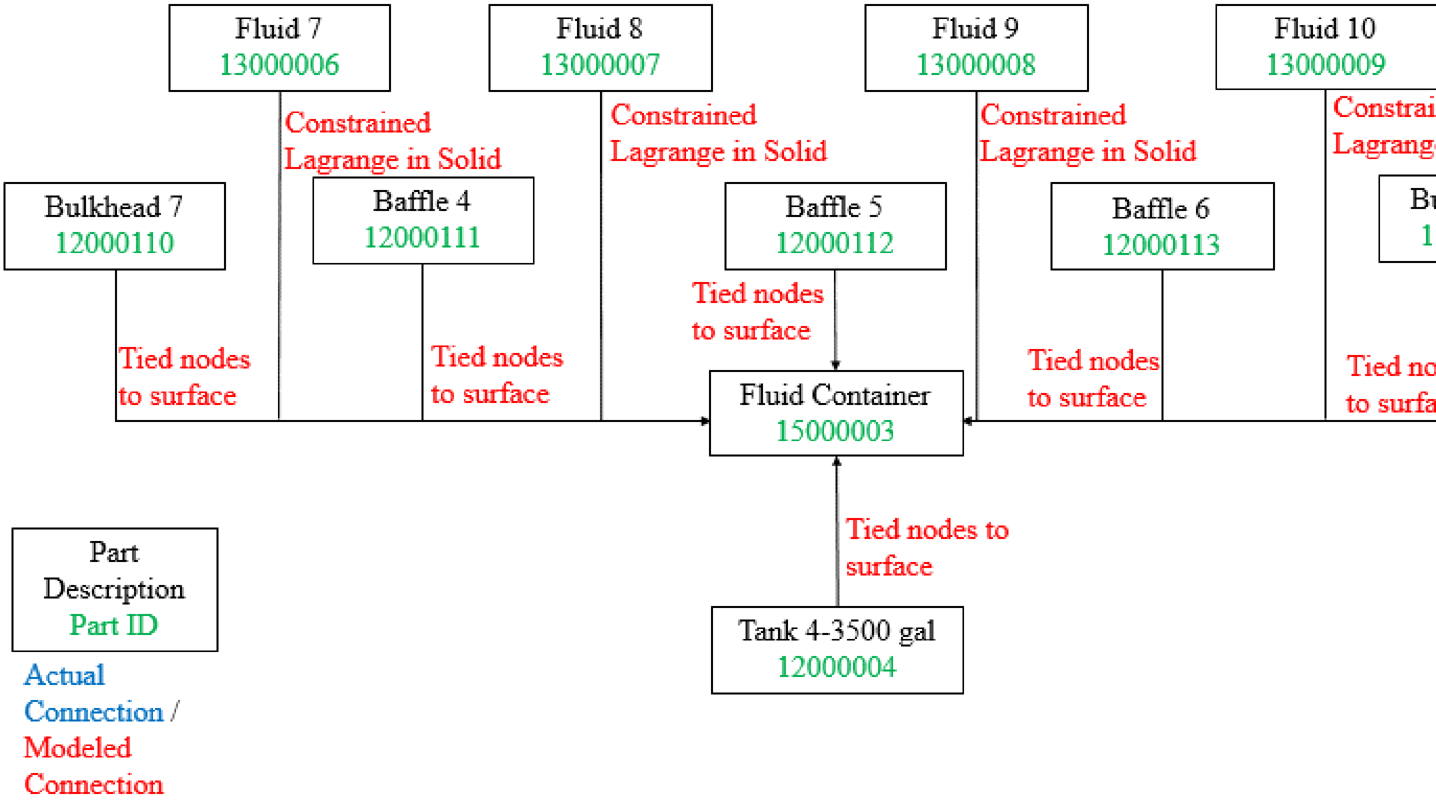

Figure E.4 ALE Fluid to Tank Connection Diagram